Hydro-mechanical response of Opalinus Clay shale: dependency on composition and burial depth

Thèse N° 7421

Présentée le 31 octobre 2019

à la Faculté de l'environnement naturel, architectural et construit
Laboratoire de mécanique des sols - Chaire gaz naturel Petrosvibri
Programme doctoral en mécanique

pour l'obtention du grade de Docteur ès Sciences

par

Eleonora CRISCI

Acceptée sur proposition du jury

Dr M. Farhat, président du jury
Prof. L. Laloui, Dr A. Ferrari, directeurs de thèse
Dr S. Giger, rapporteur
Dr D. Dewhurst, rapporteur
Prof. M. Violay, rapporteuse

2019

ÉCOLE POLYTECHNIQUE
FÉDÉRALE DE LAUSANNE

To my doubts

Acknowledgements

I am thankful to my supervisors, Prof. Lyesse Laloui and Dr Alessio Ferrari. I thank Prof. Laloui, for the great opportunity to work in such stimulating environment. He has always challenged me to get deeper insights into the things, and I believe that helped me for my professional and personal growth. I thank Dr Ferrari, to have introduced me to the joys and pains of research life, and for having transmitted me his passion for research, through his support during these years.

I wish to thank Dr M. Farhat for having chaired the examination jury, and Dr D. Dewhurst, Dr S. Giger, Prof. M. Violay for having taken part to my jury committee and for the valuable comments provided to my thesis.

I thank Nagra for the financial support to this research project. In particular I thank Dr Silvio Giger, for helping in perceiving the impact of the results I was obtaining.

I wish to thank Patrick Dubey for all the help he provided in the laboratory activities and for all the conversations we had, mostly about travels, while waiting for equipment to work. I want to thank all the laboratory technicians that have worked in the laboratory in these years, and Laurent Gastaldo and Laurent Morier for their help and support. I thank Rosana Turielle and Barbara Tinguely and their assistants for taking care of the administrative aspects of the research activities.

During these years, I had the pleasure to share the challenges of research with many wonderful people, and some of those become very good friends. I wish to thank Alessandro and Felipe, that are now enriching the research in other continents, and Alberto, whose support was essential to get through the PhD life. I wish to thank Donatella and Francesco with whom I have spent my very first time at the Lms, Valentina, my former wonderful office mate, that shared with me the title of shale-girl for a long time, and Dimitrios, for his constant cheerfulness in our laboratory days. I thank Benoit that shared the office with me in the toughest part of my PhD, and I am sure it was no piece of cake for him. I wish to thank Aldo, whose office door has always been open to discuss. I am very grateful to Angelica, Barnaby, Chiara, Corentin, Elena, Etienne, Gianluca, Jacopo, José, Jinu, Mateo, and all the former and current LMS and LEMR people with whom I had good times together, having a coffee, or, more often, a beer.

I am very thankful to some friends with whom during the last year I have had wonderful adventures everywhere in the world: Stefania, Marija, Aldo, Alberto and Ugo. I can't wait for our next trip, hopefully soon.

I am thankful for the time spent with my friends back in Italy, Antonio, Giuliana, Francesca, Katia and Roberta, that were always squeezing their schedules to meet me every time I was home.

I thank my parents Claudio and Flavia, my sister Elisabetta and my grandmother Sara, for having encouraged me in pursuing this adventure far from home, and for their endless support and love.

Last and biggest thank is for Ugo, the love of my life, for having understood me in every moment of these years, for having been by my side in good and bad times. I know I can always count on you.

Table of Contents

Abstract

Shales are sedimentary formations currently studied for their involvement in many geo-energy related applications, such as radioactive waste disposal, CO_2 sequestration, oil and gas extraction.

In Switzerland, the Opalinus Clay shale has been selected as the host formation for the construction of a repository for geological disposal for radioactive waste. Opalinus Clay is a Jurassic shale widespread in the northern part of the country, characterised by sedimentation planes (also, bedding). In the shale formation, several lithostratigraphic units have been identified. Also, the current and maximum depths that the formation has experienced are not homogeneous among the locations. Most of the research in the last 20 years have been concentrated on one of the lithofacies (characterised by high clay content), the shaly facies, in the rather shallow location of the Mont Terri Underground Rock Laboratory, and on a few other deeper sites, in the north-east of the country.

This thesis aims to study the impact of the composition and burial depth on the hydro-mechanical response of the Opalinus Clay. The results serve to estimate the geomaterial response for compositions and locations (e.g., where the disposals are planned) where the possibility to directly test the shale may be limited because of cost and time efforts.

An experimental study was carried out, to test the hydro-mechanical response, in saturated and unsaturated conditions, of samples from various locations and compositions.

Samples from shallow locations (<100 m depth) showed similar responses, at the laboratory scale, to those from deeper locations, in terms of permeability and compressibility, although clear signs of weathering were detected at the field scale for the first few tens of meters.

The hydro-mechanical response of the Opalinus Clay shale was interpreted as a layered geomaterial, composed as an alternation of two-layer types. The first (*shaly*) is composed of a clay matrix in which grains of quartz, calcite or other minerals are embedded. The latter (*sandy*) is composed by a compact quartz structure, whose pores are filled with clay. The properties of each layer type were estimated via the gathered experimental data. For each tested sample, the volumetric fraction of the shaly layer and the corresponding hydro-mechanical response were estimated. The results were verified against the experimental data, finding good agreement.

The volumetric response observed during hydraulic loading performed in free stress conditions was characterized by significant anisotropy and dependence on the sample composition. Irreversibility of the strains was investigated by performing X-ray tomographies of a specimen subjected to a hydraulic load. Cracks opening was detected both during swelling and during drying, but in different locations in the samples.

It was highlighted that samples with lower clay content, such as those belonging to the sandy facies, showed higher stiffness and shear strength, that may be considered more desirable properties for underground constructions. On the other hand, samples with higher clay content (such as those belonging to the shaly facies) were found to have a higher capacity to swell upon saturation, and therefore to potentially self-seal cracks. Further, they have lower permeability and pore throat diameter. From this perspective, the high-clay-content part of the formation has more desirable properties to behave as a barrier to fluid flow in the radioactive waste disposal context.

Keywords: Opalinus Clay, shale, radioactive waste disposal, shale characterisation, mineralogical composition, burial depth, layered structure, hydro-mechanical behaviour, anisotropy, water retention behaviour, crack opening, partial saturation.

Riassunto

Le shale sono formazioni di origine sedimentaria attualmente molto studiate per il loro coinvolgimento in applicazioni ingegneristiche di tipo geo-energetico, come lo stoccaggio di scorie radioattive, di CO_2 e l'estrazione d'idrocarburi.

L'Opalinus Clay è la shale scelta in Svizzera per la costruzione di depositi sotterranei di scorie radioattive. È molto diffusa nel sottosuolo del nord del paese, ed è caratterizzata da piani di sedimentazione. In questa formazione argillosa, diverse unità litostratigrafiche sono state identificate. La profondità alla quale la shale si trova attualmente e la massima profondità raggiunta non sono comuni a tutta la formazione, ma variano tra un sito e l'altro. Gran parte delle ricerche degli ultimi 20 anni sono state condotte su una delle *facies* della formazione ad alto contenuto d'argilla, in un sito poco profondo (il laboratorio di Mont Terri) e in alcuni altri siti più profondi nel nordest.

La presente tesi ha come obiettivo lo studio dell'impatto della composizione e della profondità della formazione sulla sua risposta idro-meccanica. I risultati ottenuti consentono di stimare la risposta della shale per composizioni e siti non ancora investigati, o dove la quantità di test che si possono effettuare è limitata, per ragioni di tempo o economiche.

È stato condotto uno studio sperimentale in cui numerosi provini provenienti da siti diversi o con diversa composizione mineralogica sono stati testati. Il comportamento idro-meccanico in condizioni sature e non sature è stato investigato.

Per i provini provenienti da siti superficiali (<100 m) sono state identificate proprietà simili ai provini più profondi (e.g., permeabilità e compressibilità), sebbene chiari segni di meteorizzazione siano stati scoperti *in situ* nelle prime decine di metri di profondità.

La risposta idro-meccanica dell'Opalinus Clay è stata interpretata come quella di un materiale stratificato, composto dall'alternanza di due tipi di strati. Il primo tipo (*shaly*) è composto da una matrice argillosa in cui grani di altri minerali sono immersi. Il secondo (*sandy*) è composto da una struttura di grani di quarzo e carbonati, nei cui pori si trova la matrice argillosa. La risposta idro-meccanica dei due strati è stata calibrata su risultati sperimentali. Per ogni provino testato in laboratorio, la frazione volumetrica dello strato *shaly* è stata stimata, e con essa, la risposta idro-meccanica, trovando buon riscontro con i dati sperimentali.

La risposta volumetrica osservata durante cicli di saturazione-desaturazione, in condizioni di rigonfiamento libero, è caratterizzata da anisotropia e dipendenza dalla composizione dei provini.

L'irreversibilità delle deformazioni è stata studiata con tomografie ai raggi X di un provino soggetto a carico idraulico, individuando l'apertura di fessure sia durante la saturazione che la desaturazione, in punti diversi del provino.

È stato messo in evidenza che i provini con un contenuto di argilla minore presentano una rigidezza e una resistenza più elevata, proprietà favorevoli per la costruzione di tunnel sotterranei. D'altra parte, i provini con un contenuto d'argilla più elevato hanno una maggiore capacità di rigonfiare durante la saturazione, e quindi di sigillare fessure che possono crearsi nella formazione. Inoltre, hanno una permeabilità e dimensione dei pori inferiore, proprietà favorevoli per l'azione di barriera che la shale deve compiere nel contesto dello stoccaggio delle scorie nucleari.

Parole chiave: Opalinus Clay, shale, stoccaggio di scorie radioattive, caratterizzazione della shale, composizione e struttura, profondità, struttura a strati, comportamento idro-meccanico, anisotropia, curve di ritenzione dell'acqua, apertura di fessure, parziale saturazione.

List of Symbols

Greek Symbols

α	Biot coefficient	-
α_{oed}	Biot coefficient in oedometric conditions	-
γ_{Hg}	Surface tension of mercury	N/m
γ_w	Unit weight of water	N/m^3
δ_{ij}	Kronecker delta	-
ε	Volumetric strain	-
ε_0	Strain at the beginning of the step	-
ε_i	Strain at the end of the step	-
ε_a	Axial strain	-
ε_r	Radial strain	-
ε_f	Strain at failure	-
ε_s	Deviatoric strain	-
$\dot{\varepsilon}$	Strain rate	1/s
$\varepsilon^{\perp}$	Strain in the direction perpendicular to bedding	-
$\varepsilon^{//}$	Strain in the direction parallel to bedding	-
ε_{ij}	Strain tensor	-
θ	Contact angle between soil and mercury	°
ϑ_i	Volumetric fraction of the *i* component	-
ϑ_{shaly}	Shaly volumetric fraction	-
ϑ_{sandy}	Sandy volumetric fraction	-
ρ	Bulk density	g/m^3
ρ_s	Solid density	g/m^3
$\rho_{s,c}$	Clay mineral density	g/m^3
$\rho_{s,nc}$	Non-clay mineral density	g/m^3
ρ_w	Deaired water density	g/m^3
σ_v	Vertical total stress	Pa
σ'_a	Axial effective stress	Pa

σ'_r	Radial effective stress	Pa
σ'_v	Vertical effective stress	Pa
σ'_{ij}	Effective stress tensor	Pa
σ_{ij}	Total stress tensor	Pa
λ	Parameter for the drainage condition in triaxial testing	-
φ'	Mohr-Coulomb parameter – shear strength angle	°
$\tilde{\varphi}_c$	Solid volume fraction of the clay component	-
$\tilde{\varphi}_{nc}$	Solid volume fraction of non-clay component	-
$\tilde{\varphi}_{shaly}$	Volumetric solid fraction of the shaly layer	%
$\tilde{\varphi}_{sandy}$	Volumetric solid fraction of the sandy layer	%
v	Poisson's ratio	-
v_1	Poisson's ratio parallel to the bedding planes	-
v_2	Poisson's ratio perpendicular to the bedding planes	-
v_1^u , v_2^u	Undrained Poisson's ratios	-
$v_{1,i\ (or\ j)}$	Poisson's ratio parallel to the bedding planes for *i (or j)* layer	-
$v_{2,i\ (or\ j)}$	Poisson's ratio perpendicular to the bedding planes for *i (or j)* layer	-
ψ	Dilatancy angle	°
Ψ	Total suction	Pa
Ψ_0	Initial total suction	Pa

Roman Symbols

a	Regression parameter in hydraulic conductivity fitting	-
A	Clay volumetric fraction in the shaly layers	-
b	Regression parameter in hydraulic conductivity fitting	-
B	Skempton *B* pore water pressure coefficient	-
B_{obs}	Measured Skempton *B* pore water pressure coefficient	-
$B_{correct}$	Corrected Skempton *B* pore water pressure coefficient	-
c	Clay volume fraction	-
c'	Mohr-Coulomb parameter - cohesion	Pa

c_v	Oedometric consolidation coefficient	m^2/s
$c_{v,i}$	Isotropic consolidation coefficient	m^2/s
$c_{v,\perp}$	Oedometric consolidation coefficient perpendicular to bedding	m^2/s
$c_{v,//}$	Oedometric consolidation coefficient parallel to bedding	m^2/s
C	Oedometric pore water pressure coefficient	-
C_i	Compressibility in isotropic conditions	Pa^{-1}
C_α	Rate of secondary compression	-
C_s	Swelling index	-
C_c	Compressibility index	-
$C_{c,i}$	Compressibility index for the *i* component	-
d	Pore diameter	m (*n*m)
D	Sample diameter	m (mm)
e	Void ratio	-
$e_{1,i}$	Void ratio of the *i* component at vertical load of 1 MPa	-
$e_{100,i}$	Void ratio of the *i* component at vertical load of 100 MPa	-
$e_0^{\perp}$	Initial void ratio of sample loaded perpendicular to bedding	-
$e_0^{//}$	Initial void ratio of sample loaded parallel to bedding	-
$e_{diff,\%}$	Percent difference in void ratio	-
e_{Hg}	Mercury intruded void ratio	-
e_{shaly}	Void ratio of the shaly layer	-
e_{sandy}	Void ratio of the sandy layer	-
E_{oed}	Oedometric modulus	Pa
$E_{oed,\perp}$	Oedometric modulus perpendicular to bedding	Pa
$E_{oed,//}$	Oedometric modulus parallel to bedding	Pa
E_1	Young's modulus parallel to the bedding planes	Pa
E_2	Young's modulus perpendicular to the bedding planes	Pa
E_1^u, E_2^u	Undrained Young's moduli	
$E_{1,ref}, E_{2,ref}$	Drained Young's moduli reference value at 1 MPa	
f	Clay-mineral content (in weight)	-

F	Clay volumetric fraction in the sandy layers	-
G_1	Shear modulus parallel to bedding	Pa
G_2	Shear modulus perpendicular to bedding	Pa
h	Sample height	m
H	Drainage length	m
I_p	Plasticity index	-
K	Bulk modulus	Pa
K_s	Bulk modulus of the solid phase	Pa
K_f	Bulk modulus of the fluid	Pa
k	Hydraulic conductivity	m/s
k_v	Hydraulic conductivity in v-direction	m/s
$k_\perp$	Hydraulic conductivity perpendicular to bedding	m/s
$k_{//}$	Hydraulic conductivity parallel to bedding	m/s
M	Failure criteria parameter	-
M^*	Slope of the volumetric – deviatoric strain curve	-
M_w	Mass of water	g
$M_{p,w}$	Mass of the calibrated pycnometer and water	g
$M_{p,w,s}$	Mass of the pycnometer, sample and water	g
$M_{s,d}$	Dry mass	g
$M_{s,w}$	Wet mass	g
M_s	Solid mass	g
$M_{s,c}$	Solid clay mass	g
$M_{s,nc}$	Solid non-clayey mass	g
$M_{s,c,shaly}$	Solid clay mass in the shaly layer	g
$M_{s,nc,shaly}$	Solid non-clayey mass in the shaly layer	g
$M_{s,c,sandy}$	Solid clay mass in the sandy layer	g
$M_{s,nc,sandy}$	Solid non-clayey mass in the sandy layer	g
n	Porosity	-
n_1	Young modulus E_1 power parameter	-
n_2	Young modulus E_2 power parameter	-

n_{cn}	Porosity of large grain structure	-
n_n	Porosity of small grain structure	-
o	Failure criteria parameter	Pa
p	Isotropic total stress	Pa
p'	Isotropic effective stress	Pa
p_{Hg}	Pressure of mercury	Pa
PI	Plasticity index	-
q	Deviatoric stress	Pa
RH	Relative humidity	%
S_r	Degree of saturation	-
S_{r0}	Initial degree of saturation	-
t	Time	s
t_f	Time at failure	s
t_{100}	Consolidation time	s
u_a	Air pressure	Pa
u_e	Excess pore water pressure	Pa
u_w	Pore water pressure	Pa
V	Volume of the specimen	m^3
V_L	Volume of fluid in the pore-water lines	m^3
V_{Hg}	Volume of mercury	m^3
V_s	Volume of the solid material	m^3
V_v	Volume of voids	m^3
V_s	Volume of the solid	m^3
$V_{s,c}$	Volume of the solid clay fraction	m^3
$V_{s,nc}$	Volume of the solid non-clayey fraction	m^3
$V_{s,c,shaly}$	Volume of the solid clay fraction in the shaly layer	m^3
$V_{s,nc,shaly}$	Volume of the solid non-clayey fraction in the shaly layer	m^3
$V_{s,c,sandy}$	Volume of the solid clay fraction in the sandy layer	m^3
$V_{s,nc,sandy}$	Volume of the solid non-clayey fraction in the sandy layer	m^3
$V_{v,shaly}$	Volume of voids in the shaly layer	m^3

$V_{v,sandy}$	Volume of voids in the sandy layer	m^3
w	Water content	-
w_0	Initial water content	-
w_L	Liquid limit	-
w_P	Plastic limit	-
x_c	Clay mass fraction	-
x_{nc}	Non-clayey mass fraction	-

Chapter 1

Introduction

1. Introduction

1.1. General background

Shales are sedimentary formations widespread in the subsurface. They are estimated to constitute about 55%[1] of the sedimentary formations on Earth and consequently are often encountered in engineering applications.

Shales are mainly constituted of clay- and silt-sized particles, compacted and partially cemented. Typical features of the shales are thin laminations in the plane of sedimentation, also referred to as bedding, and the fissility, namely the weakness in the bedding planes, that tend to cause the shale to break along those planes.

Shale composition and degree of cementation can vary largely among sites and depths. The main components are usually clay minerals, with variable percentages of carbonates and silica. Organic matter may be significant (~few %), as in the case of black organic shales which act as sources of oil and natural gas. At very shallow depth, shales can be found in highly weathered conditions, causing them to behave similarly to soils. On the other hand, at great depth, compaction and cementation make the shale to behave more similarly to sedimentary rock.

Typical characteristics are low porosity (~10%), small pore size (in the *nm* range), low permeability (in the *nD* range), high stiffness (few to tens of *GPa*) and the capacity to swell/shrink when in contact with fluids.

Shales share some characteristics with soil and others with rocks. Cementation, typical of rocks, is only partially developed in shales, which, however, present higher strength compared to overconsolidated clays. On the other hand, shales' volumetric response, stiffness and strength, similar to clays, are highly sensitive to fluid content and chemistry.

Because of the sensitivity to fluids, shale represents a problematic geomaterial for wellbores and tunnels excavation.

Currently, a significant amount of research effort is devoted to shales, mainly because they are involved in several energy-related engineering applications.

[1] Columbia Encyclopaedia

The disposal of radioactive or dangerous waste in underground tunnels

For the final disposal of radioactive/hazardous waste, shales represent a possible host material in multi-barrier repository systems. In particular, the capacity of self-sealing and self-healing cracks when in contact with wetting fluids helps to guarantee the insulation of the waste from the external environment.

Storage of CO_2

In this application, shale represents the caprock. Carbon-dioxide is injected in a reservoir rock (for instance a sandstone), and the stratum of shale on top of it prevents the leakage of the CO_2 to the atmosphere. The low porosity and the high retention capacity help in constraining the gas in the underlying reservoir.

Oil and gas extraction

As mentioned before, shale can be rich in organic matter (few %). Part of the organic matter deposited with the clay in the shale formation is transformed, because of burial and temperature increase, into oil and natural gas trapped in the small pores. This kind of shales is referred to as unconventional reservoirs for oil and gas. Conventional reservoirs are often sandstones (porosity >20%, permeability in the mD range), in which drilled wells can exploit the oil and gas. In the case of unconventional reservoirs, drilling wells is not sufficient as the oil/gas is trapped in the pores and will not naturally flow to the wells. Hydraulic fracturing (injection of a high amount of water at pressure) is employed to enhance the permeability of the reservoir.

1.1.1. A focus on radioactive waste disposal in Switzerland

Switzerland has 5 operating nuclear power plants that are responsible for about 40% of Swiss electricity production. In 2011 the Swiss Federal Council decided not to install any new reactor and to phase out the nuclear power gradually.

The radioactive waste produced by the power plants, but also from medicine, industry or research activities, needs to be handled with care and safely stored. The worldwide recognised solution for radioactive waste is the disposal in stable geological formations. Switzerland decided to adopt so-called multi-barrier systems. The radioactive waste will be vitrified, placed in metal canisters, surrounded by a buffer of swelling bentonite (engineered barriers) and emplaced in tunnels excavated in underground geological formations (geological/natural barrier).

The produced waste is generally subdivided into two categories: high-level waste (HLW), and low/intermediate level (L/ILW) waste.

The following volumes of waste are estimated[2] by considering the lifetime of the Swiss nuclear power plants and the additional waste produced in medicine, industry and research:

- High-level waste (HLW): 9'400 m^3
- Low/intermediate-level waste (L/ILW): 83'000 m^3

The ~100'000 m^3 of total volume to be stored via underground disposal necessitates the identification of a sufficiently large underground space (Figure 1-1), complying with a given set of safety criteria. Two deep geological repositories are planned in Switzerland: one for short-lived low/intermediate-level radioactive waste (L/ILW repository) and another for high-level radioactive waste (HLW repository), in which long-lived radioactive waste will be emplaced[3].

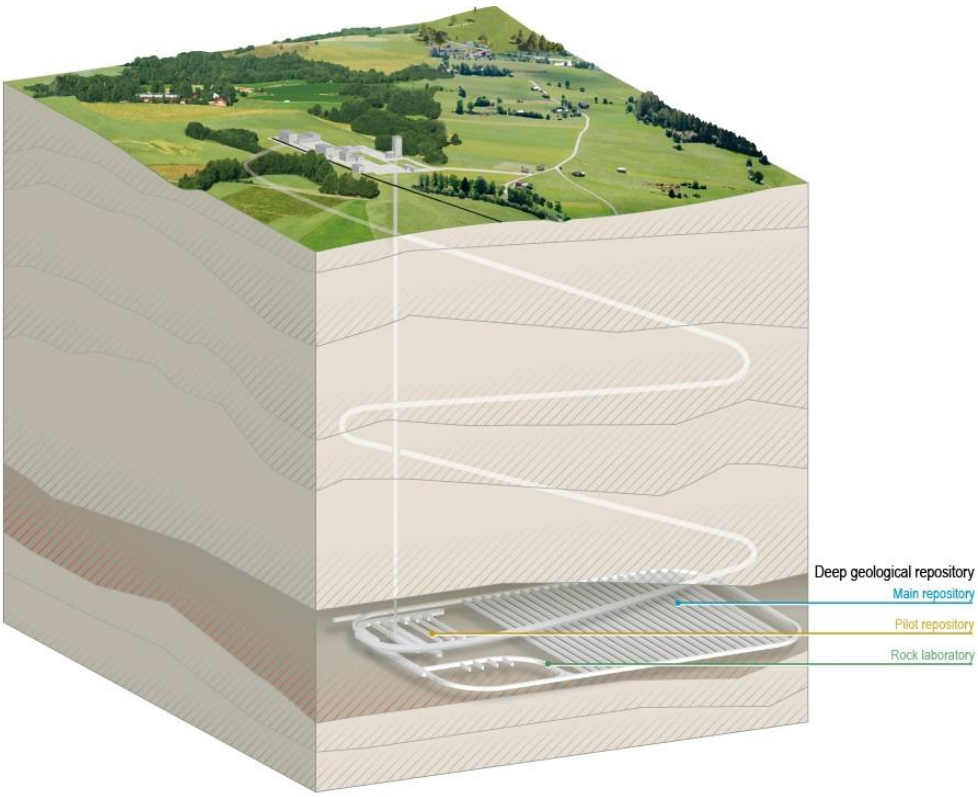

Figure 1-1 Model showing the concept for a deep geological repository (www.ensi.ch).

The site selection is regulated in the "Sectoral Plan for Deep Geological Repositories" under the responsibility of the Swiss Federal Office of Energy (SFOE), and it is carried out in three stages, in which the selection of sites is gradually narrowed down[4]. Currently, we are in *Stage 3* of the site selection, in which detailed investigations and deep boreholes are drilled to gather

[2] www.nagra.ch/en/volumesen.htm (National Cooperative for the Disposal of Radioactive Waste, NAGRA)
[3] www.ensi.ch (Swiss Federal Nuclear Safety Inspectorate, ENSI)
[4] https://www.bfe.admin.ch (Swiss Federal Office of Energy, SFOE)

detailed information on a few sites to which the selection was narrowed down at the end of *Stage 2* (November 2018).

1.2. Context and Objective of the thesis

The geological formation designated to host the repositories is the Opalinus Clay shale. This Jurassic shale is found throughout the northern part of the Switzerland, where the repository candidate sites are located. The formation has a certain degree of heterogeneity; although the main components are common to all the investigated areas (e.g., clay minerals, carbonates, quartz), the proportion among them can vary significantly within a few tens of meters.

In the last 20 years, a substantial part of the research was conducted on cores sourced at the Mont Terri (MT) Underground Rock Laboratory (URL), located at 300 m depth in the Jura Mountains. A few geotechnical studies have also been conducted on Opalinus Clay from deep boreholes in north-eastern Switzerland (e.g., Schlattingen borehole, 950 m depth).

With reference to the Mont Terri URL, many works have been dedicated to the characterisation of one of the lithofacies of the geological formation, named shaly facies, that is an argillaceous shale with lenses of sandstone. However, in the north-eastern part of the country, where the candidate sites are located, lithofacies similar to the shaly and sandy facies, defined in Mont Terri (marly shale, with lenses of sandstone), are encountered (Bossart and Thury, 2008; Jaeggi et al., 2014). Because of the large volume of waste involved, the actual repositories will most probably cross different lithofacies. The difference in the hydro-mechanical response of the two facies is therefore of great interest. While the distinction between the lithofacies is evident in some of the investigated sites (as in Mont Terri URL), the separation is less defined in others. Further, the current and maximum burial depth experienced by the formation plays a significant role in the shale response and needs to be clarified.

In this work, the main hydro-mechanical aspects of Opalinus Clay, at the laboratory scale, are studied on samples from a selection of compositions and sourcing depths. The variability of the hydro-mechanical response with respect to the composition and the burial depth is shown and analysed. From the analysis, tools to estimate the geomaterial response, based on its characterisation, are elaborated. The tools are intended to contribute to the evaluation of the expected shale response in a broad range of composition and depth conditions, and to support the identification of zones with favourable/unfavourable properties, during the design process.

1.3. Thesis structure

The thesis presents the experimental results on the hydro-mechanical behaviour of samples of Opalinus Clay in a range of composition and sourcing depths. Data from the literature are gathered and analysed in comparison with the produced data. The thesis contributes to the expansion of the knowledge on the shale response, considering the heterogeneity in the composition and the impact of the burial depth on the geomaterial performances.

Each chapter is written in a paper form, including an introduction, the adopted methodology, the results and their analyses. References backwards and forwards to other chapters are used to increase the fluency of the thesis. The chapters of the thesis are organised as follows:

Chapter 2 presents the Opalinus Clay shale characterisation. The main geological settings are provided. The sites from which Opalinus Clay samples in this thesis were collected are presented. The micro and mesostructure of the Opalinus Clay are presented. The core characterisation workflow is detailed, and the results discussed in comparison with results from the literature.

In *Chapter 3,* the one-dimensional response of saturated Opalinus Clay samples from 2 sites is presented. Intact and remoulded characteristics are discussed and the hydro-mechanical parameters are derived. The results are reviewed in light of the specimen compositions and current burial depths. In particular, the impact of geological exhumation for the Lausen borehole site is discussed. Part of this chapter has been published in a journal paper in "*Engineering Geology"*.

Chapter 4 is dedicated to the presentation of a protocol for performing saturated drained triaxial tests on low-porosity shales. The results on Opalinus Clay samples (sandy facies) are presented, and the hydro-mechanical parameters are derived.

In *Chapter 5,* using the information on the micro and mesostructure, the Opalinus Clay is re-interpreted as a layered geomaterial, in which two kinds of layers alternate: a high clay content and a high calcite-quartz content layer. Analytical solutions and empirical correlations are adopted to relate the composition to the main hydro-mechanical parameters in saturated conditions. Part of the data from Chapters 4 and 5 are used to calibrate the layer responses. The rest of the obtained experimental results and additional data from the literature are used to validate the approach.

In *Chapter 6*, the volumetric response of Opalinus Clay to water content changes is studied. Several samples, with different mineralogical compositions, were subjected to wetting and drying cycles. The impact of the composition on the volumetric response is investigated. The irreversibility in the deformational behaviour upon wetting and drying is studied following the microstructural evolution of a sample via X-ray tomography. The opening and closing of cracks during the hydraulic load are detailed. The first part of this chapter has been published in "*Geotechnique letters*".

Chapter 7 provides a general summary of the major outcomes and conclusions on the performed work. Further perspectives on future work are addressed.

1.4. References

Bossart, P., Thury, M., 2008. Mont Terri rock laboratory. Project, Programme 1996 to 2007 and results.

Jaeggi, D., Bossart, P., Wymann, L.P., 2014. Kompilation der lithologischen Variabilität und Eigenschaften des Opalinus-Ton im Felslabor Mont Terri (Expertenbericht). Swisstopo.

Chapter 2

The impact of the composition and the compaction on the Opalinus Clay characterisation

2. The impact of the composition and the compaction on the Opalinus Clay characterisation

Part of the results presented in this chapter was published in:

Journal paper: "*Crisci, E., Ferrari, A., Giger, S.B., Laloui, L., 2019. Hydro-mechanical behaviour of shallow Opalinus Clay shale. Engineering Geology 251, 214– 227. https://doi.org/10.1016/j.enggeo.2019.01.016*". The post-print version of the journal paper has been used to draft the chapter.

Contribution of the Candidate: design and performance of the experimental testing, analysis of the results, writing of the manuscript.

Additional results, not presented nor discussed in the mentioned publication are included in this chapter.

2.1. Introduction

This chapter focuses on the characterisation of samples of Opalinus Clay from various sites, from the sub-superficial site of Lausen (less than 100 m depth) to the deeper depth of Mont Terri (≈300 m depth) and Schlattingen (≈900 m depth). An extensive laboratory programme was performed on several samples sourced at different depths from Lausen borehole. Tests on the intermediate depth site of Mont Terri were also conducted. The results were compared to previous works on cores obtained from Mont Terri (Favero, 2017, Minardi et al., 2019) and Schlattingen borehole (Ferrari et al., 2012).

Some fundamental aspects of the Opalinus Clay composition and response are first introduced. The sites of origin of the Opalinus Clay samples used in this study are presented. The characterisation workflow is then described. The results of the experimental programme are shown and discussed, with a focus on the comparison among sites. The comparison represents an opportunity for investigating the effects of the composition and the sourcing depth on the characteristics of the formation.

2.2. Opalinus Clay shale: some fundamental aspects

Opalinus Clay (OPA) shale is the designated formation for the geological disposal of radioactive waste in Switzerland due to its desirable barrier properties (Gautschi, 2017). This is a sedimentary formation that was deposited approximately 170 million years ago and is currently found throughout northern Switzerland (Nagra, 2008). The name Opalinus Clay is derived from the presence of a particular fossil ammonite called *Leioceras opalinum*, widely distributed in the upper part of the formation. The formation is mainly composed of silicate sheet minerals, carbonates and quartz, with varying mineralogical content, and it is characterised by low porosity, ranging from 0.10 to 0.12 in the area with greater maximum burial (e.g., Schlattingen borehole), and from 0.12 to 0.18 in the Mont Terri laboratory, with shallower maximum burial. The bulk Opalinus Clay shows a dramatic increase in hydraulic conductivity in the uppermost tens of metres due to decompaction and weathering (Hekel, 1994; Gautschi, 2017; Vogt et al., 2017). Below a depth of 30 m, the hydraulic conductivity of the formation is estimated to be in the orders of 10^{-11} - 10^{-14} m/s (Gautschi, 2017).

In the Opalinus Clay, the clay aggregates are aligned along a preferential direction, causing the characteristic fabric, named bedding, recognisable on the decimetre to millimetre scale. The shale behaviour is transversely isotropic, with the sedimentation planes corresponding to the

planes of isotropy. The anisotropy results mainly from the orientation of the clay minerals during the depositional phase, the diagenetic history and the associated pore space distribution.

On the millimetre-centimetre scale, the Opalinus Clay shale is made of clay-rich layers, alternating with quartz and carbonate-rich layers. Some works have analysed the macro- and microstructure of specimens collected in Mont Terri (more recently, e.g., Houben et al., 2014; Philipp et al., 2017; Seiphoori et al., 2017; Lauper et al., 2018), describing the features of the layers characterising the various lithofacies. Houben et al. (2014) have characterised the different layer types of the Opalinus Clay shale retrieved in Mont Terri. In particular, clay layers are composed of a clay-mineral rich matrix, with particles preferentially oriented along the bedding direction, in which grains of other minerals – typically quartz – are immersed. Instead, quartz-rich layers are mainly made of quartz grains, and the inter-grain porosity is filled with clay particles, shifting the fabric to grain-supported as the quartz content increases. Those layers are also found to have a lower porosity compared to the clay layers.

2.3. Opalinus Clay across Switzerland

This Jurassic shale is found throughout the northern part of the country where the repository candidate sites are located. The current depth distribution of Opalinus Clay in this area varies, mainly due to the gentle dip of the Mesozoic sediments towards the south-east originating from flexural loading during the Alpine orogeny. Tectonic and erosional processes during Miocene to Quaternary times further contributed to the complexity of the current depth distribution (Mazurek et al., 2006). As a result, the formation is encountered at the surface in some location near the border of Germany with Switzerland and reaches current depths of approximately 400 to 1000 m in the candidate sites for a repository further to the south. The formation has a thickness of 80-130 m and is composed of dark grey claystone, which is subdivided into several lithostratigraphic sub-units (Nagra, 2002). In comparison with other Mesozoic sedimentary formations in Northern Switzerland, Opalinus Clay can be considered as a rather homogenous formation (Gautschi, 2017), with moderate vertical and lateral lithological variability.

The location of the three mentioned sites (Lausen, Mont Terri, Schlattingen) is shown in Figure 2-1. In the following, each site is briefly presented.

Figure 2-1 Approximate location of sites of Mont Terri, Lausen and Schlattingen, from which the samples of Opalinus Clay in this study were sourced; Swiss map from facts.co.

2.3.1. The Mont Terri Underground Rock Laboratory URL

The Jura Mountains in Switzerland are characterised by a Fold-and-Thrust belt that occurred in the late stages of Alpine formation (Bossart and Thury, 2008). Mont Terri (MT) is one of the anticlines of the Folded Jura, in which the Underground Rock Laboratory is located (Figure 2-2). This is an underground research facility, comprising about 700 m of galleries and niches situated in the north of St-Ursanne, at about 300 m depth. The research centre is devoted to the hydrogeological, geochemical and geotechnical characterisation of the Opalinus Clay shale. The shale formation is currently found there at a depth of approximately 300 m and has an actual thickness of about 90 m. It is estimated that at this location, the formation has reached a maximum burial depth of approximately 1350 m (Mazurek et al., 2006).

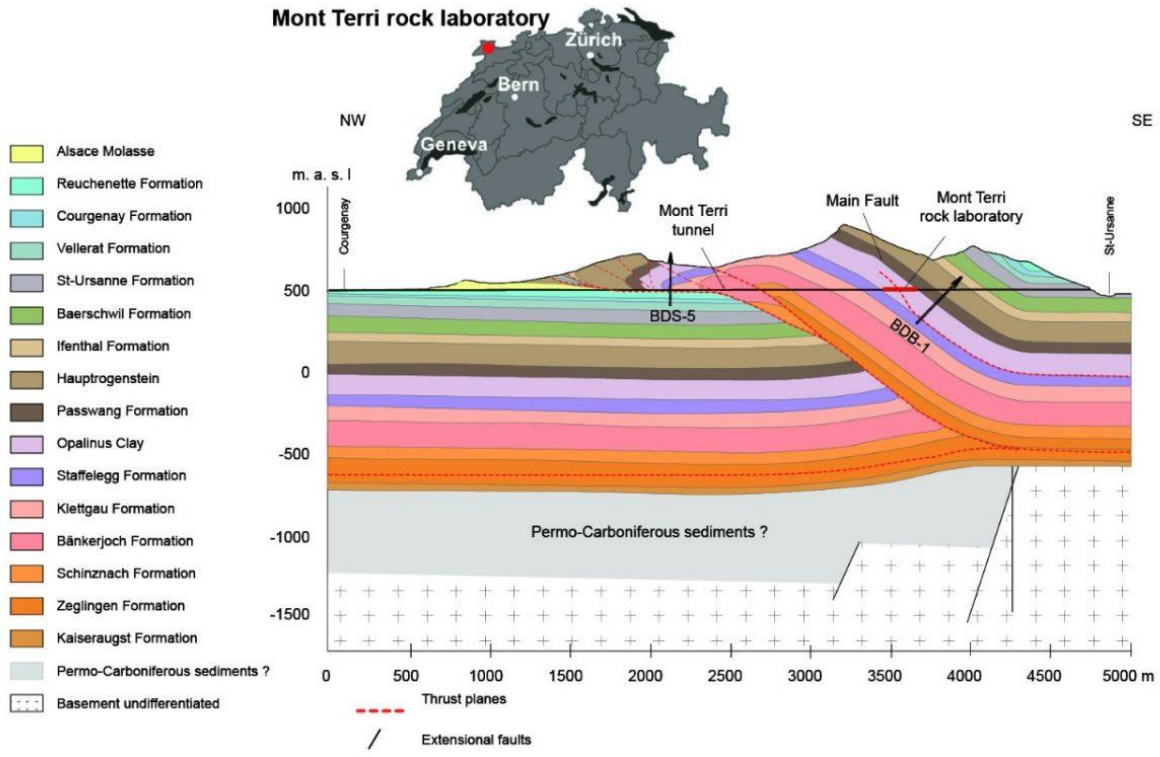

Figure 2-2 Location of the Mont Terri underground rock laboratory and geologic profile of the Mont Terri anticline (figure from www.mont-terri.ch).

In Mont Terri, the formation has been subdivided, according to the lithostratigraphy, into three main facies:

- a *shaly facies*, mainly argillaceous and marly shale with lenses and layers of millimetre thick sandstone;
- a *sandy facies*, marly shale, with lenses of limestone or sandstone with pyrite;
- a *carbonate-rich, sandy facies*, calcareous sandstones, intercalated with bioturbated limestone beds, with high detrital quartz content.

The differences in the facies composition have been attributed to the environmental settings at the coastal basin during the deposition process (Bossart and Thury, 2008). The carbonate-rich facies is more common in the western part of the country and rarely present in the north-eastern Switzerland, where the candidate repository sites are located.

Several samples from the Mont Terri URL, in particular from the sandy facies, were tested in this work. Experimental results obtained in other studies (Favero, 2017; Minardi et al., 2019) on cores from Mont Terri were considered for comparison.

2.3.2. The Schlattingen borehole

A few geotechnical studies have been conducted on Opalinus Clay from deep boreholes in northeastern Switzerland, near the villages of Benken (Nagra, 2001) and notably in Schlattingen (SLA), (Ferrari et al., 2012, 2016; Favero et al., 2016). The borehole at the Schlattingen location was drilled in 2011 in the context of a geothermal study, for harvesting geothermal energy. In Schlattingen, Opalinus Clay was encountered at a depth of 830-950 m, and maximum burial is estimated to have reached a depth of approximately 1700 m, based on estimates of the nearby borehole of Benken (Nagra, 2002; Mazurek et al., 2006). The borehole is located in the Tabular Jura, a zone that underwent less deformation during late Miocene compared to the Folded Jura. In this location, the sediments are considered to be unaffected by the Alpine thin-skinned thrusting. Experimental results obtained in previous studies on samples from Schlattingen (Ferrari et al., 2012) are used in this study as a means of comparison with the samples from shallower depth.

2.3.3. The Lausen borehole

In 2015, a borehole was drilled close to the village of Lausen (LAU), in the Tabular Jura, where Opalinus Clay is encountered immediately at the base of Quaternary sediments at a shallow depth, from 6 to 71 m, with a sub-horizontal bedding orientation (Vogt et al., 2016). In Lausen, the groundwater table was found at ≈5 m depth, within the Quaternary sediments.

The estimated past maximum burial is likely well in excess of 1000 m (Nagra, 2002; Mazurek et al., 2006). In Lausen, the formation has experienced exhumation from much greater depth over geological time-scales and therefore provides a unique analogue for the evaluation of the long-term evolution of a repository. The exhumation, driven by the erosion of the above strata, may be associated with alteration of the shale properties, including mechanical degradation, fracture propagation and weathering. It is noted that in contrast to the Jura Fold-and-Thrust belt further to the south, tectonic overprint in the Tabular Jura at the Lausen site is very low (e.g., Nagra, 2014). Geochemical analyses showed signs of weathering of the formation in the uppermost 20-30 m (Mazurek et al., 2017). In the same section (down to 20-30 m), cored samples were profoundly disturbed by fractures (Vogt et al., 2016), and in situ tests demonstrated high hydraulic conductivity (Vogt et al., 2017).

In this site, the Opalinus Clay is clay-rich in the upper part, whereas the interval 31 - 62 m contains abundant quartz-rich lenses, while the lowermost interval 62-71 m is again clay-rich. This sequence can be related to the one observed in Mont Terri, in which the interval 31-62 m

would correspond to the sandy facies in Mont Terri, embedded by the upper and lower shaly facies (Mazurek et al., 2017). Finally, in Lausen, no carbonate-rich sandy facies was found.

Several samples from the Lausen borehole were used for the experimental programme and compared to results from the other sites.

2.4. Tested samples and Characterisation workflow

2.4.1. Tested samples

Several cores were sourced along the Lausen borehole's vertical direction, between 14 and 70 m, and an extensive laboratory programme was conducted (Ferrari et al., 2018). Cores were cleaned from water-based drilling mud, wrapped and sealed air-tight immediately after recovery. They were put into PVC core barrels, and the annulus was filled with resin. The cores were also checked for mechanical integrity after conditioning by using medical X-ray tomography (Giger et al., 2018). According to depth increases, the cores have been coded with the letter L (Lausen) and an increasing number. The geotechnical characterisation of the cores was performed on specimens extracted from 9 cores. Table 2-1 lists the codes and the depths of the cores from the Lausen borehole used in this experimental programme.

A few samples from the Mont Terri URL were also characterised. The codes of the tested cores are reported in Table 2-1, along with the depth distance from the gallery's wall, when available. Cores BWS-H2, BHA18 and BGC1-14a belong to the sandy facies of the Opalinus Clay formation, as defined in the Mont Terri URL. Core BFEB021 belongs to the shaly facies.

Table 2-1 Lausen core codes and related sourcing depths.

Core	L1	L2	L3	L4	L8	L9	L11	L12	L13
Depth range (m)	14.22-14.57	17.66-18.28	22.07-22.71	25.35-26.09	37.43-38.33	57.37-58.38	61.11-61.79	61.79-62.54	69.93-70.47

Table 2-2 Mont Terri tested samples. *Distance from the gallery wall, when available.

Core	BGC1- 14a	BHA18	BWS-H2	BFEB-21-02
Depth* (m)	13.35-13.25	0.0-0.1	6.13-3.18	-

2.4.2. Geotechnical characterisation

Complete geotechnical characterisation was performed on the listed samples, and included: the density of solid particles (ρ_s), the bulk density (ρ), the water content (w), the Atterberg's limits (liquid w_L and plastic limit w_P), the void ratio (e), the porosity (n) (i.e. water-loss porosity) and the degree of saturation (S_r) (Figure 2-3).

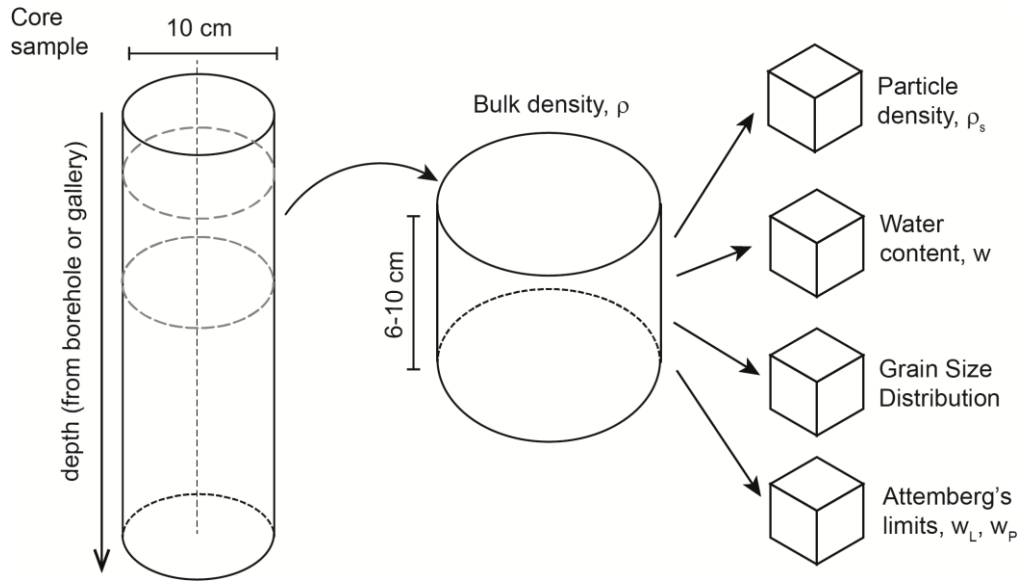

Figure 2-3 Scheme of the shale characterisation. Bulk density is calculated on a (cylindric) block of the core then divided into sub-pieces and used for determining the other properties.

Bulk Density

The bulk density is the ratio between the mass and the bulk volume of a sample. For specimens of regular geometry, the volume can be computed via its dimensions, measured with the help of a calliper. For samples of non-regular geometry, the measurement is more complicated.

For the core characterisation, the bulk density was obtained by the fluid displacement method on a block of ~6-10 cm in height (Figure 2-3), trimmed from each core (block weight of approximately 1000-2000 g). The fluid displacement technique is based on Archimedes principle. The sample mass was taken. Two coats of melted paraffin were then applied on the surface of the specimen, to protect the sample from entering in contact with fluids; the waxed specimen was weighed again to assess the amount of paraffin applied, and then it was immersed in water, and its mass in the fluid was measured. The sample volume is equivalent to the volume of water displaced, computed as the difference in sample weight (outside and inside the fluid) divided by the water density, and taking into account the volume of paraffin applied. After removing the paraffin wax, the block was divided into sub-pieces and used to determine the other geotechnical properties (Figure 2-3).

Water content

The water content was obtained after oven drying a sample at 105°C for 24h, and computed as:

$$w = \frac{M_w}{M_{s,d}} = \frac{M_{s,w} - M_{s,d}}{M_{s,d}} \quad \text{2-1}$$

where M_w is the mass of water, computed as the difference between the mass of the sample in wet $M_{s,w}$ and dry conditions $M_{s,d}$.

For core characterisation, the water content was measured on one part of the block (≈100 g) used for the bulk density. To facilitate the drying of large samples, they were fragmented in small blocks by crushing them with a rubber hammer. For samples whose shape needed to be preserved longer time of drying was required (up to few days).

Particle density

The particle density (ρ_s) is the density of the solid phase. It was measured using a water pycnometer on the material at natural water content, following the standard ASTM D854-14 (2014). The procedure allows for the determination of the volume of solid particles (and then of the particle density).

The material was preliminarily crushed, the fraction passing 0.5 mm sieve was selected. About 50 g of material were used. The water content of the powder was determined in order to obtain the dry weight ($M_{s,d}$) of the tested sample. The weight of a calibrated pycnometer (50 mL) filled with deaired water, for which the volume is known, was measured. The weight of the pycnometer, with the sample powder, and filled with deaired water was taken. The particle density is determined as:

$$\rho_s = \frac{M_{s,d}}{M_{p,w} - (M_{p,w,s} - M_{s,d})} \rho_w \quad \text{2-2}$$

where $M_{p,w}$ is the mass of the calibrated pycnometer and water, $M_{p,w,s}$ is the mass of the pycnometer, with the sample and filled with water, ρ_w is the deaerated water density, assumed to be ρ_w=1.0 Mg/m^3 at 20°. A minimum of three measurements on each sample was performed. If the difference between the results was inferior to 0.02 g/cm^3, the average value was calculated and considered as valid. Tests with results outside the admitted error range were excluded and, if needed, repeated.

Atterberg limits

About 50-60 g of powdered Opalinus Clay was mixed with distilled water until a malleable paste was obtained. The determinations of the Atterberg limits, liquid and plastic limits, were

obtained following the standard ASTM D4318-17 (2017). The Atterberg limits are the water contents of the paste, when attaining the liquid limit w_L (above which the mix is considered in a liquid condition, and below which it is in a plastic condition) and the plastic limit w_P (above which the mix is considered in a plastic condition, and below it is in a semi-solid condition). The difference between the two, w_L - w_P, is the plasticity index, *PI*.

Grain size distribution

A specific procedure for the definition of the grain size distribution was adopted in order to quantify the different grain size fractions. The procedure was developed in order to help the disaggregation of the particles without crushing coarser grains, that are expected to be abundant, in particular in the sandy facies samples.

The technique includes manual disaggregation of the shale fragments using a rubber hammer in order to minimise particle crushing (Figure 2-4a), particle dispersion in distilled water for 15 minutes by using a mixer (Figure 2-4b) and wet sieving (Figure 2-4c) the slurry with the help of a soft brush. The material fraction passing the last sieve is subsequently placed in distilled water along with a dispersing agent (sodium pyrophosphate) and shook overnight, and then analysed by standard hydrometric test (ASTM D422-63).

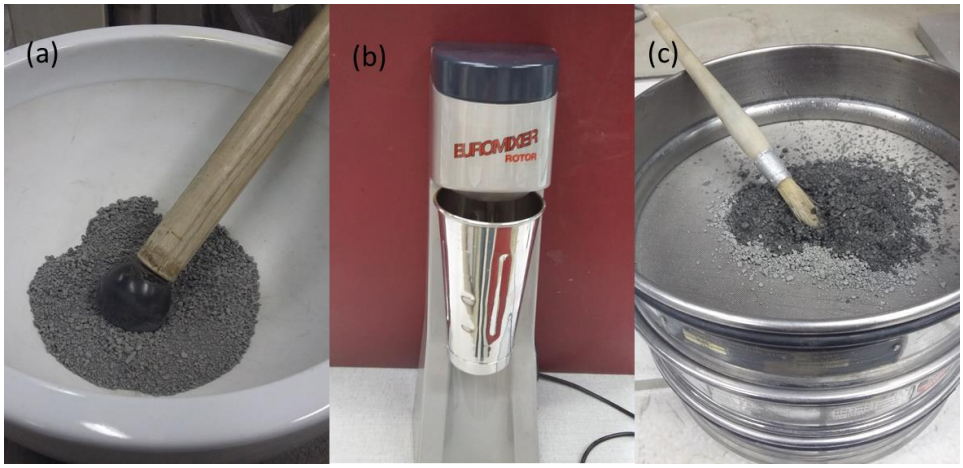

Figure 2-4 Grain size distribution procedure: (a) manual disaggregation, (b) powder mixing with water, (c) wet sieving.

The mixer was tested to detect any possible particle damage during the mixing. To check that, grain size distribution on quartz sand was performed twice. First, a standard wet sieving analysis was performed for the sand. Second, the sand was mixed in water for 15 minutes, and then wet sieved. No appreciable difference between the grain size distributions was found (Figure 2-5). It was concluded that the mixing was not damaging the coarser grains inside the sample, and therefore, it was suitable to help in the disaggregation of the particles.

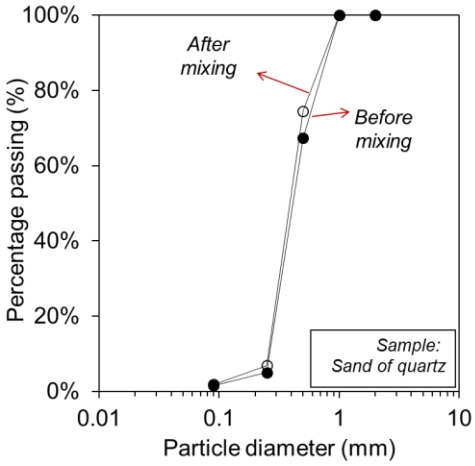

Figure 2-5 Effect of water mixing on the grain size distribution of a sample of quartz sand.

Porosity

The void ratio (*e*) is defined as the ratio of the volume of voids to the volume of solid particles; the porosity (*n*) is defined as the ratio of the volume of voids to the total volume of the sample. The void ratio and the porosity were computed according to the following relationships:

2-3 $$e = \frac{\rho_s(1+w)}{\rho} - 1,$$

2-4 $$n = \frac{e}{e+1}.$$

Degree of Saturation

The degree of saturation (S_r) is defined as the ratio of the volume of water in the pore space to the volume of voids. It can be computed using the following relation:

2-5 $$S_r = \frac{\rho_s \cdot w}{\rho_w \cdot e}$$

where ρ_w is the density of the water (assumed to be ρ_w = 1.0 Mg/m^3 at 20°).

2.4.3. Microstructural investigation

Mercury intrusion porosimetry (MIP)

The pore size distribution (PSD) was determined using the Mercury Intrusion Porosimetry (MIP) tests, performed in a Thermo Fisher Scientific porosimeter. The tests are carried out in a glass dilatometer, where the sample is initially placed. Then the dilatometer is filled with mercury under vacuum to avoid the entrapment of air bubbles. Mercury is a non-wetting fluid;

therefore, in order to force the penetration in the sample, pressure was applied all around the sample surface. Five specimens (from cores: L2, L3, L8, L11, L13), of diameter of about 8 mm and height 10 mm were retrieved, the edges smoothed with sandpaper, and tested.

Samples need to be dried before the test, to avoid the presence of other fluids in the pore space that may alter the mercury intruded volume. Different techniques can be used to dry the sample: (i) oven-drying at 105 °C for 24h, (ii) drying in a desiccator at very low relative humidity, or (iii) freeze-drying. As drying processes may induce significant volumetric deformations in shales (also causing fissure opening), freeze-drying was adopted to dry the tested shale samples. The effect of the bubbling action of liquid N_2 on sample microstructure was not investigated. Samples were initially immersed in liquid nitrogen at -196 °C for about one minute to freeze the pore water. Then, they were put inside vacuum chambers at 0.06 mbar and -50°C for 24 hours to allow for the sublimation of the pore water.

The freeze-drying technique allows minimising as much as possible the material disturbance during water removal, by inducing the passage from solid water (at very low temperature) to vapour without passing through the liquid phase, that would induce the shrinkage of the sample during drying. Also, the low temperature of the liquid nitrogen ensures a low ice recrystallization rate that does not allow the ice to expand in pores, affecting the microstructure. The impact of the low temperature on the tested materials was not investigated.

The pressure of mercury (p_{Hg}) needed to intrude the specimen is related to the pore diameter (d) according to the Washburn equation, which assumes a cylindrical shape of the pores:

$$d = -\frac{4 \cdot \gamma_{Hg} \cdot \cos\theta}{p_{Hg}} \qquad \text{2-6}$$

where γ_{Hg} is the surface tension of mercury (0.48 N/m) and θ is the contact angle between the soil and mercury (140°, typical values assumed for clayey geomaterials, Romero and Simms, 2008). According to the Washburn equation, the minimum pore size diameter that can be intruded with the available device is 4 nm, which corresponds to the maximum mercury pressure that can be applied (400 MPa). The evolution of the intruded void ratio (e_{Hg}) can be represented with respect to the pore diameter or using the pore size density function (PSD):

$$e_{Hg} = \frac{V_{Hg}}{V_s} \qquad \text{2-7}$$

2-8 $$PSD = -\frac{\Delta e_{Hg}}{\Delta \log(d)}$$

with V_{Hg} being the volume of mercury, and V_s the solid volume of the sample.

Scanning electron microscopy (SEM)

Scanning electron microscopy images were taken on a sample from the Lausen borehole (L3) and a sample from the shaly facies of the Mont Terri URL (BFEB). A thin slice, of few millimetres thickness, was cut from the sample, dried in a desiccator with silica gel and then kept under vacuum. To minimise the disturbance of the sample surface, samples were dry polished with SiC paper 4000 (5µm), and then the ionic milling was performed (ILION from Gatan company). No coating was applied. Sample preparations and Scanning electron microscopy were performed at the Interdisciplinary Centre for Electron Microscopy (CIME, EPFL), using the microscope Zeiss GEMINI 300. Images were taken at a working distance of 10.0 mm, and an acceleration voltage of 15.00 kV. Several pictures of the two samples were taken at various magnifications.

Mineralogical analysis

The mineralogical composition, including organic carbon content, of several samples of Opalinus Clay was analysed using X-ray diffractometry (XRD). Part of the results on the mineralogy was obtained on samples previously used for hydro-mechanical tests. The mineralogical analyses were performed at the Institute of Geological Sciences, University of Bern. Description of the adopted methodology can be found in Wersin et al. (2013).

2.5. Results and analysis

2.5.1. Geotechnical characterisation

The results of the geotechnical characterisation of Lausen samples are summarised in Figure 2-6. Each point represents a measurement on a specimen, sourced at the indicated depth. The core code, corresponding to each specimen, is reported along with the bulk density values, as an indication for all the reported curves. An indication of the compositional similarity among specimens can be gathered from the measurement of the void ratio, which, for Opalinus Clay, is strongly affected by the mineralogical composition (Houben et al., 2014), as discussed in Section 2.2. The results of the geotechnical characterisation of the samples from Mont Terri are reported inTable 2-3. Ranges of the geotechnical parameters of MT samples, tested at EPFL, are provided also in Table 2-3, including data from shaly and sandy facies (from this

study and Favero, 2017), together with ranges of samples from Schlattingen (Favero et al., 2016; Ferrari et al., 2016; Minardi et al., 2016) and Lausen (this study).

Lausen specimens presented wide ranges of variability, in line with the previous results from Mont Terri and Schlattingen. However, an exception is found for the shallowest specimens analysed: between 10 and 20 m, the bulk density of the investigated blocks is particularly low, approaching 2.30 Mg/m^3 for the shallowest specimen. High water contents are also measured for those specimens (≈10%). In contrast, the density of solid particles is in line with the results from greater depths. Therefore, the computed void ratio for the first two specimens of the column is particularly high (0.31 and 0.26). Below the first 20 m, the characterisation results (especially bulk density, water content and porosity) are in line with the ranges of variation from Mont Terri, while the values corresponding to the Schlattingen specimen results are slightly lower. The minimum value in the void ratio, among the tested specimens from Lausen, was found at a depth of ≈38 m. The main mineralogical components (i.e. calcite, quartz, clay minerals and others) are reported in Figure 2-6 in correspondence with the sampling depth. The results show a high heterogeneity of the tested specimens, with clay-mineral content ranging from 46% to 80%, quartz content from 12% to 33%, and calcite from 2.8% to 11.2%. The full mineralogical composition is reported in Section 2.5.3.

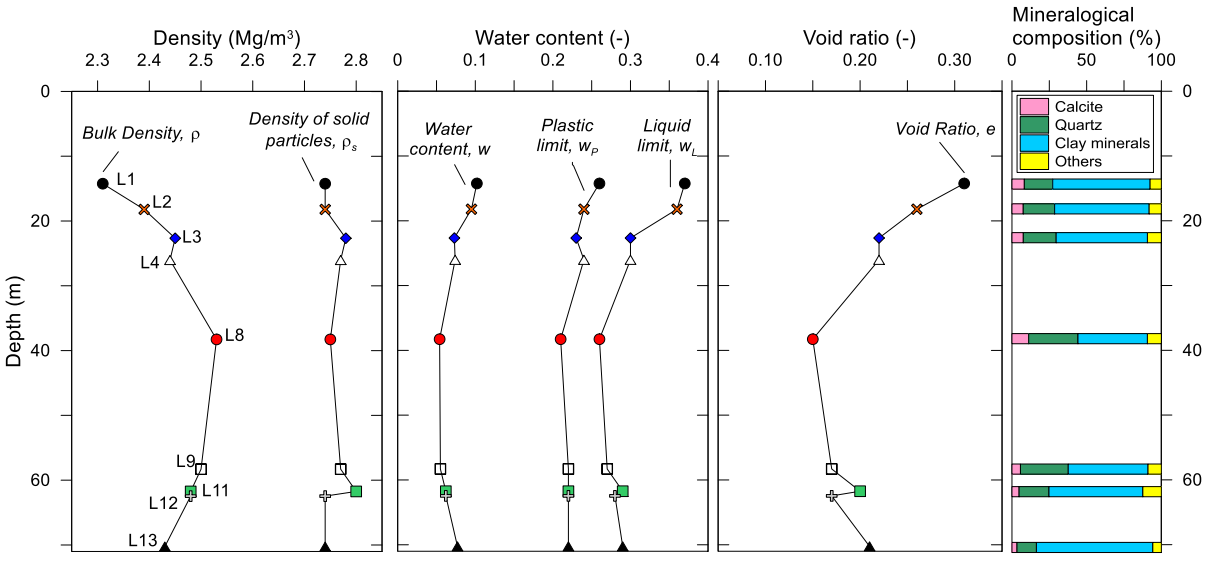

Figure 2-6 Geotechnical characteristics and main mineralogical components of Opalinus Clay (from Lausen) versus depth.

Table 2-3 Synthesis of the geotechnical properties of Opalinus Clay obtained at EPFL (continues). *Ranges include data from Favero, 2017.

Core (MT)	ρ_s (Mg/m^3)	ρ (Mg/m^3)	w (%)	e (-)	n (-)	S_r (%)	w_L (%)	w_P (%)	PI (%)
BHA-18	2.76	2.50	4.7	0.16	0.14	81	26	20	6
BWS-H2	2.72	2.49	4.0	0.13	0.12	82	32	17	15
BGC-1-14a	2.76	2.51	5.4	0.16	0.14	95	31	20	11
BFEB-21-02	2.75	2.40	6.5	0.22	0.18	83	38	26	12

Table 2-4 (*Continues*)

Site	ρ_s (Mg/m^3)	ρ (Mg/m^3)	w (%)	e (-)	n (-)	S_r (%)	w_L (%)	w_P (%)	PI (%)
Mont Terri*	2.72-2.78	2.40-2.51	4.0-7.7	0.13-0.23	0.12-0.19	81-99	26-38	17-26	6-15
Schlattingen*	2.70-2.74	2.49-2.56	3.3-4.9	0.10-0.15	0.09-0.13	80-96	29-39	19-25	9-17
Lausen	2.74-2.80	2.31-2.53	5.0-10.0	0.15-0.31	0.13-0.24	87-99	26-37	22-26	5-12

The grain size distribution was measured for each core to determine possible sand-size particles embedded in the clay matrix. The results are presented in Figure 2-7 and reveal that the amount of sand-size fraction increases for deeper specimens. However, the last specimen of the sequence (core L13) presents a low sand content, similar to the shallower specimens. Higher sand size fractions were found for specimens L8 to L12, compared to the specimens L1 to L4 and L13.

The obtained ranges of the variability of the grain size fractions are in between the values reported for the Opalinus Clay from Mont Terri, shaly and sandy facies, depicted as the dashed area in Figure 2-7, performed with the same technique. It has to be noted that the clay-size fractions obtained from the grain size distribution are always lower compared with the obtained clay-mineral contents. This result suggests that part of the clay aggregates was not completely disaggregated with the adopted procedure, but formed larger, silt-sized, aggregates.

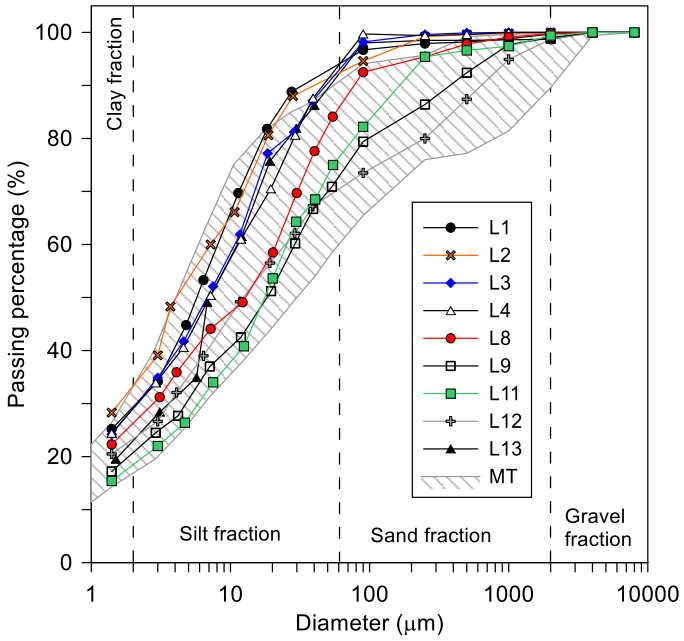

Figure 2-7 Grain size fractions of the tested cores.

2.5.2. Microstructural investigation

Figure 2-8 depicts the results of the MIP tests; for each specimen the figure reports: on the left side, the results in terms of cumulative intruded void ratio (ratio of the cumulative intruded mercury volume to the volume of the solid phase) versus the equivalent pore throat diameter

(*d*) and, on the right side, pore size density (*PSD*) function versus *d*. For comparison, the void ratios obtained from the drying of the bulk samples (i.e. water loss method, Equation 2-3), from which the sub-samples for the MIP were taken, are also reported in Figure 2-8. The maximum void ratio detected by the MIP is lower than the one measured on the samples with the drying method. This difference can be attributed to the presence of isolated pores and pores having a pore-throat diameter smaller than 4 nm (Busch et al., 2017), typically inter-platelet pores within the clay.

Figure 2-9 summarises all the obtained MIP results in the plot of the pore density function versus pore throat diameter. The modal pore throat diameter value ranges between 15 and 30 nm. The maximum value was obtained for the specimen at ≈38 m depth; this specimen is also characterised by the lowest void ratio and clay-mineral content, while lower values of modal pore throat diameters were obtained for shallower and deeper cores. For the sample at ≈38 m (Lausen 8), a small difference between the intruded porosity and the porosity from the water loss method was obtained. This can be attributed to the pore throat size of this sample, larger compared to the others (see Section 2.6.2), that would allow for a higher amount of intruded pore volume at the same maximum pressure. Also, sample Lausen 13 presents a tighter pores size distribution than the other samples. This can be related to the sample composition, that, as reported in the next Section 2.5.3 is more homogenous (about 80%) of clay. With the more homogenous composition, a more homogenous pore size distribution is envisaged.

The dominant pore throat diameters for Opalinus Clay samples from Mont Terri (20 nm) and Schlattingen (8 nm) are also reported (Favero, 2017).

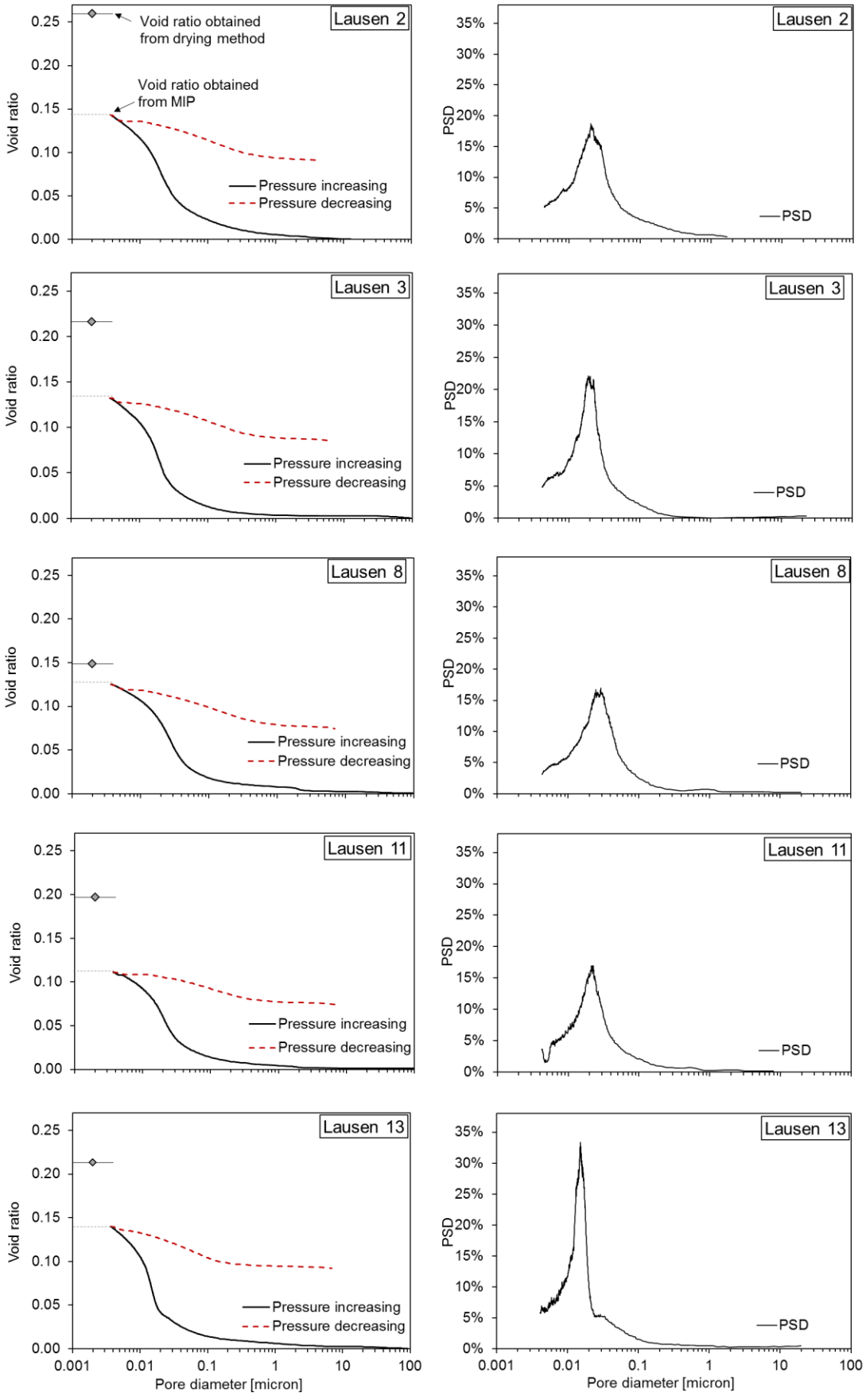

Figure 2-8 Results of the MIP tests for the Lausen samples.

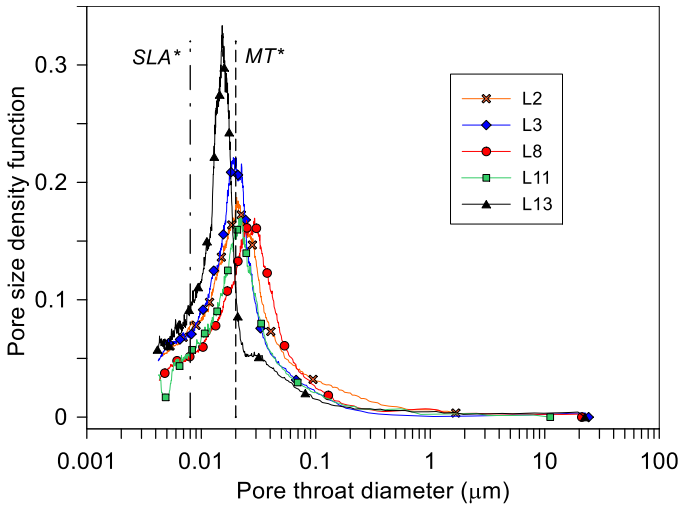

Figure 2-9 Summary of the MIP results for specimens from the Lausen borehole; pore size distribution versus pore diameter (*data from Favero, 2017)

A detailed description of the correspondence between porosity, mineralogy and pore throat size is provided in Section 2.6.2, together with the comparison with some literature data on Opalinus Clay.

In Figure 2-10, Figure 2-11 and Figure 2-12, scanning electron microscopy images of two Opalinus Clay samples, from Mont Terri and Lausen, are reported. The peculiar structure of the shale formation is shown: in the clay matrix, that looks homogenous at the millimetre scale, a high number of inclusions in the order of micrometres is embedded, e.g. carbonates, quartz, feldspars, pyrite.

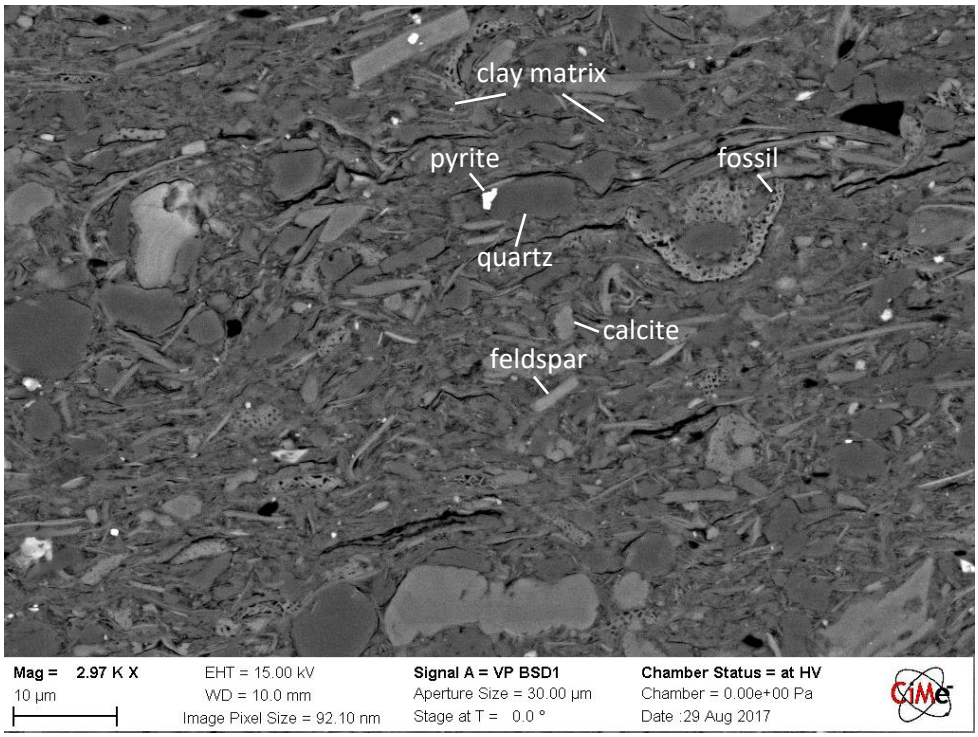

Figure 2-10 Scanning electron microscopy image of an Opalinus Clay sample from the shaly facies of Mont Terri (BFEB).

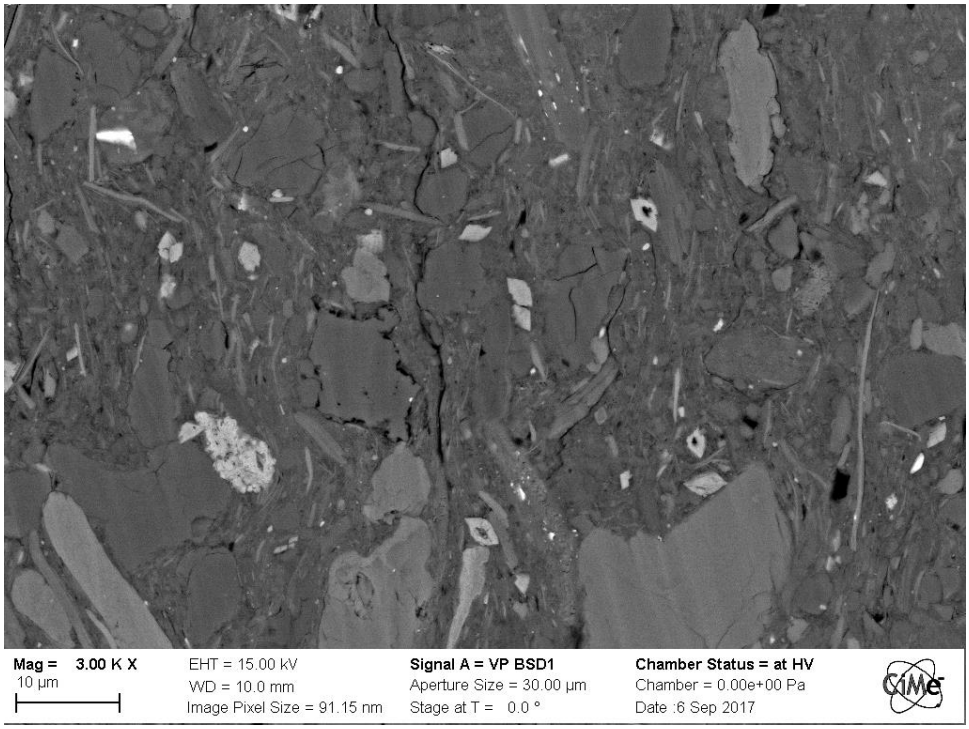

Figure 2-11 Scanning electron microscopy image of an Opalinus Clay sample from the Lausen core L3.

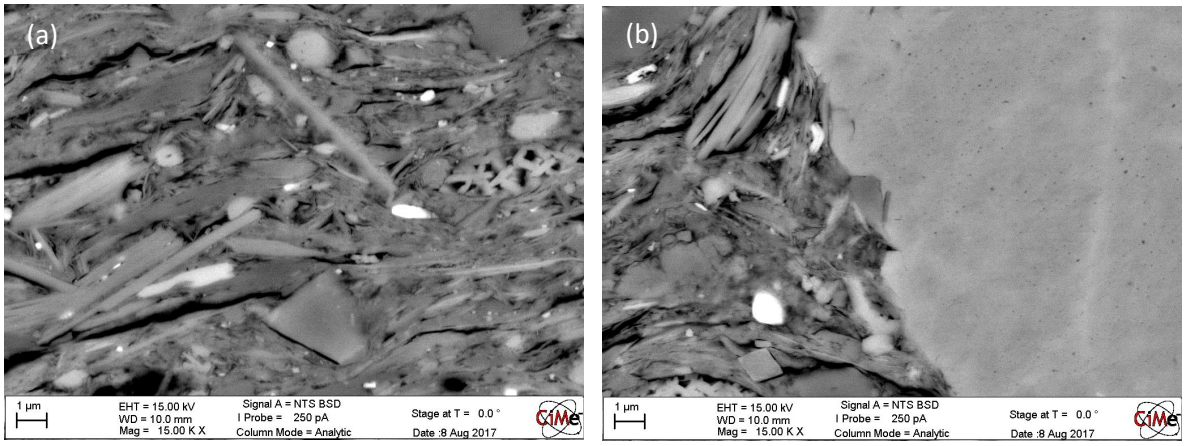

Figure 2-12 Scanning electron microscopy image of an Opalinus Clay sample: a zoom-in of the structure. (a) clay matrix, (b) deviated and deformed particles at contact with larger grain

In the clay matrix, the clay aggregates present a rather oriented structure (Figure 2-12a), with particles aligned along the bedding direction. On the other hand, at the contact points with larger grains (Figure 2-12b), the particles need to bend to accommodate the coarser particles, and slightly larger pores may form. The fissures visible in the images (at the micrometre scale) can be attributed to the crack opening generated upon drying during the sample preparation.

2.5.3. Mineralogical composition

Mineralogical analyses were performed at the University of Bern on selected specimens. The main mineralogical components (i.e. calcite, quartz, clay minerals and others) of the Lausen

samples were reported in Figure 2-6 in correspondence with the sampling depth. The complete results are reported in Table 2-5 for Lausen samples and in Table 2-5 for Mont Terri samples.

As mentioned before, the results on Lausen samples show a high heterogeneity of the tested specimens, with clay-mineral content ranging from 46% to 80%, quartz content from 12% to 33%, and calcite from 2.8% to 11.2%. In particular, the clay content is higher for shallower specimens (15 – 23 m depth), reaches a minimum at approximately 38 m, and increases again at greater depths, reaching a maximum at 70.4 m.

The ranges of variation of the main components of Lausen samples are generally in line with the results of specimens from other sites: for Mont Terri specimens (this study and Favero, 2017), values included 36-67% total clay minerals, 12-50% quartz, and 9-19% calcite; for Schlattingen specimens (Favero, 2017), the composition included 44-68% total clay minerals, 17-32% quartz and 11-21% calcite. The composition of the clay minerals was analysed for several Opalinus Clay samples (e.g., Bossart and Thury, 2008) and found similar among samples from various facies and namely, from the most to the least abundant, illite, kaolinite, illite-smectite mixed layers, chlorite. Clay mineralogy of samples from the Lausen borehole were analysed in the work of Mazurek et al. (2017) (e.g., for a sample at 25 m depth, containing 59% clay-mineral content: 20% illite, 16% illite/smectite mixed layers, 14% kaolinite, 10% chlorite), showing composition similar to Mont Terri samples. The only relevant difference between the sites is an average lower amount of calcite for Lausen samples. This outcome is attributed to calcite dissolution due to superficial water infiltration (Mazurek et al., 2017) in the Lausen site.

Table 2-5. Mineralogical compositions of specimens used in the laboratory programme; samples from Lausen borehole (data from University of Bern) (*subsample).

Site	Core	ID (if needed)	Depth (m)	Calcite (wt.%)	Dolomite/ Ankerite (wt.%)	Siderite (wt. %)	Quartz (wt.%)	Albite (wt.%)	K-feldspar (wt.%)	Pyrite (wt.%)	C (org) (wt.%)	Total clay minerals (wt.%)
Lausen	L1		14.3	8.3	1.7	1.8	19	<1	2.0	1.0	1.0	65.2
	L2		18.2	7.6	1.5	1.1	21	1.0	2.5	1.1	1.0	63.3
	L3		22.6	7.6	1.7	2.5	22	1.0	3.0	<0.2	1.1	61.1
	L4		26.0	3.4	0.0	1.1	8	<1	<1	71.1	0.4	15.9
	L8		38.2	11.2	1.5	0.4	33	1.0	5.0	0.8	0.6	46.5
	L9		58.3	5.7	1.6	0.8	32	1.5	4.0	0.3	0.7	53.4
	L11		61.7	6.6	1.5	0.6	27	1.0	3.5	0.5	0.9	58.4
	L12		61.8	4.8	2.4	5.3	20	<1	2.5	1.4	0.9	62.8
	L13	a*	70.4	3.4	1.1	<0.3	13	<1	2.0	1.6	1.0	77.9
	L13	b*	70.4	2.8	0.9	<0.3	12	<1	1.5	1.5	1.0	80.2

Table 2-6 Mineralogical compositions of specimens used in the laboratory programme; samples from Mont Terri (data from University of Bern).

Site	Core	Facies	ID (if needed)	Depth (m)	Calcite (wt.%)	Dolomite/ Ankerite (wt.%)	Siderite (wt. %)	Quartz (wt.%)	Albite (wt.%)	K-feldspar (wt.%)	Pyrite (wt.%)	C (org) (wt.%)	Total clay minerals (wt.%)
Mont Terri	BWS-H2	sandy		≈300	9.8	3.9	0.5	38	1.0	2.0	0.4	0.7	44.3
	BHA18	sandy		≈300	18.6	1.1	0.5	37	1.0	5.0	1.0	0.7	35.6
	BGC1-14a	sandy	S-1	≈300	9.0	1.9	2.4	50	3.0	3.6	0.4	1.0	29.0
	BGC1-14a	sandy	S-2	≈300	22.0	2.4	2.4	41	2.8	3.7	0.5	0.5	26.0
	BGC1-14a	sandy	S-3	≈300	22.0	2.0	2.3	41	2.7	3.3	0.2	0.6	25.0
	BFEB021	shaly		≈300	15.9	0.4	1.4	12	1.0	2.0	0.9	0.9	65.6

2.6. Discussion

2.6.1. Mineralogy across sites

The mineralogical composition of several samples is reported in Figure 2-13. In the plot, the results from Section 2.5.3 are depicted together with results from a larger dataset on the MT site (Minardi et al., 2019) and the deeper borehole of Schlattingen (Favero, 2017). The ternary plot vertexes are the sum of (*i*) calcite, siderite, albite, pyrite and dolomite/ankerite, (*ii*) quartz and k-feldspar, (*iii*) clay minerals and organics. The dotted lines indicate the reading direction for the plot. Considering that the organic content is always below or around 1%, a wide range of clay-mineral contents are involved (roughly between 15 and 80%). Samples with high clay-mineral contents have generally lower calcite (and others) content, compared to samples with high quartz content. A decrease in clay minerals corresponds to a considerable increase in quartz (between 10 and 55%) and only a limited increase in calcite content (roughly between 10 and 30%). Only a few samples are exceptions to this trend, having calcite content of about 50%, and very low clay and low quartz content. Those samples are part of the carbonate-rich sandy facies of the formation.

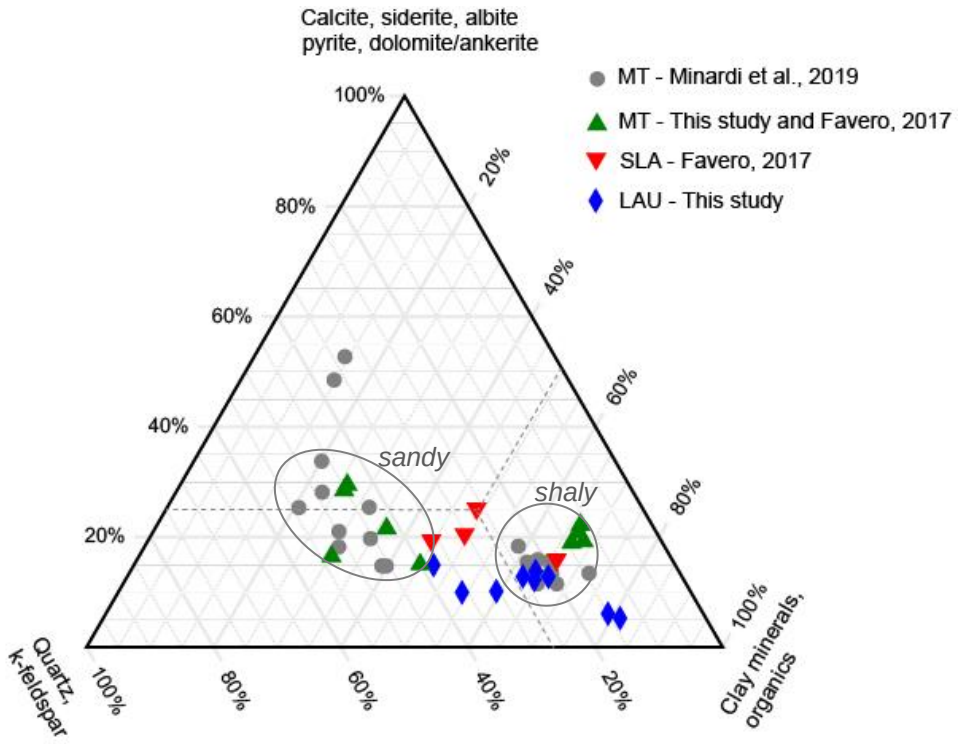

Figure 2-13 Ternary plot representing the mineralogical composition on several Opalinus Clay samples sourced from different sites (MT= Mont Terri, SLA= Schlattingen, LAU= Lausen).

Samples from MT can be easily divided into two subgroups: one with high clay content (>60%, roughly), on the right side of the plot including samples from the shaly facies; one with low clay content (<40%) on the left side of the plot, including samples from* the sandy facies. On the other hand, samples from LAU and SLA sites seem to fill the gap between these two groups, having sample compositions which are more heterogeneously spread also in the clay content range 40-60%.

2.6.2. Impact of the mineralogy and the depth on the characterisation

In Figure 2-14, the results regarding the clay-mineral content, void ratio and dominant pore throat diameter of specimens from the Lausen borehole are examined versus the depth. It is shown that higher clay-mineral contents correspond to higher void ratios, but lower dominant pore throat diameters. Consistent results, showing the correspondence between the increase in the clay-mineral content and the increase in the porosity, were provided in Mazurek et al. (2017) on a larger dataset of results from Lausen specimens. The findings relating those properties are in good agreement with the literature regarding the microstructural investigations of Opalinus Clay layers (e.g., Houben et al., 2014). In Opalinus Clay, pores can be found mainly in the clay matrix, which is also characterised by the lower pore throat diameter. The non-porous quartz/calcite particles can be considered as inclusions in the clay matrix, reducing the total porosity. Instead, when higher contents of non-clayey particles characterise the fabric,

the average pore throat diameter is found to be slightly higher, even though the global porosity is lower. This outcome is supposedly caused by the pores generated at the contact between clayey and non-clayey particles (as mentioned in Section 2.5.2), whose arrangement allows for larger pore throat diameters.

However, in the first 20 metres of the borehole, higher void ratios (0.26-0.31) were obtained compared to the rest of the borehole results. This outcome is explained by the alteration of the formation at very shallow depths, as documented in Vogt et al. (2017), that is represented at the scale of the sample for the characterisation of the cores (approximately 10 cm), but not observed at the millimetre-centimetre scale of the laboratory mechanically tested specimens.

Clay-mineral content and void ratio values of the intact specimens retrieved from the three sites mentioned in this work (Lausen, Mont Terri and Schlattingen) are reported in Figure 2-15, and show the trend of increasing void ratio with increasing clay-mineral content. The results from Mont Terri and Lausen are easily fitted in a common, increasing trend with the clay-mineral content. However, the results on specimens from the greatest depth (SLA) are located at void ratios lower than the others are. This outcome can be interpreted primarily as the effect of the more pronounced diagenesis and mechanical compaction that is expected to have occurred in Schlattingen (Favero et al., 2016), because of the different geological burial history (Nagra, 2002; Mazurek et al., 2006) compared to the Mont Terri and Lausen locations.

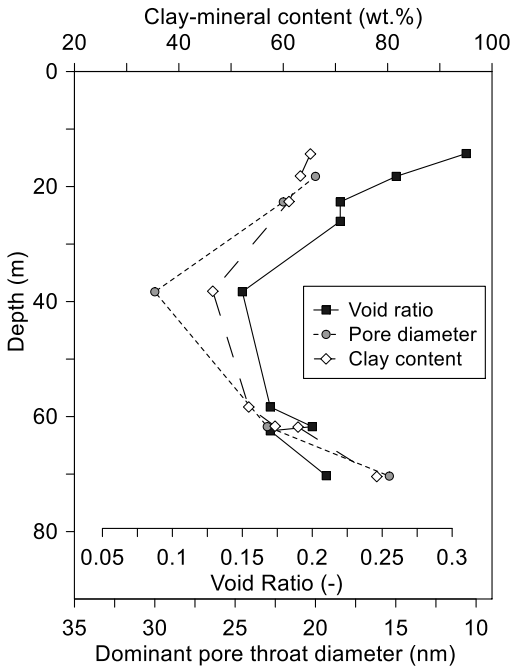

Figure 2-14 Summary plot of the void ratio, clay-mineral content and dominant pore throat diameter of specimens from the Lausen borehole, plotted versus the depth.

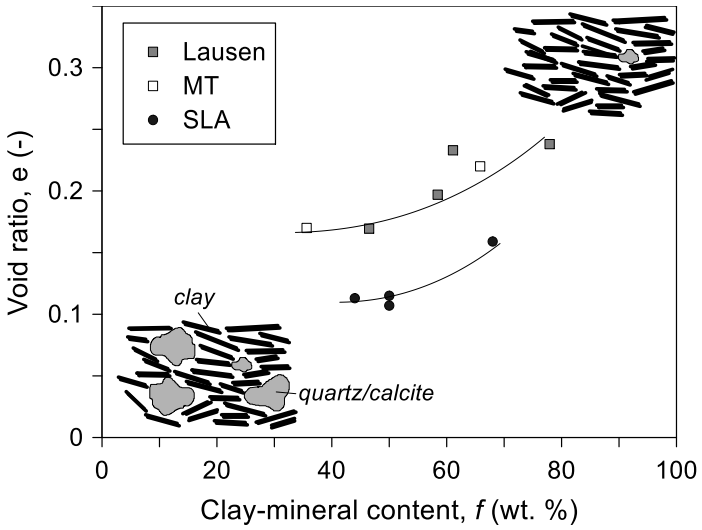

Figure 2-15 Void ratio and clay-mineral content of several specimens from various sites. Schematic representation of the shale structure.

2.6.3. Interpretation of the evolution of the porosity with the composition

The correlation between porosity and composition of the shale is here evaluated, adopting two models. The first model is the one proposed by Marion et al. (1992), based on the ideal packing of a binary mixture. The packing of binary mixtures depends primarily upon the diameter ratio of the particles, which are assumed spherical. When the diameter ratio (large/small) of the spheres is large (typically greater than 100), packing of the mixture is close to ideal. That is, the very small spheres do not disturb the original packing of the large spheres and vice-versa. For the Opalinus Clay, the structure is hypothesised to be simplified to a mixture of clay matrix (small particles) and non-clayey particles, including e.g. quartz, calcite (large particles) having spherical shapes.

In Marion et al. (1992) model, the following equations write:

a) if $c < n_{nc}$, $n = n_{nc} - c(1 - n_c)$

b) if $c = n_{nc}$, $n = n_{nc} n_c$

c) if $c > n_{nc}$, $n = c n_c$

In which c is the clay volume fraction, n is the porosity of the mixture, n_{nc} is the porosity among larger particles (non-clay, e.g., quartz, calcite), n_c is the porosity of the smaller particles (i.e. clay particles) porosity.

Case a) corresponds to the condition in which the clay volume fraction is less than the pure sand porosity, and clay particles fit into the pores and reduce the overall porosity. Case b) occurs when all the porosity is filled with clay particles. For higher clay volumetric fraction,

case c) applies, in which the sand lattices is expanded to leave space to the clay, that controls the structure. The equations to move from clay volume to clay mass fraction were reported in the work of Marion et al. (1992).

The data on the porosity of Opalinus Clay are interpreted with the mentioned model. Two cases are considered: a high porosity OPA (i.e. data from Mont Terri and Lausen) and a low porosity OPA (from the deeper site of Schlattingen). Since the measurements of very low porosity geomaterial are sensitive to the technique used (Busch et al., 2017), only the results obtained with the same technique, the drying method (water loss, Equation 2-3), were used for the interpretation.

Table 2-7 Parameters for the Marion et al., 1992 model for binary mixtures.

	Solid density (Mg/m^3)	**High porosity (LAU, MT)**		**Low porosity (SLA)**	
		n (-)	**e (-)**	**n (-)**	**e (-)**
Non-clay	2.72	0.38	0.61	0.30	0.43
Clay	2.68	0.21	0.27	0.17	0.20

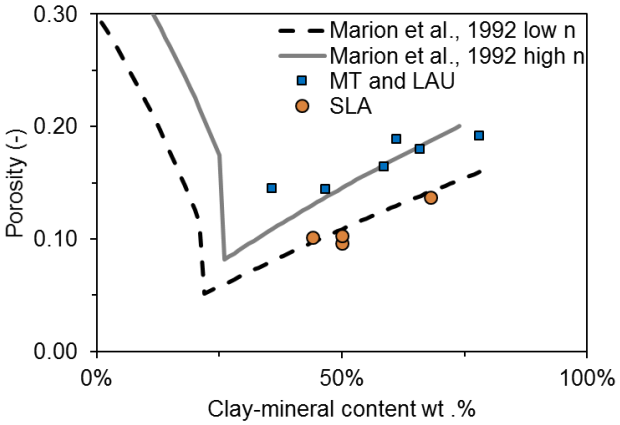

Figure 2-16 Porosity evolution with the composition, interpreted as a binary mixture.

Results are shown in Figure 2-16, as porosity versus clay-mineral content. Two representative fitting curves (model parameters in Table 2-7) are obtained for higher and lower porosity samples. The fitting curves show a good agreement for the data from the deeper samples (low porosity). For the shallower (high porosity) samples, the model predicts an overestimated decrease in porosity with decreasing clay-mineral content. The model, in fact, assumes that when the non-clayey particles increase, they substitute the porous matrix, decreasing the overall porosity. Also, the model assumes spherical particles. The incompatible geometry between the various grain sizes lead to slightly larger pores at the contact clay/non-clay (e.g., Figure 2-12). Therefore the porosity remains higher than what the model would predict.

A second model was therefore used in the attempt to reproduce the porosity change with decreasing clay content. Considering the structure of Opalinus Clay at the millimetre-centimetre scale (Section 2.2), it is hypothesised that the samples can be schematized as layered materials, alternating two kinds of layer: layers of high clay content, in which the grains are embedded, hereafter called *shaly layers*, and layers of the quartz-calcite structure where pores are filled with clay, hereafter called *sandy layers* (full description in Chapter 6.2.). The schematisation follows the microstructural studies on the layers of Opalinus Clay (e.g., Houben et al., 2014; Philipp et al., 2017; Seiphoori et al., 2017). Each layer has a porosity, associated with the structure and the mineralogical composition. The void ratio of the ensemble is calculated as the weighted sum of the void ratio of each layer kind, considering the solid volumetric fraction of each layer type:

2-9 $$e = e_{shaly} \cdot \tilde{\varphi}_{shaly} + e_{sandy} \cdot \tilde{\varphi}_{sandy}$$

where e is the total void ratio, e_{shaly} and e_{sandy}, the shaly and sandy layer void ratios, $\tilde{\varphi}_{shaly}$ and $\tilde{\varphi}_{sandy}$ are the volumetric solid fraction of the shaly and sandy layers, i.e. the solid volume of the layer type, over the total solid volume. Void ratios are converted to porosity, and vice-versa, using Equation 2-4.

The detailed description of the layer composition and the derivation of the solid fraction of the shaly and sandy layers are reported in Chapter 6.2, in which the schematization is used to interpret also the mechanical behaviour of the shale.

The parameters adopted are shown in Table 2-8, reporting for each layer kind the porosity and the void ratio of the shaly and sandy layers. As mentioned before, two sets of parameters need to be defined for the deep and shallow Opalinus Clay. The results are reported in Figure 2-17. For consistency with the first model results, the plot shows porosity versus the gravimetric clay-mineral content.

Table 2-8 Parameters for the layered structure model.

	High porosity (LAU, MT)		**Low porosity (SLA)**	
	n (-)	**e (-)**	**n (-)**	**e (-)**
Shaly layer	0.19	0.23	0.13	0.15
Sandy layer	0.12	0.13	0.05	0.05

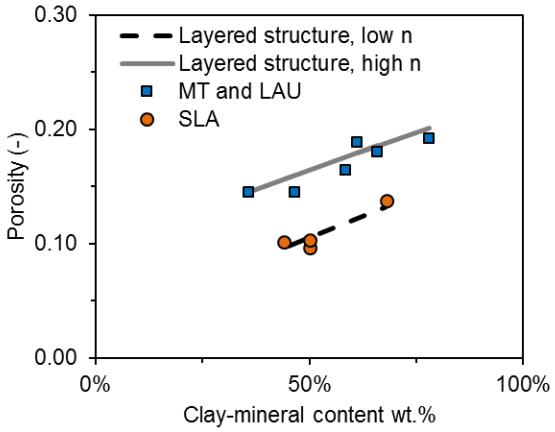

Figure 2-17 Porosity evolution with the composition, interpreted as a layered structure

In this hypothesis, the experimental results are better reproduced, and the decrease in porosity with the decrease in clay-mineral content is reflected. The two curves for high and low porosity samples have the same trend, but the latter is shifted towards lower porosity values.

2.7. Conclusions

In this Chapter, the sites from which Opalinus Clay samples were sourced were presented, with a focus on the different geological histories and current depths. The workflows for geotechnical and microstructural investigations have been discussed. The results show the similarity and differences among samples obtained from different sites and among samples sourced from the same location. The Opalinus Clay mineralogical components are the same among the various samples, although the proportions between them can vary significantly (e.g., clay content varying from 15 to 80 wt.%).

The key impacts of the mineralogical composition, in particular the clay component, on the Opalinus Clay porosity has been identified by the comparison of specimens sourced from various sites. Higher clay-mineral contents correspond to higher porosity, but to lower pore throat diameters. Porosity results from Lausen were found to be in line with Mont Terri results, except for the first 20-30 m where the impact of the exhumation on the fissuring is expected. The porosity of samples from Schlattingen appears to be considerably lower, likely because of a higher impact of diagenesis and maximum burial attributed to the different geological history.

The variation of porosity with respect to the composition has been interpreted with two simplified models: (i) a binary mixture of clay matrix and embedded particles and (ii) alternation of clay-rich and quartz-calcite-rich layers. The second leads to a better representation of the experimental results, capturing the dependency of the porosity on the composition. For both hypotheses, the data corresponding to samples from greater depth

needed to be interpreted separately to be able to take into account the reduced porosity of shale from the greater depth.

2.8. References

ASTM D422-63, 2007. Test Method for Particle-Size Analysis of Soils. ASTM International, West Conshohocken, PA. https://doi.org/10.1520/D0422-63R07E02

ASTM D854-14, 2014. Test Methods for Specific Gravity of Soil Solids by Water Pycnometer. ASTM International, West Conshohocken, PA. https://doi.org/10.1520/D0854-14

ASTM D4318-17, 2017. Standard Test Methods for Liquid Limit, Plastic Limit, and Plasticity Index of Soils [WWW Document]. URL https://compass.astm.org/download/D4318.33125.pdf (accessed 8.5.19).

Bossart, P., Thury, M., 2008. Mont Terri rock Laboratory. Project, Programme 1996 to 2007 and results.

Busch, A., Schweinar, K., Kampman, N., Coorn, A., Pipich, V., Feoktystov, A., Leu, L., Amann-Hildenbrand, A., Bertier, P., 2017. Determining the porosity of mudrocks using methodological pluralism. Geological Society, London, Special Publications 454, 15–38. https://doi.org/10.1144/SP454.1

Favero, V., 2017. Multiphysical behaviour of shales from Northern Switzerland. https://doi.org/10.5075/epfl-thesis-7539, urn:nbn:ch:bel-epfl-thesis7539-7

Favero, V., Ferrari, A., Laloui, L., 2016. On the hydro-mechanical behaviour of remoulded and natural Opalinus Clay shale. Engineering Geology 208, 128–135. https://doi.org/10.1016/j.enggeo.2016.04.030

Ferrari, A., Crisci, E., Laloui, L., 2018. Arbeitsbericht NAB 17-27 - Geotechnical Experimental Characterisation of Opalinus Clay Cores from the Borehole Lausen.

Ferrari, A., Favero, V., Laloui, L., 2016. One-dimensional compression and consolidation of shales. International Journal of Rock Mechanics and Mining Sciences 88, 286–300. https://doi.org/10.1016/j.ijrmms.2016.07.030

Ferrari, Favero, Manca, Laloui, 2012. Geotechnical characterization of core samples from the geothermal well Schlattingen SLA-1 by LMS/EPFL (No. Arbeitsbericht NAB 12-50).

Gautschi, A., 2017. Safety-relevant hydrogeological properties of the claystone barrier of a Swiss radioactive waste repository: An evaluation using multiple lines of evidence. Grundwasser 22, 221–233. https://doi.org/10.1007/s00767-017-0364-1

Giger, S.B., Ewy, R.T., Favero, V., Stankovic, R., Keller, L.M., 2018. Consolidated-undrained triaxial testing of Opalinus Clay: Results and method validation. Geomechanics for Energy and the Environment 14, 16–28. https://doi.org/10.1016/j.gete.2018.01.003

Hekel, U., 1994. Hydrogeologische Erkundung toniger Festgesteine am Beispiel des Opalinustons (Unteres Aalenium).

Houben, M.E., Desbois, G., Urai, J.L., 2014. A comparative study of representative 2D microstructures in Shaly and Sandy facies of Opalinus Clay (Mont Terri, Switzerland) inferred form BIB-SEM and MIP methods. Marine and Petroleum Geology 49, 143–161. https://doi.org/10.1016/j.marpetgeo.2013.10.009

Lauper, B., Jaeggi, D., Deplazes, G., Foubert, A., 2018. Multi-proxy facies analysis of the Opalinus Clay and depositional implications (Mont Terri rock laboratory, Switzerland). Swiss J Geosci 111, 383–398. https://doi.org/10.1007/s00015-018-0303-x

Marion, D., Nur, A., Yin, H., Han, D., 1992. Compressional velocity and porosity in sand-clay mixtures. GEOPHYSICS 57, 554–563.

Mazurek, M., Hurford, A.J., Leu, W., 2006. Unravelling the multi-stage burial history of the Swiss Molasse Basin: integration of apatite fission track, vitrinite reflectance and biomarker isomerisation analysis. Basin Research 18, 27–50. https://doi.org/10.1111/j.1365-2117.2006.00286.x

Mazurek, M., Wersin, P., Hadi, J., 2017. Opalinus Clay in the shallow decompaction zone: Geochemical investigations on drill core samples from borehole Lausen KB (No. NAB 16-58).

Minardi, A., Crisci, E., Ferrari, A., Laloui, L., 2016. Anisotropic volumetric behaviour of Opalinus clay shale upon suction variation. Géotechnique Letters 6, 1–5. https://doi.org/10.1680/jgele.16.00023

Minardi, A., Ferrari, A., Laloui, L., 2019. Benchmark study on triaxial testing of Opalinus Clay: analysis and comparative evaluation of tests results. Swiss Federal Institute of Technology, EPFL.

Nagra, 2014. Sicherheitstechnischer Vergleich und Vorschlag der in Etappe 3 weiter zu untersuchenden geologischen Standortgebiete (No. Technischer Bericht 14-01).

Nagra, 2008. Vorschlag geologischer Standortgebiete für das SMA- und das HAA-Lager (No. NTB 08-04). Wettingen.

Nagra, 2002. Projekt Opalinuston Synthese der geowissenscha. Technischer Bericht 02-03.

Nagra, 2001. Sondierbohrung Benken: Untersuchungsbericht (No. NTB 00-01). Wettingen.

Philipp, T., Amann-Hildenbrand, A., Laurich, B., Desbois, G., Littke, R., Urai, J.L., 2017. The effect of microstructural heterogeneity on pore size distribution and permeability in Opalinus Clay (Mont Terri, Switzerland): insights from an integrated study of laboratory fluid flow and pore morphology from BIB-SEM images. Geological Society, London, Special Publications 454, 85–106. https://doi.org/10.1144/SP454.3

Romero, E., Simms, P.H., 2008. Microstructure Investigation in Unsaturated Soils: A Review with Special Attention to Contribution of Mercury Intrusion Porosimetry and Environmental Scanning Electron Microscopy. Geotechnical and Geological Engineering 26, 705–727. https://doi.org/10.1007/s10706-008-9204-5

Seiphoori, A., Whittle, AndrewJ., Krakowiak, KonradJ., Einstein, HerbertH., 2017. Insights Into Diagenesis and Pore Structure of Opalinus Shale Through Comparative Studies of Natural and Reconstituted Materials. Clays and Clay Minerals 65, 135–153. https://doi.org/10.1346/CCMN.2017.064055

Vogt, T., Ebert, A., Häring, C., Becker, J.K., Traber, D., Deplazes, G., Bläsi, H., Rufer, D., 2016. Kernbohrung Lausen: Geologische, hydrogeologische und bohrlochgeophysikalische Untersuchungen (Rohdatenbericht) (No. NAB 15-10).

Vogt, T., Hekel, U., Ebert, A., Becker, J.K., Traber, D., Giger, S., Brod, M., Häring, C., 2017. Hydrogeologische Untersuchungen im oberflächennahen Opalinuston (Bohrloch Lausen, Schweiz)Hydrogeological investigations in shallow Opalinus Clay (borehole Lausen, Switzerland). Grundwasser 22, 209–220. https://doi.org/10.1007/s00767-017-0363-2.

Wersin, P., Mazurek, M., Waber, H.N., Mäder, U.K., Gimmi, T., Rufer, D., de Haller, A., 2013. Rock and porewater characterisation on drillcores from the Schlattingen borehole, NAB 12-54.

Chapter 3

Hydro-mechanical one-dimensional behaviour of Opalinus Clay from various sites

3. Hydro-mechanical one-dimensional behaviour of Opalinus Clay from various sites

Part of the results presented in this chapter was published in:

Journal paper: "*Crisci, E., Ferrari, A., Giger, S.B., Laloui, L., 2019. Hydro-mechanical behaviour of shallow Opalinus Clay shale. Engineering Geology 251, 214– 227. https://doi.org/10.1016/j.enggeo.2019.01.016*". The post-print version of the journal paper has been used to draft the chapter.

Conference paper: "*Crisci, E., Ferrari, A., Giger, S.B., Laloui, L., 2019. Anisotropic Behaviour of Shallow Opalinus Clay, in: Ferrari, A., Laloui, L. (Eds.), Energy Geotechnics. Springer International Publishing, Cham, pp. 442–448. https://doi.org/10.1007/978-3-319-99670-7_55".*

Contribution of the Candidate: performance of the experimental testing, analysis of the results, writing of the manuscript.

Additional results, not presented nor discussed in the mentioned publications are included in this chapter.

3.1. Introduction

In the context of nuclear waste storage, numerous studies have been conducted to analyse the hydro-mechanical behaviour of intact Opalinus Clay (e.g., Bossart et al., 2002; Corkum and Martin, 2007; Ferrari et al., 2014; Giger et al., 2018; Heitzmann, 2004; Minardi et al., 2016), fault-gouge material (e.g., Orellana et al., 2018), as well as microstructural features (e.g., Houben et al., 2014; Keller et al., 2013). A substantial part of the research was conducted on cores sourced at the Mont Terri (MT) Underground Rock Laboratory, where Opalinus Clay is currently found at a depth of approximately 300 m. It is estimated that at this location, the formation has reached a maximum burial depth of approximately 1350 m (Mazurek et al., 2006). A few geotechnical studies have also been conducted on Opalinus Clay from deep boreholes in northeastern Switzerland, near the villages of Benken (Nagra, 2001) and notably Schlattingen (SLA), (Favero et al., 2016; Ferrari et al., 2012, 2016). At the borehole Schlattingen, Opalinus Clay was encountered at a depth of 830-950 m, and maximum burial is estimated to have reached a depth of approximately 1700 m based on estimates of the nearby borehole of Benken (Mazurek et al., 2006; Nagra, 2002).

The shale behaviour is transversely isotropic, with the sedimentation planes corresponding to the planes of isotropy. The anisotropy results mainly from the orientation of the clay minerals during the depositional phase, the diagenetic history and the associated pore space distribution. Several studies have highlighted the anisotropic mechanical behaviour of the geomaterial (e.g., Amann et al., 2011; Bossart and Thury, 2008; Giger et al., 2018; Salager et al., 2013). In particular, the stiffness of the material was found to be higher when loaded in the direction of the bedding planes, rather than in the orthogonal directions. The effect of the diagenesis on the Opalinus Clay compressibility has been investigated in the work of Favero et al. (2016), by comparing the behaviour of remoulded and intact specimens. The results showed that the diagenesis had a non-negligible influence on the reduction of porosity, while on the other hand, it did not seem to have a substantial impact on the permeability of the material.

On the millimetre-centimetre scale, the Opalinus Clay shale is made of clay-rich layers, alternating with quartz and carbonate-rich layers. Among the works in which the microstructure of Opalinus Clay have been studied (Chapter 2, Section 2.2), we recall the work of Houben et al. (2014), characterising the different layer types of the Opalinus Clay shale retrieved in Mont Terri. Clay layers are composed of a clay-mineral rich matrix, with particles preferentially oriented along the bedding direction, in which grains of other minerals – typically quartz – are immersed. Instead, quartz-rich layers are mainly made of quartz grains, and the inter-grain

porosity is filled with clay particles, shifting the fabric to grain-supported as the quartz content increases. Those layers are also found to have a lower porosity compared to the clay layers. As a consequence of the layer alternation, it has been assessed that Opalinus Clay samples with higher quartz and carbonate contents present higher rigidity (Gräsle and Plischke, 2010) and lower volumetric sensitivity to changes in water content (Minardi et al., 2016). The influence of carbonate on the strength of Opalinus Clay has been studied in Klinkenberg et al. (2009) and a positive correlation between the carbonate content and the strength has been derived in the work of Kaufhold et al. (2013).

For the design of a radioactive waste repository in Switzerland, the range of possible construction depths currently considered is between approximately 400 m and 900 m below ground. The maximum depth is controlled by construction suitability, while a minimum depth is required for safe long-term isolation of the waste (time period to be considered for high-level waste: 1 million years and beyond). Therefore, future erosion scenarios need to be developed, and the effects of host rock decompaction and repository exhumation need to be assessed as part of the long-term safety analysis (ENSI, 2009).

In 2015, a borehole was drilled close to the village of Lausen, in the Tabular Jura (Switzerland), where Opalinus Clay is encountered immediately at the base of Quaternary sediments at a shallow depth, from 6 to 71 m, with a sub-horizontal bedding orientation (Vogt et al., 2016), and past maximum burial likely well in excess of 1000 m (Mazurek et al., 2006; Nagra, 2002). At Lausen, the formation has already experienced exhumation from much greater depth over geological time-scales and therefore provides a unique analogue for the evaluation of the long-term evolution of a repository. The exhumation may be associated with alteration of the shale properties, including mechanical degradation, fracture propagation and weathering. Geochemical analyses showed signs of weathering of the formation in the uppermost 20-30 m (Mazurek et al., 2017). In the same section (down to 20-30 m), cored samples were profoundly disturbed by fractures (Vogt et al., 2016), and in situ tests demonstrated high hydraulic conductivity (Vogt et al., 2017).

The analysis of the material hydro-mechanical properties at the laboratory scale, compared to samples from greater depths, represents an exceptional opportunity for investigating the effects of the erosion of the above strata on the material properties. Little previous research has involved heavily overconsolidated Opalinus Clay samples from shallow current depths (e.g., Aristorenas, 1992; Bellwald, 1990; Hekel, 1994).

This Chapter focuses on the hydro-mechanical volumetric behaviour of specimens from shallow depths, and the results are compared to the characteristics of specimens of Opalinus Clay from greater depths. In this Chapter, the material volumetric response and associated hydraulic properties are investigated in oedometric conditions; conversely, the material strength is addressed in Chapter 4. An extensive laboratory programme performed on several samples sourced at different depths from the Lausen borehole is presented (Ferrari et al., 2018). The volumetric hydro-mechanical behaviour of the shallow Opalinus Clay (intact core samples) was characterised through one-dimensional consolidation and hydraulic conductivity tests, with a focus on the anisotropic features of the material. The stress variations typical of burial and unloading of geological formations can be reproduced, in the laboratory, in laterally confined conditions (i.e. oedometric test); this type of test, in fact, is suitable for simulating load changes which involve large areas compared to the thickness of the formation, so that lateral deformation may be neglected.

The results were compared to previous works on cores obtained from greater depths, namely, from the Mont Terri URL (300 m, Favero, 2017) and the Schlattingen borehole (at approximately 900 m, Ferrari et al., 2012). The comparison allows inferring the effect of the exhumation process experienced by the formation on the consolidation and hydraulic conductivity features of the intact and remoulded specimens.

The experimental programme is briefly presented; the testing and interpretation procedures are reported. The results of the experimental programme are then presented and discussed, with a focus on the comparison with the results of samples from other sites, from greater depths. Lastly, conclusions are drawn.

3.2. Tested samples

Several samples were tested in oedometric conditions. The cores from which the samples were extracted have been presented in Chapter 2, Section 2.4.1, and their geotechnical properties have been discussed in Section 2.5.

Two samples were obtained from cores sourced at the Mont Terri URL (≈300 m depth), in the sandy facies of the formation (core BHA18) and tested in oedometric conditions. Consolidation and hydraulic conductivity tests were carried out also on intact specimens obtained from four selected depths in Lausen (from cores L3, L8, L11-12, L13). For each depth, two oedometric tests were performed on twin specimens, retrieved within a short distance (within 20 cm), in order to minimize possible bias effects due to small-scale material heterogeneity (Figure 3-1).

Although local composition variabilities could be expected, even at this scale, the initial characteristics of the twin specimens were analysed to verify the similarity of the specimens. An indication of the compositional similarity among specimens can be gathered from the measurement of the void ratio, which, for Opalinus Clay, has been shown to be strongly affected by the mineralogical composition, as discussed in Chapter 2, Section 2.2. Therefore, the void ratio of the prepared specimens was chosen as an indication of composition similarities between two twin specimens. Differences in the void ratios of twin specimens higher than 5% were attributed to a non-comparable mineralogical composition.

For each depth, one specimen was prepared to be loaded in the direction perpendicular (⊥) to the bedding planes (usually referred to as S-samples), and the second was prepared to be loaded in the direction parallel (//, P-samples). In addition, consolidation tests were performed on remoulded material obtained from two specimens from Lausen (cores L3 and L13), to analyse the differences between intact and remoulded state.

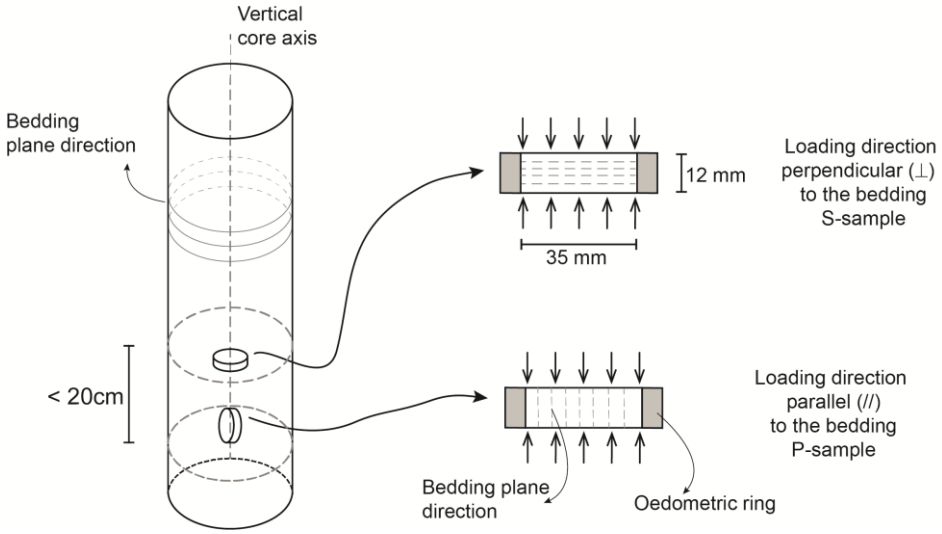

Figure 3-1 Schematic representation of the core and the twin samples, retrieved at similar depths, tested in the loading direction: perpendicular and parallel to the bedding direction.

For the oedometric and hydraulic conductivity tests, synthetic pore water was used in order to reproduce the chemical composition of the in situ pore water, which may affect the hydro-mechanical response of clayey geomaterials. Following preliminary pore water analysis results (data from Uni Bern, written communication, 09-02-2017), it was highlighted that the pore water chemistry in Lausen is not constant with depth. In particular, chloride concentration is very low (≈50 mg/l) down to the first 20 m (where meteoric water has infiltrated into the formation), increases fairly linearly between 20 and 40 m (up to ≈1700 mg/l), and remains stable at this concentration below 40 m. In addition, the proportion of the chemical components was found to be relatively constant with depth and similar to that found in Opalinus Clay from

the Schlattingen borehole. For these reasons, it was chosen to adopt the water recipe proposed by Wersin et al. (2016) for Schlattingen and to use a factor of dilution of the water concentration to reproduce the variability in depth. The adopted factor of dilution was equal to *20* for samples retrieved at a depth of 15-20 m, *8* for 20-25 m, *4* for 25-30 m, *3* for 35-45 m, and *2* for 45-75 m. For the samples sourced from Mont Terri, Pearson's water was used as the circulating fluid (Pearson, 2003).

As only one pair of specimens for hydro-mechanical testing was obtained from each core, hereafter the specimens are named after the core code (e.g., L3) and the loading direction (e.g., L3⊥ or L3//).

3.3. Set up and procedures

3.3.1. Intact sample preparation and testing setup

A systematic procedure was adopted to obtain the intact specimens for the oedometric and hydraulic conductivity tests: a slice with a thickness of approximately 30 mm was sawn from the core without unpacking it, in order to minimize the disturbance to the specimen; then, a smaller piece was cut, in order to be further handled in a lathe machine. The high resistance tip removed the material continuously, without encountering resistance from the specimen, therefore minimising any disturbance. A cylinder with a diameter slightly larger than the final confining ring was obtained; final re-coring was performed with the oedometric ring, by using a hydraulic press; lastly, the lower and upper faces were smoothed using sandpaper, in order to obtain parallel and plane surfaces. No fluid (e.g., water, air) was used during the specimen preparation phase, in order to preserve the original water content/composition as much as possible and to reduce the disturbance of the material. However, a slight drying of the material occurred during the preparation. The comparison between the water content of the cores (as received) and of the specimens after preparation revealed a water loss ranging from 0.4 wt% to 1.9 wt%, corresponding to a degree of saturation at the end of the preparation between 61% and 85%. Re-saturation of the specimens was carried out directly inside the testing device, immediately after the specimen preparation, in isochoric conditions.

The testing apparatus used for these tests is a specially designed high-pressure oedometric cell allowing a maximum attainable vertical stress of 100 MPa (Ferrari and Laloui, 2013), with an accuracy of about 60 kPa. The high level of applicable vertical stress is required in order to observe the transition from the pre- to the post-yield behaviour of the shale. The vertical pressure is applied from the bottom base by means of a hydraulic jack, in which a

pressure/volume controller maintains the pressure. The vertical displacement is measured via two LVDTs fixed on the loading piston and in contact with the top base of the cell (resolution of 1 μm). At the top and bottom bases, the specimen is in contact with two drainage lines, connected to pressure/volume controllers.

Each specimen was first subjected to a small vertical load (≈0.1 MPa), to ensure contact between the specimen and the loading piston, and then saturated using the synthetic pore water corresponding to the sampling depth. When in contact with the water, a tendency to swell occurred. Rapid swelling can induce specimen damage with microcrack formation due to the inhomogeneous swelling between the bases, in direct contact with the water supply, and the rest of the specimen. Therefore, it was chosen to keep quasi-isochoric conditions, increasing the applied vertical total stress as swelling occurred. The displacements were maintained within a value corresponding to a vertical strain of ±0.1%. Therefore, the void ratio was not significantly affected by the saturation phase (impact on the third decimal digit of the void ratio computation). Once the deformation stabilized (10 to 14 days were needed), the saturation phase was considered complete, and the total vertical stress corresponded to the swelling pressure. Constant water backpressure (50-100 kPa) was applied throughout the test. Stress increases were applied using a pressure-volume controller at the fastest possible rate. Each stress level was maintened constant until the primary consolidation process was completed. Unloading/reloading phases were performed, in steps, at various stages during the test.

3.3.2. Application of the one-dimensional consolidation theory to shales

The application of high instantaneous stress in the laboratory is rarely feasible. Because of the high-stress level reached, some time is required to complete the loading phase. To analyse the settlement-over-time curve of each loading increment, an analytical solution that considers the time-dependent load was adopted (Ferrari et al., 2016). The solution uses a modified form of the Biot theory (Biot, 1941), accounting for the oedometric conditions, and an extension of the one-dimensional consolidation theory, to consider the poroelastic behaviour of shales and the non-instantaneous loading conditions. The following equation describes the one-dimensional consolidation process in shales:

3-1 $$c_v \frac{\partial^2 u_e}{\partial z^2} = \frac{\partial u_e}{\partial t} - C \frac{\partial \sigma_v}{\partial t}$$

where c_v is the coefficient of consolidation, u_e is the excess of pore water pressure to be dissipated, σ_v is the total stress in the vertical direction v, and t is the time. The consolidation coefficient in the consolidation theory extended to poroelastic behaviour is defined as:

3-2 $$c_v = \frac{k_v E_{oed} C}{\alpha_{oed} \gamma_w}$$

where k_v is the hydraulic conductivity in the *v*-direction; E_{oed} is the oedometric modulus (the incremental vertical effective stress divided by the incremental vertical strain); C is the ratio of the increment in pore water pressure to the increment in the vertical total stress under one-dimensional and undrained conditions; α_{oed} is the Biot coefficient, defined for the oedometric case as the ratio of the variation in the fluid content to the vertical deformation; γ_w is the water unit weight.

For each loading step, the method (Ferrari et al., 2016) allows for the identification of the parameters E_{oed}, c_v, C and α_{oed}. The primary consolidation settlement was identified, and the void ratio evolution was interpreted in the oedometric plane (i.e., the void ratio at the end of the primary consolidation versus vertical effective stress). The secondary compression settlement was computed through the rate of secondary compression, also called *secondary compression coefficient*, C_α, considering that those settlements develop after the degree of consolidation reaches 95%. This coefficient was therefore fitted on the last part of the *settlement – log(time)*, for each loading step. In Figure 3-2 an example of settlement versus time during a loading step is reported. The derivation of the main parameters is depicted.

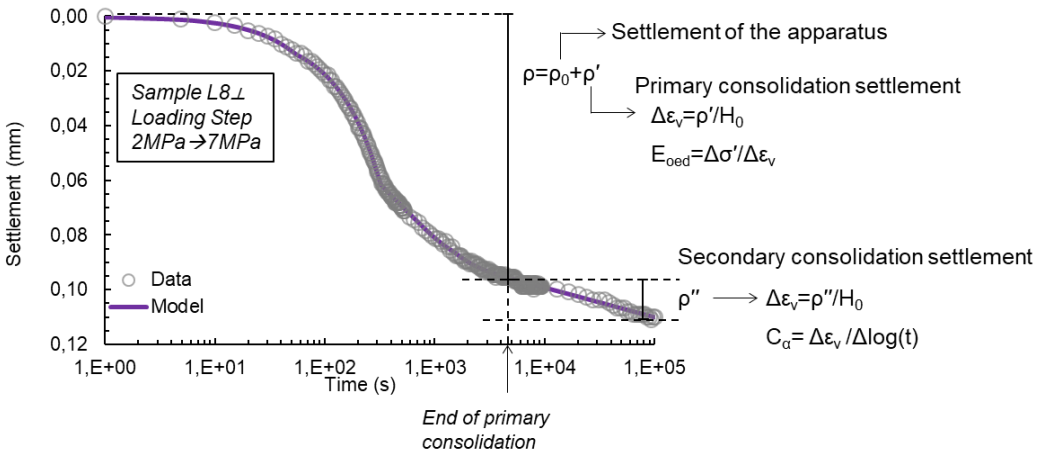

Figure 3-2 Example of settlement versus time curve and derivation of the main parameters.

The interpretation of each loading curve allows deriving also additional information on the hydro-mechanical behaviour of the shale, such as the bulk modulus of the solid phase (K_S). As mentioned before, shales are known to have a transversely isotropic behaviour. Consequently, the Biot coefficient α_{oed} for oedometric conditions can be related to Young's moduli and

Poisson ratios in the direction perpendicular to the bedding (E_2 and ν_2) and parallel to the bedding (E_1 and ν_1), as derived in Ferrari et al. (2016):

3-3 $$\alpha_{oed} = 1 - \frac{E_{oed}}{3K_s}\left[1 + \frac{2\nu_2 E_1}{E_2(1-\nu_1)}\right]$$

The definition of elastic moduli in transversely isotropic conditions is discussed in details in Chapter 6. In the case of isotropy, Equation 3-3 reduces to the classic Biot coefficient definition, that requires only the determination of the bulk modulus K:

3-4 $$\alpha = 1 - \frac{K}{K_s}.$$

Equation 3-4 is used in the following as a simplification to estimate K_s, considering the difficulties in determining the anisotropic values of poroelastic parameters. However, it has to be considered that minimal variation of α, within a few per cent, significantly affects the derivation of K_s, even of 1-2 orders of magnitude in the high α range.

3.3.3. Remoulded samples

In addition, remoulded specimens were tested in conventional and high-pressure oedometric cells. As proposed by Burland (1990), the remoulded specimens were prepared with material that has been carefully mixed with water at a water content 1.5 times the liquid limit (w_L), without air drying or oven drying, and then consolidated in one-dimensional conditions. The intact Opalinus Clay was crushed by means of a grinder, and the fraction passing through a 0.5 mm sieve was selected. The slurry, having water content 1.5 times w_L, was prepared by mixing the powdered shale with synthetic water and by vigorously working with a metal spatula in a container. After 24 h of equalisation in a closed environment, the slurry was placed in the oedometric ring for the low-pressure test (diameter: 60 mm) with the aid of the metal spatula, and small portions of material were progressively disposed to avoid trapping any air; the upper and lower bases were finally smoothed. Precompressed filter papers, saturated in distilled water, were inserted between the specimen and the porous stones.

First, the specimens were loaded in a conventional oedometer apparatus to receive a pre-consolidation, with up to 1 MPa of vertical stress. After consolidation, the specimens were carefully extruded from the oedometric ring to be later installed in the high-pressure device. To fit the specimen in the oedometric ring for the high-pressure test (35 mm), the specimen diameter was initially reduced, and finally, the specimens were re-cored using the oedometric

ring; the upper and lower bases were finally smoothed. The results from the low-pressure oedometer were interpreted using the classic consolidation theory, while those from the high-pressure device were interpreted using the analytical solution by Ferrari et al. (2016), discussed above.

3.3.4. Hydraulic conductivity

The mentioned extended consolidation theory allows for the derivation of the hydraulic conductivity of the geomaterial at each loading step. In addition, constant-head hydraulic conductivity tests were carried out on 5 specimens tested in the advanced oedometric cell. Tests were performed using the synthetic pore water corresponding to the core depth. The hydraulic conductivity was measured in the direction perpendicular (⊥) to bedding for cores L8 and L13, and parallel (//) to bedding for cores L3, L8 and L13. During the tests, the vertical total stress was kept constant. For the specimen L3//, the measured swelling pressure was of 0.7 MPa, and the hydraulic conductivity test was run after the first loading steps, at a constant vertical total stress of 5 MPa. For specimens L8 (⊥, //) and L13 (⊥, //), the hydraulic conductivity was measured immediately after the saturation phase; therefore, the applied constant total vertical stress for these tests corresponds to the obtained swelling pressure. The swelling pressure obtained in these tests involve a range of values, from few hundreds up to few thousand kPa, that can be attributed to a combined effect of the mineralogy, the initial void ratio, the actual stiffness of the material, the initial degree of saturation, and of the limited strains that were allowed (within ± 0.1%). Table 3-1 summarises the performed tests and the stress conditions during the tests.

Table 3-1 Summary of the performed hydraulic conductivity tests.

Core	Flow direction with respect to the bedding	Total vertical stress applied σ_z (MPa)	Hydraulic gradient (m/m)
L3	//	5.0	246.5
L8	//	0.3	247.5
	⊥	1.0	250.8
L13	//	0.1	252.6
	⊥	0.9	256.0

A pressure gradient was applied using two independent water pressure/volume controllers, connected to the two bases of the specimen in the oedometer cell. The water pressure applied at the top and bottom basis of the specimens were 0.02 MPa and 0.05 MPa, respectively. Once the inflow and outflow water flows equilibrated (2 weeks on average), the hydraulic conductivity *k* was computed assuming the validity of Darcy's law. The short length of the oedometric samples (≈12 mm) in the flow direction allows to adopt the constant head method

also on low porosity materials. The results were compared with the values determined via the consolidation theory (Section 3.4.3), finding good agreement.

3.4. Experimental Results

3.4.1. Intact specimens, Lausen and Mont Terri

The results of 5 pairs of intact specimens are considered here. The initial void ratios, for the specimens loaded in the directions perpendicular ($e_0^{\perp}$) and parallel ($e_0^{//}$) to the bedding, were computed via the specimen mass, volume, water content and density of solid particles and are reported in Table 3-2, along with the sourcing depth and the core code.

Table 3-2 Initial void ratio of specimens prepared for oedometric tests; *distance from the gallery wall.

Site	Core	Depth ±0.1 m	Specimen initial void ratio	
			$e_0^{\perp}$	$e_0^{//}$
LAU	L3	22.6	0.23	0.23
	L8	38.2	0.17	0.17
	L11-L12	61.8	0.16	0.20
	L13	70.4	0.23	0.24
MT	BHA	0.1*	0.18	0.18

The twin specimens sourced from L3, L8 and L13 and BHA had similar initial void ratios. The specimens sourced at a depth of 61.8 ± 0.1 m (straddling cores L11 and L12) showed a significant difference, equal to 25%, in the void ratio ($e_{diff,\%}$), computed as $e_{diff,\%} = (e_0^{//} - e_0^{\perp}) / e_0^{\perp} \cdot 100$. This difference could be attributed to local mineralogical heterogeneities at the investigated depth. For this reason, the mentioned specimens were not considered as comparable (i.e., twin), as an effect of the mineralogy on the investigated hydro-mechanical behaviour is expected.

All the experimental results are reported from Figure 3-3 to Figure 3-12. The results for each couple of tests are presented in the same form: first, the oedometric curves and the swelling indexes, then the oedometric modulus and the consolidation coefficient versus the vertical effective stress. The results from L3 and L8 (from Figure 3-3 to Figure 3-6) samples are here discussed in details. All the considerations are also valid for specimens L13 (Figure 3-9, Figure 3-10), and BHA (Figure 3-11, Figure 3-12), which results are also considered in all the analyses reported in the discussion section. Results on samples L11 and L12 (Figure 3-7, Figure 3-8) are not comparable, and the discussion on the differences between the two loading directions does not concern those results.

In Figure 3-3*a* and Figure 3-5*a*, the oedometric curves at the end of primary consolidation, for the specimens loaded in the direction // and ⊥ to the bedding, are reported. Upon saturation,

different swelling pressures were achieved from the specimens; therefore, the oedometric curves start from those values of applied stress. In particular, a slightly higher swelling pressure was obtained for ⊥-specimens, compared to //-specimens.

Unloading/reloading paths were performed at various stress levels. The slopes of the unloading/reloading branches were not equal from different stress states. Swelling indexes, C_s, slope of the unloading curve, are reported in Figure 3-3*b*, and Figure 3-5*b*, versus the maximum applied vertical effective stress. The C_s was found to increase with the applied stress for both loading directions, highlighting the impact of the damage of the specimens upon loading. In the analysis of the elastic rebounds, a clear difference is found between specimens ⊥ and //, with C_s being 1.5-2 times higher for ⊥-specimens than for //-specimens, that are expected to have higher stiffness.

During the first unloading path, reversible behaviour is generally observed. An exception is represented by sample L13⊥ (Figure 3-9), in which at the first loading step the specimen was subjected to a non-negligible irreversible reduction in void ratio, incompatible with the elastic response that is expected at the beginning of the loading. This response is more likely to be attributed to fissures in the sample, that close during the first loading phase.

During the following loading paths, irreversible deformations are shown in the transition from the elastic to the elasto-plastic domain. However, the transition is not sharp, but evolves over a wide range of vertical effective stresses, increasing the complexity of the determination of the yield point. Casagrande construction would suggest that the yield corresponds to stress values in the range of 7-20 MPa for ⊥-specimens, and 18-30 MPa for //-specimens. However, the plastic deformation shown upon unloading-reloading cycles, suggests that the transition from the elastic to the elasto-plastic domain happened for lower stress values, compared to the estimated ones (e.g., the ⊥-specimen in Figure 3-3*a*, the unloading step from vertical effective stress of 5 MPa). It is observed that the estimated yield stress is higher for specimens loaded parallel to the bedding, compared to the results for specimens loaded in the orthogonal direction. A number of independent geological and petrophysical data suggests that maximum burial of Opalinus Clay in Northern Switzerland was approximately 1000 m greater than at present depth (Mazurek et al., 2006; Nagra, 2002). A plausible maximum past vertical effective stress at Lausen site is thus estimated of the order of 15 MPa, 20 MPa at Mont Terri, in good general agreement with the yield stresses derived from the oedometric tests.

Compressibility indexes, C_C, at high-stress levels, computed on the last section of the compression curve (for a vertical effective stress range between approximately 20 MPa and 100 MPa), are reported in Figure 3-3*a* and Figure 3-5*a*. At high-stress levels, above the yield stress, the two oedometric curves tend to become parallel (C_C being similar), envisaging a progressive reduction of the bedding influence on the compressibility, along with the virgin behaviour.

Oedometric moduli and consolidation coefficients are presented in Figure 3-4 and Figure 3-6 parts *a* and *b*, respectively. For the sake of simplicity, only the coefficients derived from the primary loading coefficients are plotted versus the vertical effective stress at the beginning of the step. It is observed that, following classical soil behaviour (Lambe and Whitman, 1969), the oedometric modulus tends to increase as stress increases. Concerning the consolidation coefficient, it decreases rapidly for low-stress levels. At approximately the estimated value of the yield stress, the coefficient stabilizes towards a constant value. At the maximum stress level achieved, c_v is approximately the same for the two loading directions. The results for //-specimens lie above those for ⊥-specimens, as the specimens loaded in the direction of the bedding present higher oedometric moduli and consolidation coefficients than those for ⊥-specimens.

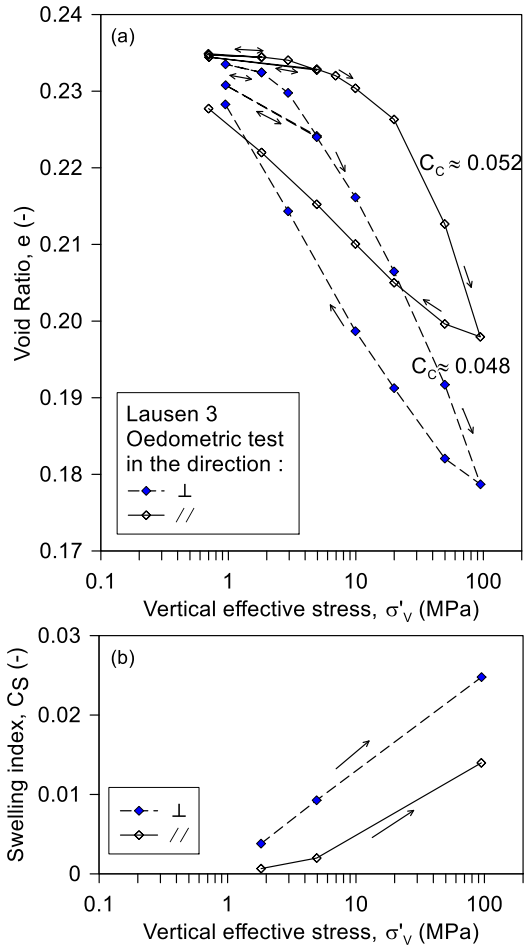

Figure 3-3 Oedometric test results on core L3, specimens loaded in the directions perpendicular (⊥) and parallel (//) to the bedding: (a) end of primary consolidation curves and (b) swelling indexes evolution with applied stress.

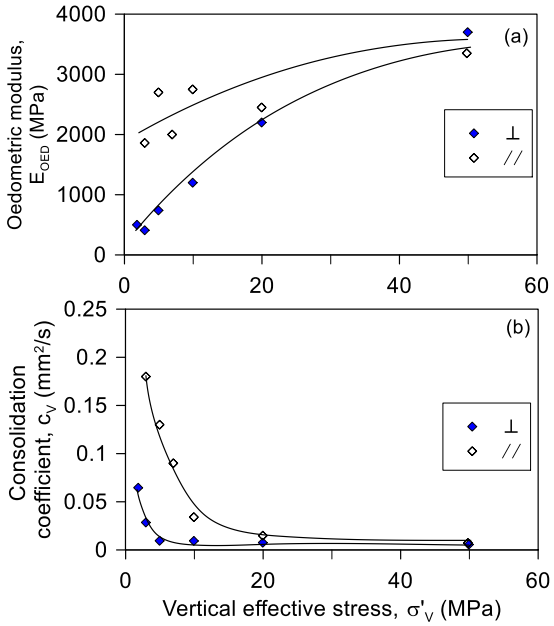

Figure 3-4 Oedometric modulus (a) and consolidation coefficient (b) for the primary loading steps of the oedometric tests on the specimens of core L3, loaded in the direction perpendicular (⊥) and parallel (//) to the bedding plane.

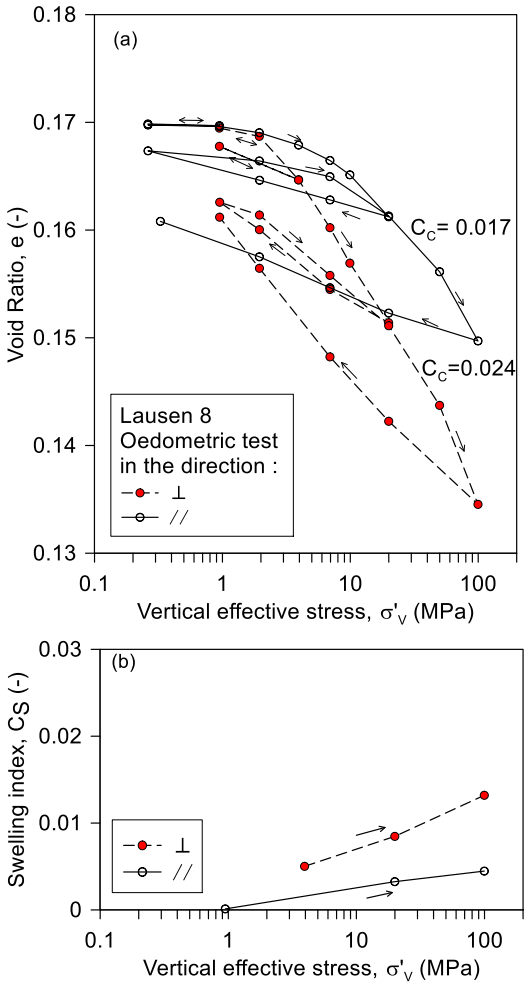

Figure 3-5 Oedometric test results on core L8; specimens loaded in the directions perpendicular (⊥) and parallel (//) to the bedding: (a) end of primary consolidation curves and (b) swelling indexes evolution with applied stress.

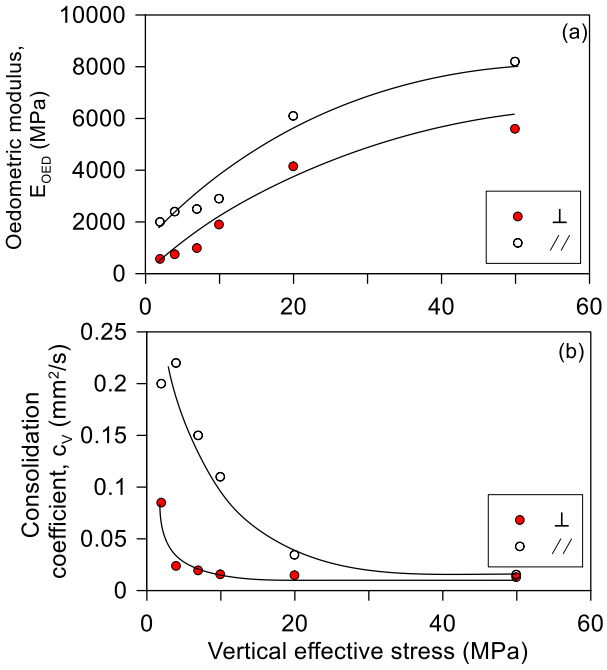

Figure 3-6 Oedometric modulus (a) and consolidation coefficient (b) of the primary loading steps of the oedometric tests on the specimens of core L8, loaded in the direction perpendicular (⊥) and parallel (//) to the bedding plane.

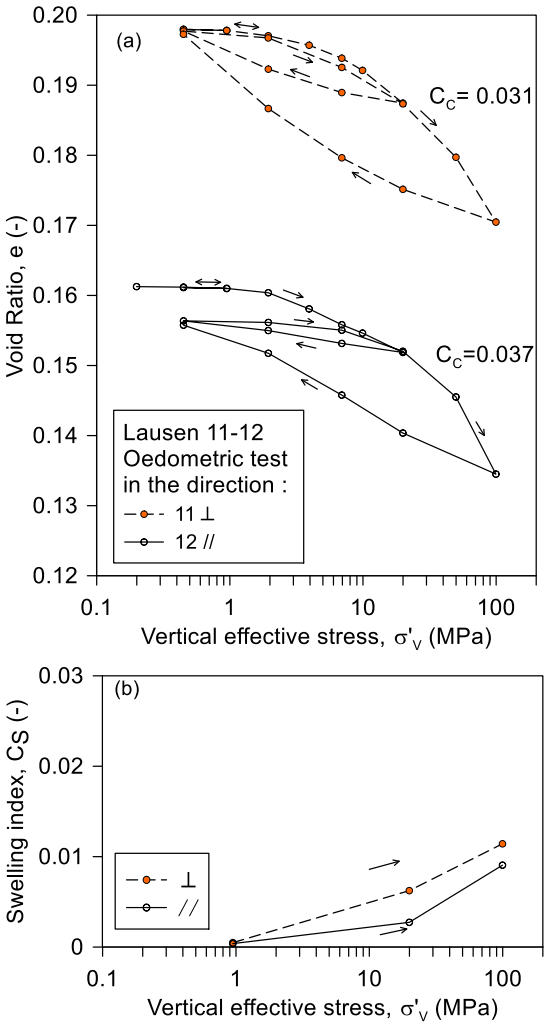

Figure 3-7 Oedometric test results on cores L11-L12 (not twins); specimens loaded in the directions perpendicular (⊥) and parallel (//) to the bedding: (a) end of primary consolidation curves and (b) swelling indexes evolution with applied stress.

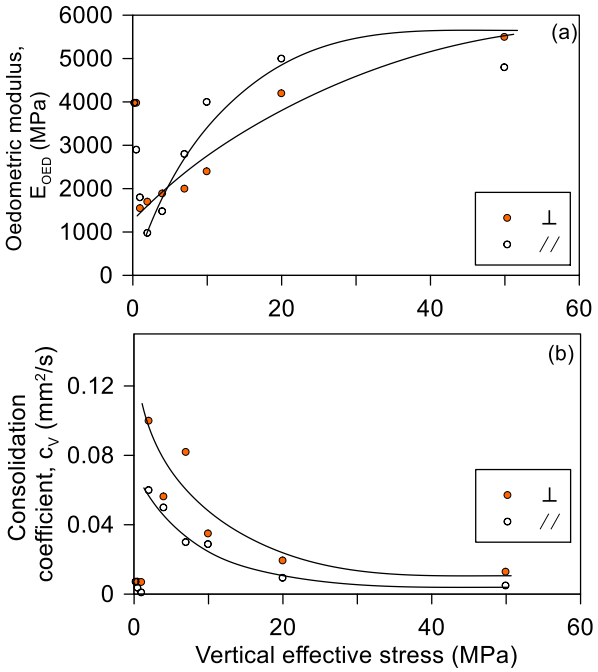

Figure 3-8 Oedometric modulus (a) and consolidation coefficient (b) of the primary loading steps of the oedometric tests on the specimens of cores L11-L12, loaded in the direction perpendicular (⊥) and parallel (//) to the bedding plane.

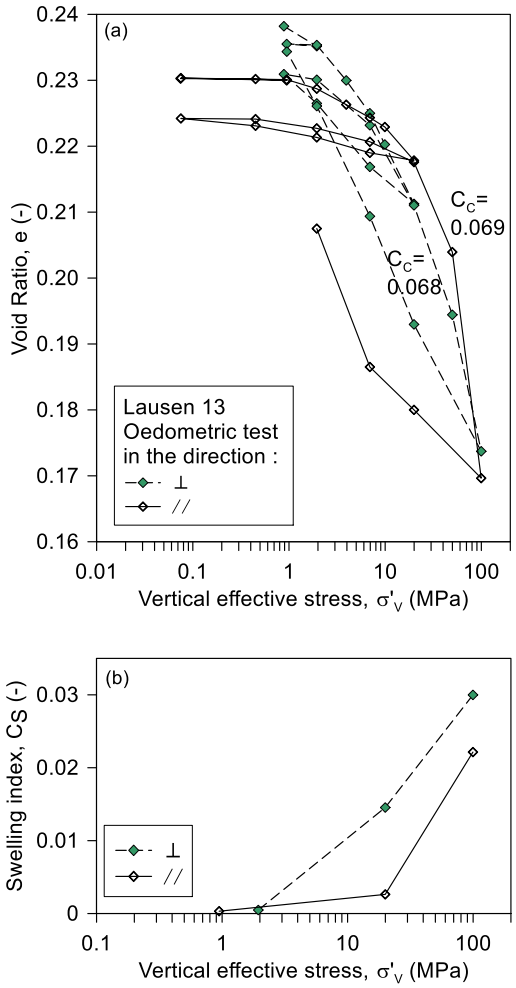

Figure 3-9 Oedometric test results on core L13; specimens loaded in the directions perpendicular (⊥) and parallel (//) to the bedding: (a) end of primary consolidation curves and (b) swelling indexes evolution with applied stress.

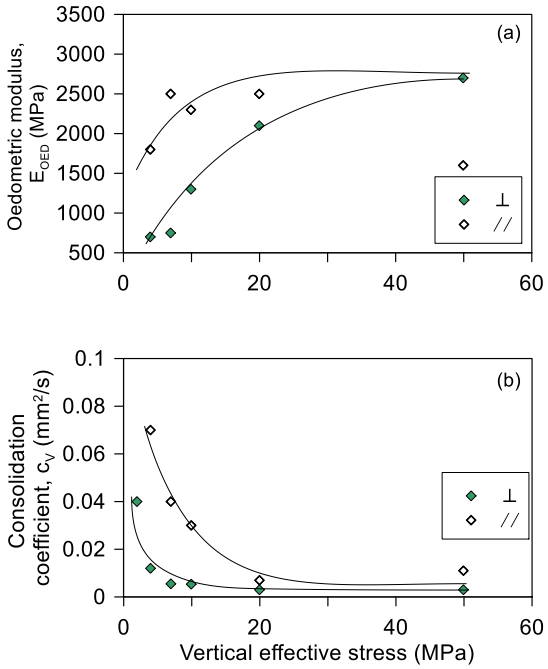

Figure 3-10 Oedometric modulus (a) and consolidation coefficient (b) of the primary loading steps of the oedometric tests on the specimens of core L13, loaded in the direction perpendicular (⊥) and parallel (//) to the bedding plane.

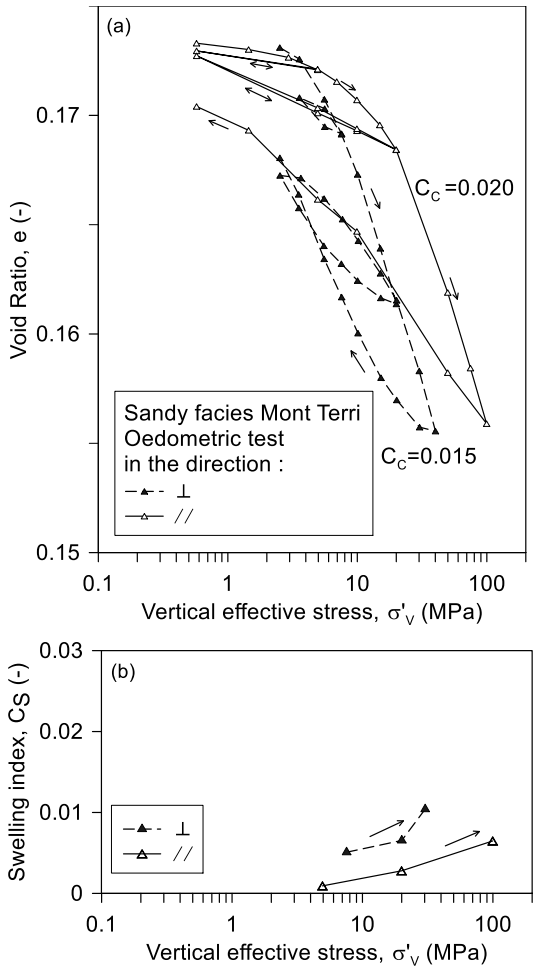

Figure 3-11 Oedometric test results on specimens from the sandy facies (Mont Terri); specimens loaded in the directions perpendicular (⊥) and parallel (//) to the bedding: (a) end of primary consolidation curves and (b) swelling indexes evolution with applied stress.

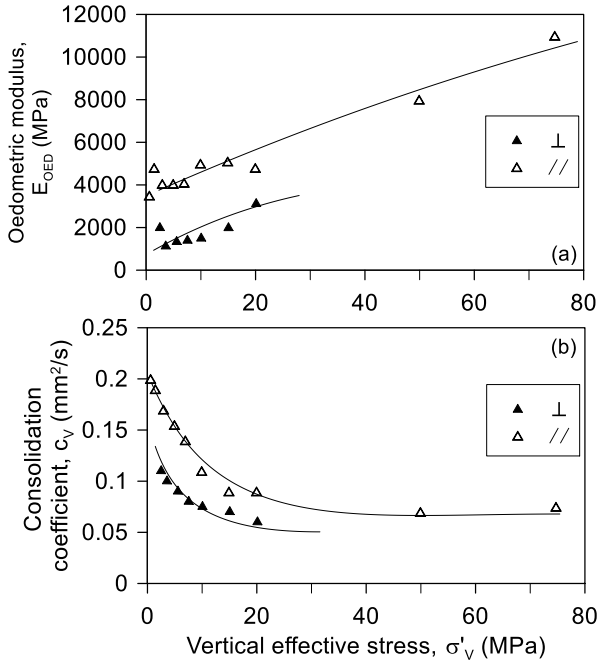

Figure 3-12 Oedometric modulus (a) and consolidation coefficient (b) of the primary loading steps of the oedometric tests on the specimens from the sandy facies (Mont Terri), loaded in the direction perpendicular (⊥) and parallel (//) to the bedding plane.

Besides the primary consolidation parameters, oedometric tests allow deriving information on the short term viscous response of samples. Indeed, each step lasts about 24 hours, while only a few hours are needed to complete the dissipation of the water overpressure induced by the load. The deformations developed during the remaining of the loading step occur at constant load, i.e. they are of viscous nature. Figure 3-13 shows the rate of secondary compression, C_α, versus the vertical effective stress at the end of the loading step, at which the creep occurred.

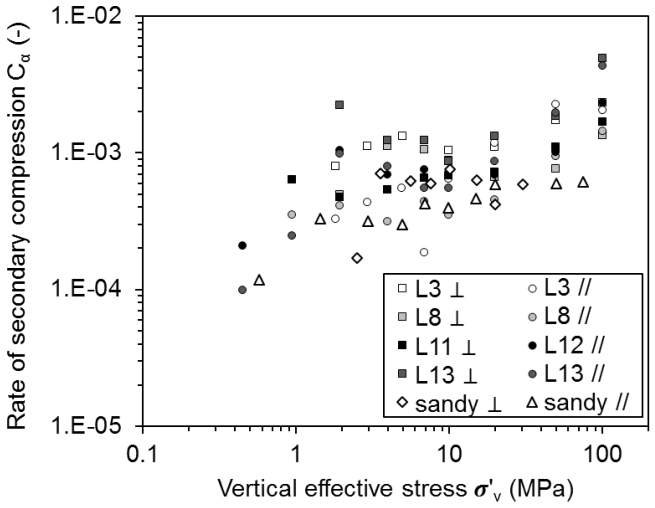

Figure 3-13 Rate of secondary compression, C_α, versus the vertical effective stress at the end of the loading step; samples from Lausen and Mont Terri sites.

The rate of secondary compression was found to range in the order of 10^{-3}-10^{-4} over the analysed stress range, as typical for overconsolidated clays (Lambe and Whitman, 1969), and tending to be higher for higher stress values. The results obtained perpendicular to the bedding showed slightly higher secondary compression coefficients, compared to the results parallel to the bedding. Results from samples with higher clay content (i.e., L3, L13) lies in the upper part of the cloud of points, having higher coefficients. The rates of deformation of Opalinus Clay under constant load are in line with the creep behaviour of similar geomaterials, such as the Callovo-Oxfordian Claystone (Zhang et al., 2019), and Boom Clay (Yu et al., 2015).

Using Equation 3-4, an estimation of the bulk modulus of the solid phase may be derived from the elastic paths of the oedometric tests, under the assumption of isotropic behaviour. Poisson's ratio is assumed to be equal to 0.3, that is a reasonable value for Opalinus Clay S-samples (loaded in the direction perpendicular to bedding), as found in Favero et al. (2018). Values of K_s ranging over two orders of magnitude (between few GPa and few tens, up to 50-60 GPa) were found. High variability of the derived parameter is attributed to the optimisation of α value for each loading step. The α was found to be generally between 0.85 and 0.99. However,

minimal variation in the attribution of α, within a few point percentage causes a dramatic change in K_s, that is therefore difficult to estimate. The results of this value have to be carefully used. An approximated average value of K_s=25 GPa was found for the sandy sample, while lower values (12-14 GPa, Ferrari et al., 2016) were estimated for samples with higher clay content (>60 wt.%). The results are in line with the analysis provided in Ferrari et al. (2016), on shaly samples of Opalinus Clay from Mont Terri and Schlattingen.

3.4.2. Remoulded specimens

For remoulded material, the results of specimens from cores 3 and 13 are shown in Figure 3-14. The oedometric curves obtained from the low- and high-pressure oedometric cells on remoulded specimens are presented together with the oedometric curves obtained for the intact specimens, from the same core, loaded in the direction perpendicular to the bedding.

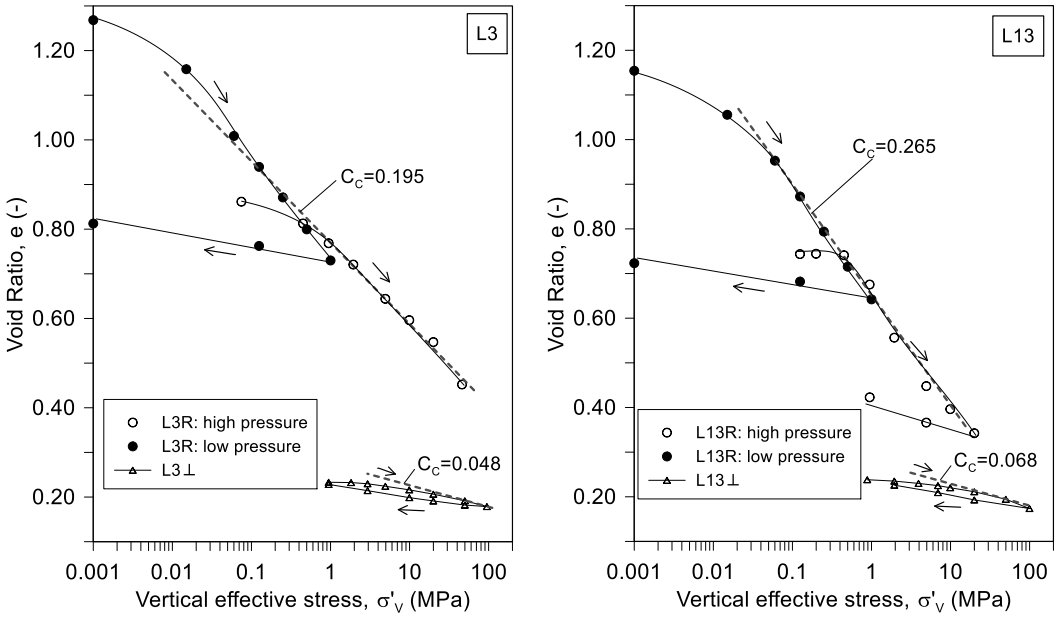

Figure 3-14 Oedometric test results on remoulded (R) material from cores 3 (left) and 13 (right), tested in low and high-pressure oedometric cells. Comparison with intact specimens loaded in the direction perpendicular to the bedding.

The compressibility of the remoulded material is by far higher than the intact material. As already observed on Opalinus Clay from the Mont Terri URL and Schlattingen borehole (Favero et al., 2016), the porosity of the natural Opalinus Clay is related not only to the mechanical compaction and fabric configuration but also to diagenetic effect.

In the comparison of the porosities of remoulded and intact samples, the potential impact of time needs to be acknowledged. The coefficient of secondary compression determined in oedometric tests (load step duration of 1 day) at the in situ effective stress (estimated to be 5-15 MPa) was approximately C_α=0.001 (Section 3.4.1). Taking this value as a reference, and hypothesizing that it remained constant in time, the impact of 180 My, i.e. from the material

sedimentation to today, on the porosity variation would be of Δe=0.014. Altough contributing to the porosity reduction, with the information available on the laboratory time scale, the impact of creep can be considered as marginal.

Indeed, the porosity achieved at the end of the compaction of the remoulded material (up to 50 and 20 MPa for cores 3 and 13, respectively) is 1.5-2 times higher than the porosity of the intact specimens An impact of the preparation technique (i.e. the shale disaggregation method) on the actual structure of the remoulded specimens, and then on their compressibility, could be further investigated.

3.4.3. Hydraulic conductivity

The results of the hydraulic conductivity, computed via the consolidation theory (primary loading steps) and from constant head permeability tests, are represented in Figure 3-15, against the vertical effective stress. The results from the two methods were found to be in good agreement. In the logarithmic plane, a common trend for all the tested specimens can be easily identified, disregarding the sourced depth and the composition heterogeneity. As the effective stress is increased, a reduction in hydraulic conductivity is obtained. The reduction is more pronounced in the low-stress range. Linear regression was performed to derive the equation of the linear correlation in the logarithmic plane:

3-5 $$k=a\cdot(\sigma'_v)^b$$

where k is the hydraulic conductivity [m/s], σ'_v the vertical effective stress [MPa], and a [m/s/kPa] and b [-] are the regression parameters. For the analysed case of the Opalinus Clay from the Lausen borehole, the regression parameters are equal to a=1.32·10^{-12} and b=-1.085 (R^2=0.75). Despite the scatter, the correlation gives a hint on the evolution of the parameter with the load, disregarding loading direction and specimen properties (e.g., void ratio, dominant void diameter, and mineralogical composition).

Analysing the results in Figure 3-15, the difference in k-value between the two tested directions, parallel and perpendicular to the bedding, is not clearly defined. However, the ratio between the hydraulic conductivity in the two loading directions is expected to be in the order of 5 (Nagra, 2002), i.e. below the dispersion of the results for a same vertical effective stress.

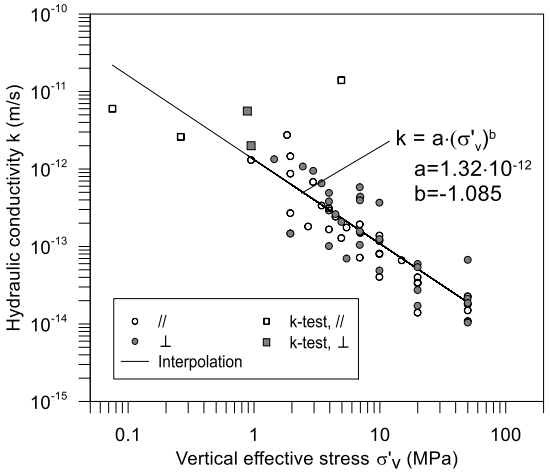

Figure 3-15 Hydraulic conductivity computed from oedometric and constant-head (k-test) permeability tests in the directions parallel and perpendicular to the bedding.

The *k*-values for corresponding stress values in the two loading directions were compared. It was observed that the ratio of the hydraulic conductivities, $k_{//}/k_{\perp}$, is generally higher than 1, meaning that the hydraulic conductivity in the direction parallel to the bedding is higher than the one in the direction perpendicular to the bedding. The ratio tends to be closer to one for high stresses, suggesting that the difference in hydraulic conductivities reduces and that for high-stress values, the matric hydraulic conductivity is the same, disregarding the flow direction.

3.5. Discussion

The results obtained in this experimental programme aimed to deliver a key piece of the complex puzzle of the behaviour of the Opalinus Clay. The investigated site had experienced a complex geological history that is envisaged to correspond to possible future development in the site, which will be chosen for nuclear waste storage. Therefore, it is important to understand the impact on the material properties as the overburden is subsequently removed. In the following discussion, an analysis of the formation properties and the differences/similarities among sites (i.e., depths) is proposed to lay the foundation for answering these questions. However, in the scenarios of the long term evolution of the repository, other aspects and processes may need to be taken into account.

3.5.1. Impact of the mineralogy on Opalinus Clay

From a hydro-mechanical point of view, it is essential to analyse the differences between Opalinus Clay from shallow and deeper sites, in order to infer the impact of the exhumation on the material properties. To this aim, the results of the compressibility indexes of specimens from Lausen have been compared to results found on the same formation from other sites (data from this study and Favero, 2017). In Figure 3-16*a*, the compressibility indexes of specimens

(from Mont Terri, Schlattingen and Lausen) loaded in the direction perpendicular (⊥) to the bedding are plotted versus their clay-mineral content (*f*, wt. %). As the clay-mineral content decreases and leaves space for more rigid minerals (e.g., quartz, carbonates), the compressibility index decreases. Therefore, higher compressibility indexes correspond to higher clay-mineral contents. The increase in compressibility with the clay percentage seems to be low for contents below 50-60 wt. %, while the increment is higher for clay-mineral contents above it. The results, in the investigated range of clay-mineral contents (roughly 30 wt. % to 80 wt. %), are interpolated with an exponential function with the equation: $C_c = e^{a \cdot f} \cdot b$ with $a = 3.16 \cdot 10^{-2}$, $b = 5.42 \cdot 10^{-3}$. The results from Schlattingen specimens (greatest depth) lies in the lower range of obtained values. This may be related to the higher compaction (and lower porosity) of specimens from this location. However, the limited distance between the sets of points does not allow to extrapolate a different trend for each site.

It can be inferred that, despite the exhumation process that affected the formation in Lausen, the obtained results are comparable with those from deeper sites, envisaging a marginal impact of the de-compaction on the elastoplastic parameter C_c of intact specimens.

A similar correlation between the swelling index and clay-mineral content has been derived, where C_s was computed on the final unloading path of each oedometric test (Figure 3-16*b*), on specimens (un)loaded in the direction perpendicular to the bedding planes. The swelling index, computed on the final unloading path (maximum vertical effective stress ≈100 MPa), follows the same trend as the compressibility index: C_s is higher for specimens with a higher clay-mineral content, where the elastic rebound is expected to be more pronounced. An exponential function can also be used to interpolate the C_s data: $a = 3.56 \cdot 10^{-2}$, $b = 1.76 \cdot 10^{-3}$.

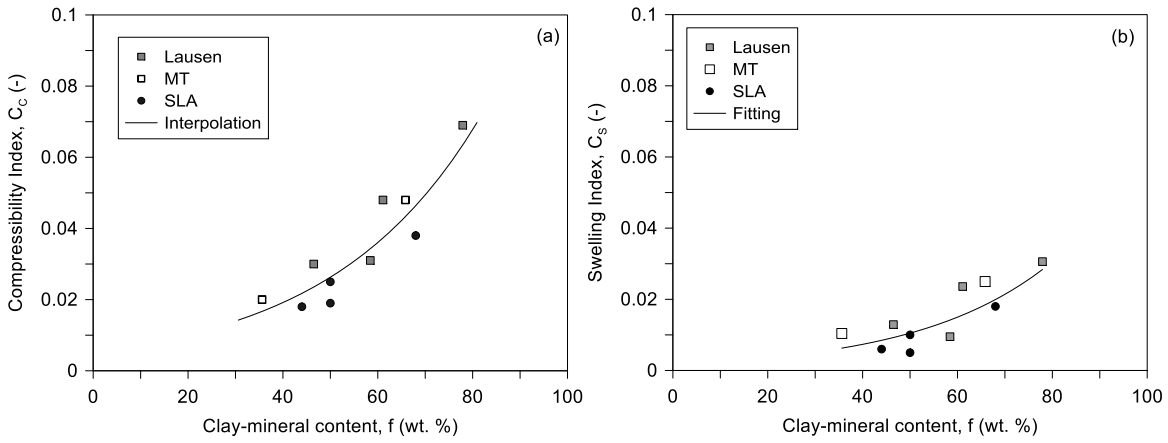

Figure 3-16 Compressibility (a) and swelling (b) indexes of Opalinus Clay specimens sourced from various sites (SLA=Schlattingen, MT=Mont Terri, Lausen borehole) versus the clay-mineral content.

3.5.2. Stiffness and anisotropy

The effect on the oedometric curves of orthogonal loading directions on corresponding specimens revealed considerable differences at low-stress levels, while they tended to be parallel in the high-stress ranges. Moreover, it is shown that the differences between the two loading directions in the oedometric modulus and the consolidation coefficients, computed via the consolidation theory, tend to decrease as stress increases. The evolution of the two parameters with the stress is reported as the ratio between the parameters obtained in the two orthogonal loading directions ($E_{oed,//}/E_{oed,\perp}$ and $c_{v,//}/c_{v,\perp}$), versus the applied vertical effective stress (Figure 3-17). The values are computed upon the primary loading steps, and the results are plotted at the value of effective stress at the beginning of the load increment. Figure 3-17 depicts (*a*) the ratios $E_{oed,//}/E_{oed,\perp}$ and (*b*) $c_{v,//}/c_{v,\perp}$. The results of the four sets of tests are reported, and they indicate a common behaviour. The different response of the material in the two directions is clearly identifiable during loading at low-stress levels, with the parameters in the parallel (//) direction being higher (4-12 times) than the ones in the orthogonal direction ($\perp$), corresponding to a stiffer behaviour in the // direction. As stress increases, the ratios rapidly fall, and the curve slope decreases sharply in the ranges of stresses close to the estimated yield stress, suggested by Casagrande's method (≈7-30 MPa). At higher stress levels, in the elasto-plastic domain, the ratios tend towards a value of one. The increase in loading in the direction perpendicular to bedding would first cause the closure of the porosity oriented in the direction of the bedding plane. At high-stress level, the response would suggest de-structuration (i.e., bond breaking and particle rearrangement) of the specimens upon loading, with a consequent reduction of the anisotropy of the material, as already found in few cases (e.g., Dao et al., 2015). The ratios of the consolidation coefficients of sample BHA were found to be lower (ratios 1.5-2) compared to the other samples at very low stress, but converging towards the general trend towards higher stress values.

The available data does not allow deriving a dependency of the ratios on the material composition.

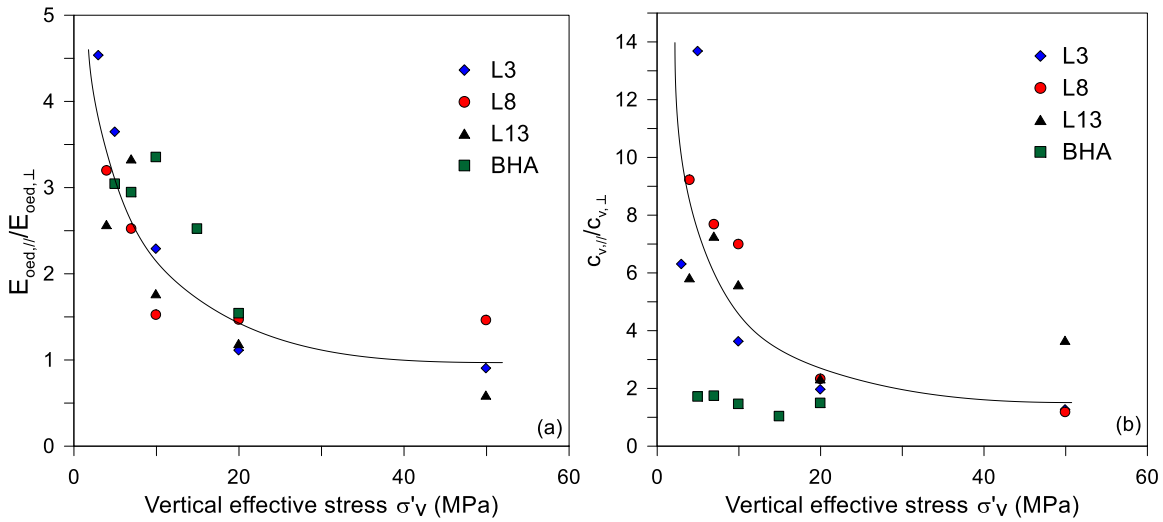

Figure 3-17 Ratios of the oedometric moduli (a) and the consolidation coefficients (b) in the direction parallel to and the direction perpendicular to the bedding planes.

While during loading at high stress the response in the two loading directions tends to become similar, during unloading the anisotropy is clearly identified. The compressibility (C_c) and the swelling (C_s) indexes (obtained on the last unloading path, from σ'_v=100 MPa) for the Lausen tested specimens are reported in Figure 3-18*a*, together with *b*, the percentages of the three main mineralogical components (calcite, quartz and clay minerals), plotted over the sourcing depths. At all the investigated depths, C_s is lower for specimens loaded in the direction parallel to the bedding than perpendicular to the bedding. On the other hand, the elasto-plastic parameters C_c do not present any clear difference between the two loading directions. The same outcome was also found for Mont Terri sandy sample BHA (Figure 3-11). In Lausen borehole, both the compressibility and swelling indexes are higher for the shallower specimens, reaching a minimum for the specimen at a depth of 38.2 m, and increasing for specimens from greater depths. These trends are in agreement with the variability in the clay-mineral content, and opposite to the quartz and calcite contents.

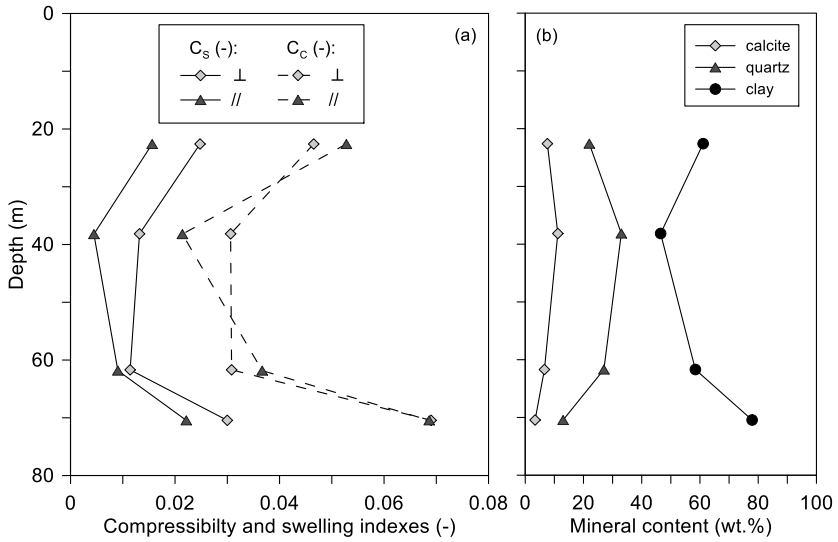

Figure 3-18 (a) Compressibility C_c and Swelling C_s indexes of specimens loaded in the directions perpendicular and parallel to the bedding, and (b) the three main mineralogical components of specimens, plotted over the sourcing depth.

3.5.3. Void ratio history

Although high stresses are applied, the mechanical compaction cannot entirely explain the difference in porosity observed between remoulded and intact specimens, and post-depositional processes (i.e., diagenesis) are considered to be the cause (Favero et al., 2016). In Lausen, an additional phenomenon had an impact on the shale current compaction state: the erosion of the above strata, resulting in a considerable reduction of the stress acting on the formation. This phenomenon can be envisaged as a one-dimensional unloading of the formation, after the compaction and the diagenesis occurred.

Similar mechanisms can be pictured for the formation in Mont Terri, where, however, the tectonic overprint of the formation is expected to have had an additional impact on the current material characteristics. In Figure 3-19, the oedometric curves of remoulded and intact specimens of material sourced from the three mentioned sites (Mont Terri, Schlattingen and Lausen) are compared. The initial test conditions of the three remoulded specimens are highlighted in the dashed box. The remoulded tests simulate the compressional behaviour of the material without cementation, which, upon loading, lead to a higher void ratio compared to intact specimens. The compressibility curves of the intact material are also reported. Interestingly, the intact specimens from Mont Terri and Lausen showed similar properties, both on the loading and unloading path, as shown by the curve overlap in the σ'_v-e plane.

On the other hand, the Schlattingen specimen, although showing a similar compressibility index, presents a considerably lower void ratio, which is attributed to a higher level of diagenesis and mechanical compaction that occurred for the deeper Opalinus Clay. Given the

similar porosities and compaction response of the Opalinus Clay in Lausen and Mont Terri, one could hypothesise that the formation in the two sites has had a similar depth history.

The sequence of processes that have actually occurred represents the link between the two testing conditions (remoulded and intact conditions) that are usually adopted, and it can be summarized as follow (arrows depicted in Figure 3-19): the soil, after deposition, was subjected to compaction and diagenetic processes that induced the reduction in porosity and a decrease in the compressibility of the formation. Different levels of compaction and diagenesis led to different void ratio reductions. Afterwards, in the shallowest site, geological phenomena caused a substantial vertical stress decrease, bringing the formation to a very low depth and stress level, and leading to a slightly higher void ratio.

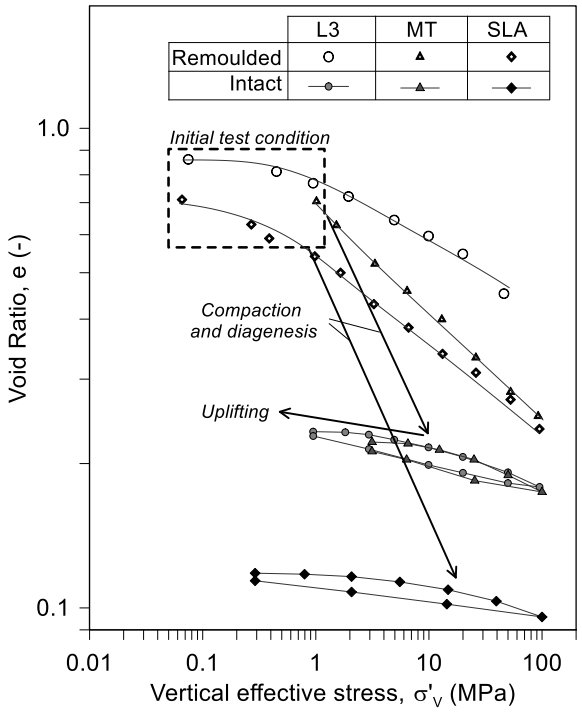

Figure 3-19 Mechanics of porosity reduction: comparison of the data from different sites and in remoulded and intact conditions. Data of MT and SLA from Favero et al. (2016).

From the mechanical information gathered from the testing programme, an idealised exhumation path can be drawn to predict void ratio evolution by one-dimensional unloading (due for instance to the erosion of the above strata) from the in situ initial conditions (the measured sample porosities and the current depths). It is hypothesised that the elastic unloading processes are according to the measured swelling indexes until the minimum considered depth of 10 m. For each specimen, the initial effective stress was computed considering the current overburden and hypothesising the water table at ground level; a depth of 300 m was considered for Mont Terri. The results are reported in Figure 3-20. The void ratios of the as-received cores

are reported. C_S values from the unloading paths performed close to the estimated yield stresses were adopted to compute the void ratio variation upon stress reduction. The evolution of the void ratios with the ideal depth decrement (i.e., the stress decrease) are reported. From the figure, it can be deduced that the void ratios of the shallowest cores (notably *L1* and *L2*) are not compatible with an ideal unloading process from greater depth, while the void ratios for specimens below 20 m can be approximated by a simple unloading phenomenon. This outcome is in agreement with the observation that, to the depth of a few tens of metres, the Opalinus Clay has been found to be highly fractured (Vogt et al., 2017); hence, it is in a condition far from an ideal elastic unloading process.

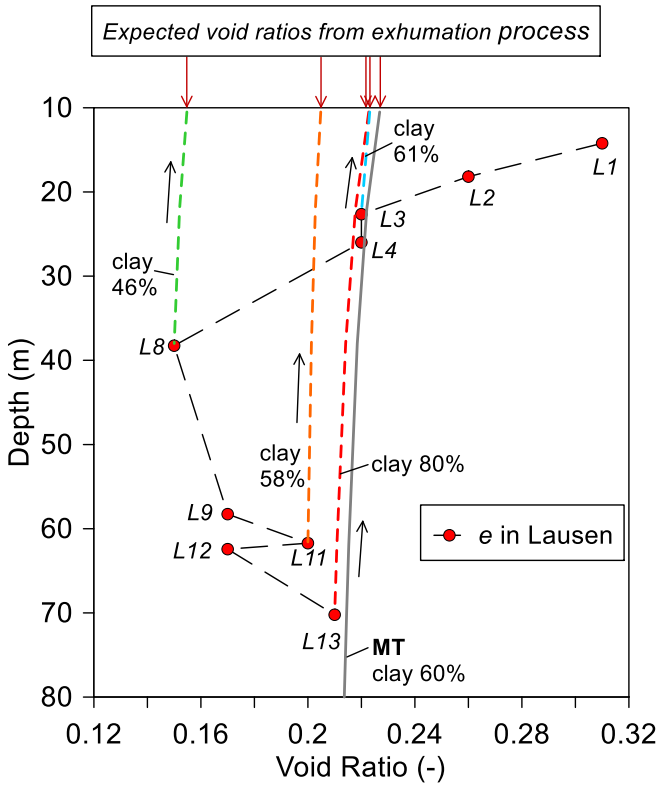

Figure 3-20 Estimation of the void ratio evolution with depth, in an up-lifting (elastic unloading) process.

3.5.4. Void ratio and hydraulic conductivity

In Figure 3-21, the hydraulic conductivity results, obtained from the primary loading steps of the oedometric tests from Lausen ⊥-specimens and the Mont Terri sandy specimen (BHA), are compared to results from Mont Terri shaly samples (MT1, MT2) and Schlattingen samples (SLA 2, 6, 18, 20) (Favero, 2017). Each point in Figure 3-21 corresponds to a value of hydraulic conductivity obtained for one loading step and is plotted versus the void ratio at the beginning of the step.

Interestingly, although a wide range of void ratios is involved, the hydraulic conductivity varies over the same order of magnitudes: 10^{-12}-10^{-14} m/s. As expected, the results show a decrease in the hydraulic conductivity as the void ratio decreased, with the mechanical compaction (range of stress: from a few MPa up to 100 MPa). All the tests present a similar decreasing trend: the hydraulic conductivity decreases faster at the initial conditions, while at high stress, the reduction is smaller.

For specimens with lower initial void ratios (curves on the left), very small changes in void ratio induced a considerable reduction in hydraulic conductivity.

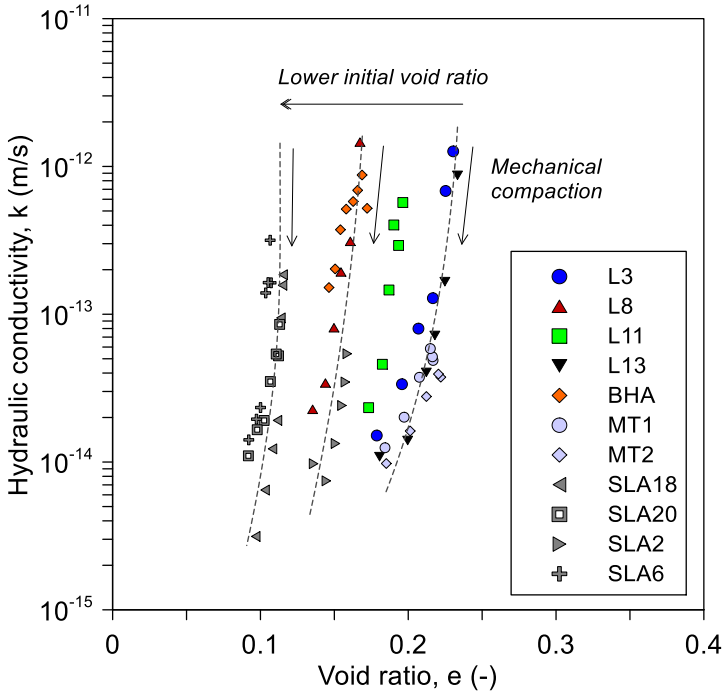

Figure 3-21 Hydraulic conductivity, computed via consolidation theory of primary loading steps, versus void ratio. Comparison of the results of specimens from the Lausen borehole to the results from Mont Terri and Schlattingen (⊥-specimens).

An in-depth analysis of the impact of the void ratio on the permeability is performed in Figure 3-22 by classifying the results by clay content (symbols), and by applied stress (greyscale). The results of Lausen and Mont Terri (BHA) samples, loaded in the direction perpendicular to bedding are reported in the graph since comparable loading steps were performed.

As already discussed, lower clay content corresponds to lower porosity. For the same stress level, a slightly higher hydraulic conductivity (within the same order of magnitude) is detected for lower porosity specimens (dashed arrows in Figure 3-22 indicate the graph-reading direction). This is in agreement with the analysis of the structure of the shale (Chapter 2): for lower clay content (i.e., higher quartz, calcite etc. content), lower porosity is found, but larger pore throat diameters are accommodated at the contact between clay and non-clayey particles,

The larger pores would allow an enhanced fluid flow. The increase in hydraulic conductivity for lower clay content specimens is in agreement with the literature findings (e.g., Dewhurst et al., 1998; Yang and Aplin, 2010). This trend is roughly found throughout the stress range analysed, although scatter is detected.

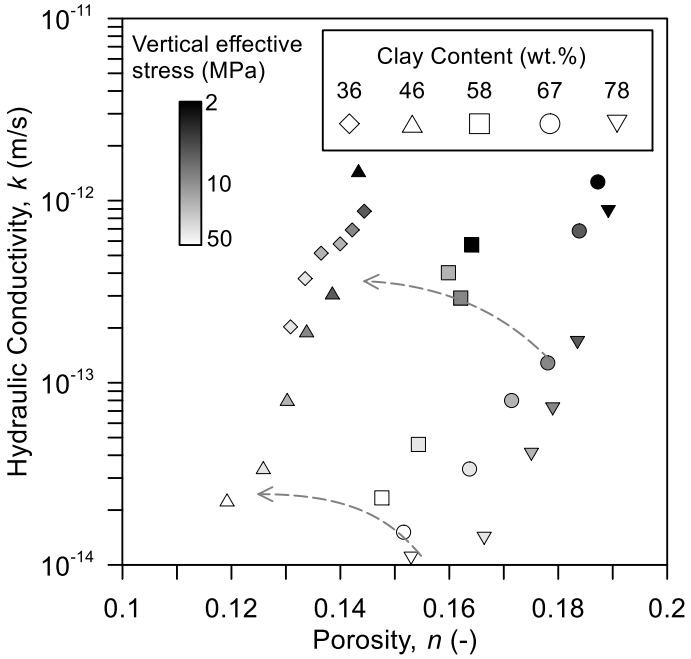

Figure 3-22 Hydraulic conductivity of Lausen and MT-BHA samples versus porosity, classified in terms of clay content (%) and vertical effective stress applied (MPa).

Lastly, the hydraulic conductivities of Lausen specimens from tests parallel to bedding were compared to a series of hydraulic in situ tests, ranging from pumping tests to pulse tests (Vogt et al., 2017). In Figure 3-23, the results of laboratory tests (primary loading steps) are plotted as coloured bars, in which the colour intensity depends on the vertical effective stress applied at the beginning of the loading step: light colour represents low stress, and dark colour represents high stress. The results are plotted versus the depth corresponding to the specimen sourcing depth, for laboratory experiments, or to the average depth of the section involved in the field tests. For the latter, a range of hydraulic conductivity results for each investigated depth is reported. From the comparison of the results, it can be stated that the laboratory tests, in particular in the low effective stress range, compatible with the in situ one, are able to capture the hydraulic conductivity for depths below ≈30 m. For shallower depths, laboratory test results are a few orders of magnitude lower than the in situ hydraulic packer tests, where the flow is envisaged to be enhanced by fractures and not represented at the laboratory specimen scale (Vogt et al., 2017). Below 30 m, the fractures are supposed to be closed, and the matrix flow dominates the hydraulic conductivity.

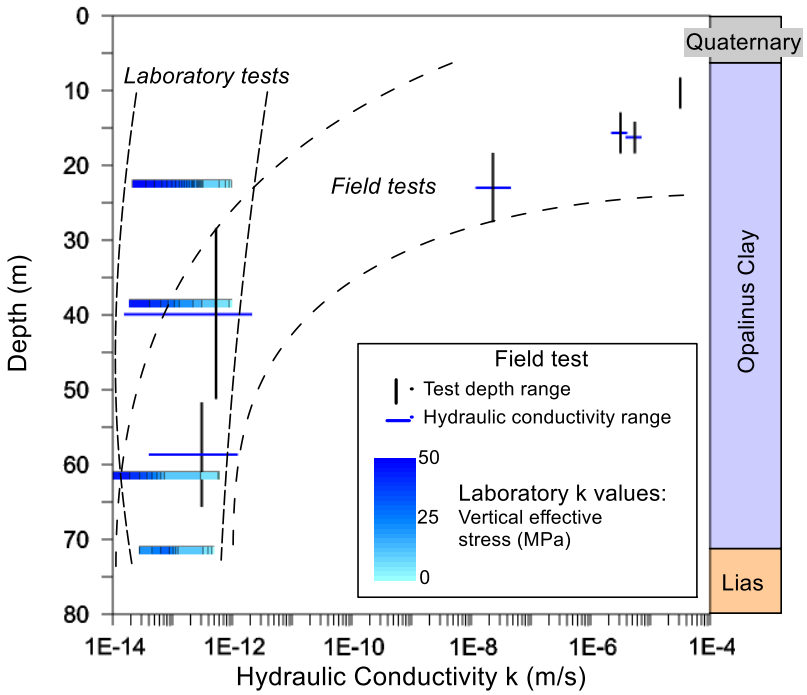

Figure 3-23 Hydraulic conductivity from oedometric tests (specimens loaded parallel, //, to the bedding planes) compared to field data (borehole Lausen).

3.6. Conclusions

The results of the experimental study on the hydro-mechanical behaviour of Opalinus Clay shale from Lausen and Mont Terri sites are presented. Intact twin specimens, from the same depth, have been loaded, mechanically and hydraulically, either parallel or perpendicular to the bedding direction. The results have been compared to previous findings on the same formation, from sites at greater depths, allowing for an evaluation of the effect of geological uplifting on the shale properties.

The key impacts of the mineralogical composition, in particular the clay component, on the Opalinus Clay mechanical parameters have been identified by the comparison of specimens sourced from various sites. It was found that higher clay-mineral contents correspond to higher swelling and compressibility indexes, for specimens irrespective of the sourcing depth.

The anisotropic features of the shallow Opalinus Clay, in terms of oedometric compressibility and hydraulic conductivity, have been investigated. The results have shown that, while the elastic behaviour is significantly different in the two loading directions, the elasto-plastic behaviour is comparable. For high-stress levels, the oedometric moduli in the two loading directions tend to be similar, revealing that the differences diminish at high stresses, post-yielding, where the effect of the prior loading history is reduced.

The porosity of Opalinus Clay in the shallow site was analysed, in the light of the mechanical compaction and diagenetic process, but also considering an ideal unloading process. In the first 20-30 m of the formation, porosity values greater than those estimated from an ideally elastic unloading process are found and are compatible with the fracturing and the weathering of the material, phenomena well documented in other studies (Mazurek et al., 2017; Vogt et al., 2017). On the other hand, below the mentioned depth, a good agreement is found between the porosity of the samples from Lausen and from Mont Terri (at greater depth).

The hydraulic conductivity was obtained through the consolidation theory and the constant-head tests. All of the results can be linearly interpolated in the log-log plane, versus the applied stress. For the same material composition, to lower porosity corresponds lower permeability. For specimens subjected to the same stress level, as it can be for geomaterial at the same depth, a higher permeability is found for specimens with lower porosity, corresponding to lower clay contents. This is the result of the larger pore throats detected for samples with lower clay content and higher quartz and calcite content.

Although a higher hydraulic conductivity is mostly found in the direction of the bedding plane, the difference reduced with high applied stress. The comparison with the results from deeper samples has shown good agreement, although a slightly lower hydraulic conductivity was found for the deepest samples, especially at low-stress levels. The higher hydraulic conductivity for low-stress values can be attributed to the presence of micro-fissures, due to the exhumation decompaction. The laboratory hydraulic conductivities obtained on Lausen specimens were compared to in situ tests. The comparison highlights, that at greater depths than approximately 30 m, the hydraulic conductivity values from in situ and laboratory testing are in broad agreement. In contrast, in the uppermost 30 m of Opalinus Clay, the in situ measurements clearly deviate from the laboratory test results, lending strong support that flow is fracture-dominated (Vogt et al., 2017).

In conclusion, despite the considerable exhumation in the order of 1000 m, the hydro-mechanical properties of the Opalinus Clay only seem to be significantly affected in the uppermost 30 m.

3.7. References

Amann, F., Button, E.A., Evans, K.F., Gischig, V.S., Blümel, M., 2011. Experimental Study of the Brittle Behavior of Clay shale in Rapid Unconfined Compression. Rock Mechanics and Rock Engineering 44, 415–430. https://doi.org/10.1007/s00603-011-0156-3

Aristorenas, G.V. (George V., 1992. Time-dependent behavior of tunnels excavated in shale (Thesis). Massachusetts Institute of Technology.

Bellwald, P., 1990. A contribution to the design of tunnels in argillaceous rock (Thesis). Massachusetts Institute of Technology.

Biot, M.A., 1941. General Theory of Three-Dimensional Consolidation. Journal of applied physics 12, 155–164.

Bossart, P., Meier, P.M., Moeri, A., Trick, T., Mayor, J.-C., 2002. Geological and hydraulic characterisation of the excavation disturbed zone in the Opalinus Clay of the Mont Terri Rock Laboratory. Engineering Geology 66, 19–38.

Bossart, P., Thury, M., 2008. Mont Terri rock Laboratory. Project, Programme 1996 to 2007 and results.

Burland, J.B., 1990. On the compressibility and shear strength of natural clays. Géotechnique 40, 329–378.

Corkum, A.G., Martin, C.D., 2007. The mechanical behaviour of weak mudstone (Opalinus Clay) at low stresses. International Journal of Rock Mechanics and Mining Sciences 44, 196–209. https://doi.org/10.1016/j.ijrmms.2006.06.004

Dao, L.-Q., Cui, Y.-J., Tang, A.-M., Delage, P., Li, X.-L., Sillen, X., 2015. Anisotropy in Oedometer Test on Natural Boom Clay, in: Lollino, G., Giordan, D., Thuro, K., Carranza-Torres, C., Wu, F., Marinos, P., Delgado, C. (Eds.), Engineering Geology for Society and Territory - Volume 6. Springer International Publishing, Cham, pp. 499–502. https://doi.org/10.1007/978-3-319-09060-3_87

Dewhurst, D.N., Aplin, A.C., Sarda, J.-P., Yang, Y., 1998. Compaction-driven evolution of porosity and permeability in natural mudstones: An experimental study. Journal of Geophysical Research: Solid Earth 103, 651–661. https://doi.org/10.1029/97JB02540

ENSI, 2009. Spezifische Auslegungsgrundsätze für geologische Tiefenlager und Anforderungen an den Sicherheitsnachweis. Richtlinie für die schweizerischen Kernanlagen ENSI-G03. Eidgenössisches Nuklearsicherheitsinspektorat (ENSI), Villigen.

Favero, V., 2017. Multiphysical behaviour of shales from Northern Switzerland. https://doi.org/10.5075/epfl-thesis-7539, urn:nbn:ch:bel-epfl-thesis7539-7

Favero, V., Ferrari, A., Laloui, L., 2018. Anisotropic Behaviour of Opalinus Clay Through Consolidated and Drained Triaxial Testing in Saturated Conditions. Rock Mech Rock Eng 51, 1305–1319. https://doi.org/10.1007/s00603-017-1398-5

Favero, V., Ferrari, A., Laloui, L., 2016. On the hydro-mechanical behaviour of remoulded and natural Opalinus Clay shale. Engineering Geology 208, 128–135. https://doi.org/10.1016/j.enggeo.2016.04.030

Ferrari, A., Crisci, E., Laloui, L., 2018. Arbeitsbericht NAB 17-27 - Geotechnical Experimental Characterisation of Opalinus Clay Cores from the Borehole Lausen.

Ferrari, A., Favero, V., Laloui, L., 2016. One-dimensional compression and consolidation of shales. International Journal of Rock Mechanics and Mining Sciences 88, 286–300. https://doi.org/10.1016/j.ijrmms.2016.07.030

Ferrari, A., Favero, V., Marschall, P., Laloui, L., 2014. Experimental analysis of the water retention behaviour of shales. International Journal of Rock Mechanics and Mining Sciences 72, 61–70. https://doi.org/10.1016/j.ijrmms.2014.08.011

Ferrari, A., Laloui, L., 2013. Advances in the testing of the hydro-mechanical behaviour of shales, in: Multiphysical Testing of Soils and Shales. Springer, pp. 57–68.

Ferrari, Favero, Manca, Laloui, 2012. Geotechnical characterization of core samples from the geothermal well Schlattingen SLA-1 by LMS/EPFL (No. Arbeitsbericht NAB 12-50).

Giger, S.B., Ewy, R.T., Favero, V., Stankovic, R., Keller, L.M., 2018. Consolidated-undrained triaxial testing of Opalinus Clay: Results and method validation. Geomechanics for Energy and the Environment 14, 16–28. https://doi.org/10.1016/j.gete.2018.01.003

Gräsle, W., Plischke, I., 2010. LT Experiment: Mechanical Behavior of Opalinus Clay, Final report from Phases 6 – 14 (No. Mont Terri Project, Technical Report 2009-07). BGR, Germany.

Heitzmann, P., 2004. Mont Terri project: hydrogeological synthesis, osmotic flow. Bundesamt für Wasser und Geologie, BWG, Bern-Ittigen.

Hekel, U., 1994. Hydrogeologische Erkundung toniger Festgesteine am Beispiel des Opalinustons (Unteres Aalenium).

Houben, M.E., Desbois, G., Urai, J.L., 2014. A comparative study of representative 2D microstructures in Shaly and Sandy facies of Opalinus Clay (Mont Terri, Switzerland) inferred form BIB-SEM and MIP methods. Marine and Petroleum Geology 49, 143–161. https://doi.org/10.1016/j.marpetgeo.2013.10.009

Kaufhold, A., Gräsle, W., Plischke, I., Dohrmann, R., Siegesmund, S., 2013. Influence of carbonate content and micro fabrics on the failure strength of the sandy facies of the Opalinus Clay from Mont Terri (Underground Rock Laboratory). Engineering Geology 156, 111–118. https://doi.org/10.1016/j.enggeo.2013.01.014

Keller, L.M., Holzer, L., Schuetz, P., Gasser, P., 2013. Pore space relevant for gas permeability in Opalinus clay: Statistical analysis of homogeneity, percolation, and representative volume element. Journal of Geophysical Research: Solid Earth 118, 2799–2812. https://doi.org/10.1002/jgrb.50228

Klinkenberg, M., Kaufhold, S., Dohrmann, R., Siegesmund, S., 2009. Influence of carbonate microfabrics on the failure strength of claystones. Engineering Geology 107, 42–54. https://doi.org/10.1016/j.enggeo.2009.04.001

Lambe, T.W., Whitman, R.V., 1969. Soil Mechanics. John Wiley & Sons.

Mazurek, M., Hurford, A.J., Leu, W., 2006. Unravelling the multi-stage burial history of the Swiss Molasse Basin: integration of apatite fission track, vitrinite reflectance and biomarker isomerisation analysis. Basin Research 18, 27–50. https://doi.org/10.1111/j.1365-2117.2006.00286.x

Mazurek, M., Wersin, P., Hadi, J., 2017. Opalinus Clay in the shallow decompaction zone: Geochemical investigations on drill core samples from borehole Lausen KB (No. NAB 16-58).

Minardi, A., Crisci, E., Ferrari, A., Laloui, L., 2016. Anisotropic volumetric behaviour of Opalinus clay shale upon suction variation. Géotechnique Letters 6, 144–148. https://doi.org/10.1680/jgele.16.00023

Nagra, 2002. Projekt Opalinuston Synthese der geowissenscha. Technischer Bericht 02-03.

Nagra, 2001. Sondierbohrung Benken: Untersuchungsbericht (No. NTB 00-01). Wettingen.

Orellana, L.F., Scuderi, M.M., Collettini, C., Violay, M., 2018. Frictional Properties of Opalinus Clay: Implications for Nuclear Waste Storage. Journal of Geophysical Research: Solid Earth 123, 157–175. https://doi.org/10.1002/2017JB014931

Pearson, F.J., 2003. Mont Terri project: geochemistry of water in the Opalinus Clay Formation at the Mont Terry rock laboratory. Bundesamt für Wasser und Geologie, BWG, Bern-Ittigen.

Salager, S., François, B., Nuth, M., Laloui, L., 2013. Constitutive analysis of the mechanical anisotropy of Opalinus Clay. Acta Geotechnica 8, 137–154. https://doi.org/10.1007/s11440-012-0187-2

Vogt, T., Ebert, A., Häring, C., Becker, J.K., Traber, D., Deplazes, G., Bläsi, H., Rufer, D., 2016. Kernbohrung Lausen: Geologische, hydrogeologische und bohrlochgeophysikalische Untersuchungen (Rohdatenbericht) (No. NAB 15-10).

Vogt, T., Hekel, U., Ebert, A., Becker, J.K., Traber, D., Giger, S., Brod, M., Häring, C., 2017. Hydrogeologische Untersuchungen im oberflächennahen Opalinuston (Bohrloch Lausen, Schweiz)Hydrogeological investigations in shallow Opalinus Clay (borehole Lausen, Switzerland). Grundwasser 22, 209–220. https://doi.org/10.1007/s00767-017-0363-2

Wersin, P., Mazurek, M., Mäder, U.K., Gimmi, T., Rufer, D., Lerouge, C., Traber, D., 2016. Constraining porewater chemistry in a 250m thick argillaceous rock sequence. Chemical Geology 434, 43–61. https://doi.org/10.1016/j.chemgeo.2016.04.006

Yang, Y., Aplin, A.C., 2010. A permeability–porosity relationship for mudstones. Marine and Petroleum Geology, Compaction Processes - Porosity, Permeability and Rock Properties Evolution in Sedimentary Basins 27, 1692–1697. https://doi.org/10.1016/j.marpetgeo.2009.07.001

Yu, H.D., Chen, W.Z., Gong, Z., Tan, X.J., Ma, Y.S., Li, X.L., Sillen, X., 2015. Creep behavior of boom clay. International Journal of Rock Mechanics and Mining Sciences 76, 256–264. https://doi.org/10.1016/j.ijrmms.2015.03.009

Zhang, C.-L., Armand, G., Conil, N., Laurich, B., 2019. Investigation on anisotropy of mechanical properties of Callovo-Oxfordian claystone. Engineering Geology 251, 128–145. https://doi.org/10.1016/j.enggeo.2019.02.008

Chapter 4

Hydro-mechanical behaviour of the sandy facies of the Opalinus Clay in drained triaxial testing conditions

4. Hydro-mechanical behaviour of the sandy facies of the Opalinus Clay in triaxial drained testing conditions

The results presented in this chapter are intended to be submitted as a technical note:

Technical note: "*Crisci, E., Ferrari, A., Laloui, L., Drained triaxial tests on low porosity shale: testing protocol and application to Opalinus Clay shale (sandy facies)"*

The pre-print version of the journal paper has been used to draft the chapter.

Contribution of the Candidate: design and performance of the experimental testing, analysis of the results, writing of the manuscript.

4.1 Introduction

In the locations currently considered for the final repository, Opalinus Clay formation is expected to present both clay-rich sections and quartz-rich lenses. With reference to the lithofacies defined in the Mont Terri Underground Rock laboratory, the sandy facies, as mentioned in Chapter 2, is characterised by a high degree of variability in the layering composition that is visible at the centimetre to the decimetre scale. This heterogeneity, for the laboratory samples, has two main consequences.

The first consequence is related to the difficulties in assigning specific parameters to the material. Samples located within a close distance could respond differently to the same hydro-mechanical load, because of their specific composition and layering configuration. It is of primary importance to accurately determine the location and composition of the samples, in order to match the hydro-mechanical response with other sources of information (mineralogical composition, X-ray images, borehole logging) and determine which are the factors driving the different response of apparently similar samples, to predict their behaviour. An extensive description of the relation between the material composition and the hydro-mechanical properties is provided in Chapter 5 and uses the data from this Chapter, and Chapter 3.

The second consequence is related to a practical aspect of sample testing: the higher the stiffness/strength heterogeneity within a sample, the higher the stress localisation is during any applied load, with the consequent risk of sample breakage even during the preparation phase. Careful handling of brittle samples of rather big dimensions for preparation (e.g. cylinders with a diameter of 50 mm and height of 100 mm, or more) requires long times, increasing the possibility of drying, and therefore of causing cracks in the samples. Because of the very low permeability of the formation, the sample dimensions are impacting significantly also the needed re-saturation and consolidation time. Also, lower strain rates are required to test samples in drained conditions compared to undrained conditions, thus increasing the testing time. Reducing the drainage length is, therefore, advantageous for the test duration.

Often, to cope with the very low permeability, in literature, the samples are tested in partially saturated conditions. However, the partial saturation and the suction generated inside the sample can significantly modify the shale response upon hydro-mechanical testing (e.g., Wild et al., 2015; Ferrari et al., 2018; Minardi et al., 2018), and the parameters can be considerably overestimated compared to the saturated state. Sample resaturation is particularly crucial since

it can damage the sample (e.g., Wang et al., 2014), causing an underestimation of the mechanical properties.

Very few tests in drained conditions have been performed on low porosity geomaterials such as shales and claystones (e.g., Belmokhtar et al., 2018; Favero et al., 2018; Giger et al., 2018). To the author's knowledge, no tests on samples of the Opalinus Clay sandy facies have been performed so far in drained, saturated conditions. The characterisation of the sandy facies has been limited to cases in which only partial saturation of the rock was achieved (e.g., Gräsle, 2011), bringing to an overestimation of the rock properties (both in terms of elastic response and in terms of strength).

In this Chapter, a rigorous protocol for testing low porosity shale is detailed. The protocol is applied to the testing of Opalinus Clay samples from the sandy lithofacies. Three drained triaxial tests have been performed on saturated samples from the sandy facies of the Mont Terri URL. To cope with the testing difficulties, samples of reduced dimensions (diameter 38 mm, height 76 mm) compared to the original set-up (allowing samples of 50 mm in diameter, 100 mm in height) were adopted. To improve the accuracy of the measurements of small deformation ranges, internal measurement sensors (Linear Variable Differential Transducers, LVDTs) were installed. A detailed description of the tested samples, the adopted testing procedures and the results of the test, is provided in this chapter.

4.2 Set-up and procedures

4.2.1 Testing set-up

The triaxial tests were performed in a high-pressure triaxial apparatus, described in Favero et al. (2018), Seiphoori et al. (2011). The device was modified in order to test smaller samples (38 mm in diameter, 76 mm in height) compared to the original set-up (allowing samples of 50 mm in diameter, 100 mm in height), by replacing the top and bottom caps. Each cap allows for a fluid drainage line. The 2:1 ratio (height: diameter) usually suggested for triaxial samples was adopted. Two internal vertical LVDTs (resolution 1 μm) were added to the previous configuration, in order to measure the vertical displacements between the two bases of the samples, therefore minimizing the error due to the apparatus deformation. The LVDTs were mounted on two annular support system, fixed around the top and bottom caps.

The set-up is shown in Figure 4-1. Two pre-compressed steel porous plates are located to the top and bottom bases of the sample to allow the uniform distribution of the pore water pressure. The sample is inserted in a neoprene membrane (or sleeve), to prevent any contact with the

confining fluid. The membrane is fixed at each cap with three O-rings, two positioned above and one below the membrane. The strains in the radial direction are obtained using a circumferential LVDT (resolution 1 μm), mounted on a chain system positioned at the middle of the sample height. The axial load is applied by a hydraulic press, either in load-controlled mode or in displacement-controlled mode. The maximum possible force is 450 kN, which corresponds, in the new configuration, to axial total stress of 396 MPa. The confinement is applied through a confining fluid (mineral oil), whose pressure is controlled by a pressure/volume controller (PV controller—resolution of 1 kPa), up to 30 MPa. Two PV controllers are used to independently control the pore water pressure at the top and bottom bases of the specimen: the maximum applicable fluid backpressure at the top base is 6 MPa, while the maximum at the bottom base is 10 MPa. The independent control of the pore water pressure at the two extremes of the specimen allows running constant head permeability tests by applying a hydraulic gradient between the specimens' edges.

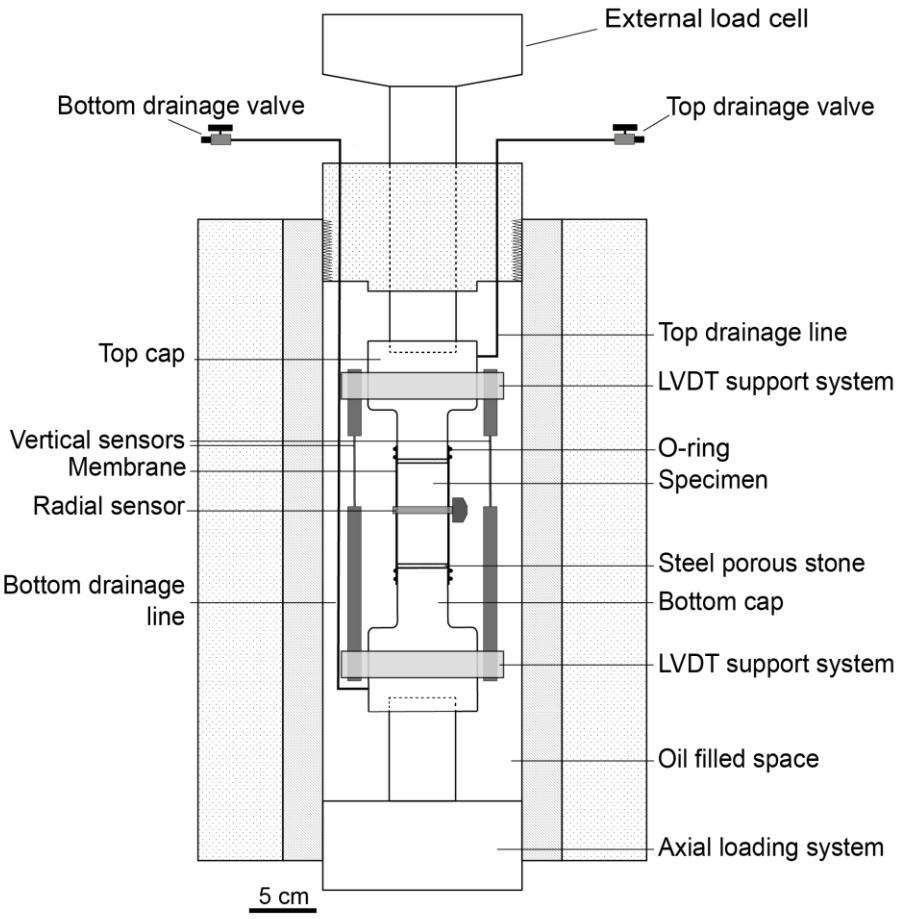

Figure 4-1 Triaxial testing set-up.

4.2.2 Saturation and saturation check

Adopted saturation procedure

The samples were re-saturated directly inside the triaxial apparatus. First, a small isotropic load was applied (about 0.5-1 MPa). Secondly, a vacuum pump was connected to the bottom drainage line during some minutes, in order to empty the drainage system and the porous stones from any air. While vacuum was applied, demineralised and deaerated water was injected via the pressure/volume controller on the other side of the same drainage line, flushing it. In this way, the drainage line was filled with the desired fluid, avoiding any contact with air. The same procedure was applied to the top drainage line. The pore water was injected with an initial pressure of a few hundreds of kPa. Then, the pressure was raised from both specimen bases, and a small pressure gradient was established to help trapped air to migrate towards the lower pressure end, that is flushed a few times during the saturation phase.

As saturation progress, a tendency to swell occurs in shales. The rapid swelling could induce microcracks formation in the sample (see also the experiment in Chapter 6, Section 6.6), because of the non-homogeneous saturation, and therefore of the stress distribution, between the parts in direct contact with the waters, and those who are not. Therefore, to prevent the formation and propagation of the cracks, the samples were saturated in isochoric conditions: as swelling deformations higher than few tens of microns occurred (maximum allowed deformation ≈0.1 % of vertical or radial strains, corresponding to a change in the void ratio of about $3 \cdot 10^{-3}$-$4 \cdot 10^{-3}$), the vertical and radial stresses were increased to confine the swelling and maintain the sample at the original dimensions as much as possible. This operation lasted up to two weeks. When strains stabilised, the top and bottom pore water pressures were equalised.

Despite the flushing, air bubbles may be trapped in the shale matrix. For this reason, the pore water pressure at the end of the saturation phase was increased up to 2-2.5 MPa in order to dissolve possible air trapped into the water phase. When the pore liquid solutes all gas bubbles, its compressibility corresponds to the one of the pure state (Fredlund, 1976). The confining stress was increased consequently in order to keep the effective stress constant. Afterwards, the saturation check was performed.

Why re-saturating in isochoric conditions?

The disturbance that the coring, the preparation and the reconditioning cause to the sample may affect the sample response upon hydro-mechanical loading. Although a perfect sampling of shales is rarely feasible, efforts are devoted to the minimisation of sample disturbance. In the

following, the stress history of a sample is analysed, from the in-situ stress condition to core extraction, sample preparation and reconditioning. A qualitative description of the stress path to which a sample is subjected is proposed in Figure 4-2 in terms of mean effective stress versus (a) suction and (b) void ratio. In what follows, the validity of the Bishop's effective stress formulation is assumed (Bishop, 1959):

4-1 $$\sigma'_{ij} = (\sigma_{ij} - u_a\delta_{ij}) + S_r(u_a - u_w)\delta_{ij}$$

Where σ'_{ij} is the effective stress tensor, σ_{ij} the total stress tensor, the u_a air (or non-wetting fluid) pressure, u_w is the water (or wetting fluid) pressure, δ_{ij} the Kronecker delta, S_r the degree of saturation, and u_a-u_w the matric suction.

For the sake of simplicity, it is hypothesised that the material behaves as an isotropic elastic material, although limitations of the approach and some of the common non-elastic responses are mentioned. As a first approximation, the Skempton's B values is assumed equal to 1.

In situ, the material is assumed to be saturated and subjected to initial stress (*point 0*). Because of sample extraction, the total stress is released, and negative pore water pressure is generated. If the process is quick enough to occur in undrained condition, and the sample behaves as an isotropic elastic material with B=1, the variation of total stress Δp is equal to the variation of pore water pressure Δu_w, and the effective stress remains constant. It results in the development of suction inside the sample (*point 1*), without changes in volume. Afterwards, samples are trimmed from the core. Depending on the technique adopted for the sample preparation, the exposure to the atmosphere and the mechanical load, the sample may be partially desaturated (*point 2*), and therefore subjected to an increase in effective mean stress, due to the increase of the suction. The position of point 2 on the graph is merely indicative and strictly depends on the induced degree of (de)saturation, and the validity of the mentioned effective stress definition. Wherever this point is, testing without a proper resaturation would yield the behaviour of a partially saturated material, that is widely known to differ from the saturated (as in situ) state (Wild et al., 2015; Minardi et al., 2018). Various ways to resaturate samples (*point 3*) can be envisaged. Here three possibilities are analysed:

3a) in free-swelling conditions, e.g., by the use of vapour transfer technique or by the direct contact of the sample with water supply;
3b) at the stress level corresponding to the in situ condition, i.e. applying the stress inside the triaxial cell, and then putting the sample in contact with water;

3c) in isochoric conditions, i.e., putting the sample in contact with the water, and preventing the swelling deformation that would occur by progressively increasing the radial and vertical stress.

The paths (a, b, c) are reported in Figure 4-2. In the first case (a) the effective stress is brought to zero by reducing the suction without any confinement, resulting in the swelling of the sample. The free swelling phenomenon is known to be non-elastic, and damage occurs because of cracking induced by inhomogeneities of sample texture and saturation (Section 6.6), therefore inhomogeneous effective stress distribution. At the end of the saturation, the sample is cracked and may behave differently from the original material. In the second case (b), the final condition is similar to the in situ condition. However, before the saturation, the sample is subjected to an increase in effective stress, which is higher than the initial and the in situ condition, and may cause yielding of the sample. Given the uncertainties related to the effective stress determination in shales, the maximum effective stress that the sample experienced is in this case unknown, yet different from the one of that the formation experienced in situ.

In the third case (c) the sample volume is kept constant, and, in the isotropic elastic hypothesis, the mean effective stress stays constant. The final mean effective stress is supposed to be higher than the in situ one and should correspond to the increase in effective stress induced by the initial sample desaturation. Although the stress condition at the end of saturation is not necessarily the same than the in situ one, the maximum stress experienced during the conditioning process is constrained, while it is not in case (b). For the mentioned reasons, it was decided to adopt the third methodology to recondition all the samples.

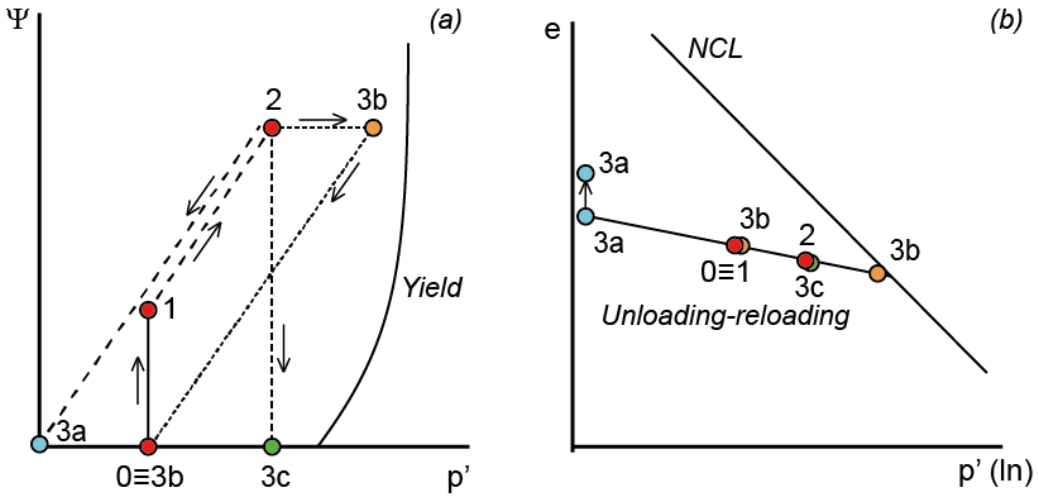

Figure 4-2 Various stress paths, from the in situ condition to the sample resaturation: (a) mean effective stress versus suction, (b) mean effective stress versus void ratio.

Saturation verification: B-check

In order to verify the saturation of the samples, B-check tests were performed. The B-check test consists in measuring the Skempton *B* pore water pressure coefficient (Skempton, 1954), that corresponds to the increment of pore water pressure induced by an increment of mean total stress when isotropic stress is changed in undrained conditions. Undrained conditions are imposed by closing the valves of the cell drainage lines; total stress is increased isotropically, and the pore water pressure response is registered by a pressure transducer located at the outlet of one of the drainage lines.

While saturating soils, the *B* value increases until it became equal or very close to unity. On the other hand, for stiff geomaterials, such as shales and rocks, the coefficient may assume values lower than one even at full saturation (e.g., Gutierrez et al., 2015). These low values are due to the compressibility of the solid skeleton, that is comparable to the compressibility of the pore water and the solid particles. When saturation is not fully achieved, the measured *B* value increases with increasing backpressure. This fact is due to the increasing degree of saturation, and decreasing compressibility of the pore fluid as the backpressure is increased (Wissa, 1969; Fredlund, 1976).

Three to five consecutive isotropic compression increments were performed in undrained conditions, and the corresponding *B* values were computed until they were assessed to be reasonably stable (not increasing nor decreasing with total stress changes).

When dealing with stiff geomaterials, the compressibility of the apparatus can affect the quality of the measured *B* values. Wissa (1969) proposed a correction to the *B* value to take into account the compressibility of the dead volume of water (i.e., the water in the drainage system) and the compressibility of the system (tubes and transducers). However, several researchers (e.g., Ghabezloo and Sulem, 2010) show that the compressibility of modern types of steel tubes and transducers has a negligible impact on the B measurements compared to the dead water volume impact. Therefore, the corrected B-values ($B_{correct}$) were obtained using the following formulation (Wissa, 1969; Favero et al., 2018):

$$B_{correct} = \frac{1}{\frac{1}{B_{obs}} - \frac{V_L}{V} - \frac{K}{K_f(1-K/K_s)}} \qquad 4\text{-}2$$

where B_{obs} is the measured B value, V_L is the volume of fluid in the pore-water lines, V is the volume of the specimen, K is the bulk modulus of the specimen, K_f bulk modulus of the pore

fluid, and K_s is the bulk modulus of the solid phase. For sandy Opalinus Clay, K_s was estimated from the oedometric test results (Chapter 3) to be approximately 25 GPa.

4.2.3 Consolidation phase

Once the saturation is completed, drained conditions are established, by opening the drainage valves and equilibrating the pressure to the one imposed by the pressure-volume controllers. Afterwards, the sample is isotropically loaded (or unloaded) to reach the desired confining pressure. Enough time is allowed to ensure the dissipation of the pore water overpressure induced by the isotropic load. Backpressure is maintained constant throughout the test.

As indicated in Head (1998), the coefficient of consolidation in isotropic conditions c_{vi}, can be determined from the consolidation stage by using a graphical procedure by reporting the volume change during the consolidation stage versus the square root time. The linear part (usually up to 50% of the consolidation) is extended to intersect the tangent line to the last part of the curve. The time corresponding to the intersection point, t_{100}, represents the theoretical 100% consolidation, and is used to compute the coefficient of consolidation:

$$c_{vi} = \frac{\pi D^2}{\lambda t_{100}} \qquad 4\text{-}3$$

where D is the diameter of the specimen, λ is a constant depending on the drainage boundary conditions (from both ends, λ=4). The coefficient of consolidation is used to compute the strain rate to apply in order to perform a drained shearing.

Some time (few hours) is required to apply a high isotropic load (or unload). Therefore part of the consolidation may take place already during the loading phase. In this case, the standard estimation procedure may lead to a potential overestimation of the time to consolidate, therefore to an underestimation of the coefficient of consolidation. The resulting strain rate may be slower than the minimum one needed to ensure the drained condition. Consequently, drainage is undoubtedly assured.

4.2.4 Shear phase

The shear phase was carried out in drained conditions in vertical strain control and maintaining constant the radial stress and pore water pressure. Vertical compression must be applied slowly enough to ensure that pore water pressure changes during shearing are negligible. The time required to reach the failure in drained conditions, t_f, is calculated from the t_{100} multiplying by an amplifying factor of *8.5* (Head, 1998). The strain rate $\dot{\varepsilon}$ is obtained as:

4-4 $$\dot{\varepsilon} = \frac{\varepsilon_f}{t_f} = \frac{\varepsilon_f}{0.15 \cdot H^2} c_{vi}$$

where ε_f is the deformation at failure, estimated to be about 1% for brittle materials as Opalinus Clay (Favero et al., 2018), H the drainage length.

The computed strain rate is applied during the shearing phase. At an intermediate phase of the shearing, the deformation is halted and several hours are waited before continuing with shearing. During the pause in the applied strain rate, stress relaxation occurs. After the pause, the shearing is continued with the same strain rate as before. No change in rigidity (which would be caused by further dissipation of residual excess pore water pressures) was observed during the continuation of the shearing phase. Dissipation in the water overpressure during the pause would induce an increase in effective stress acting on the sample, therefore the sample would result more rigid after the dissipation. If no change occurs, the drained conditions can be considered attained.

4.3 Tested samples and loading paths

4.3.1 Tested samples

The tested samples were obtained from core BGC1–14a, retrieved in Mont Terri Underground Rock laboratory from the sandy facies of the Opalinus Clay formation. The core characterization was discussed in Chapter 2, Section 2.5.1. The core was extracted from a depth of 1302-1395 cm from the gallery wall, in the direction perpendicular to the sedimentation planes. The exact location of the portion of the core from which each sample was obtained was noted down, and is reported in Table 4-1 together with the characteristics of the samples at the beginning of the test: h, the sample height; D the sample diameter; ρ the sample bulk density; e, void ratio; w, water content; S_{r0}, initial degree of saturation. Void ratio and degree of saturation were computed assuming solid density, ρ_s, obtained from core characterization (Chapter 2, Table 2-3).

The sample pictures (before and after testing) and the sample locations within the core are indicated on the X-ray core scan in the Appendixes B and A, respectively.

In order to obtain the samples, slices with a thickness of approximately 80-100 mm were sawn from the core without unpacking it, in order to minimise the disturbance to the specimen; then, the block was removed from the packing, and it was cut in several pieces along the axis direction. Parallelepiped pieces were cut, in order to be further handled in the lathe machine. Cylinders with dimensions appropriated for the apparatus were obtained; particular attention

was used to obtain parallel and plane surfaces. No fluid (e.g., water, air) was used during the specimen preparation phase, in order to preserve the original water content/composition as much as possible and to reduce the disturbance of the material. However, the drying of the material partly occurred during the preparation. The drying was more severe for the sample S-1 than for samples S-2 and S-3 (Table 4-1) and was attributed to handling of the sample with the lathe machine. Re-saturation of the specimens was carried out directly inside the testing device, immediately after the specimen preparation, maintaining isochoric conditions as much as possible.

Table 4-1 Initial characteristics of the triaxial samples.

Sample	h	D	ρ	e	w	S_{r0}	Depth
	(mm)	(mm)	(g/cm^3)	(-)	(%)	(%)	(cm)
S-1	71.36	37.68	2.41	0.16	1.31	22	1358-1350
S-2	76.48	37.94	2.47	0.14	2.31	45	1342-1350
S-3	77.29	38.24	2.52	0.14	4.23	78	1324-1316

After the tests, the samples were dried, in order to measure the water content, and then used to measure the mineralogical content (performed at the University of Bern).

4.3.2 Loading paths

A scheme of the performed loading paths is reported in Figure 4-3, in deviatoric stress (q), isotropic effective stress (p') plane. In test S-1, right after saturation, the shearing of the sample was performed. In tests S-2 and S-3 after saturation, the samples were consolidated, performing isotropic unloading to the desired confining stresses.

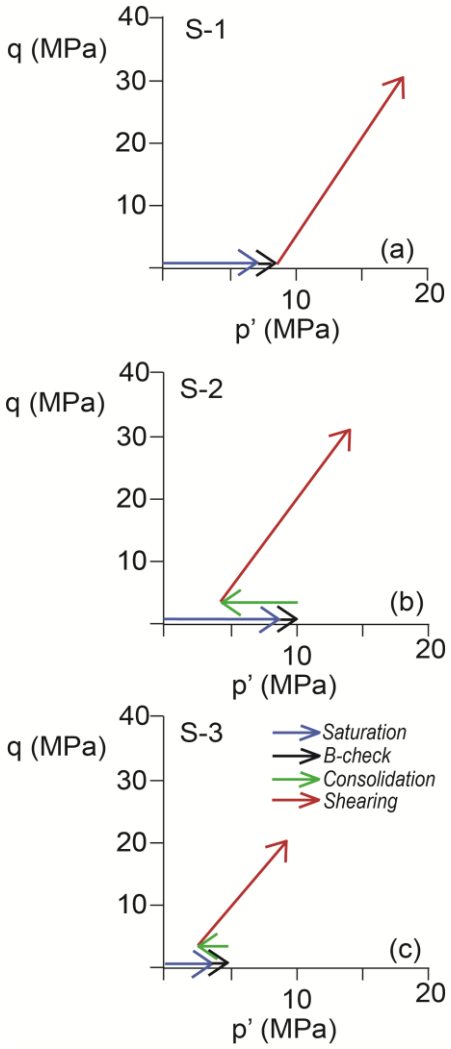

Figure 4-3 Stress paths adopted for the performed triaxial tests. The 4 phases of the tests are highlighted.

4.4 Test results

4.4.1 Saturation and B-check

During saturation, a tendency to swell occurred. The swelling of the samples was constrained by increasing the radial and vertical total stress. In Figure 4-4, Figure 4-5, Figure 4-6, the saturation phases of the three samples are reported.

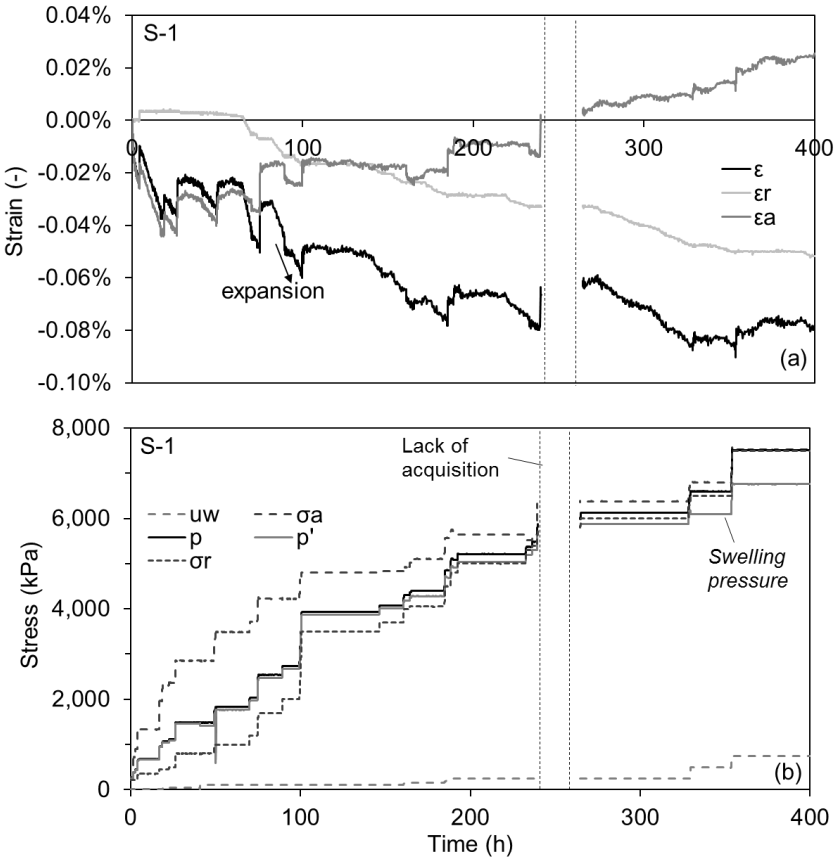

Figure 4-4 Saturation phase of sample S-1: (a) strains and (b) stress evolution in time.

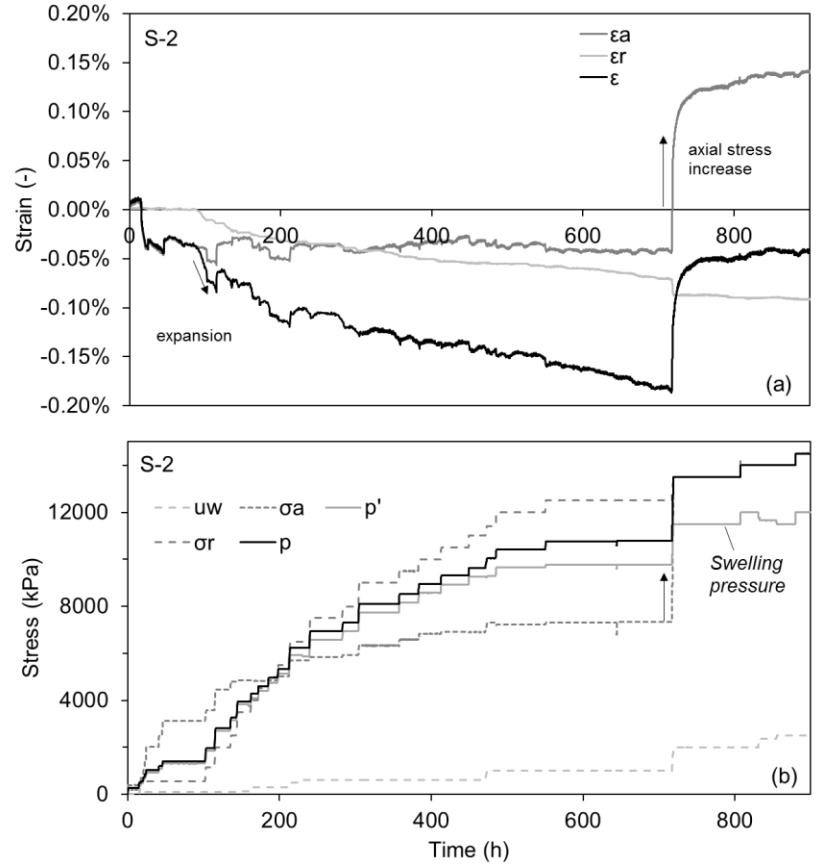

Figure 4-5 Saturation phase of sample S-2: (a) strains and (b) stress evolution in time.

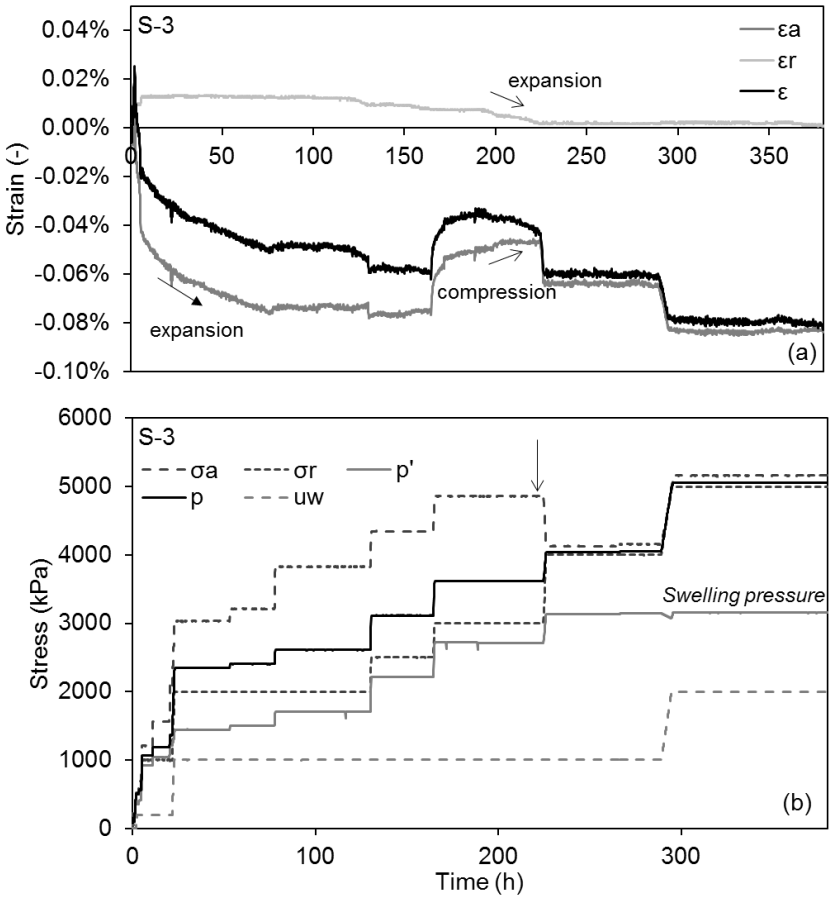

Figure 4-6 Saturation phase of sample S-3: (a) strains and (b) stress evolution in time.

It was noted that the tendency to swell occurred first in the direction perpendicular to bedding. The stress was, therefore increased in the axial direction. Later during the saturation phase, swelling strains in the direction parallel to the bedding occurred. The stress in the axial and radial direction was adjusted to compensate for the swelling of the sample. When no further deformation was recorded, the pore water pressure was increased at 2 MPa, and the total stress was increased simultaneously to keep the effective stress constant. An additional small swelling was detected in this phase.

The swelling strains in the radial direction required higher stress increases to be constrained compared to the axial direction, that is in agreement with the stiffer response of the shale along the bedding direction. For sample S-1 and S-3, very close effective stress values were obtained in the two directions at the end of saturation. In one case (S-2 sample) the radial effective stress was increased at about the double the axial effective stress (σ'_a=11.5 MPa, σ'_r=6.3 MPa), in order to constrain the swelling; after that, strain continued to develop at a very slow rate and the stresses were re-equilibrated to $\sigma'_a=\sigma'_r$=11.5 MPa. The resulting volumetric deformation was in the accepted range (ε<-0.1%). The final mean effective stresses and volumetric swelling strains obtained at the end of these phases are reported in Table 4-2.

Table 4-2 Mean effective stress and volumetric swelling strains at the end of the saturation phase for the performed triaxial tests.

Test	Swelling pressure p'	Swelling strain ε
	(MPa)	(%)
S-1	6.8	-0.08%
S-2	11.5	-0.04%
S-3	3.1	-0.08%

The swelling pressures obtained in these tests involve a range of values of few MPa. The differences can be attributed to a combined effect of the mineralogy, the initial void ratio, the stiffness of the sample, the initial degree of saturation, and of the limited strains that were allowed, within ± 0.1%. Consistently, a smaller swelling pressure was obtained for sample S-3, which had an initial degree of saturation (78%) closer to the full saturation compared to samples S-1 and S-2 (22% and 45%, respectively). On the other hand, sample S-1 was found to have a slightly lower stiffness, that would induce a smaller swelling pressure.

In particular, for specimen S-2, the swelling strain at the end of the saturation was better constrained (≈-0.04%) than those for S-1 and S-3 (≈-0.08%). In order to compare the swelling pressures for the three samples, the swelling strains should be the same. The strain obtained for S-2 can be corrected, simulating an unloading from the end of the saturation phase (ε_0 =-0.04%), until the same swelling strain (ε_i =-0.08%) as in the other cases is reached: $\Delta\varepsilon = \varepsilon_i - \varepsilon_0 = -0.08\% - (-0.04\%) = -0.04\%$. In the hypothesis of isotropic elastic behaviour, and considering the elastic properties obtained from the performed tests (discussed in Section 4.5.2) it can be estimated that, for mean effective stress range of 10-12 MPa (range at the end of the saturation of the specimen S-2), the Young modulus is approximately 6.5 GPa, and the Poisson's ratio is 0.18. The bulk modulus, $K = E/[3(1-2\nu)]$, would be 3.4 GPa, that, for an imposed expansion deformation of $\Delta\varepsilon$= –0.04%, would induce a decrease in mean effective stress, $\Delta p' = K \cdot \Delta\varepsilon$, of about 1.4 MPa. The swelling pressure of S-2 can be corrected, considering a common allowed swelling strain of -0.08%, by assuming a p'≈10.1 MPa. Figure 4-7 shows the plot of the measured swelling pressure versus the degree of saturation and the values for the same allowed volumetric swelling strains (-0.08%). Specimen S-1 has a higher porosity, and an overall slightly smaller stiffness, that may explain the lower swelling pressure, although a lower saturation was found compared to the other specimen.

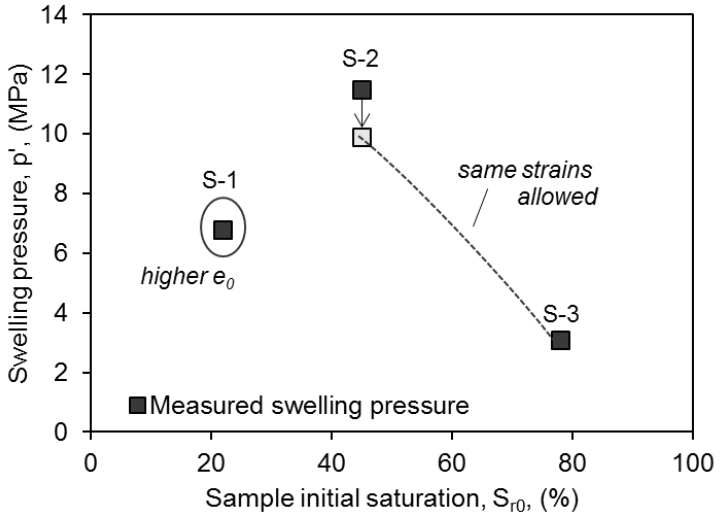

Figure 4-7 Swelling pressure versus sample saturation, in consideration of the allowed swelling strains and initial void ratio.

At the end of this phase, the saturation was verified by performing B-checks. The measured B are reported in Figure 4-8 for samples S-2 and S-3 as a function of the applied backpressure. For sample S-2 (Figure 4-8a), the second step failed, and it was excluded by the following considerations. B-check for sample S-1 is omitted, as the pressure results were affected by a leakage in the drainage line.

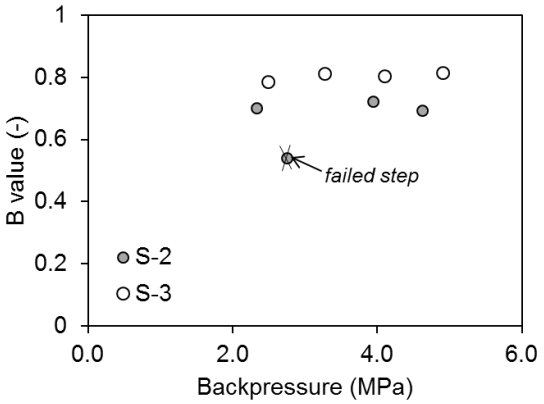

Figure 4-8 measured B-values for samples S-2 and S-3 as a function of the applied backpressure.

As an example, the evolution of the pore water pressure and the mean total stress for sample S-3 are reported in time in Figure 4-9.

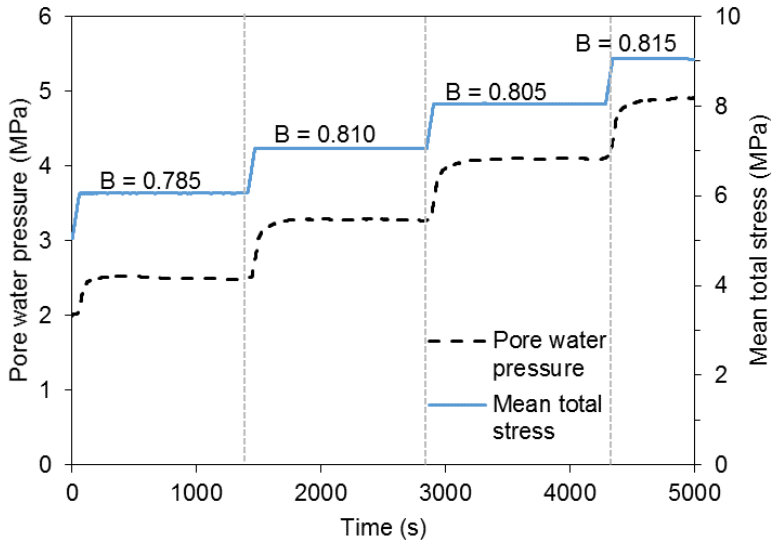

Figure 4-9 Evolution in time of the pore water pressure and the mean total stress during saturation check for sample S-3.

The obtained experimental B-values were corrected by considering the compressibility of the dead volume of water in the drainage lines (≈9 cm^3), with the formulation presented in Equation 4-2. The comparison, between the corrected and measured values, is presented in Figure 4-10.

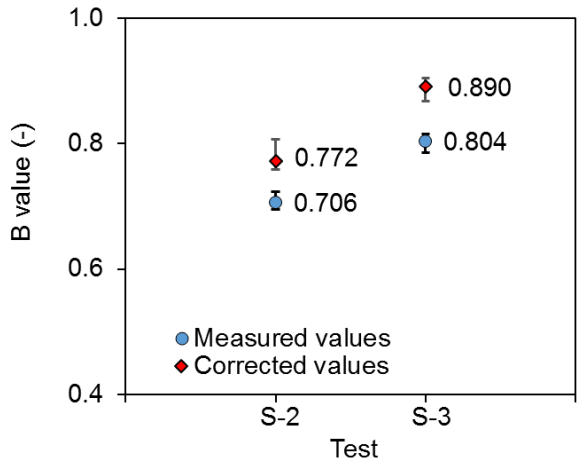

Figure 4-10 Measured and corrected B-values for samples S-2 and S-3.

The obtained values of the parameter B were slightly higher for samples S-3 rather than S-2. In both cases, the achievement of a result higher than 0.77 is considered as satisfactory and accepted as a confirmation of the saturation of the samples. Similar values were already reported for the samples from the shaly facies of the Opalinus Clay in Favero et al. (2018), and on the sandy facies in Minardi et al. (2019).

4.4.2 Consolidation phase

After the completion of the saturation, the samples were brought to the desired isotropic effective stress. Sample S-1 was already at the desired stress level (p′=8 MPa). S-2 and S-3 were unloaded to the mean effective stress of 4 MPa and 2 MPa, respectively.

The evolution in time (square root) of the volumetric strain and the mean effective stress for sample S-2 is reported in Figure 4-11. The sample was subjected to the unloading of $\Delta p' = 4$ MPa, and the final load was left constant for about 10 days. The volumetric deformation did not reach a horizontal asymptote, but after four days (about 10 $h^{1/2}$) it kept a constant strain rate (in the square root of time scale) that was attributed to creep behaviour.

The consolidation time (t_{100}) was estimated to be around 18 h, therefore the estimated consolidation coefficient, using Equation 4-3, is $c_{vi} = 0.02$ mm^2/s. The c_{vi} is considerably lower compared to the results obtained for the sandy facies in oedometric condition (Chapter 3). At the same stress level, the c_v in oedometric conditions, for samples loaded perpendicular to the bedding direction was 0.1-0.05 mm^2/s. A higher c_v would correspond to faster strain rate. The adoption of a lower strain rate would guarantee the water overpressure dissipation and, therefore, the drained condition. The computed strain rate according to Equation 4-4 is: $\dot{\varepsilon} \approx 10^{-8}$ s^{-1}.

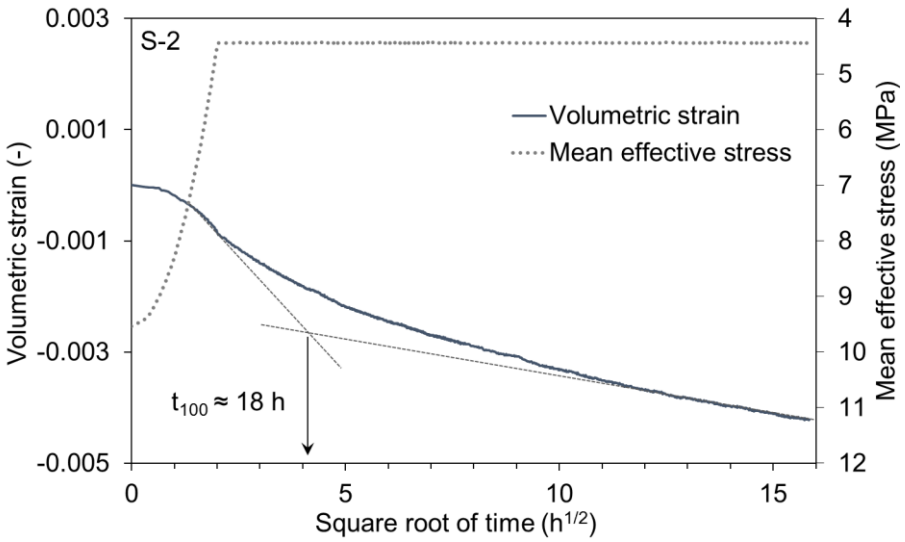

Figure 4-11 Evolution of volumetric strain and mean effective stress in the square root of time for sample S-2.

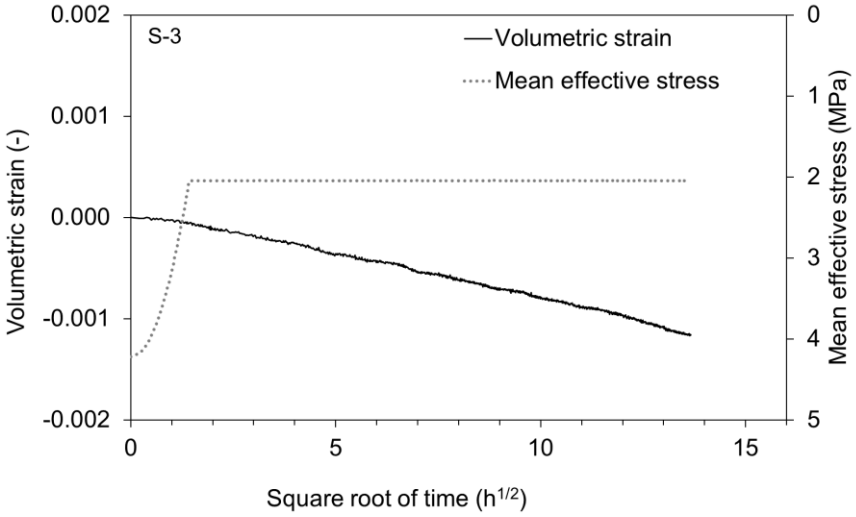

Figure 4-12 Evolution of volumetric strain and mean effective stress in the square root of time for sample S-3.

For sample S-3, a $\Delta p'$ of about 2 MPa was applied during consolidation (Figure 4-12). The unloading yielded limited strains (about 0.1% in 8 days) that in this case as well did not stabilise. The expected consolidation time, considering previous tests in triaxial conditions on Opalinus Clay shaly facies and in oedometric conditions (Favero et al., 2018; Crisci et al., 2019), would be between few tens of hour and a couple of days. In this case, no significant change in slope was observed in this plot. The rate of deformation for the last part of the curve was also evaluated in the semi-logarithmic plane ε-log *time*, obtaining a slope of about $3 \cdot 10^{-4}$ for sample S-3, and $1 \cdot 10^{-3}$ for sample S-2. Those values of strain rate are compatible with the viscous response of the shale under constant load, whose C_α values, investigated in oedometric conditions, were reported in Chapter 3, Section 3.4.1.

4.4.3 Shear phase

The shear phase was conducted by controlling the axial strain rate (10^{-8} s^{-1}) and maintaining the radial total stress and the pore water pressure constant. The axial stress developed while shearing at the mentioned strain rate was measured. The results are shown in Figure 4-13, Figure 4-14 and Figure 4-15 for samples S-1, S-2 and S-3, respectively, in terms of radial (ε_r), axial (ε_a) and volumetric (ε) strain evolutions with deviatoric stress. The volumetric strains were computed as:

4-5 $$\varepsilon = 2 \cdot \varepsilon_r + \varepsilon_a$$

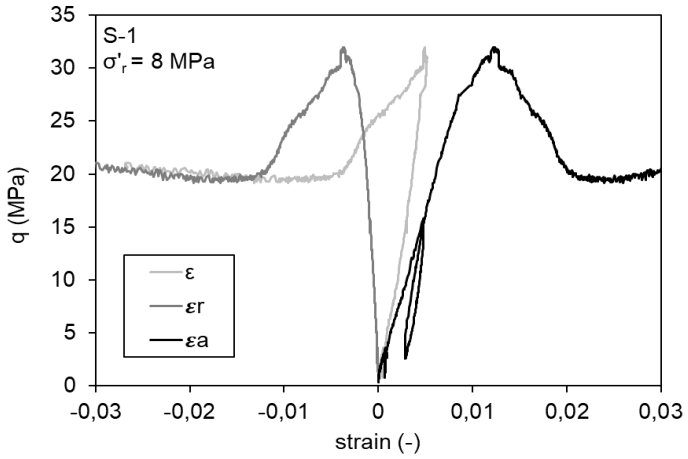

Figure 4-13 Test S-1 results: strains evolution (axial εa, radial εr, volumetric ε) with the deviatoric stress.

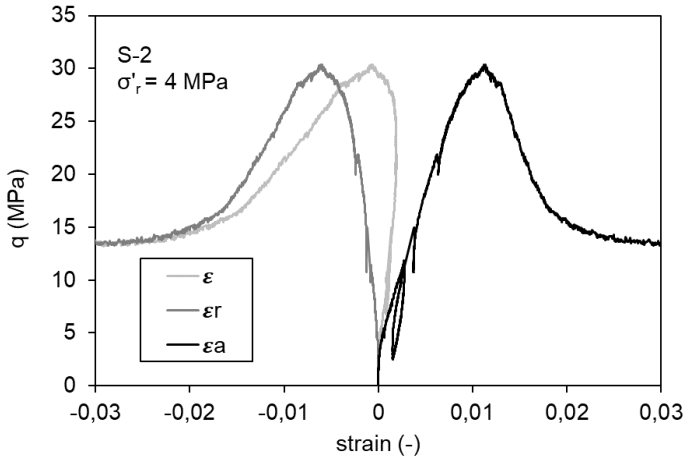

Figure 4-14 Test S-2 results: strains evolution (axial εa, radial εr, volumetric ε) with the deviatoric stress.

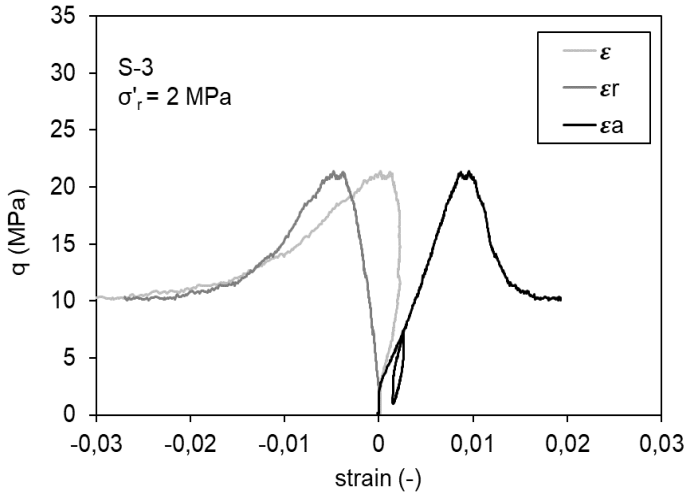

Figure 4-15 Test S-3 results: strains evolution (axial εa, radial εr, volumetric ε) with the deviatoric stress.

Figure 4-16 depicts a summary of the results of the triaxial tests, including (a) the evolution of the deviatoric stress and (b) the volumetric strains with the axial strain. The radial sensor did not respond during the unloading phases, therefore the radial strain during those phases are

excluded from the figures. As expected, a somewhat brittle behaviour was shown from the tested samples. The response upon loading was almost linear up to the peak, and a considerable drop in sustained shear stress was observed after the maximum value. After this point, the sample starts to separate in two blocks sliding one on the other. The continuity of the sample is not anymore ensured from the peak on. Therefore, the radial measurement does not represent the response of the overall sample behaviour anymore, but only of the part of the sample where the chain system is located; the same applies for the computed volumetric strain (dotted lines in Figure 4-16).

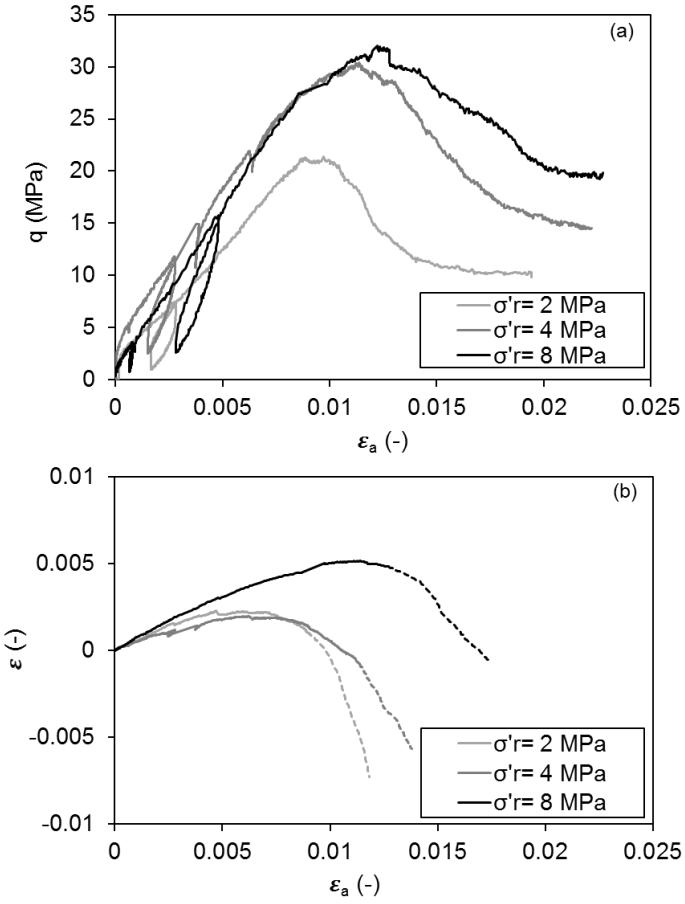

Figure 4-16 Synthesis of the performed drained triaxial tests: (a) deviatoric stress and (b) volumetric strain versus axial strain.

4.4.4 Composition and water content

After each test, the cell was dismantled, and the sample water content was measured by drying the whole sample in the oven at 105°C for about one week. The dry weight of the sample was measured after a few days of drying, and in a later stage of the drying, to assess the weight stabilisation, meaning the drying was completed. The mineralogical composition of the samples was performed (Chapter 2).

The results of the composition are here reported (Table 4-3).

Table 4-3 Mineralogical composition (data from the University of Bern), and water content of the tested samples.

Sample ID	C(org) (wt.%)	C(inorg) (wt.%)	S (wt.%)	N (wt.%)	Calcite (wt.%)	Dolomite / Ankerite (wt.%)	Siderite (wt.%)	Quartz (wt.%)	Albite (wt.%)	K-feldspar (wt.%)	Pyrite CNS (wt.%)	Total clay minerals (wt.%)
S-1	0.97	1.60	0.21	0.03	9	1.9	2.4	50	3.0	3.6	0.4	29
S-2	0.51	3.15	0.25	0.03	22	2.4	2.4	41	2.8	3.7	0.5	26
S-3	0.56	3.16	0.12	0.00	22	2.0	2.3	41	2.7	3.3	0.2	25

The composition of samples S-2 and S-3 are very similar, while S-1 contains slightly higher clay minerals and lower calcite content.

4.5 Analysis and discussion

4.5.1 Shear strength

The strength of the three S-samples of the sandy facies of the Opalinus Clay has been investigated in triaxial conditions. The peak strength and the ultimate strength (after the softening) are reported in the *q-p′* plane in Figure 4-17. The points at the peak condition do not align, and the derived parameters are profoundly affected by that. The reason lies in the difference in the composition of the samples, primarily of S-1 (loaded at higher effective stress). Full description of the impact of the mineralogy on the shear strength is reported in Chapter 5. For the purpose of this Chapter, in order to analyse the difference between the peak and ultimate condition, linear interpolation in the *q-p′* plane is hypothesised:

4-6 $$q = o + M \cdot p'$$

with $$\sin\varphi' = \frac{3M}{M+6}$$ and $$c' = o\frac{\tan\varphi'}{M}$$

where the parameters *o* and *M* are related to the parameters of the Mohr-Coulomb failure criteria, effective cohesion *c′* and angle of shearing resistance (or friction angle) *φ′*.

The obtained parameters are:

- Peak shear strength: φ'=28.8°, c'=5.5 MPa
- Ultimate shear strength: φ'=23.0°, c'=2.7 MPa.

The friction angle is usually higher in materials which are composed by a higher fraction of coarse particles. For those materials, as the one here reported, high friction angles are expected both before and after the peak. On the other hand, the cementation loosens during the shearing,

the intercept of the ultimate shear strength curve decreases, and the curve shifts towards lower strength values.

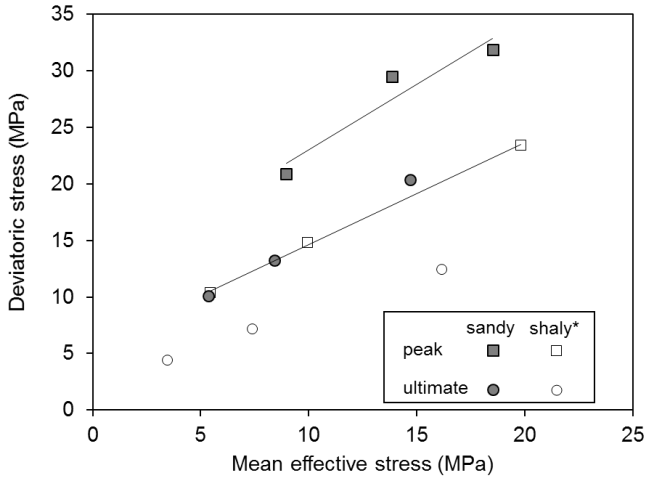

Figure 4-17 Peak and ultimate shear strength of Opalinus Clay sandy and shaly facies. *Data from Favero et al., 2018.

Compared to the results on the shaly facies (Favero et al., 2018), higher peak and ultimate shear strength were obtained for the sandy facies. The shear strength results are analysed with respect to the composition in Chapter 5.

4.5.2 Elastic properties

Elastic drained properties of Opalinus Clay S-samples from the sandy facies of Mont Terri URL have been derived. Initial loading phase or unloading-reloading phases of the shearing were used to determine the parameters. The behaviour of the shale is known to be trasversely

isotropic, so the elastic response is described by 5 independent parameters (two Young moduli, E_1 and E_2, two Poisson's ratios, v_1 and v_2, one shear modulus, G_2). Assuming that the directions radial and axial (i.e. two directions in the bedding plane, one perpendicular to it) are principal directions, the cross anisotropic elastic equations reduce to:

4-7
$$\begin{Bmatrix} \delta\varepsilon_r \\ \delta\varepsilon_a \end{Bmatrix} = \begin{bmatrix} \frac{1-\nu_1}{E_1} & -\frac{\nu_2}{E_2} \\ -\frac{2\nu_2}{E_2} & \frac{1}{E_2} \end{bmatrix} \begin{Bmatrix} \delta\sigma'_r \\ \delta\sigma'_a \end{Bmatrix}$$

During shearing, the axial stress, σ'_a, is changed, while the radial, σ'_r, is kept constant. The matrix in 4-7 leads to 2 equations in two unknown parameters, E_2, and v_2, that can be therefore easily derived. E_2 is the shale stiffness in the axial direction, and v_2 is the Poisson's ratio, the ratio of the strains in the radial and axial directions when an axial load is applied.

The Young Moduli E_2 were computed on the unloading paths. Given the non-linearity of the unloading branches, it was decided to compute the E_2 moduli for a pre-determined vertical strain range (0.2%-0.4%), common to all the unloading paths and to the other tests these results were compared. More details on the selection of the strain range and the comparison with other test results are provided in Chapter 5.

Due to a radial sensor issue, the Poisson's ratios v_2 could only be obtained on the first loading phases, at the beginning of the shearing. Results are reported in Table 4-4 and Figure 4-18. As already obtained for the shaly facies in Favero et al. (2018), the elastic modulus E_2 increases non-linearly with the confining stress. On the other hand, the Poisson's ratio v_2 seems to be slightly higher for sample S-1, compared to the others. In the absence of other pieces of evidence, a constant value will be considered for further analyses. Compared to the results on the shaly facies (Favero et al., 2018) higher E_2 and lower v_2 were obtained for the sandy facies.

Table 4-4 Elastic parameters E2 and v2 obtained from the shearing phases of the triaxial tests.

Test	**E_2**	**p'**	**v_2**	**p'**
	(GPa)	**(MPa)**	**(-)**	**(MPa)**
S-3	4.2	3.2	0.22	3.2
S-2	6.0	6.3	0.18	5.3
S-1	7.0	11.5	0.17	8.3

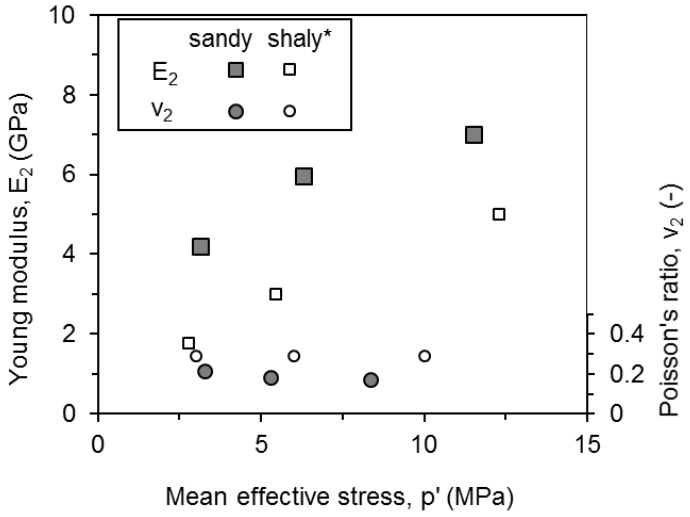

Figure 4-18 Elastic parameters for Opalinus Clay sandy and shaly facies. *Data from Favero et al., 2018

The complete description of the non-linear anisotropic elastic response of Opalinus Clay and the effect of composition on the elastic parameters are addressed in Chapter 5.

4.5.3 Dilatancy

The measurements of the radial deformation are obtained until the peak shear strength is reached. Given the quasi-brittle nature of Opalinus Clay samples, after the peak, the integrity

of the sample is not anymore assured. Therefore, the radial measurement, obtained on a circumference around the sample, cannot be considered as representative for the full height. Until the peak, the measurements are representative and can be used to estimate the dilatancy of the sample.

The dilatancy is particularly relevant for modelling purpose. When associated flow rules are adopted for modelling the response of geomaterials, the volumetric response may be overestimated, which in kinematically constrained problems lead to the overestimation of the confining stresses and the pore water pressure.

The performed tests allow for the estimation of the angle of dilation in the sandy facies of the Opalinus Clay. The deviatoric strain ε_s are computed, and the slope M^* of the curve in the ε_s – ε plane, close to the peak, is evaluated using the following formulation (Wood, 2003; Puzrin, 2012):

4-8 $$\varepsilon_s = \frac{2}{3}\sqrt{3I_{2D}} = \frac{2}{3}(\varepsilon_a - \varepsilon_r)$$

4-9 $$-M^* = \frac{\delta\varepsilon}{\delta\varepsilon_s} \quad \text{where} \quad -M^* = \frac{6\sin\psi}{3-\sin\psi}$$

where ψ is the angle of dilation, typically smaller than the friction angle φ'.

The obtained results are reported in Table 4-5.

Table 4-5 Angle of dilation obtained from the performed drained triaxial tests

Test	p′	M*	ψ
	(MPa)	(-)	(°)
S-1	18.0	-0.35	9.5
S-2	13.8	-0.75	19.4
S-3	9.0	-0.80	20.7

An impact of the confinement stress on the angle of dilation is envisaged: the higher the confinement, the smaller the angle of dilation. The dilatancy angle is more than halved compared to the estimated friction angle. Thus, for modelling purpose, an associated flow rule or a constant angle of dilatancy would induce considerable errors in the estimation of volumetric strain or the pore pressure.

4.6 Conclusions

In this chapter triaxial saturated drained tests on Opalinus Clay samples from the sandy facies were presented.

The high rigidity, compositional heterogeneity and brittleness of the sandy samples required a modification of the triaxial set-up to improve the quality of the measurements, to decrease possible sample damage due to the preparation of large samples, and to reduce the testing time. Internal LVDTs were adopted to deal with the first aspect in order to exclude the deformation of the apparatus from the measurements. The other two aspects were coped with by decreasing the sample size, although respecting the height-diameter ratio needed for triaxial tests.

Highly accurate saturated drained triaxial tests on samples from the sandy facies were produced, which are the first results obtained in these conditions.

The advantage of the drained conditions is that the drained elastic properties can be obtained (in particular, E_2 and ν_2). Non-linear evolution of E_2 with the applied confining stress was found, while the ν_2 remained relatively constant.

A quasi-brittle response was found for all the sandy samples during the shearing phase. The peak and ultimate shear strength were obtained. It was highlighted that at the ultimate conditions, samples showed a significant lower cohesion parameter (intercept of the interpolating curve). The friction angles determined in peak and ultimate conditions were found to be similar.

The dilatancy of the sample was characterised. The angle of dilation was found to be more than halved compared to the mobilised friction angle, and dependent on the confining stress level which is particularly relevant for the determination of an appropriate flow rule to model the shale behaviour.

Further analysis is provided in Chapter 5, by considering the sample compositions and comparing the obtained results with the literature.

4.7 References

Belmokhtar, M., Delage, P., Ghabezloo, S., Conil, N., 2018. Drained Triaxial Tests in Low-Permeability Shales: Application to the Callovo-Oxfordian Claystone. Rock Mech Rock Eng 51, 1979–1993. https://doi.org/10.1007/s00603-018-1442-0

Bishop, A.W., 1959. The principle of effective stress. Tecnisk Ukeblad 39, 869–863.

Crisci, E., Ferrari, A., Giger, S.B., Laloui, L., 2019. Hydro-mechanical behaviour of shallow Opalinus Clay shale. Engineering Geology 251, 214–227. https://doi.org/10.1016/j.enggeo.2019.01.016

Favero, V., 2017. Multiphysical behaviour of shales from Northern Switzerland. https://doi.org/10.5075/epfl-thesis-7539.

Favero, V., Ferrari, A., Laloui, L., 2018. Anisotropic Behaviour of Opalinus Clay Through Consolidated and Drained Triaxial Testing in Saturated Conditions. Rock Mech Rock Eng 51, 1305–1319. https://doi.org/10.1007/s00603-017-1398-5

Ferrari, A., Minardi, A., Ewy, R., Laloui, L., 2018. Gas shales testing in controlled partially saturated conditions. International Journal of Rock Mechanics and Mining Sciences 107, 110–119. https://doi.org/10.1016/j.ijrmms.2018.05.003

Fredlund, D.G., 1976. Density and compressibility characteristics of air–water mixtures. Can. Geotech. J. 13, 386–396. https://doi.org/10.1139/t76-040

Ghabezloo, S., Sulem, J., 2010. Effect of the volume of the drainage system on the measurement of undrained thermo-poro-elastic parameters. International Journal of Rock Mechanics and Mining Sciences 47, 60–68. https://doi.org/10.1016/j.ijrmms.2009.03.001

Giger, S.B., Ewy, R.T., Favero, V., Stankovic, R., Keller, L.M., 2018. Consolidated-undrained triaxial testing of Opalinus Clay: Results and method validation. Geomechanics for Energy and the Environment, Themed Issue on Selected Papers from the International Workshop on Advances in Laboratory Testing and Modelling of Soils and Shales 14, 16–28. https://doi.org/10.1016/j.gete.2018.01.003

Gräsle, W., 2011. Multistep triaxial strength tests: Investigating strength parameters and pore pressure effects on Opalinus Clay. Physics and Chemistry of the Earth, Parts A/B/C, Clays in Natural & Engineered Barriers for Radioactive Waste Confinement 36, 1898–1904. https://doi.org/10.1016/j.pce.2011.07.024

Gutierrez, M., Katsuki, D., Tutuncu, A., 2015. Determination of the continuous stress-dependent permeability, compressibility and poroelasticity of shale. Marine and Petroleum Geology PA, 614–628. https://doi.org/10.1016/j.marpetgeo.2014.12.002

Head, K.H., 1998. Manual of soil laboratory testing. Volume 3: Effective stress tests, Second Edition. ed. John Wiley and Sons.

Minardi, A., Ferrari, A., Ewy, R., Laloui, L., 2018. Nonlinear Elastic Response of Partially Saturated Gas Shales in Uniaxial Compression. Rock Mech Rock Eng 51, 1967–1978. https://doi.org/10.1007/s00603-018-1453-x

Minardi, A., Ferrari, A., Laloui, L., 2019. Benchmark study on triaxial testing of Opalinus Clay: analysis and comparative evaluation of tests results. Swiss Federal Institute of Technology, EPFL.

Puzrin, A.M., 2012. Constitutive Modelling in Geomechanics. Springer Berlin Heidelberg, Berlin, Heidelberg.

Seiphoori, A., Ferrari, A., Laloui, L., 2011. An advanced calibration process for a thermo-hydro-mechanical triaxial testing system, in: Deformation Characteristics of Geomaterials: Proceedings of the Fifth International Symposium on Deformation Characteristics of Geomaterials, IS-Seoul 2011, 1-3 September 2011, Seoul, Korea. IOS Press, p. 396.

Skempton, A.W., 1954. The Pore-Pressure Coefficients A and B. Géotechnique 4, 143–147. https://doi.org/10.1680/geot.1954.4.4.143

Wang, L.L., Bornert, M., Héripré, E., Yang, D.S., Chanchole, S., 2014. Irreversible deformation and damage in argillaceous rocks induced by wetting/drying. Journal of Applied Geophysics 107, 108–118. https://doi.org/10.1016/j.jappgeo.2014.05.015

Wild, K.M., Wymann, L.P., Zimmer, S., Thoeny, R., Amann, F., 2015. Water Retention Characteristics and State-Dependent Mechanical and Petro-Physical Properties of a Clay Shale. Rock Mechanics and Rock Engineering 48, 427–439. https://doi.org/10.1007/s00603-014-0565-1

Wissa, A.E.Z., 1969. Pore Pressure Measurement in Saturated Stiff Soils. Journal of the Soil Mechanics and Foundations Division 95, 1063–1074.

Wood, D.M., 2003. Geotechnical modelling. CRC Press.

Chapter 5

Impact of the mineralogical composition on the elastoplastic hydro-mechanical response of Opalinus Clay shale

5. Impact of the mineralogical composition on the elastoplastic hydro-mechanical response of Opalinus Clay shale

The results presented in this chapter are intended to be submitted as a journal paper:

Journal Paper: "*Crisci, E., Ferrari, A., Giger, S.B., Laloui, L., Impact of the mineralogical composition on the elastoplastic hydromechanical response of the Opalinus Clay shale"*

The pre-print version of the journal paper has been used to draft the chapter.

Contribution of the Candidate: analysis of the literature data, choice and application of the analytical and empirical solutions, writing of the manuscript.

5.1. Introduction

The Opalinus Clay is a shale widely spread in the underground of northern Switzerland and southern Germany that has been studied as a possible natural barrier for engineering applications such as radioactive waste disposal and CO_2 sequestration.

The shale has a very low porosity and permeability, good self-sealing potential and yet relatively high mechanical strength. The combination of these characteristics designates Opalinus Clay an ideal geological barrier (Gautschi, 2017). It has a transversely isotropic behaviour; in the sedimentation direction, at the centimetre to decimetre scale, the shale presents a layered structure, with an alternation of clay-rich and quartz-calcite rich layers, whose differences in composition have been attributed to the environmental conditions in the coastal basin during the deposition process (Bossart and Thury, 2008). At the scale of the Mont Terri Underground Rock Laboratory, several lithostratigraphic sub-units have been identified (Nagra, 2002). Due to their predominance in the sites of interest for practical applications, two of those facies are of primary importance: the shaly facies (argillaceous shale with quartz-rich lenses) and the sandy facies (a marly shale, with lenses of sandstone). Heterogeneities in the composition of the sandy facies were identified (Peters et al., 2011). A large part of the research has so far focused on the behaviour of the more homogeneous shaly facies of the formation. To explore the effect of material variability, e.g. for engineering suitability of underground openings, the sandy facies is increasingly of interest.

The impact of composition on sample porosity at the micrometre scale has been shown by microstructural observations (e.g., Houben et al., 2014; Philipp et al., 2017), by laboratory measurements at the centimetre scale (e.g., Mazurek et al., 2017; Crisci et al., 2019) and by density calibrated tomographic scans at the core scale (e.g., Keller and Giger, 2019). Few experimental studies highlighted the effect of the composition on the mechanical behaviour. Samples of Opalinus Clay with higher quartz and carbonate contents showed higher rigidity (Gräsle and Plischke, 2010), and minor volumetric sensitivity to changes in total suction (Minardi et al., 2016), lower compressibility and swelling indexes in one-dimensional consolidation (Crisci et al., 2019). Attempts to relate the composition to the shear strength have been proposed in Kaufhold et al. (2013), based on triaxial test results obtained on non-saturated samples (Gräsle and Plischke, 2011, 2010). The saturation has been shown to play a significant role in the mechanical response of shales and gas shales (e.g., Minardi et al., 2016).

Recently, new sets of triaxial tests were conducted on saturated samples of Opalinus Clay in undrained (Minardi et al., 2019) and drained conditions (Favero et al., 2018 and Chapter 4). Besides, compressibility in oedometric condition has been explored on samples from different locations (Ferrari et al., 2016; Crisci et al., 2019). The newly gathered experimental information under fully saturated conditions represents an opportunity to revise the response of the Opalinus Clay based on the material composition, excluding the possible influence of the degree of saturation in the analysis. Part of the dispersion in the experimental data is here explained as a function of the heterogeneity among the tested samples.

Several studies have included the composition or layering structure for explaining the behaviour of shale and rock samples. A number of works considered the effect of soft layers and fissures in weakening the geomaterial response (e.g., Adhikary and Dyskin, 2007; Amann et al., 2011; Lisjak et al., 2014). Others have shown experimentally (e.g., Hu et al., 2013) and through finite or distinct element modelling (e.g., Kim et al., 2016) the impact of the alternation of soft and hard layers on the geomaterial strength and stiffness. Pieces of evidence show a weakening of the geomaterial's response as clay content increases in the geomaterials. This work aims to deliver a simplified yet accurate interpretation of the response of Opalinus Clay samples, that allows predicting the shale response based on analytical solutions and empirical correlations with the geomaterial composition.

The shale is schematized as an alternation of two kinds of layers (a clay-rich layer and a quartz-calcite rich one). The properties of the two kinds of layers are first calibrated on a subset of the available data. The mineralogical composition of the samples is used to determine the layer-type fraction in the sample. The mechanical response is evaluated as a combination of layers and compared with the experimental evidence. The elastic properties and the elastoplastic compressibility in oedometric conditions are obtained via analytical solutions. The shear strength (peak and ultimate) are predicted via empirical correlations with the mineralogical composition.

The approach shows that the properties of Opalinus Clay can be predicted with good approximation adopting a layered structure approach.

The approach may be used to give a preliminary estimation of the properties of not tested samples, and to guide experimental testing programs for the type and number of tests to be performed, potentially with significant savings in cost and time.

Moreover, estimations of the sample compositions are now available also on the meter scale, by calibrated tomography scans (Keller and Giger, 2019). By combining this information with log data, the approach can be potentially extended to a larger scale, in order to obtain a map of the hydro-mechanical properties of the shale at the site investigation scale.

5.2. Layered structure

The Opalinus Clay shale, at the centimetre scale, is composed of an alternation of clay-rich and quartz and calcite-rich layers. Several works have analysed the macro and microstructure of specimens collected in Mont Terri (Houben et al., 2014; Philipp et al., 2017; Seiphoori et al., 2017; Lauper et al., 2018; Peters et al., 2011), and recognised the alternation of the sedimentary structures. Houben et al. (2014) have characterised the different layer types of the Opalinus Clay shale retrieved in the Mont Terri Underground Research Laboratory. Clay-rich layers are composed of a clayey matrix, with particles preferentially oriented along the bedding direction, in which grains of other minerals – typically quartz, calcite – are immersed. Quartz/calcite-rich layers are mainly made of quartz grains, and the inter-grain porosity is occupied with clay particles, shifting the fabric to a grain-supported type as the quartz content increases. The quartz-rich layers are also found to have a lower porosity compared to the clay-rich ones. The clay layers in samples coming from the sandy and the shaly facies of the formation were found to have a similar structure and clay-mineral composition, namely, from the most to the least abundant, illite, kaolinite, illite-smectite mixed layers, chlorite (Bossart and Thury, 2008).

The observation of the core samples, together with the X-ray images at that scale, confirms the systematics of the Opalinus Clay composition (Keller and Giger, 2019), in which an alternation of layers with higher clay content and layers with higher quartz-calcite content is found with layers of few millimetres up to centimetres in thickness.

In this work, it is assumed that the Opalinus Clay structure can be schematized as a stratified material (Figure 5-1), composed of parallel strata of variable thickness, in which one can distinguish two types of layers. The first type of strata is here called the “shaly” layer (Figure 5-1b), composed of clay matrix, with particles of other minerals embedded in it. Samples from the shaly facies are composed only by shaly layers. The second type of strata is the “sandy” layer (Figure 5-1c), composed of silt to sand-size particles, made of non-clayey minerals, in which the porosity is filled with the clay matrix. Samples coming from the shaly facies of the formation are composed of shaly layers, while samples coming from the sandy facies are composed of an alternation of shaly and sandy layers in variable thickness (Figure 5-1d).

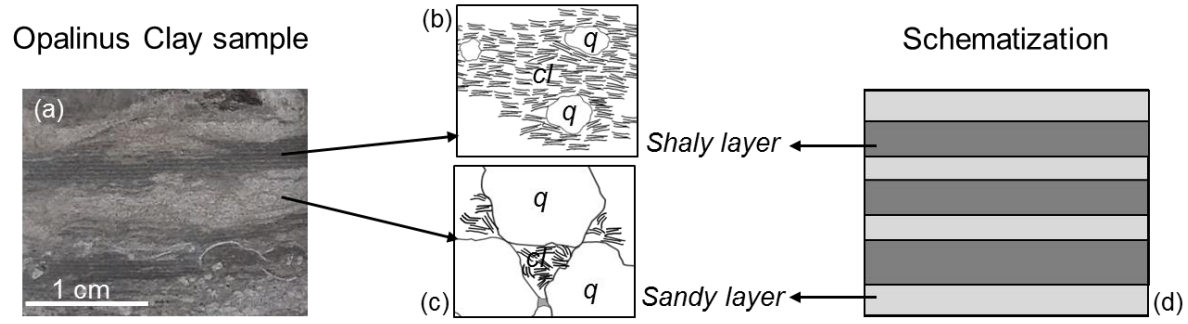

Figure 5-1 Schematic view of the Opalinus Clay as a layered material: (a) a sandy sample picture; (b) shaly and (c) sandy layer structure (q: quartz, cl: clay matrix); (d) schematized layered structure of a sandy sample.

In the following, the relationships between the phases (Figure 5-2) and the derivation of the shaly and sandy volumetric fractions, i.e. the percentages in volume of the shaly and sandy layers in a sample, are shown.

The derivation moves from the definition of the mineralogical mass contents of clayey and non-clayey, that is the results usually obtained from a mineralogical analysis (e.g., from X-ray diffractometry). This input is converted into the shaly and sandy percentage output, assuming a fixed mineralogical composition and porosity, for each layer kind.

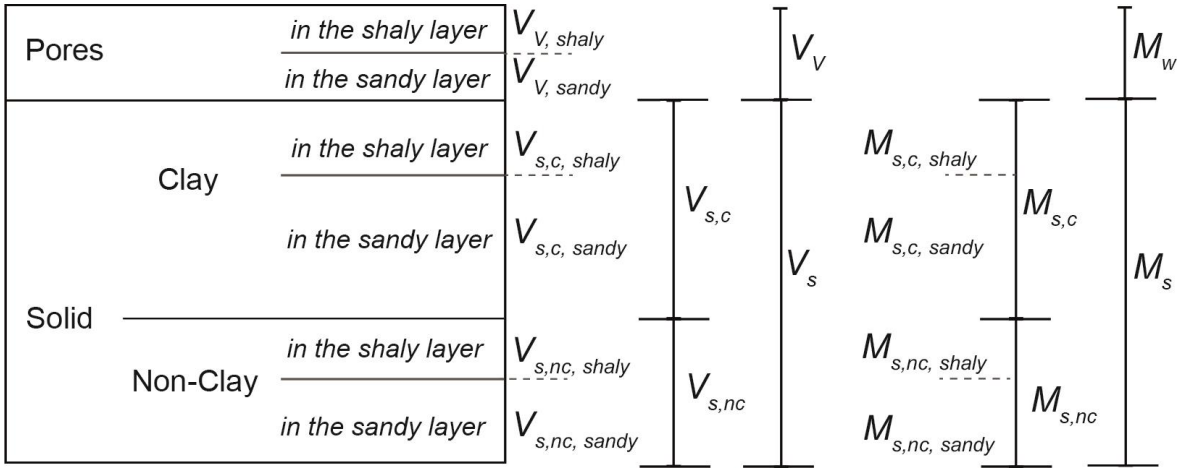

Figure 5-2 Relationship among the phases for Opalinus Clay, considering shaly and sandy layers. Saturated condition.

The clayey minerals x_c and of the non-clayey minerals x_{nc} contents by mass are defined as:

5-1 $$x_c = M_{s,c} / M_s$$

5-2 $$x_{nc} = M_{s,nc} / M_s$$

where $M_{s,c}$ and $M_{s,nc}$ are the solid mass of the clayey and non-clayey minerals, M_s is the total solid mass.

The solid density ρ_s is computed as:

5-3 $$\frac{1}{\rho_s} = \frac{x_c}{\rho_{s,c}} + \frac{x_{nc}}{\rho_{s,nc}}$$

where $\rho_{s,c}$ and $\rho_{s,nc}$ are the average clayey mineral and average non-clayey mineral densities.

The above defined densities, allow the content by weight to be converted in solid volume fraction (i.e. porosity excluded) of the clayey ($\tilde{\varphi}_c$) and non-clayey ($\tilde{\varphi}_{nc}$) components:

5-4 $$\tilde{\varphi}_c = V_{s,c} / V_s = x_c \cdot \rho_s / \rho_{s,c}$$

5-5 $$\tilde{\varphi}_{nc} = V_{s,nc} / V_s = x_{nc} \cdot \rho_s / \rho_{s,nc}$$

where $V_{s,c}$ is the clay mineral volume, $V_{s,nc}$ is the non-clay mineral volume, V_s, is the total solid volume.

For each layer type, the solid volume ($V_{s,shaly}$ or $V_{s,shaly}$) is given by the sum of the solid volume of clay $V_{s,c}$ and non-clay minerals $V_{s,nc}$:

5-6 $$V_{s,shaly} = V_{s,c,shaly} + V_{s,nc,shaly}$$

5-7 $$V_{s,sandy} = V_{s,c,sandy} + V_{s,nc,sandy}$$

The parameters A and F are defined as the volumetric fractions of clay content attributed to the shaly and the sandy layers, respectively:

5-8 $$A = V_{s,c,shaly} / V_{s,shaly}$$

5-9 $$F = V_{s,c,sandy} / V_{s,sandy}$$

The void ratios of the shaly and sandy layers are defined as:

5-10 $$e_{shaly} = V_{v,shaly} / V_{s,shaly}$$

5-11 $$e_{sandy} = V_{v,sandy} / V_{s,sandy}$$

The void ratio of the entire sample is:

5-12 $$e = V_V / V_s$$

Starting from the mineralogical and microstructural analysis reported in Houben et al. (2014), reference compositions and void ratios for the shaly and the sandy layer were adopted:

- shaly layer: A = 65%, void ratio e_{shaly}=0.23
- sandy layer: F = 15%, void ratio e_{sandy} =0.11.

The solid volume fractions of clayey $\tilde{\varphi}_c$ and non-clayey minerals $\tilde{\varphi}_{nc}$ are converted in the solid volume fraction of shaly $\tilde{\varphi}_{shaly}$ and sandy layers $\tilde{\varphi}_{sandy}$, assuming the average composition and porosity of each kind of layer. The fractions are obtained as follows:

5-13
$$\begin{cases} \tilde{\varphi}_c = A \cdot \tilde{\varphi}_{shaly} + F \cdot \tilde{\varphi}_{sandy} \\ \tilde{\varphi}_{nc} = (1-A) \cdot \tilde{\varphi}_{shaly} + (1-F) \cdot \tilde{\varphi}_{sandy} \end{cases}$$

where $\tilde{\varphi}_{shaly}$ and $\tilde{\varphi}_{sandy}$ are:

5-14
$$\begin{aligned} \tilde{\varphi}_{shaly} &= (V_{s,c,shaly} + V_{s,nc,shaly}) / V_s \\ \tilde{\varphi}_{sandy} &= (V_{s,c,sandy} + V_{s,nc,sandy}) / V_s \end{aligned}$$

Equation 5-12 can also be written as $e = e_{shaly} \cdot \tilde{\varphi}_{shaly} + e_{sandy} \cdot \tilde{\varphi}_{sandy}$, adopting the solid volumetric fraction definitions, as mentioned in Chapter 2.

The shaly and sandy volumetric fractions, i.e. the fraction of shaly layers and sandy layers over the total volume (V), can now be defined considering the porosity attributed to each layer type:

5-15
$$\vartheta_{shaly} = \frac{V_{s,shaly} + V_{v,shaly}}{V} = \frac{\tilde{\varphi}_{shaly}}{1+e}(1+e_{shaly})$$

5-16
$$\vartheta_{sandy} = \frac{V_{s,sandy} + V_{v,sandy}}{V} = \frac{\tilde{\varphi}_{sandy}}{1+e}(1+e_{sandy})$$

The sum of the two fractions is equal to one.

Thanks to the observations of the microstructure of the layers and their consistency among samples and facies, from the knowledge of only the clay-mineral content, obtained in mineralogical analysis or derived from log results, it is possible to estimate the amount of shaly fraction (in volume) in every sample. Hereafter, the shaly volumetric fraction (ϑ_{shaly}) is used as an indication of the sample composition.

In Figure 5-3, the correspondence between clay-mineral content x_c and shaly volumetric fraction ϑ_{shaly} for the whole range of clay-mineral content is reported. The extremes of the curve correspond to the cases in which only shaly layers or only sandy layers compose the sample.

The correspondence x_c-ϑ_{shaly} is used hereafter to define the layers distribution and therefore is the starting point to study the hydro-mechanical behaviour of the Opalinus Clay as a layered geomaterial.

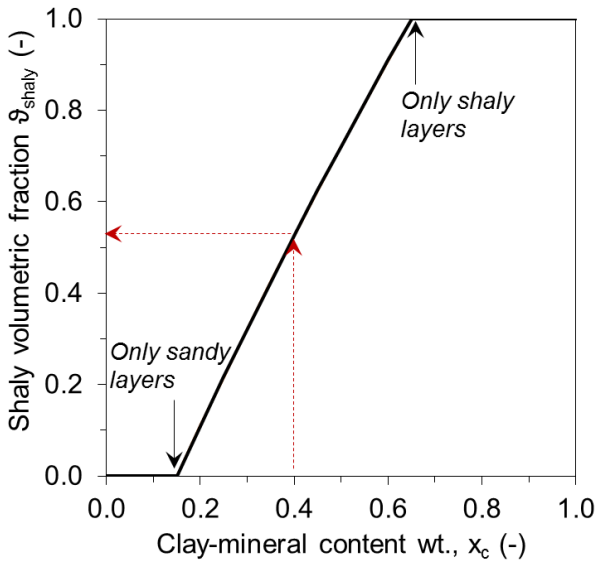

Figure 5-3 Correlation between the clay-mineral content and the shaly fraction of the layered structure. The dotted arrows suggest the reading direction of the graph.

5.3. Elastic response

5.3.1. Non-linear transversely isotropic elastic parameters, in drained and undrained conditions

Opalinus Clay is known to have a transversely isotropic behaviour (e.g. Favero et al., 2018; Salager et al., 2013). While for an isotropic elastic material, only two parameters are needed to describe its elastic response, for a transversely isotropic material, five independent parameters are needed. However, often the experimental tests allow deriving only a part of this set. The definition of the elastic parameters for a transversely isotropic material, adopted in the following, is illustrated in Figure 5-4. The coordinate system in Figure 5-4 is defined with respect to the bedding direction: directions 1 and 2 are in the plane of isotropy, direction 3 is perpendicular to it.

The elastic parameters for shale are usually stress-dependent. In Figure 5-4 and in equations from 5-17 to 5-21 the relations are written in incremental form, while the stress-dependency is addressed later in this section.

The five parameters (E_1, E_2, ν_1, ν_2, G_2) are independent, while G_1 and ν_3 are dependent on the other parameters:

5-17 $$G_1 = \frac{E_1}{2(1+\nu_1)} \quad \text{and} \quad \nu_3 = \nu_2 \frac{E_1}{E_2}$$

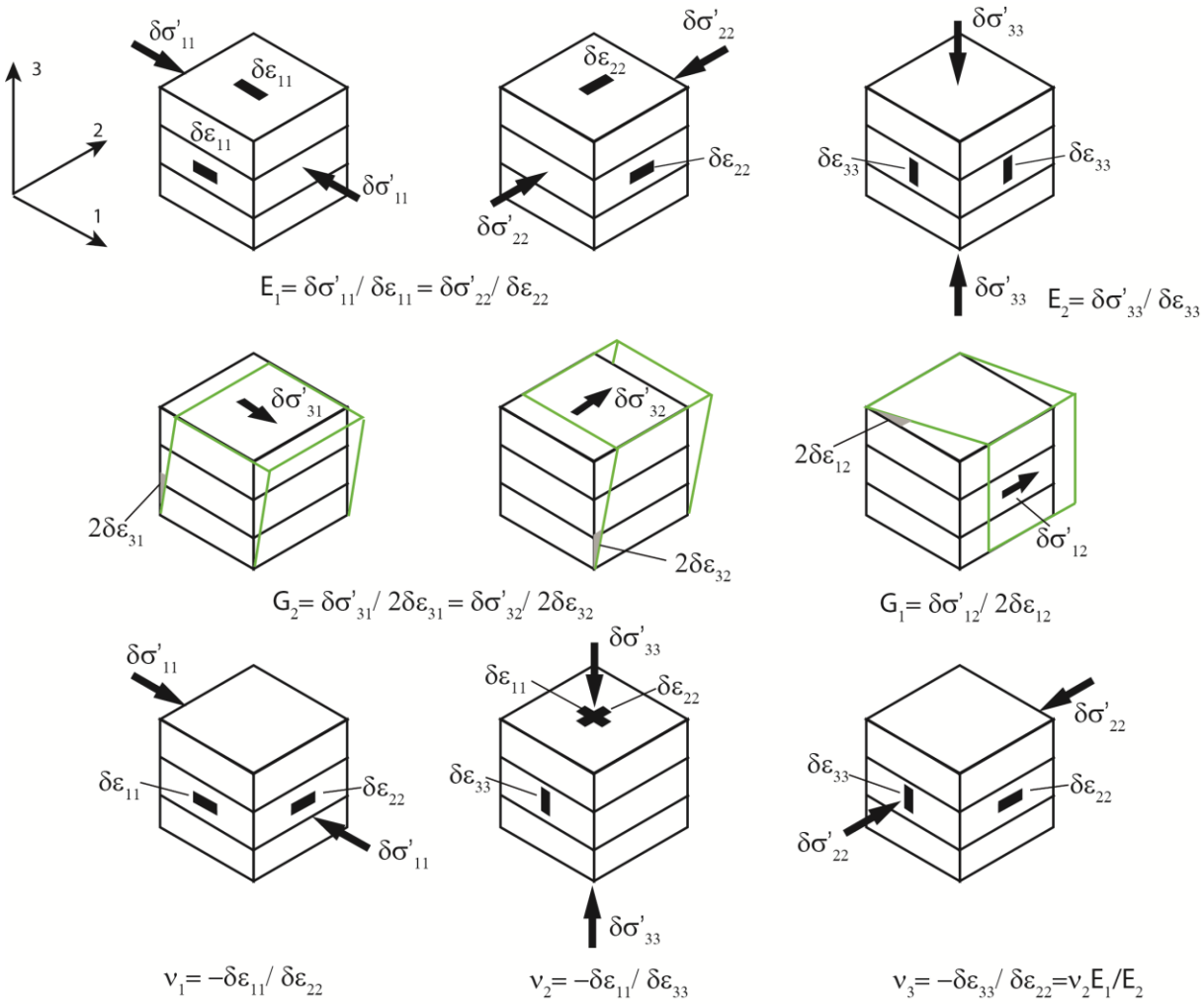

Figure 5-4 Definition of the elasticity parameters for a transversely isotropic material.

In transversely isotropic conditions, the elastic laws write as in Equation 5-18.

$$5\text{-}18 \qquad \begin{pmatrix} \delta\varepsilon_{11} \\ \delta\varepsilon_{22} \\ \delta\varepsilon_{33} \\ \delta\varepsilon_{12} \\ \delta\varepsilon_{23} \\ \delta\varepsilon_{13} \end{pmatrix} = \begin{pmatrix} \frac{1}{E_1} & -\frac{\nu_1}{E_1} & -\frac{\nu_2}{E_2} & 0 & 0 & 0 \\ -\frac{\nu_1}{E_1} & \frac{1}{E_1} & -\frac{\nu_2}{E_2} & 0 & 0 & 0 \\ -\frac{\nu_2}{E_2} & -\frac{\nu_2}{E_2} & \frac{1}{E_2} & 0 & 0 & 0 \\ 0 & 0 & 0 & \frac{1}{2G_1} & 0 & 0 \\ 0 & 0 & 0 & 0 & \frac{1}{2G_2} & 0 \\ 0 & 0 & 0 & 0 & 0 & \frac{1}{2G_2} \end{pmatrix} \begin{pmatrix} \delta\sigma'_{11} \\ \delta\sigma'_{22} \\ \delta\sigma'_{33} \\ \delta\sigma'_{12} \\ \delta\sigma'_{23} \\ \delta\sigma'_{13} \end{pmatrix}$$

Although it is an independent parameter, G_2 is often not measured, because of practical difficulties of obtaining it in the laboratory. Several authors proposed correlations, obtained by empirical observations, among the other elastic parameters to estimate G_2 (e.g., Barden, 1963;

Wittke, 1984; Talesnick et al., 2000). For instance, Wittke (1984) proposed the relation $G_2=E_2/[2(1+\nu_2)]$, analogue to Equation 5-17 for G_1.

For samples loaded in triaxial conditions in the direction perpendicular (S-samples) or parallel (P-samples) to the bedding, the directions 1, 2 and 3 in Figure 5-4 are aligned to the principal directions.

The cross anisotropic matrix further simplifies as follows:

5-19
$$\begin{pmatrix}\delta\varepsilon_{11}\\ \delta\varepsilon_{22}\\ \delta\varepsilon_{33}\end{pmatrix}=\begin{pmatrix}\frac{1}{E_1} & -\frac{\nu_1}{E_1} & -\frac{\nu_2}{E_2}\\ -\frac{\nu_1}{E_1} & \frac{1}{E_1} & -\frac{\nu_2}{E_2}\\ -\frac{\nu_2}{E_2} & -\frac{\nu_2}{E_2} & \frac{1}{E_2}\end{pmatrix}\begin{pmatrix}\delta\sigma'_{11}\\ \delta\sigma'_{22}\\ \delta\sigma'_{33}\end{pmatrix}$$

For S-samples, the two stress components in the radial directions, $\delta\sigma'_{11}$ and $\delta\sigma'_{22}$, are equal. For P-samples the bedding is rotated with respect to S-samples, and in the radial direction the two equal stress components are $\delta\sigma'_{33}$ and $\delta\sigma'_{22}$.

For the total stress, hereafter used for the undrained conditions, the matrix will be written as:

5-20
$$\begin{pmatrix}\delta\varepsilon_{11}\\ \delta\varepsilon_{22}\\ \delta\varepsilon_{33}\end{pmatrix}=\begin{pmatrix}\frac{1}{E_1^u} & -\frac{\nu_1^u}{E_1^u} & -\frac{\nu_2^u}{E_2^u}\\ -\frac{\nu_1^u}{E_1^u} & \frac{1}{E_1^u} & -\frac{\nu_2^u}{E_2^u}\\ -\frac{\nu_2^u}{E_2^u} & -\frac{\nu_2^u}{E_2^u} & \frac{1}{E_2^u}\end{pmatrix}\begin{pmatrix}\delta\sigma_{11}\\ \delta\sigma_{22}\\ \delta\sigma_{33}\end{pmatrix}$$

in which the elastic parameters with superscript *u* are obtained in undrained conditions. The undrained elastic parameters can be derived from the drained ones.

The equations relating drained and undrained parameters had been derived from several authors independently (e.g, Pickering, 1970; Bishop and Hight, 1977; Lings, 2001), assuming no drainage or cavitation, and neglecting the volume compressibility of the soil grains. Bishop and Hight (1977) also considered the value of the Skempton's B parameter as different from 1, as often is the case for shale and rocks:

$$E_2^u = \frac{E_2 E_1^2 C_i}{E_1^2 C_i - B\left(\frac{E_1}{E_2} - 2\nu_2\right)^2 E_2}$$

$$E_1^u = \frac{E_1^2 C_i}{E_1 C_i - B\left(1-\nu_2-\nu_1\right)^2}$$

5-21 $$\nu_2^u = \frac{E_2}{E_1}\frac{\nu_2 E_1 C_i + B\left(\frac{E_1}{E_2} - 2\nu_2\right)(1-\nu_2-\nu_1)}{E_1 C_i - B(1-\nu_2-\nu_1)^2}$$

$$\nu_1^u = \frac{\nu_1 E_1 C_i + B(1-\nu_2-\nu_1)^2}{E_1 C_i - B(1-\nu_2-\nu_1)^2}$$

$$C_i = \frac{1}{E_1}\left(\frac{E_1}{E_2} - 4\nu_2 - 2\nu_1 - 2\right)$$

with the compressibility C_i being the ratio of the variation in volumetric strain to the variation in isotropic effective stress, defined for the transversely isotropic material.

Also, Opalinus Clay elastic behaviour has been experimentally proven to be non-linearly dependent on the mean effective stress. In particular, the Young moduli E_1, E_2, increase for high compressive stress states while, for confining effective stress below 15 MPa, the Poisson's ratios seem to be only marginally affected by the stress state (Favero et al., 2018, Giger et al., 2018). The Poisson's ratios are therefore are here hypothesised as constant.

The evolution of Young's moduli with the mean effective stress can be described using power laws:

5-22 $$E_1 = E_{1,ref}\left(\frac{p'}{p'_{ref}}\right)^{n_1} \quad \text{and} \quad E_2 = E_{2,ref}\left(\frac{p'}{p'_{ref}}\right)^{n_2}$$

where p'_{ref} is a reference value for the mean effective stress, and $E_{1,ref}$ and $E_{2,ref}$ are the corresponding E_1 and E_2 values at that stress level; n_1 and n_2 are the power increase parameters.

During unloading and reloading, shales present a hysteretic and non-linear behaviour. For rocks, the hysteretic response is usually attributed to the presence of microcracks (David et al., 2012; Zimmerman, 1985), that tend to slide after reaching the crack strength resistance. Several values of Young's moduli can be derived depending on the selected strain and stress ranges. In Figure 5-5 an example of the hysteretic and non-linear response upon unloading is reported in the plane of the deviatoric stress (q) versus the deformation in the shearing direction (ε_a). The result refers to the drained shearing phase of a triaxial test on Opalinus Clay sample from the

sandy facies (S-sample)(Chapter 4), used for the hydro-mechanical parameter evaluation. The confining effective stress for the reported example is $\sigma'_{11}=\sigma'_{22}=4$ MPa.

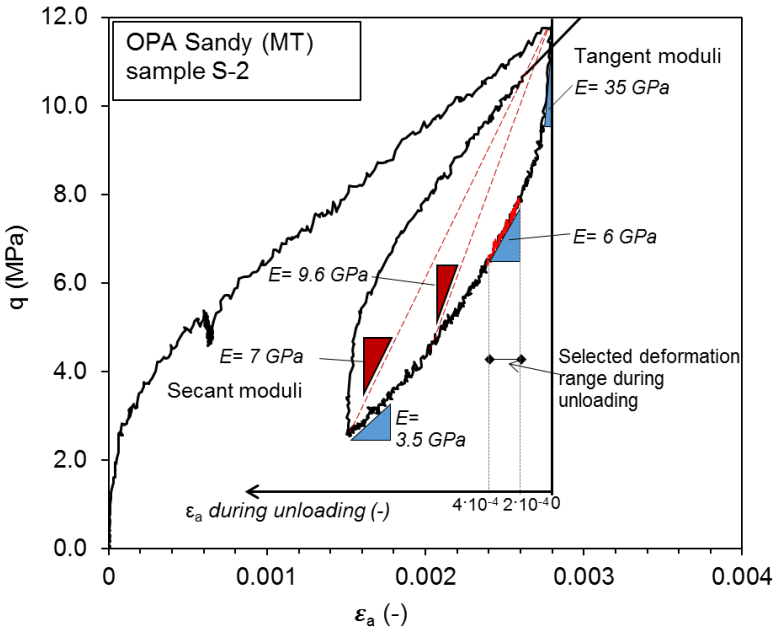

Figure 5-5 Determination of the Young modulus during drained shearing of sandy Opalinus Clay sample.

Depending on the amplitude of the unloading-reloading loop (i.e., whether zero deviatoric stress is reached or not) the secant moduli may vary significantly. Also, some friction of the piston in the loading system may affect the tangent moduli computation in the first part of the curve, during the inversion of the loading direction (from load to unload and the opposite). As a consequence, the first part of the unloading may result significantly stiffer than the real shale behaviour.

In Figure 5-5 several possible secant and tangent moduli at different unloading stages are shown, and it is highlighted that the possible Young's moduli vary over one order of magnitude, from 3.5 MPa to 35 MPa.

To cope with the before mentioned sources of error, in this work the Young modulus for all the analysed tests is computed as the tangent modulus for a fixed strain range during unloading: 0.02%-0.04% (Figure 5-5), measuring the strain from the beginning of the unloading phase. Strain calculation refers to the intial sample height. For the considered test, this would correspond to E_2= 6 MPa. The strain range was selected since it is common to all the analysed tests, and the potential errors coming from the first part of the curve are in this way excluded.

5.3.2. Elastic parameters dependency on the composition

As described in Section 5.2, the structure of the Opalinus Clay can be schematized as a layer alternation of shaly and sandy strata. In this section, the elastic properties of the stratified material, at the sample scale, are inferred from the behaviour of the single strata.

Given the stratification of the samples, the elastic properties of a transversely isotropic continuum medium can be derived by the properties of the layers (Figure 5-6) as analytically derived in several works (Adhikary and Dyskin, 1997; Chou et al., 1972; Gerrard, 1982; Salamon, 1968).

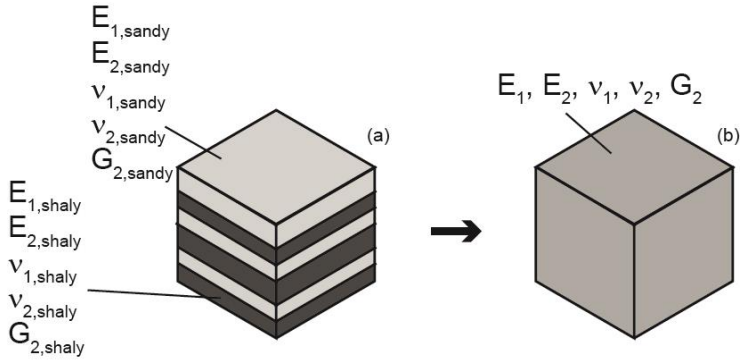

Figure 5-6 (a) Stratified medium as alternation of shaly and sandy layers, and (b) continuum homogeneous medium and related elastic parameters.

The equations to move from the single layers properties (Figure 5-6a) to those of a continuum homogeneous medium (Figure 5-6b) were derived based on the strain energy equivalence of the two media (Salamon, 1968), considering the following hypotheses:

- each layer is homogeneous and transversely isotropic (or isotropic);
- the size of the sample is representative of the material; in the presented case, the size is representative of the material with a certain shaly volumetric fraction;
- the material remains continuous after deformation, and no relative displacements occur at the interfaces among layers;
- the variation of stresses and strains across the equivalent medium are negligible.

The several micro and macrostructural studies (Sections 5.1 and 5.2) that lead to the layered structure hypothesis support the validity of the layer homogeneity and transverse isotropy hypotheses. The size of the sample (about 76 mm) is considered sufficient to guarantee the representativeness of the hydro-mechanical behaviour of the sample with a certain composition, i.e., shaly volumetric fraction. The homogeneity of the stress and strain distribution is assumed to be valid in the limited strain range adopted for the elastic properties estimation. The results will confirm the acceptability of the hypothesis.

The resulting parameters (Equations 5-23) are combinations of the parameters of each layer type and the corresponding volumetric fraction, ϑ_i, with i referring in this case either to the shaly or sandy volumetric fraction. Parameters without the i subscript refer to the equivalent continuum medium.

$$\nu_1 = \sum \frac{\vartheta_i \nu_{1i} E_{1i}}{1-\nu_{1i}^2} \Bigg/ \sum \frac{\vartheta_i E_{1i}}{1-\nu_{1i}^2}$$

$$\nu_2 = (1-\nu_1) \sum \frac{\vartheta_i \nu_{2i}}{1-\nu_{1i}}$$

5-23 $$E_1 = (1-\nu_1^2) \sum \frac{\vartheta_i E_{1i}}{1-\nu_{1i}^2}$$

$$E_2 = \frac{1}{\sum \frac{\vartheta_i}{E_{1i}} \left(\frac{E_{1i}}{E_{2i}} - \frac{2\nu_{2i}^2}{1-\nu_{1i}} \right) + \frac{2\nu_2^2}{(1-\nu_1)E_1}}$$

$$G_2 = \frac{1}{\sum \vartheta_i / G_{2i}}$$

In the considered approach, the elastic properties can be derived neglecting the actual layer arrangement but using only the volumetric fraction of each layer type.

5.3.3. Elastic property determination of the layers

The elastic parameters for the shaly and sandy layers were obtained using the experimental results obtained in saturated drained triaxial tests. The layered structure proposed in Section 5.2 was adopted.

Three new tests on sandy samples (shearing direction perpendicular to the layers, S-samples) (Chapter 4) were used to calibrate the sandy layer elastic parameter. The three tested samples had shaly volumetric fractions of 20%, 20% and 30%, respectively.

Figure 5-7 reports the elastic parameters obtained experimentally for shaly (E_1, E_2, ν_1 and ν_2) and sandy (E_2, ν_2) samples, as a function of the mean effective stress (average value of p' in the selected strain range used for the computation of the elastic parameters). Data on E_1 and ν_1 are available on the shaly samples (Favero et al., 2018). Ratios between Young moduli, of shaly samples, in the direction parallel and perpendicular to the bedding are about 1.5-2. Similar ratios were found for the swelling index computed on the elastic path of oedometric tests (Section 3.4.1).

The non-linear stress dependency of the Young moduli on the mean effective stress is highlighted. On the other hand, the Poisson's ratio variations with the stress were found to be limited in the analysed confining stress range, and are therefore neglected. A substantial difference was found between Young's moduli of the shaly and sandy samples: E_2 of the sandy samples are about twice E_2 of the shaly samples.

For each mean effective stress, knowing the sample compositions, it is possible to derive the elastic parameters for the shaly and sandy layers.

As mentioned before, the shaly samples are composed only of shaly layers. Therefore, the results on the shaly samples directly give the elastic properties of the shaly layer ($E_{1,shaly}$, $E_{2,shaly}$, $\nu_{1,shaly}$ and $\nu_{2,shaly}$).

The parameters of the sandy layer were back-calculated adopting Equations 5-23 and the information on the shaly layer and the shaly volumetric fraction. Since only S-samples are available for the sandy facies, E_1 and ν_1 are not derived. Therefore, the sandy layer is hypothesised to have an isotropic non-linear response ($E_{1,sandy}= E_{2,sandy}$; $\nu_{1,sandy}= \nu_{2,sandy}$).

Equations 5-22 are applied for each layer, to describe the evolution of Young's modulus with the mean effective stress. The obtained parameters are reported in Table 5-1. Poisson's ratios are assumed as constant and their values are $\nu_{1,shaly}$=0.10, $\nu_{2,shaly}$=0.29, $\nu_{2,sandy}$=0.20.

The evolution of the elastic parameters of the samples given by Equations 5-23 is depicted in Figure 5-7 with the experimentally derived parameters. These calibrated trends match very well the dataset, suggesting that the selected forms for Equations 5-22 and 5-23 can describe the dependency of the elastic parameters on the stress level and the sample composition.

Table 5-1 Parameters for the non-linear evolution of Young's modulus for each layer.

	E_{ref} (GPa)	**n_1 or n_2 (-)**	**p'_{ref} (MPa)**
$E_{1,shaly}$	1.8	0.48	1
$E_{2,shaly}$	1.8	0.35	1
$E_{1,sandy}$, $E_{2,sandy}$	2.4	0.57	1

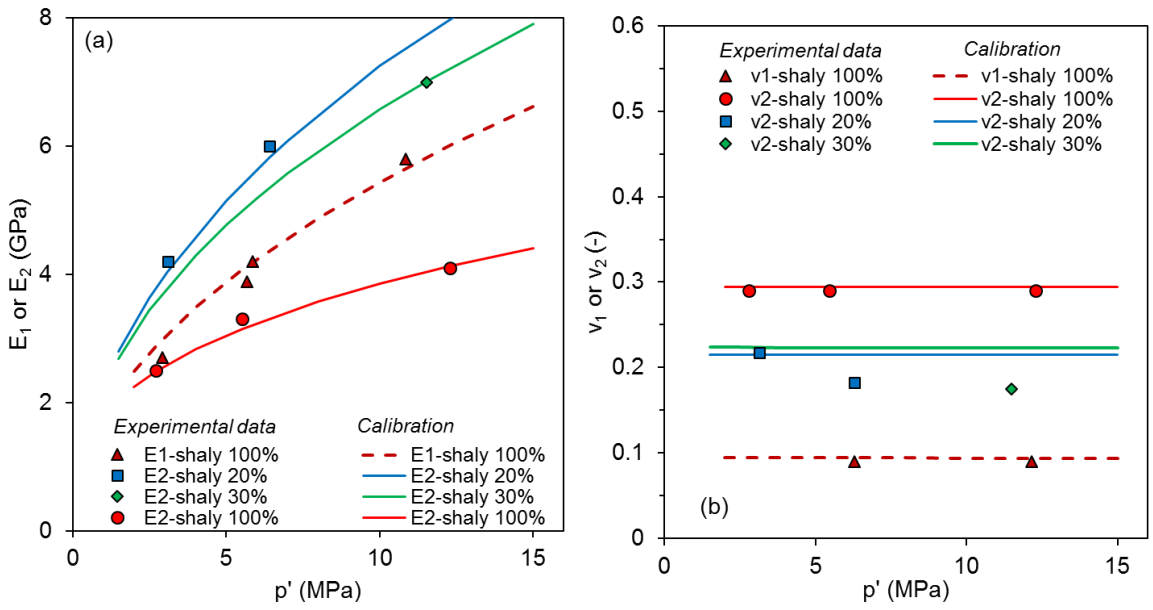

Figure 5-7 Elastic moduli (a) and Poisson's ratio (b) versus mean effective stress calibrated on the drained test results from this study (shaly 20%, shaly 30%) and Favero et al. (2018) (shaly 100%).

5.3.4. Application to the undrained elastic properties

In order to show the applicability of the mentioned procedure, this is tested against experimental data from undrained triaxial tests.

In Figure 5-8, the variation of the elastic moduli E_2 in drained and undrained conditions (for B=1 and B=0.8) with the shaly volumetric fraction is computed applying Equations 5-21 to 5-23, for two mean effective stress levels (p'=8 MPa and $p' = p'_{ref}$ =1 MPa). The plot shows the predicted non-linear response of the elastic modulus with the composition between the two extreme cases: from a 100% to 0% shaly volumetric fraction, the last being equal to a sample of only sandy layers.

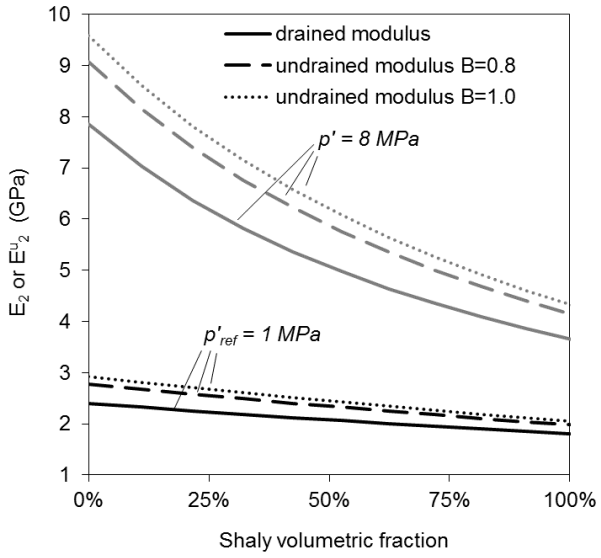

Figure 5-8 Evolution of the drained and undrained elastic moduli as a function of the shaly volumetric fraction, at constant mean effective stress.

A high number of undrained E_2^u values were obtained in Minardi et al. (2019), on S-samples tested in saturated undrained conditions and with known mineralogical composition.

For the drained triaxial tests in Favero et al., 2018 and in this work, distilled and deaerated water was adopted, while in the undrained tests (Minardi et al., 2019), synthetic pore water (Pearson, 2003) was used, to mimic the in situ pore water composition (total concentration of ions about 0.5M). The pore water chemistry is known to have an impact on the clay mineral response, whose extent strictly depends on the clay abundance, composition, and on the ionic concentration of the water. When exposing shales to brines, volumetric deformation occurs and can have a significant impact on the sample structure (e.g., crack formation) with consequent impact on the mechanical properties (Ewy et al., 2008). In the experimental tests considered in this work, swelling was constrained since saturation was conducted in isochoric conditions. An impact of the saturating fluid on the swelling pressure may be expected. Opalinus Clay samples present a low plasticity index (below 20%) generally associated with the sensitivity to chemical loads. The major part of the clay component in Opalinus Clay comprises minerals with low activity, and, as a consequence, a limited impact of water chemical composition on the mechanical response can be envisaged (Di Maio and Fenella, 1994; Mitchell and Soga, 2005). The impact is expected to be limited for samples of Opalinus Clay with low clay content (e.g., sandy facies). Preliminary studies showed no differences in the shear strength of samples of Opalinus Clay saturated with different chemical waters under applied load (Belmokhtar and Delage, 2018). The possible effects of water chemistry are hereafter neglected.

The compositions reported in Minardi et al. (2019) were here converted into shaly volumetric fractions. The drained elastic parameters were estimated using Equation 5-23 and then converted to undrained parameters using the correlations described in Section 5.3.1. The evaluation was performed adopting Bishop and Hight (1977) equations for a B value equal to 0.8, that is considered a reasonable value for Opalinus Clay in the considered effective confining stress range (<15 MPa), considering the results obtained in Chapter 4, and the works of Favero et al. (2018), Giger et al. (2018), Minardi et al. (2019). The dependency of the B value on sample compositions is here neglected, as no specific trend was identified within the mentioned stress range. For Skempton's B value B=0.8, the computed undrained elastic moduli are slightly lower compared to the results of B=1.0, i.e. assuming B=1.0 would overestimate the undrained elastic properties.

Figure 5-9 depicts Young's moduli in undrained conditions derived from the experimental testing, and the computed estimation (solid lines) for various compositions, with respect to the

mean effective stress. The computed values provide a good match with the experimental results. The results are particularly accurate in the high shaly volumetric fraction range, while the procedure tends to slightly overestimate Young's modulus in the low shaly volumetric fraction range.

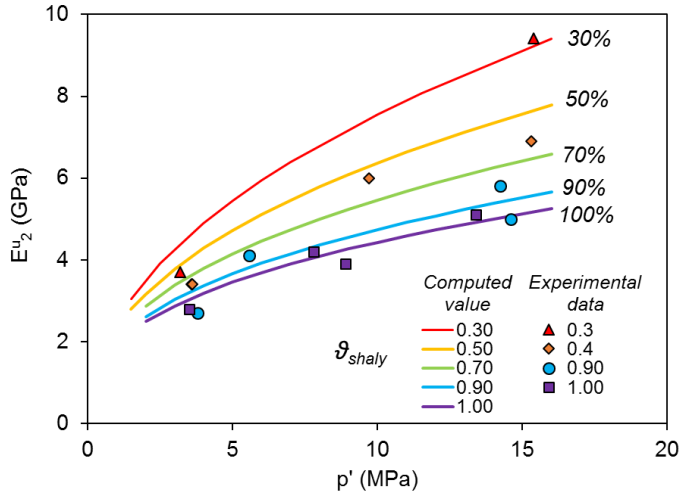

Figure 5-9 Measured versus computed elastic moduli (drained or undrained results), B=0.8.

Overall, considering the layering alternation and taking into account the pore pressure coefficient B, the elastic properties of Opalinus Clay can be estimated based on the sample composition.

5.4. Elastoplastic compressibility

Often in geotechnical practice, correlations between intrinsic properties of the geomaterials and their compressibility in oedometric conditions have been built. In many cases, empirical correlations have been drawn (e.g., Dysli and Steiner, 2011). In the cases of remoulded or soft clay, parameters depending on the Attemberg's limits (i.e., on the clay composition) (Biarez and Favre, 1972; Burland, 1990), and on structural information, as the void ratio or the water content, have been employed with success.

An approach similar to the latter is here adopted. The intact Opalinus Clay response in oedometric conditions is determined adopting an intrinsic parameter, the clay content, here converted into the shaly volumetric fraction, and a structural parameter, being the initial reference porosity for each layer type.

5.4.1. Compressibility of a layered geomaterial in oedometric conditions

Tests in radially prevented strain conditions (i.e. oedometric tests) has been carried out in previous works (Crisci et al., 2019; Ferrari et al., 2016), and allow for extrapolating information on the impact of the layering on the mechanical response. In Crisci et al. (2019), a positive

correlation between the compressibility index and the clay-mineral content was drawn. The results of the elastoplastic compressibility of S-samples (i.e. loaded perpendicular to bedding direction) (Figure 5-10) are here reinterpreted adopting the definition of the shaly and sandy layers proposed in Section 5.2.

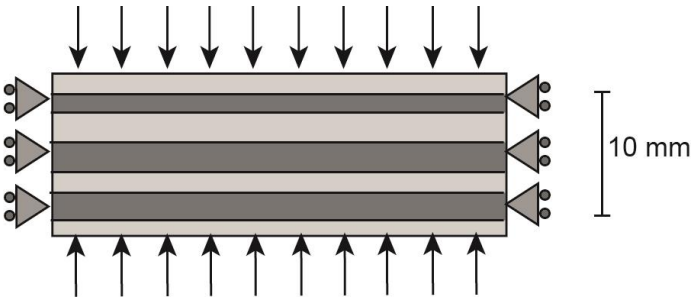

Figure 5-10 Stratified medium in oedometric conditions (lateral strain prevented).

Given the specific boundary conditions, the increment in the deformation of the layered sample, $\delta\varepsilon_{33}$, can be computed as the sum of the displacement that the load-induced in each layer divided by the total height of the sample.

5-24 $$\delta\varepsilon_{33} = \frac{1}{h_t}\sum \frac{\delta\sigma'_{33}}{E_{oed,i}} h_i$$

with $\delta\sigma'_{33}$ is the increment of vertical stress, $E_{oed,i}$ is the oedometric modulus of the i^{th} component in the loading step, h_i is the initial thickness of the layer i, h_t is the initial total height. In the case of the two layer-type samples, the ratio h_i/h_t corresponds to the volumetric fraction of the shaly (or sandy) layers ($\vartheta_{shaly}=h_i/h_t$).

In the post-yield condition, Equation 5-24 can be written in terms of the compressibility index of each layer i ($C_{c,i}$ as represented in Figure 5-11a) by considering the dependency of $E_{oed,i}$ on σ'_{33} (Lambe and Whitman, 1969):

5-25 $$\delta\varepsilon_{33} = \sum_i \frac{\delta \log \sigma'_{33}}{(1+e_{0,i})} \cdot C_{c,i} \cdot \vartheta_i$$

Where $e_{0,i}$ is the initial void ratio of the i layer.

Also, the total axial strain, $\delta\varepsilon_{33}$, can be computed with reference to the entire sample behaviour:

5-26 $$\delta\varepsilon_{33} = \frac{\delta \log \sigma'_{33}}{(1+e_0)} \cdot C_c$$

where e_0 is the void ratio of the entire sample (derived as Equation 5-12) and C_c is the sample compressibility index.

Combining Equation 5-26 and 5-25, one can derive the relation between the compressibility indexes of the sample and those of the layers:

5-27 $$C_c = (1+e_0)\sum_i \frac{C_{c,i}\cdot \vartheta_i}{(1+e_{0,i})}$$

5.4.2. Post-yield behaviour evolution with the composition

To identify the post-yield behaviour of each layer (linear in the semi-logarithmic plane logσ'_{33}-e) two parameters are needed: the layer compressibility ($C_{c,i}$) and a reference void ratio ($e_{1,i}$) defined at the vertical effective stress of 1 MPa, prolonging the post-yield compression line, with slope $C_{c,i}$ (Figure 5-11a).

These layer parameters were calibrated on the results of shaly and sandy samples from the Mont Terri URL (Crisci et al., 2019; Ferrari et al., 2016). In Figure 5-11b two experimental oedometric curves are reported: a sample from the shaly facies of the Mont Terri URL (Ferrari et al., 2016) and a sample from Lausen borehole (Crisci et al., 2019) with similar clay content (≈61% wt.).

As for the drained elastic parameters, the shaly layer parameters correspond to those of a shaly sample. The parameters of the sandy layer were back-calculated adopting Equations 5-27 and the information on the shaly and sandy volumetric fractions, and the results are reported in Table 5-2.

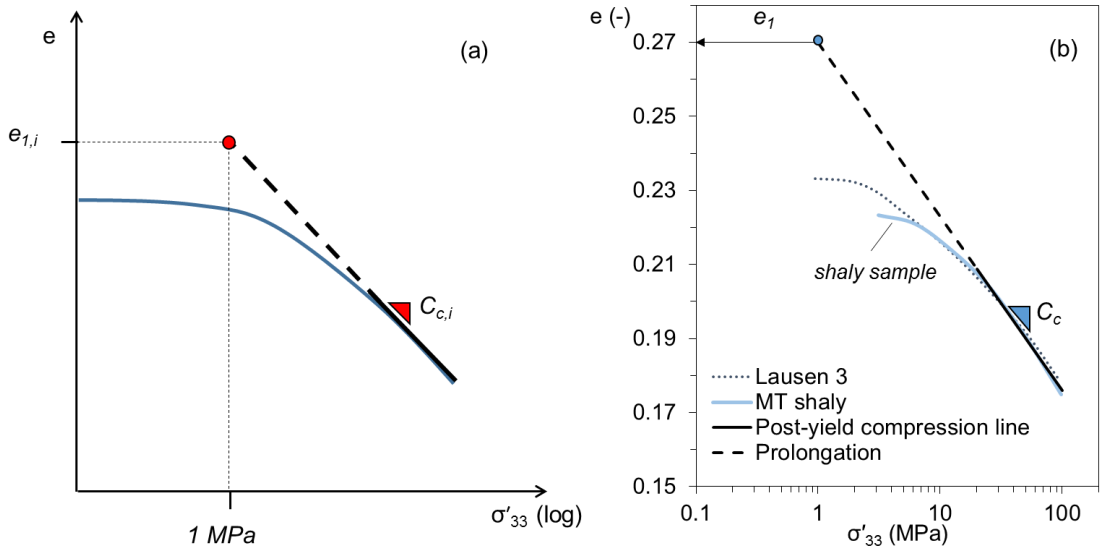

Figure 5-11 (a) Compressibility index and reference initial void ratio for the ith layer; (b) example on a shaly sample (corresponding to the response of a shaly layer), Experimental data from Ferrari et al., 2016 and Crisci et al., 2019.

Table 5-2 Initial void ratio in normally consolidated conditions and compressibility index of a sandy and shaly layer.

	Sandy layer	**Shaly layer**
$e_{0,i}$	0.13	0.27
$C_{c,i}$	0.008	0.047

The compressibilities (C_c) resulting from the combination between shaly and sandy layers are reported in Figure 5-12, that shows the evolution of the oedometric curves with the shaly volumetric fraction. The initial void ratio $e_{0,i}$ of each curve is the weighted average of the sandy and shaly. C_c is calculated as reported in Equation 5-27.

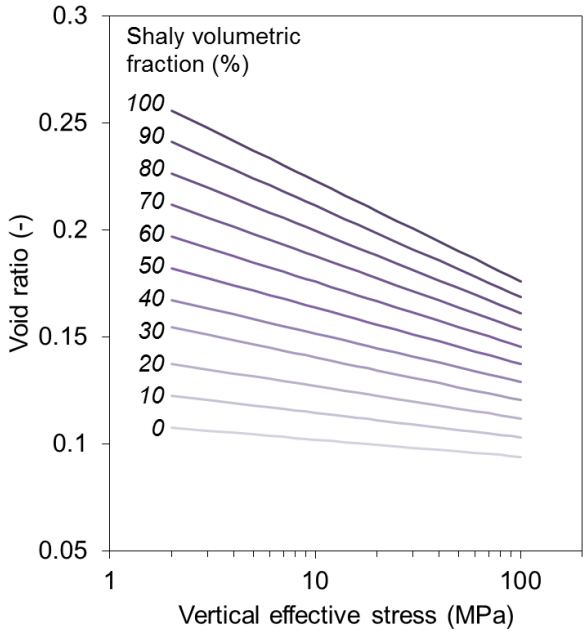

Figure 5-12 Change in the normal compression line (elasto-plastic compressibility) of Opalinus Clay as a function of the shaly volumetric fraction (numbers refer to volumetric percentage).

The comparison between modelled and experimental compressibility index values is reported in Figure 5-13. Compressibility index for several tests on samples coming from three investigation sites are reported: Lausen borehole (Crisci et al., 2019), Schlattingen borehole (SLA) and Mont Terri Rock Laboratory (MT) (Crisci et al., 2019; Ferrari et al., 2016). In the three sites, the Opalinus Clay is found at different depths, and the formation has been subjected to different loading histories. The interpretation of the material behaviour as a layered structure is in agreement with the experimental increase of compressibility with the shaly volumetric fraction increase. The different loading history is likely to be among the causes of the gap between model and experiments. The data on samples from the greater depth (SLA) lies in the lower part of the group of points, and the layered structure model is overestimating the compressibility. However, a limited number of points for each site is available, which may hinder a dependency on the diagenetic processes.

It has to be noted that the approach considers as an extreme, the case in which the material is composed at 100% by shaly layers, that have an average clay content of 67 wt.%. In one case, a sample with even higher clay content (L13, Chapter 3, about 80 wt.%) was found. For these samples, the proposed model would simulate the material as a 120% shaly volumetric fraction, above the maximum possible, although the actual geomaterial may have a different structure compared to the proposed one.

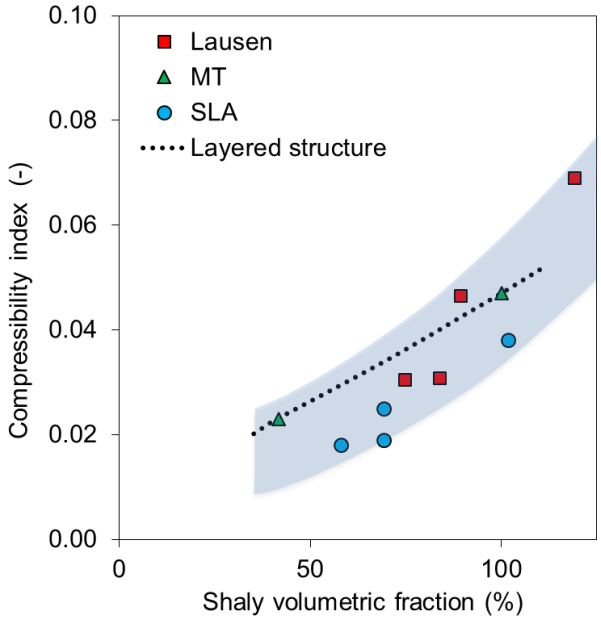

Figure 5-13 Comparison between the estimated Compressibility index Cc for a layered material and the experimental results. Experimental data from Crisci et al. (2019) and Ferrari et al. (2016). The shaded area is meant to help reading the graph.

5.5. Shear strength

The peak and ultimate strength of Opalinus Clay samples tested in saturated triaxial conditions are here analysed. The results from the sandy facies (Chapter 4) and shaly facies (Favero et al., 2018) are compared with the larger dataset of experimental data in Minardi et al. (2019), and the impact of the mineralogy on the shear strength is analysed, assuming the layered composition presented in Section 5.2. Empirical correlations are drawn between the shaly volumetric fraction and the peak and ultimate shear strength.

5.5.1. Strength evolution with the composition

The results obtained from drained (Chapter 4 and Favero et al., 2018) and undrained saturated triaxial tests (Minardi et al., 2019) are summarised in Figure 5-14. All the results refer to S-samples. For some tests, either the peak or the ultimate shear strength was not available (e.g., in multistage tests). Therefore, not all the points in the peak shear strength plot have a corresponding value in the ultimate shear strength plot, and vice-versa.

The clouds of points show an apparent dispersion of the results, that can be explained when grouping the points by the sample composition. The results in the plot are categorised, based on the shaly volumetric fraction. Samples with a similar composition (within ±3%) have been grouped, and the results have been linearly interpolated to obtain the failure criteria corresponding to each composition range, adopting Equation 4-6, here recalled:

5-28 $$q = o + M \cdot p'$$

with $$\sin\varphi' = \frac{3M}{M+6} \quad \text{and} \quad c' = o\frac{\tan\varphi'}{M}$$

where the parameters *o* and *M* are related to the parameters of the Mohr-Coulomb failure criterion, effective cohesion, c', and friction angle, φ'. The evolution of the parameters *o* and *M* is reported in Figure 5-15 versus the shaly volumetric fraction.

Towards lower values of shaly volumetric fraction, the *M* parameter increases. This increase corresponds to an increase of friction angle in the shale as the coarser mineral components increase (Figure 5-15a). A power law interpolation was obtained from the available data (Equation 5-29). The intercept parameter, *o*, has a limited variability. Therefore, it was chosen to adopt a constant value (Figure 5-15b):

5-29 $$M = 5.33 \cdot \vartheta_{shaly}^{-0.39} \quad \text{and} \quad o = 4.65\,\text{MPa}$$

The M values correspond to a φ' ranging between 44° for low shaly volumetric fraction, and 24° for the 100% shaly samples. The *o* corresponds to a c' of 2.2 MPa.

The same type of analysis was performed, considering the ultimate shear strength of all the involved samples:

5-30 $$M = 5.33 \cdot \vartheta_{shaly}^{-0.45} \quad \text{and} \quad o = 2.2\,\text{MPa}$$

That corresponds to φ' between 35° and 17°, and a c' = 1 MPa.

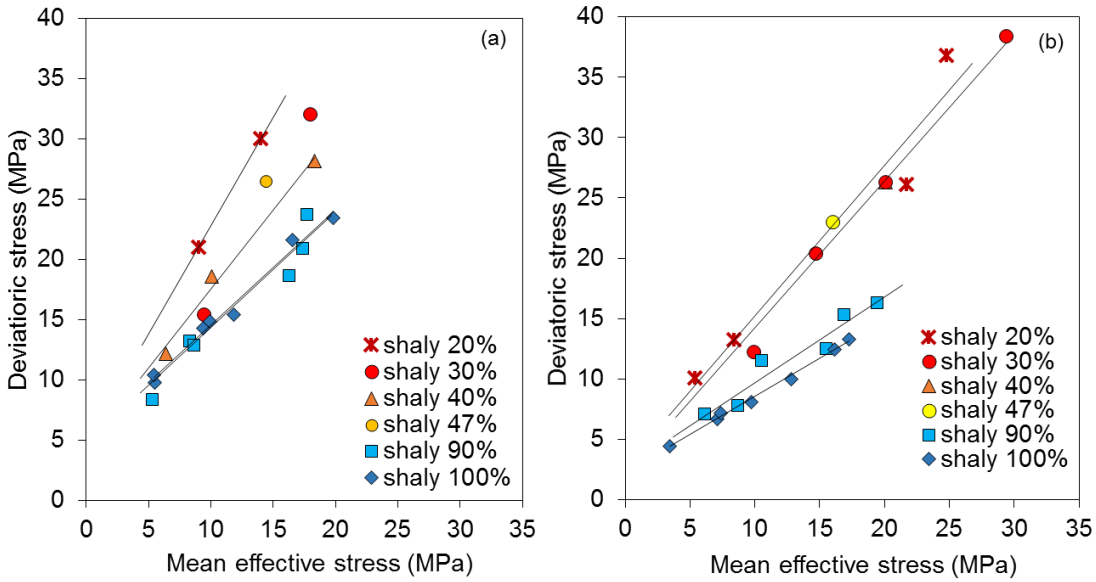

Figure 5-14 Peak (a) and ultimate (b) shear strength for all the analysed tests, grouped by the shaly volumetric fraction.

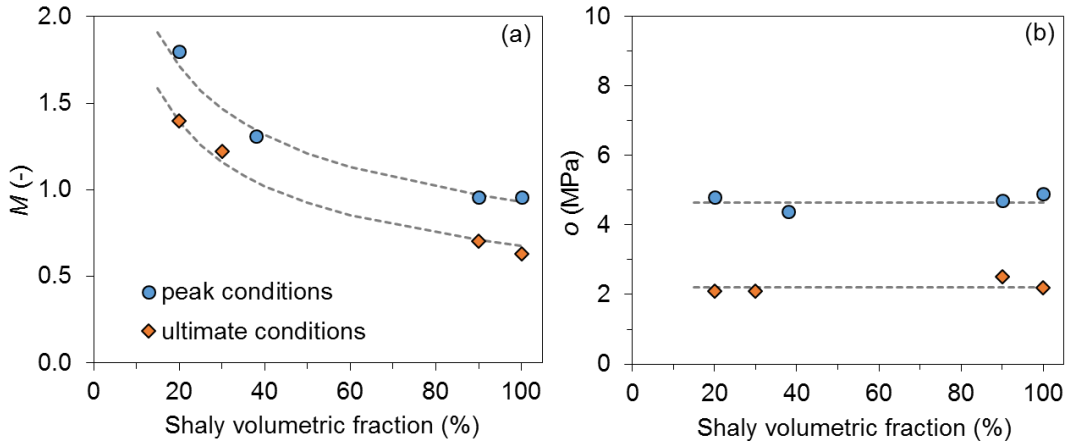

Figure 5-15 Evolution of the parameters (a) M and (b) a with the shaly volumetric fraction, at peak and ultimate shear strength.

The shape of the *M* and *o* functions for the ultimate shear strength are similar to the ones found for the peak shear strength, although shifted towards lower values. A relevant change in the strength occurs in the intercept parameters (here, *o*), that is more than halved compared to the peak condition. This reduction can be attributed to the loss of cementation in the samples after the peak, that reduces the shear strength significantly. The validity of the parameters for the failure criteria refers to the analysed stress range.

Using the power law interpolation of the *M* parameter, peak and ultimate shear strength can be determined, as surfaces in the 3D space: deviatoric stress, mean effective stress and shaly volumetric fraction. As an example, the surface for the peak shear strength is reported in Figure 5-16. Corresponding contour lines are reported in the plane *q*-*p′* in Figure 5-16. The coloured curves are labelled with the corresponding shaly volumetric fraction. The lower the shaly

volumetric fraction, the higher the peak (and ultimate) shear strength, due to the increasing friction angle.

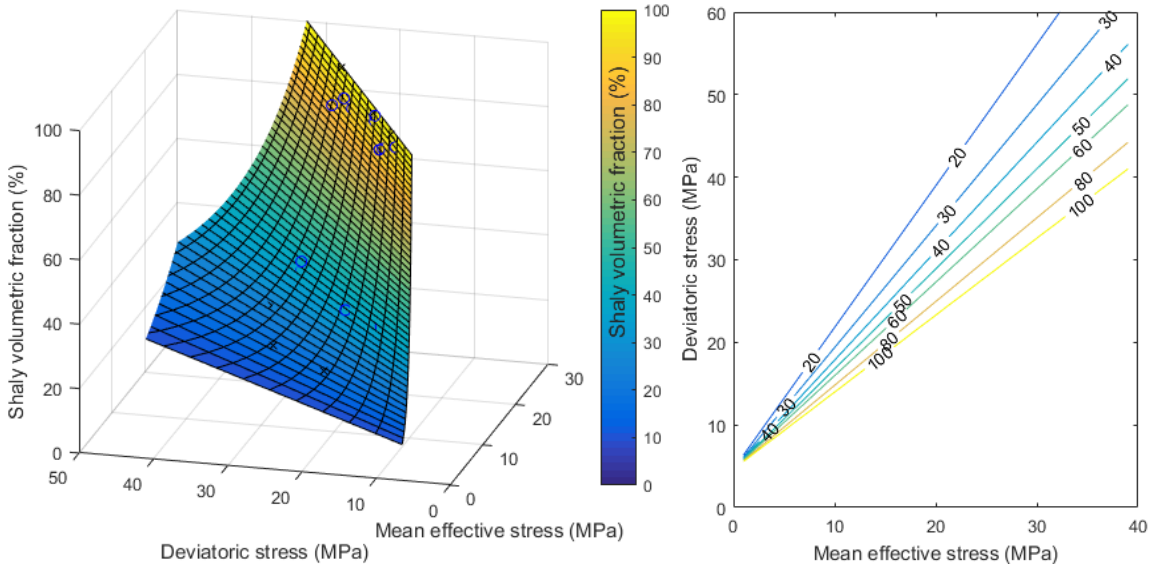

Figure 5-16 (left) peak shear strength surface, in the 3D space: deviatoric stress, mean effective stress, shaly volumetric fraction. Colours represent the shaly volumetric fraction. (right) Peak shear strength, contour plot. Labels on the lines refer to the shaly volumetric fraction (%).

The accuracy of the developed correlations is hereafter evaluated. The calculated peak shear strength is plotted versus the measured value in Figure 5-17. The results from the Minardi et al. (2019) are reported with blue circles and the results from this study (Chapter 4) and (Favero et al., 2018), in drained conditions, are reported with black cross markers. The correspondence is considered good, and the error is limited to approximately ± 10%.

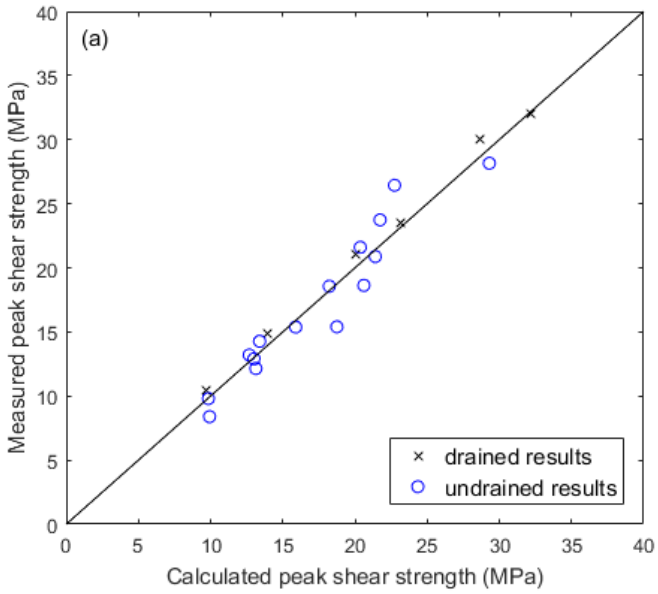

Figure 5-17 Comparison between the measured and the computed peak shear strength. The blue circles refer to the undrained results; the black crosses refer to the drained results (i.e. this study and Favero et al. (2018)).

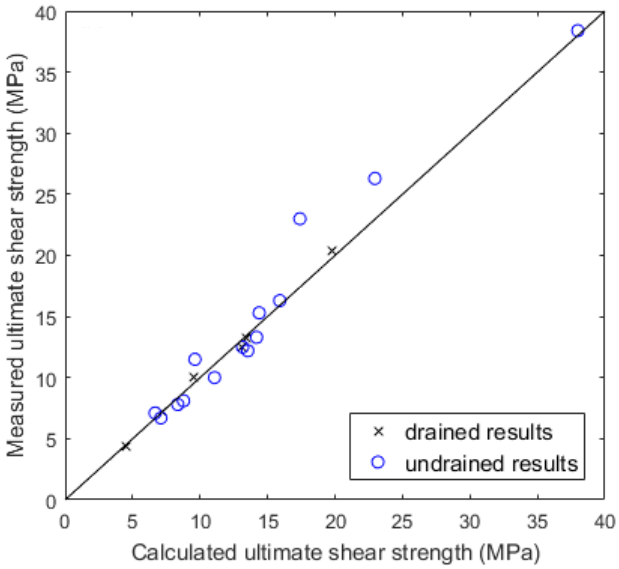

Figure 5-18 Comparison between the measured and the computed ultimate shear strength. The blue circles refer to the undrained results; the black crosses refer to the drained results (i.e. this study and Favero et al. (2018)).

The results of the interpretation of the ultimate shear strength are reported in Figure 5-18. In this case as well, the interpolating surface led to a reasonable estimation of the strength, with an error limited to very few cases.

The correlation between the shaly volumetric fraction and the shear strength led to satisfactory results in the whole analysed range of composition, across a broad spectrum of analysed stresses.

With a good approximation, it is possible to estimate the shear strength of the formation (peak and ultimate), with the only information on the amount of clay (i.e. shaly volumetric fraction) in the sample.

5.6. Conclusion

The Opalinus Clay shale microstructure and composition has been described in several studies. A significant amount of experimental data on samples in accurately saturated conditions are nowadays available. The controlled testing conditions allow to compare the results of the tests and attribute the difference among the tested samples to the sample composition. Usually, the shale formation is divided into lithofacies. Nonetheless, within the same facies, high heterogeneity can be identified. Therefore the testing results may lead to an incorrect parameter attribution to the lithofacies in its totality, while they may represent only part of it.

In this Chapter, the extensive information on the sample structure and composition was interpreted, and a layered structure of the shale was proposed. The shale was defined as characterised by shaly-type and sandy-type of layers with given composition, porosity and

hydro-mechanical parameters. The first layer type is composed by a clay matrix in which grains of quartz, calcite or other minerals are embedded. The latter is composed by a compact quartz structure, whose pores are filled with clay. Based on this structure, the information on the mineralogical composition was used to determine the shaly volumetric fraction.

Experimental results in triaxial and oedometric conditions were analysed to determine the dependency of the hydro-mechanical parameters on the shaly volumetric fraction. It was highlighted that the higher the shaly fraction, the lower the rigidity, the peak and ultimate shear strength and the higher the sample compressibility are.

The elastic properties for the transversely isotropic material were determined adopting an analytical solution for the layered materials. The stress dependence of the elastic parameters was evaluated, and the values were calibrated on results obtained in triaxial drained conditions. Then the undrained elastic parameters were computed and compared to experimental results. It was highlighted that a good correspondence is found between computed parameters and experimental values when adopting a Skempton B coefficient of 0.8.

The elastoplastic compressibility of Opalinus Clay samples in oedometric condition has been interpreted as a layering structure as well, attributing compressibility and porosity values to each layer type. The combination of layers was analytically solved and compared to the experimental results. The correlation well adapts to the shallow Opalinus Clay samples, while for the ones sourced from a greater depth, the correlation tends to overestimate the compressibility.

Peak and ultimate shear strength of a large number of tests, obtained both in drained or undrained shearing conditions, have been subdivided into categories based on the shaly volumetric fraction and for each group, the parameters for the Mohr-Coulomb failure criteria have been determined with a good approximation to the experimental results. It was highlighted that the friction angle decreases, with a power law, as the shaly volumetric fraction increase, while the cohesion stays approximately constant among the various compositions. On the other hand, the cohesion halved in the ultimate state.

Most of the scatter in the experimental results on the hydro-mechanical parameters of Opalinus Clay can be explained when analysing the sample composition, especially for samples belonging to the sandy facies. The layered structure appears to be a good approximation of the shale response at the laboratory scale. The approach may be extended by combining the

analytical and empirical correlations to information on the shale composition at a larger scale, inferred, for instance, from log data or core scans.

5.7. References

Adhikary, D.P., Dyskin, A.V., 2007. Modelling of Progressive and Instantaneous Failures of Foliated Rock Slopes. Rock Mech. Rock Eng. Wien 40, 349–362. http://dx.doi.org/10.1007/s00603-006-0085-8

Adhikary, D.P., Dyskin, A.V., 1997. A Cosserat continuum model for layered materials. Comput. Geotech. 20, 15–45.

Amann, F., Button, E.A., Evans, K.F., Gischig, V.S., Blümel, M., 2011. Experimental Study of the Brittle Behavior of Clay shale in Rapid Unconfined Compression. Rock Mech. Rock Eng. 44, 415–430. https://doi.org/10.1007/s00603-011-0156-3

Barden, L., 1963. Stresses and Displacements in a Cross-Anisotropic Soil. Géotechnique 13, 198–210. https://doi.org/10.1680/geot.1963.13.3.198

Belmokhtar, M., Delage, P., 2018. Drained triaxial compression tests and hydromechanical characterization of Opalinus Clay core from the Lausen borehole (No. Arbeitsbericht NAB 17-33). Nagra.

Biarez, J., Favre, J.L., 1972. Table ronde sur les corrélations des paramètres en mécanique des sols. Ecole Cent. Paris.

Bishop, A.W., Hight, D.W., 1977. The value of Poisson's ratio in saturated soils and rocks stressed under undrained conditions. Géotechnique 27, 369–384. https://doi.org/10.1680/geot.1977.27.3.369

Bossart, P., Thury, M., 2008. Mont Terri rock Laboratory. Project, Programme 1996 to 2007 and results.

Burland, J.B., 1990. On the compressibility and shear strength of natural clays. Géotechnique 40, 329–378.

Chou, P.C., Carleone, J., Hsu, C.M., 1972. Elastic constants of layered media. J. Compos. Mater. 6, 80–93.

Crisci, E., Ferrari, A., Giger, S.B., Laloui, L., 2019. Hydro-mechanical behaviour of shallow Opalinus Clay shale. Eng. Geol. 251, 214–227. https://doi.org/10.1016/j.enggeo.2019.01.016

David, E.C., Brantut, N., Schubnel, A., Zimmerman, R.W., 2012. Sliding crack model for nonlinearity and hysteresis in the uniaxial stress–strain curve of rock. Int. J. Rock Mech. Min. Sci. 52, 9–17. https://doi.org/10.1016/j.ijrmms.2012.02.001

Di Maio, C.D., Fenelli, G.B., 1994. Residual strength of kaolin and bentonite: the influence of their constituent pore fluid. Géotechnique 44, 217–226. https://doi.org/10.1680/geot.1994.44.2.217

Dysli, M., Steiner, W., 2011. Correlations in soil mechanic, Génie Civil. PPUR Presses polytechniques.

Ewy, R.T., Bovberg, C.A., Stankovich, R.J., 2008. Shale Triaxial Strength Alteration due to Brine Exposure, in: ARMA-08-304. Presented at the The 42nd U.S. Rock Mechanics Symposium (USRMS), American Rock Mechanics Association, ARMA.

Favero, V., Ferrari, A., Laloui, L., 2018. Anisotropic Behaviour of Opalinus Clay Through Consolidated and Drained Triaxial Testing in Saturated Conditions. Rock Mech. Rock Eng. 51, 1305–1319. https://doi.org/10.1007/s00603-017-1398-5

Ferrari, A., Favero, V., Laloui, L., 2016. One-dimensional compression and consolidation of shales. Int. J. Rock Mech. Min. Sci. 88, 286–300. https://doi.org/10.1016/j.ijrmms.2016.07.030

Gautschi, A., 2017. Safety-relevant hydrogeological properties of the claystone barrier of a Swiss radioactive waste repository: An evaluation using multiple lines of evidence. Grundwasser 22, 221–233. https://doi.org/10.1007/s00767-017-0364-1

Gerrard, C.M., 1982. Equivalent elastic moduli of a rock mass consisting of orthorhombic layers. Int. J. Rock Mech. Min. Sci. Geomech. Abstr. 19, 9–14. https://doi.org/10.1016/0148-9062(82)90705-7

Giger, S.B., Ewy, R.T., Favero, V., Stankovic, R., Keller, L.M., 2018. Consolidated-undrained triaxial testing of Opalinus Clay: Results and method validation. Geomech. Energy Environ. 14, 16–28. https://doi.org/10.1016/j.gete.2018.01.003

Gräsle, W., Plischke, I., 2011. LT-A Experiment: Mechanical Behavior of Opalinus Clay, Data report from Phase 15 (No. Mont Terri Project, Technical Note 2010-86). BGR, Germany.

Gräsle, W., Plischke, I., 2010. LT Experiment: Mechanical Behavior of Opalinus Clay, Final report from Phases 6 – 14 (No. Mont Terri Project, Technical Report 2009-07). BGR, Germany.

Houben, M.E., Desbois, G., Urai, J.L., 2014. A comparative study of representative 2D microstructures in Shaly and Sandy facies of Opalinus Clay (Mont Terri, Switzerland) inferred form BIB-SEM and MIP methods. Mar. Pet. Geol. 49, 143–161. https://doi.org/10.1016/j.marpetgeo.2013.10.009

Hu, D.W., Zhang, F., Shao, J.F., Gatmiri, B., 2013. Influences of Mineralogy and Water Content on the Mechanical Properties of Argillite. Rock Mech. Rock Eng. 47, 157–166. https://doi.org/10.1007/s00603-013-0413-8

Kaufhold, A., Gräsle, W., Plischke, I., Dohrmann, R., Siegesmund, S., 2013. Influence of carbonate content and micro fabrics on the failure strength of the sandy facies of the Opalinus Clay from Mont Terri (Underground Rock Laboratory). Eng. Geol. 156, 111–118. https://doi.org/10.1016/j.enggeo.2013.01.014

Keller, L.M., Giger, S.B., 2019. Petrophysical Properties of Opalinus Clay Drill Cores Determined from Med-XCT Images. Geotech. Geol. Eng. https://doi.org/10.1007/s10706-019-00815-2

Kim, K.Y., Zhuang, L., Yang, H., Kim, H., Min, K.-B., 2016. Strength Anisotropy of Berea Sandstone: Results of X-Ray Computed Tomography, Compression Tests, and Discrete Modeling. Rock Mech. Rock Eng. 49, 1201–1210. https://doi.org/10.1007/s00603-015-0820-0

Lauper, B., Jaeggi, D., Deplazes, G., Foubert, A., 2018. Multi-proxy facies analysis of the Opalinus Clay and depositional implications (Mont Terri rock laboratory, Switzerland). Swiss J. Geosci. https://doi.org/10.1007/s00015-018-0303-x

Lings, M.L., 2001. Drained and undrained anisotropic elastic stiffness parameters. Geotechnique 51, 555–565.

Lisjak, A., Tatone, B.S.A., Grasselli, G., Vietor, T., 2014. Numerical Modelling of the Anisotropic Mechanical Behaviour of Opalinus Clay at the Laboratory-Scale Using FEM/DEM. Rock Mech. Rock Eng. 47, 187–206. https://doi.org/10.1007/s00603-012-0354-7

Mazurek, M., Wersin, P., Hadi, J., 2017. Opalinus Clay in the shallow decompaction zone: Geochemical investigations on drill core samples from borehole Lausen KB (No. NAB 16-58).

Minardi, A., Crisci, E., Ferrari, A., Laloui, L., 2016. Anisotropic volumetric behaviour of Opalinus clay shale upon suction variation. Géotechnique Lett. 6, 144–148. https://doi.org/10.1680/jgele.16.00023

Minardi, A., Ferrari, A., Ewy, R., Laloui, L., 2018. Nonlinear Elastic Response of Partially Saturated Gas Shales in Uniaxial Compression. Rock Mech. Rock Eng. 51, 1967–1978. https://doi.org/10.1007/s00603-018-1453-x

Minardi, A., Ferrari, A., Laloui, L., 2019. Benchmark study on triaxial testing of Opalinus Clay: analysis and comparative evaluation of tests results. Swiss Federal Institute of Technology, EPFL.

Mitchell, J.K., Soga, K., 2005. Fundamentals of soil behavior., John Wiley & Sons Ltd. ed.

Nagra, 2002. Projekt Opalinuston Synthese der geowissenscha. Technischer Bericht 02-03.

Pearson, F.J., 2003. Mont Terri project: geochemistry of water in the Opalinus Clay Formation at the Mont Terry rock laboratory. Bundesamt für Wasser und Geologie, BWG, Bern-Ittigen.

Peters, M., Mazurek, M., Jaeggi, D., Müller, H., R., 2011. WS-H Experiment: Heterogeneities in the sandy facies of Opalinus Clay on a scale of millimeters to centimetres (Mont Terri Technical Note No. TN 2010-76). University of Bern.

Philipp, T., Amann-Hildenbrand, A., Laurich, B., Desbois, G., Littke, R., Urai, J.L., 2017a. The effect of microstructural heterogeneity on pore size distribution and permeability in Opalinus Clay (Mont Terri, Switzerland): insights from an integrated study of laboratory fluid flow and pore morphology from BIB-SEM images. Geol. Soc. Lond. Spec. Publ. 454, 85–106. https://doi.org/10.1144/SP454.3

Pickering, D.J., 1970. Anisotropic Elastic Parameters for Soil. Géotechnique 20, 271–276. https://doi.org/10.1680/geot.1970.20.3.271

Salager, S., François, B., Nuth, M., Laloui, L., 2013. Constitutive analysis of the mechanical anisotropy of Opalinus Clay. Acta Geotech. 8, 137–154. https://doi.org/10.1007/s11440-012-0187-2

Salamon, M.D.G., 1968. Elastic moduli of a stratified rock mass. Int. J. Rock Mech. Min. Sci. Geomech. Abstr. 5, 519–527. https://doi.org/10.1016/0148-9062(68)90039-9

Seiphoori, A., Whittle, AndrewJ., Krakowiak, KonradJ., Einstein, HerbertH., 2017. Insights Into Diagenesis and Pore Structure of Opalinus Shale Through Comparative Studies of Natural and Reconstituted Materials. Clays Clay Miner. 65, 135–153. https://doi.org/10.1346/CCMN.2017.064055

Talesnick, M.L., Katz, A., Ringel, M., 2000. An Investigation of the Elastic Stress-Strain Behavior of a Banded Sandstone and a Sandstone-Like Material. Geotech. Test. J. 23, 257–273. https://doi.org/10.1520/GTJ11050J

Wittke, W., 1984. Felsmechanik. Springer-Verlag.

Zimmerman, R.W., 1985. The effect of microcracks on the elastic moduli of brittle materials. J. Mater. Sci. Lett. 4, 1457–1460. https://doi.org/10.1007/BF00721363

Chapter 6

Volumetric behaviour upon suction variation of Opalinus Clay from various sites

6. Volumetric behaviour upon suction variation of Opalinus Clay from various sites

The methodology and the results on the Mont Terri samples (sections 6.2.1, 6.3, 6.4.1) presented in this chapter were published in:

Journal paper: *Minardi, A., Crisci, E., Ferrari, A., Laloui, L., 2016. Anisotropic volumetric behaviour of Opalinus clay shale upon suction variation. Géotechnique Letters 6, 144–148. https://doi.org/10.1680/jgele.16.00023.*

Conference paper: *Minardi, A., Crisci, E., Ferrari, A., Laloui, L., 2017. The Role of Anisotropy on the Volumetric Behaviour of Opalinus Clay upon Suction Change, in: Ferrari, A., Laloui, L. (Eds.), Advances in Laboratory Testing and Modelling of Soils and Shales (ATMSS), Springer Series in Geomechanics and Geoengineering. Springer International Publishing, pp. 315–321. https://doi.org/10.1007/978-3-319-52773-4_36*

The post-print version of the journal paper has been used to draft the chapter.

Contribution of the Candidate: performance of the experimental testing, analysis of the results, writing of the manuscript.

The results on the Lausen samples (Section 6.4.2), the discussion on the impact of the mineralogy on the volumetric response, and the swelling and shrinkage induced investigation (Sections 6.5 and 6.6) are intended to be submitted as a journal paper:

Journal paper: "*Crisci, E., Ferrari, A., Laloui, L., Macro and microstructural analysis of shales upon wetting and drying."*

The pre-print version of the journal paper has been used to draft the chapter.

Contribution of the Candidate: design and performance of the experimental testing, analysis of the results, writing of the manuscript.

6.1. Introduction

Opalinus Clay shale (OPA) is under consideration to serve as the host geomaterial for the underground storage of high-level nuclear wastes in Switzerland. Proper knowledge of its geomechanical behaviour is thus a basic requirement for safe and reliable disposal. Among the several aspects of Opalinus Clay shale that have been investigated, its anisotropic fabric and water retention properties have been identified to play a significant role over the lifespan of the repository, during which the shale formation is subjected to a sequence of hydro-mechanical loadings.

The anisotropic response to the mechanical loading of shales has been observed and analysed in several studies (e.g., Delle Piane et al., 2011; McLamore and Gray, 1967; Niandou et al., 1997), particularly on Opalinus Clay shale (e.g., Popp et al., 2008; Salager et al., 2013); for example, this aspect must be considered to appropriately predict the development and extent of the excavation damage zone around the tunnel (Popp et al., 2008). However, due to the significant amount of clay particles in the grain size distribution and pores of nanometric dimensions (Ferrari and Laloui, 2013), Opalinus Clay shale has important water retention properties (Ferrari et al., 2014), and its volumetric response has also been found to be sensitive to suction variations: indeed, significant void ratio variations due to shrinkage (Soe et al., 2009) and swelling are observed when this geomaterial is subjected to drying and wetting cycles, respectively.

The simultaneous analysis of these aspects may have a significant impact on the prediction of the behaviour of Opalinus Clay shale during the tunnel excavation, ventilation and resaturation phases of the repository. For instance, under confined conditions, the anisotropic volumetric behaviour upon suction reduction may induce different swelling stresses in the directions parallel and perpendicular to the bedding.

In this framework, a few studies have provided analyses of the anisotropic response of different hydric states of clayey geomaterials (e.g., Valès et al., 2004 on Tournemire shale, Pham et al., 2007 on Bure mudstone), but without focusing on its coupling with the water retention properties. In some works, the micro and nanostructural evolutions in clayey geomaterials subjected to saturation changes was investigated (Wang et al., 2014; Stavropoulou et al., 2019). These aspects have not yet been investigated for Opalinus Clay shale.

In the first part of this chapter a detailed analysis of the suction effects on the anisotropic volumetric behaviour of specimens of Opalinus Clay shale, from both Mont Terri, Section 6.4.1

and Lausen site, Section 6.4.2, is presented. An advanced experimental methodology is used for this purpose. The laboratory test results demonstrate the anisotropic response of the materials upon suction variation, the impact of the water content evolution on the volumetric response, and the different behaviour among specimens with different compositions.

In the second part (Section 6.6) of this Chapter, an insight into the microscopic mechanisms that affect the shale response when subjected to suction loading is provided. An Opalinus Clay specimen is subjected to the wetting-drying cycle, and at selected steps, X-ray micro-tomography scans are performed. The experiment allows combining the macroscopic deformation and water content changes during the suction variation, with the microstructural modification, adopting a non-destructive technique. The results show that, during both drying and wetting, fissures open inside the specimen: during drying most of the fissures form in the direction of the bedding plane; those fissures close during wetting, and new fissures open at the contact between different components, in particular between the clay matrix and the more rigid inclusions.

The results highlight the impact of the suction variation on shales response and on their integrity. Such effects need to be taken into account at the laboratory scale while handling samples to be tested, in order to guarantee their integrity, and in practical applications, as desaturation and resaturation may contribute to the crack opening and propagation in the formation.

6.2. Tested shales

The core samples used in this study were collected from the Mont Terri Underground Laboratory (URL) and the Lausen borehole. Core characterisations were presented and discussed in Chapter 2. Hereafter the properties of the specimens at the end of the preparation phase are reported. During preparation specimens tended to dry out. For all the specimens, the initial total suction was determined by the use of a dew-point chilled mirror psychrometer (WP4C, e.g., Leong et al., 20-03; Cardoso et al., 2007) on a fragment of shale cut from the same slice used to prepare the specimen (having height minor than 1 cm, to fit into the device). The WP4C measures the water potential by determining the relative humidity of the air above a sample in a closed chamber. At temperature equilibrium, relative humidity is a direct measurement of water potential. The device operates in the range of suction 0-300 MPa, with an accuracy of ±0.05 MPa from 0 to 5 MPa and of 1% from 5 to 300 MPa.

6.2.1 Mont Terri tested samples

Two different facies of the Opalinus Clay shale were tested: the shaly facies and the sandy facies. The shaly core sample was cored in the FE gallery at the tunnel wall. The sandy core sample was cored in the niche TT (core BHA).

Table 6-1 reports the sourcing facies and core of each sample, the geotechnical properties of the specimens measured after preparation: initial water content w_0, initial void ratio e, porosity n, degree of saturation S_r, initial total suction Ψ_0.

Table 6-1 Initial conditions of Mont Terri tested samples.

Facies	Core	w_0	e	n	S_r	Ψ_0 (at 25°C)
		(%)	(-)	(-)	(%)	(MPa)
Sandy	BHA	2.4	0.163	0.140	43	74.8
Shaly	FE	3.1	0.234	0.190	37	96.0

6.2.2 Lausen tested samples

The water retention behaviour of the specimens obtained from the cores L2, L3, L8, L11 and L13 of Lausen borehole was studied. Table 6-2 reports the geotechnical properties of the specimens from Lausen borehole used in the experimental programme. The table includes the core code, the sampling depth, the initial water content w_0, the initial void ratio e, porosity n, degree of saturation S_r, initial total suction Ψ_0.

Table 6-2 Initial conditions of Lausen tested samples.

Core	Depth	w_0	e	n	S_r	Ψ_0 (at 25°C)
	(m)	(%)	(-)	(-)	(%)	(MPa)
L2	18.20	5.5	0.226	0.184	65	43.1
L3	22.57	6.0	0.217	0.178	67	18.9
L8	38.12	4.2	0.177	0.150	64	22.9
L11	61.71	2.8	0.201	0.167	41	61.0
L13	70.37	5.3	0.221	0.181	64	43.4

For the microstructural investigation, a Lausen specimen was selected. The initial characteristics of the specimen are presented in Table 6-3.

Table 6-3 Initial conditions for the microstructural investigation specimen.

Core	Depth	w_0	e	n	S_r	Ψ_0 (at 25°C)
	(m)	(%)	(-)	(-)	(%)	(MPa)
L8	38.1	2.0	0.147	0.130	37	110

6.3. Experimental methodology for the volumetric response of Opalinus Clay subjected to suction changes

To analyse the anisotropic behaviour of the tested shales upon suction changes, an advanced testing methodology was developed that combines total suction control with an accurate assessment of the deformations in two orthogonal directions.

The vapour equilibrium technique was used for the application of wetting/drying processes and the consequent definition of water retention behaviour. The technique allows for the control of the relative humidity inside a closed desiccator with saturated saline solutions. Within a closed environment, each saturated saline solution induces a known value of relative humidity.

Considering the psychrometric law (Fredlund and Rahardjo, 1993), relative humidity can be converted to total suction. By using several types of salt, different total suction values can be imposed inside the desiccator. Table 6-4 summarises the salts used for the investigation and the corresponding reference values of relative humidity and total suction at 25°C, as measured using the dew-point chilled mirror psychrometer (WP4C). Tests were performed at a reference temperature of 25°C; the unwanted temperature fluctuation during the entire test period was in the range of ± 1°C; the consequent variations of total suction were within 2% of the target values and could be considered to be negligible compared with the whole range of total suction values applied during the wetting/drying cycle.

In order to assess the anisotropic volumetric response upon suction variations, the specimen deformations were measured in directions perpendicular and parallel to the bedding. The tested specimens were equipped with two biaxial temperature-compensated strain gauges (with a resistance of 120 Ohm, gauge factor of 2.03±1%, max. excitation voltage of 5 V), two perpendicular and two parallel to the bedding, that provide strain measurement with microstrain accuracy.

Cylindrical specimens were used (diameter of 25 mm and height of 20 mm), with bedding perpendicular to the axis of the cylinder (Figure 6-1a). For each core, two specimens were placed inside the desiccator (Figure 6-1b). One specimen was equipped with strain gauges; the second specimen was used to monitor the mass variation during each step of total suction in order to assess the water content changes.

In order to comprehensively analyse the coupling between the water retention and volumetric behaviour, wetting/drying cycles were performed.

The initial specimen suction was evaluated after the preparation, right before starting the test, using the WP4C on a fragment of shale cut from the same slice used to prepare the specimen. The first suction value to apply through the vapour transfer technique was chosen to be close to the initial suction of the specimens.

At each suction step, the achievement of the equilibrium condition was assessed by checking the stabilisation of both the strains and the mass of the specimen without the strain gauges (accepted mass variation in 24h lower than ±0.007 g corresponding to a water content change of ±0.03-0.04%).

After the equalisation was achieved, the specimens were moved in a few seconds into a new desiccator prepared with the saline solution corresponding to the next total suction value to be imposed. At the end of the cycle, the specimen for water content determination was dried in an oven at 105°C until a constant mass was reached. This allowed for the back-calculation of the water content evolution throughout all the steps, including also its variation during the preparation of the specimens.

Table 6-4 Salts used for the preparation of the saturated saline solutions and corresponding values of total suction and relative humidity at 25.0 °C.

Salt	**LiCl**	**$MgCl_2$**	**K_2CO_3**	**$Mg(NO_3)_2$**	**NaCl**	**KCl**	**KNO_3**	**K_2SO_4**	**Distilled water**
Total suction (MPa)	300.0	139.0	112.6	86.0	39.0	23.0	9.8	3.8	≈0
Relative humidity (%)	11	36	44	53	75	85	93	97	100

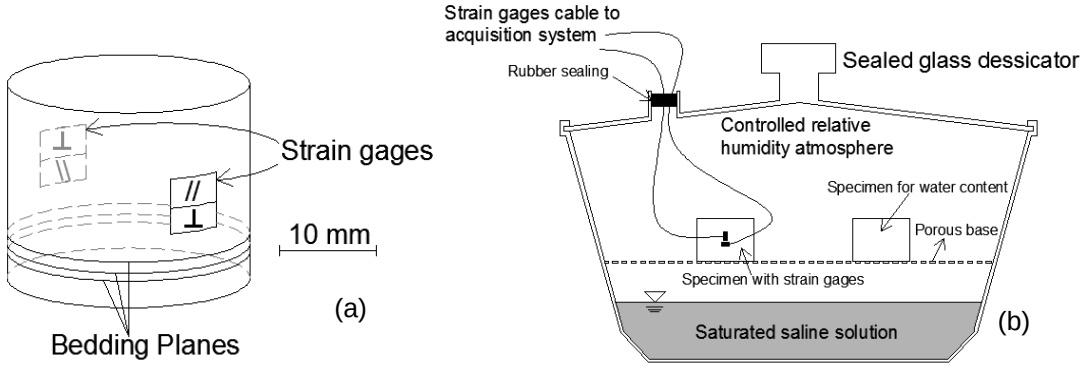

Figure 6-1 Experimental setup: (a) strain gage configuration: "⊥" in the direction perpendicular to the bedding, "//" in the direction parallel to the bedding; (b) glass desiccator for total suction application (Minardi et al., 2016).

6.4. Test results

In this section, the test results for the specimens from Mont Terri and Lausen are reported, in terms of water content and strains evolutions. The average values of the strains perpendicular

and parallel to the bedding measured during each suction step are reported; the homologous strain gauges showed consistent measurements with average differences equal to 0.05% and 0.01% for the perpendicular and parallel directions, respectively. Six to fourteen days were required to reach the water content and strain stabilisation at each suction step.

6.4.1. Mont Terri test results

Figure 6-2 and Figure 6-4 show the results of the tests on the shaly and the sandy specimens, respectively, in terms of the water content and strain evolution. The two materials showed different initial values of total suction, 96.0 MPa and 74.8 MPa, for the shaly and sandy specimens, respectively. These initial total suction values are the consequence of the ventilation of the tunnel, the unloading associated with the extraction of the cores but also of some drying occurred during the preparation of the specimens and the installation of the strain gauges. Hence, the initial equalisation to 86 MPa resulted in wetting for the shaly specimen and in drying for the sandy specimen. The strain and water content variation due to this first equalisation are small compared with the overall response of the materials in the whole wetting/drying cycle. For both specimens, sandy and shaly, first, a wetting path was performed in steps until a suction of 9.8 MPa. Subsequently, drying was performed in steps until reaching a suction of 139 MPa.

The swelling/shrinkage response is evident for the two facies in both directions perpendicular and parallel to the bedding (Figure 6-3 and Figure 6-5). The response of both specimens upon hydraulic loading is remarkably anisotropic, with the amount of strain parallel to the bedding significantly lower than that in the perpendicular direction. In particular, this dependency on the bedding orientation is more significant for the sandy facies; at the end of the wetting path, the ratio between the deformations perpendicular and parallel to the bedding is 2.7 and 4 for the shaly and sandy specimens, respectively.

Figure 6-3b and Figure 6-5b illustrate the evolution of water content with total suction, highlighting the different water retention capacities of the two facies. During the wetting path, the shaly specimen has a higher water uptake than the sandy specimen. In the wetting/drying cycle, a hysteresis of the water retention curves is observed. The typical hydration mechanisms of clayey geomaterials are considered to be involved during the wetting path, with a progressive transition from an adsorption-based mechanism to a capillary-dominated mechanism as total suction decreases.

Figure 6-3a and Figure 6-5a depict the strain (volumetric ε^{vol}, perpendicular $\varepsilon^{\perp}$ and parallel $\varepsilon^{//}$ to the bedding) evolution with the total suction for both facies. A nonlinear response is observed upon suction change. This aspect is strictly related to the evolution of the water content (Figure 6-3b and Figure 6-5b), which is sharper for suction values less than 40 MPa. This coupling demonstrates the impact of the volumetric response on the water retention behaviour of the tested shales and the importance of analysing these two aspects simultaneously.

Considering the overall volumetric behaviour of the two facies, the swelling deformation of the shaly specimen is almost double the response of the sandy specimen. This is in good agreement with the results of the granulometric and mineralogical analysis in which the clay content of the shaly facies was significantly higher (Chapter 2). Finally, the volumetric behaviour over the whole wetting/drying cycle seems reversible for the sandy facies, whereas a small accumulation of swelling deformation is detected at the end of the cycle for the shaly specimen.

6.4.2. Lausen results

For Lausen specimens, it was decided to perform first a wetting, a drying and then a second wetting phase, in order to investigate possible irreversible deformations upon the cycle. Also, a broader suction range was applied, varying between about 300 MPa to about 0 MPa total suction.

The water retention behaviour of the specimens obtained from the cores L2, L3, L8, L11 and L13 are shown from Figure 6-6 to Figure 6-15.

Figure 6-6, Figure 6-8, Figure 6-10, Figure 6-12 and Figure 6-14 show the evolution over time of the strains perpendicular (⊥) and parallel (//) to bedding, and the water content. Negative values indicate swelling of the material. Figure 6-7, Figure 6-9, Figure 6-11, Figure 6-13 and Figure 6-15 display the evolution over suction of (a) the perpendicular (⊥) and parallel (//) to bedding and the volumetric strains, (b) the water content.

The initial suction value was evaluated after the specimen preparation, right before starting the test, by the use of the WP4C on a fragment of shale cut from the same slice used to prepare the specimen. Among the Lausen specimens, a range of initial suctions varying between approximately 60 and 20 MPa was obtained. Considering that the formation is saturated in situ, and the cores resulted to be close to saturation during the characterization (Chapter 2), the

desaturation is the result of the specimens cut and handling, including the exposition to the laboratory environment during the application of the strain gauges.

The first suction value to apply through the vapour transfer technique was chosen to be close to the initial suction of the specimens. The state of the specimens at the end of the first equalisation steps, in terms of water content and strains, was used as an initial reference condition for computing the water content and strains evolution over the test.

Similarly to what was obtained for Mont Terri specimens, the swelling/shrinkage response is evident in both directions perpendicular and parallel to the bedding. The response of all the specimens upon hydraulic loading is remarkably anisotropic, with the amount of strain parallel to the bedding significantly lower than the one in the perpendicular direction. In particular, at the end of the wetting path, the deformations perpendicular to the bedding are 2-4 times higher than the deformations parallel to the bedding.

Along the suction cycle, the strains are found to be not wholly reversible: the drying path follows the first wetting path for low suctions; then, approaching the initial suction value, the strains deviate from the initial trend, and the strain rate with the suction change is reduced.

For all the tests, the second wetting phase is characterised by a higher increase in water content with respect to the decrease in the corresponding drying phase. Consequently, the induced strains (in absolute value) are higher in the second wetting than in the drying phase, and accumulation of swelling strains occurred. A non-uniform swelling/shrinkage inside the specimens can be envisaged, considering the heterogeneity of the formation at the microscopic scale, that would induce the formation of microcracks (Yang et al., 2012; Wan et al., 2013; Wang et al., 2014).

It has to be mentioned that at 100% relative humidity (i.e., 0 MPa of imposed total suction), drops of water condense on the specimen surface, and the water content determination for this step may be affected by an error. As far as possible, the water drops were removed with a clean tissue before measuring the specimen weight at the 0 MPa suction step.

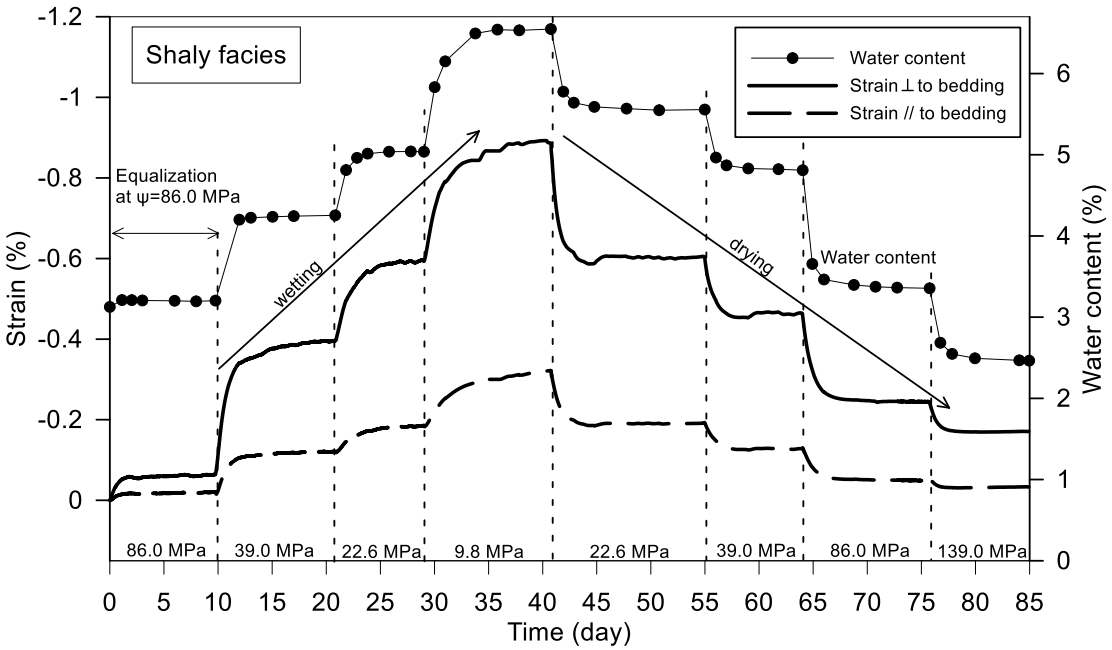

Figure 6-2 Test results of Opalinus Clay shaly facies: evolution in time of the water content and strains (perpendicular ⊥ and parallel // to bedding, negative strains for swelling).

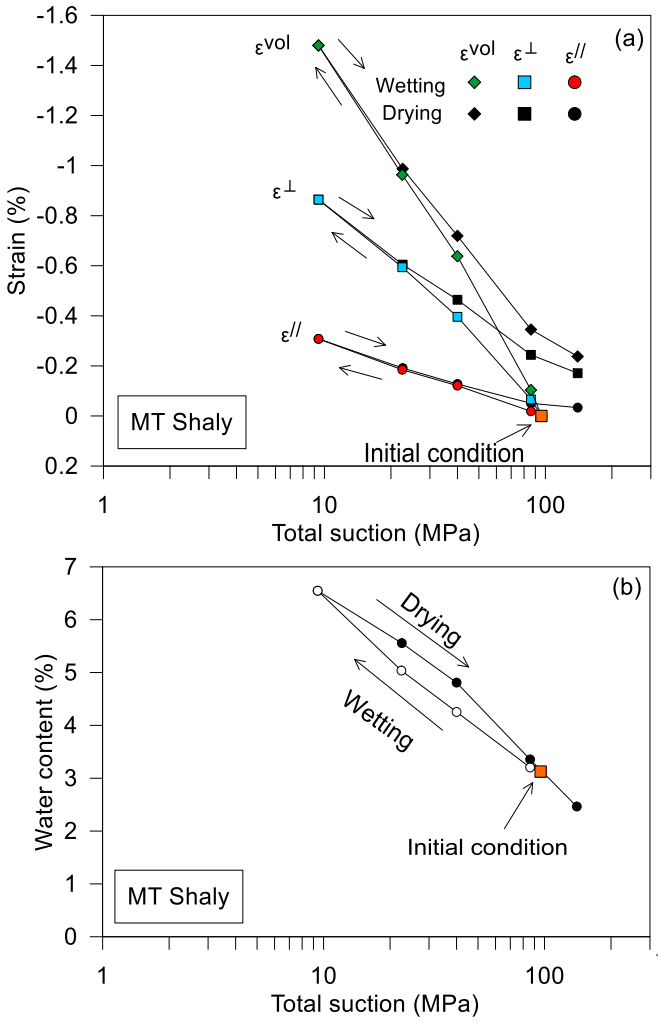

Figure 6-3 Water retention curves (a) and strain evolution (b) (volumetric ε^{vol}, perpendicular $\varepsilon^{\perp}$, and parallel $\varepsilon^{//}$ to bedding) versus suction for the shaly specimen.

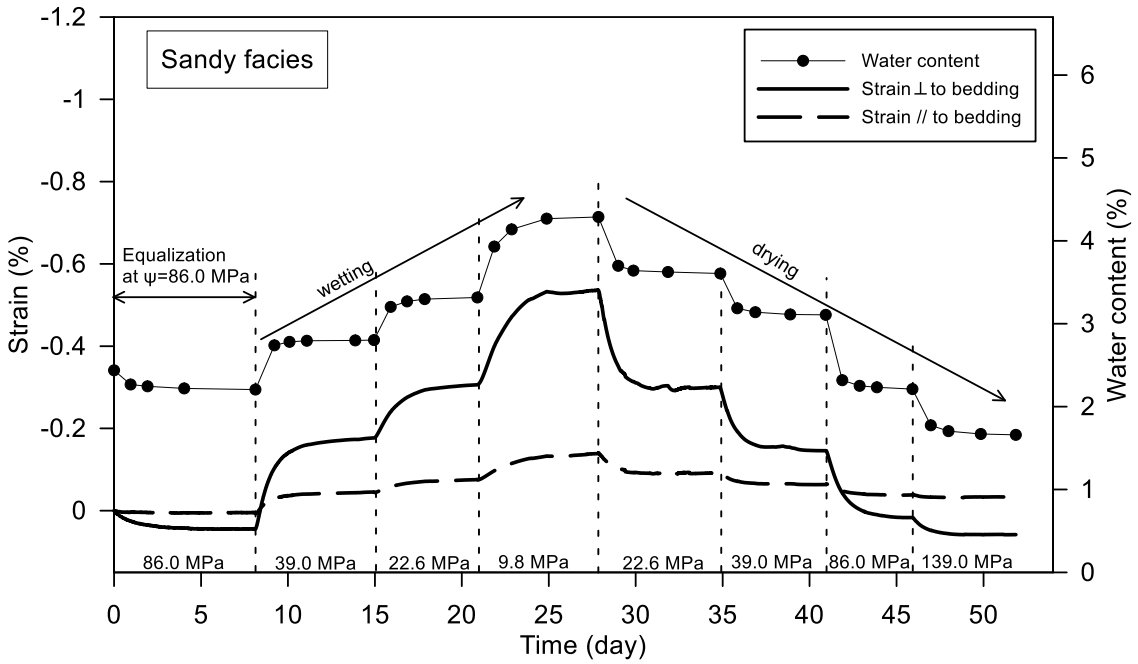

Figure 6-4 Test results of Opalinus Clay sandy facies: evolution in time of the water content and strains (perpendicular ⊥ and parallel // to bedding, negative strains for swelling).

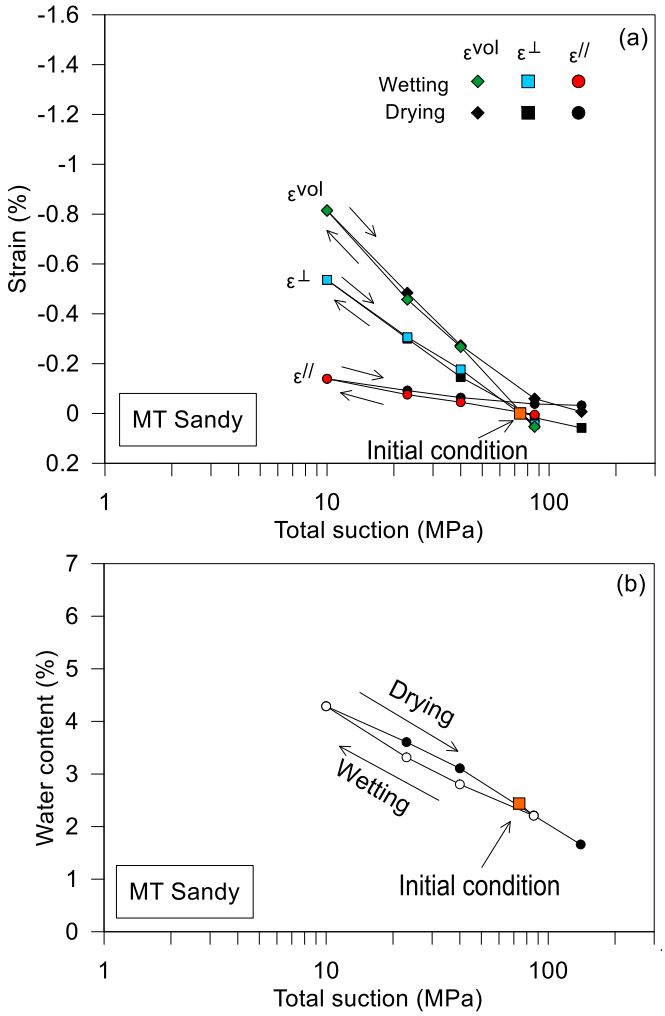

Figure 6-5 Water retention curves (a) and strain evolution (b) (volumetric ε_{vol}, perpendicular $\varepsilon_{\perp}$, and parallel $\varepsilon_{//}$ to bedding) versus suction for the sandy specimen.

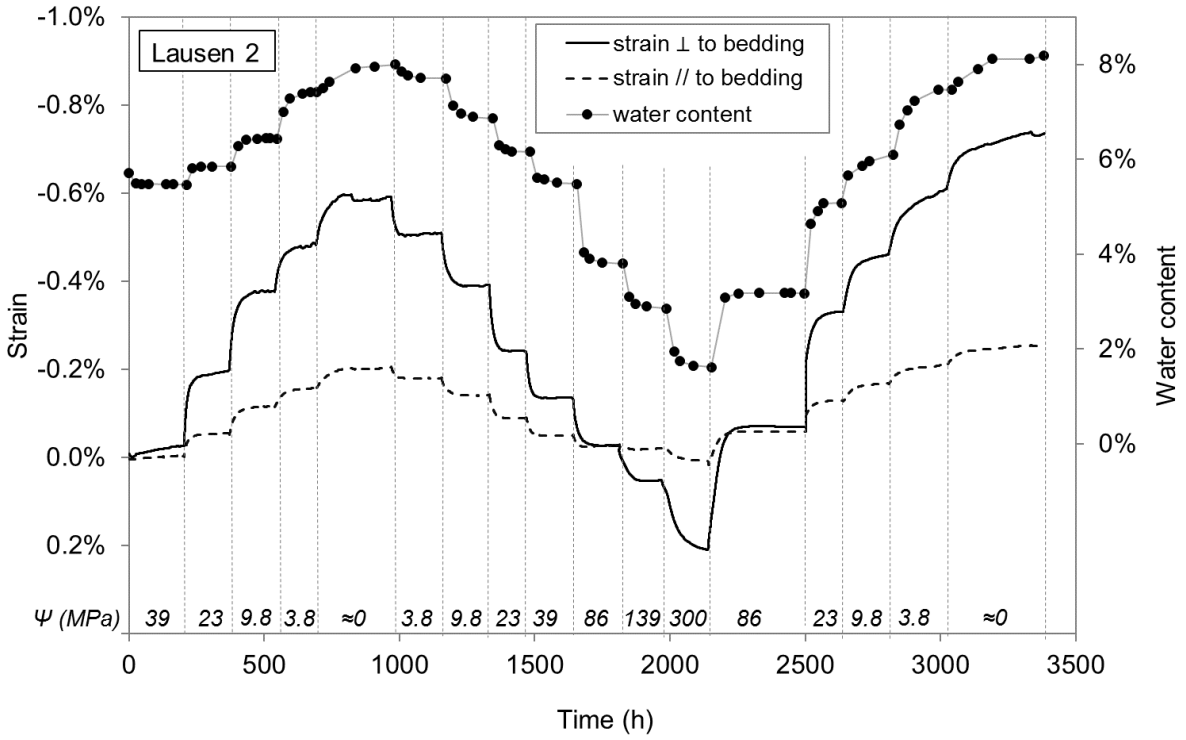

Figure 6-6 Test results of Core 2: evolution in time of the water content and strains (perpendicular ⊥ and parallel // to bedding, negative strains for swelling).

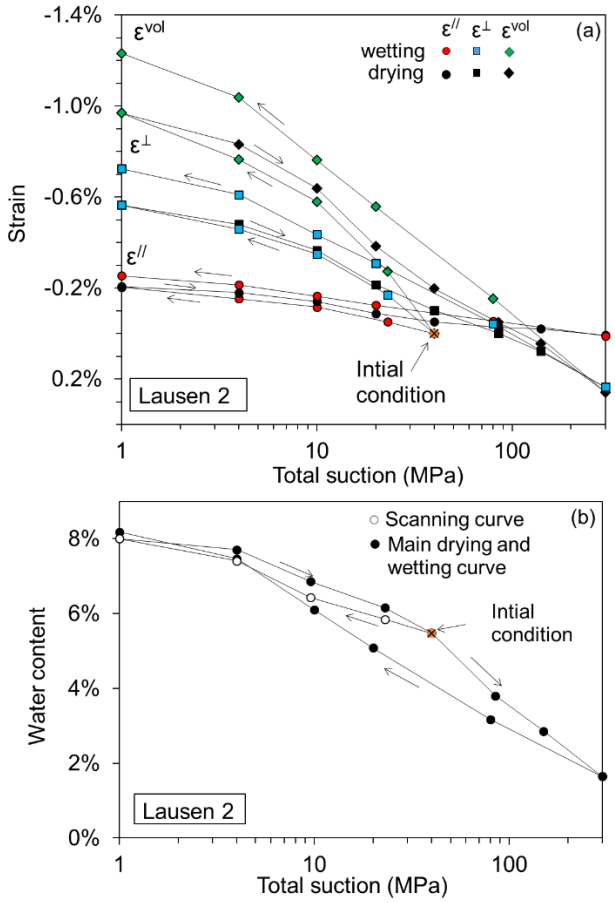

Figure 6-7 Strain evolution versus suction (top) (volumetric εvol, perpendicular ε⊥, and parallel ε// to bedding) and (bottom) water retention curve for the specimen from core 2.

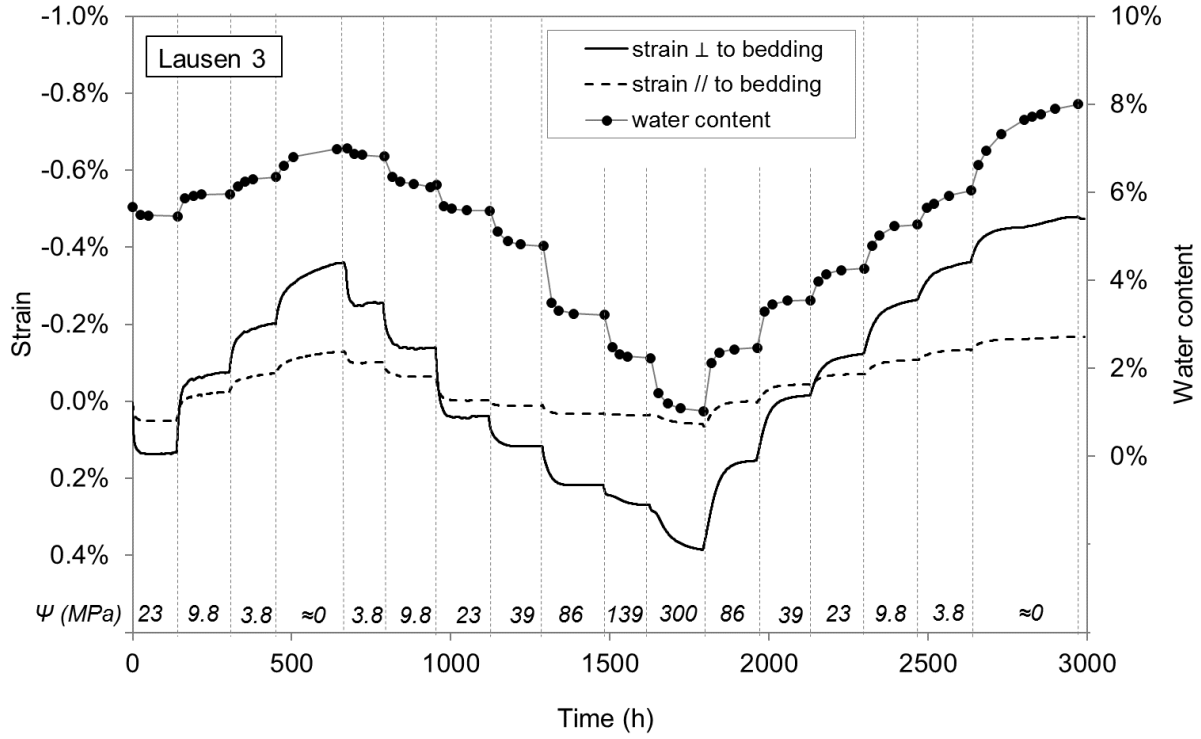

Figure 6-8 Test results of Core 3: evolution in time of the water content and strains (perpendicular ⊥ and parallel // to bedding, negative strains for swelling).

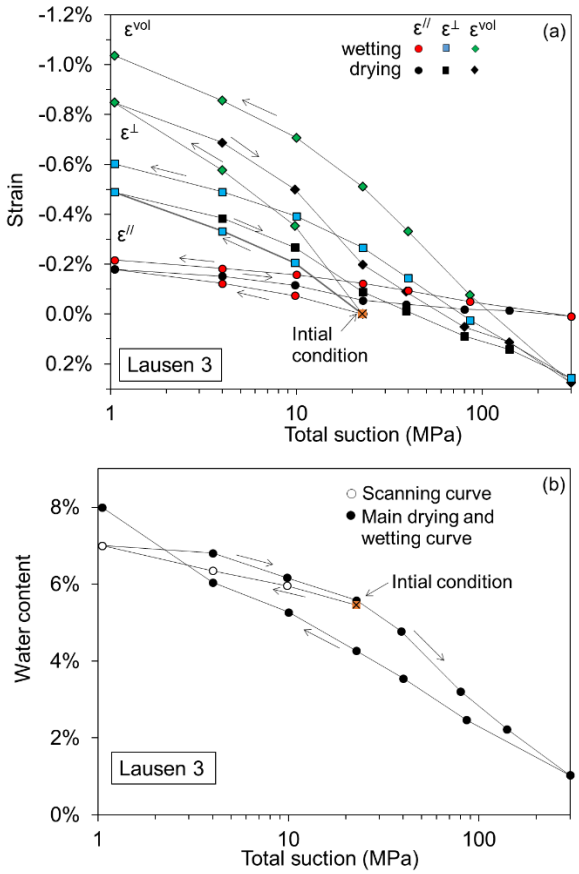

Figure 6-9 Strain evolution versus suction (top) (volumetric εvol, perpendicular ε⊥, and parallel ε// to bedding) and (bottom) water retention curve for the specimen from core 3.

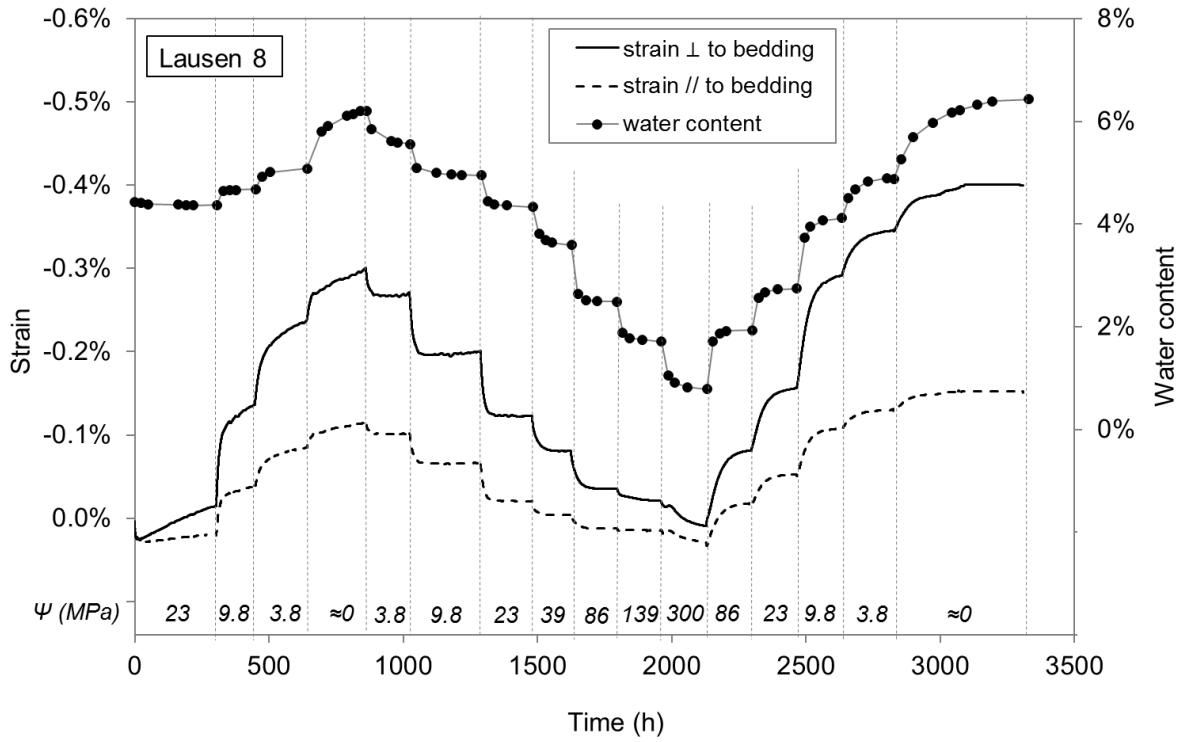

Figure 6-10 Test results of Core 8: evolution in time of the water content and strains (perpendicular ⊥ and parallel // to bedding, negative strains for swelling).

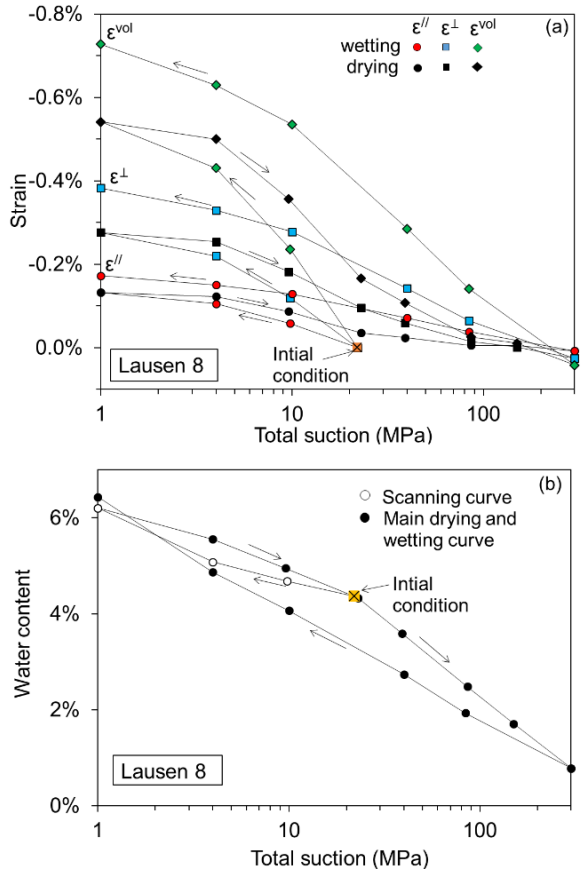

Figure 6-11 Strain evolution versus suction (top) (volumetric εvol, perpendicular ε⊥, and parallel ε// to bedding) and (bottom) water retention curve for the specimen from core 8.

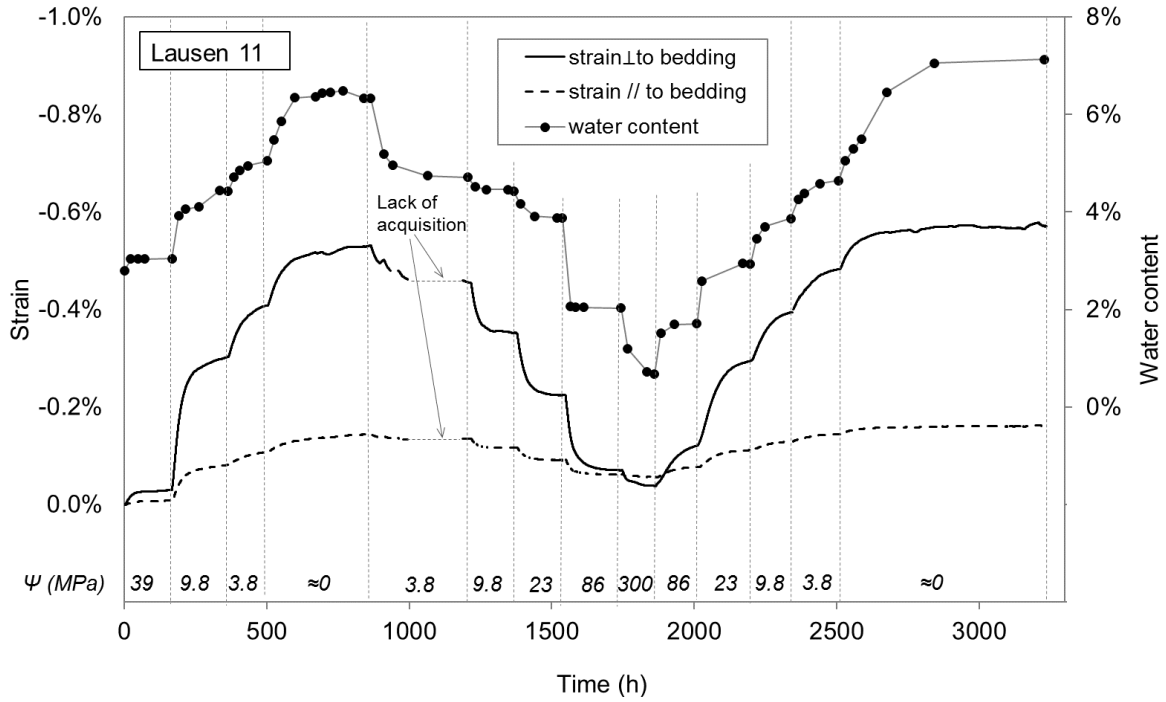

Figure 6-12 Test results of Core 11: evolution in time of the water content and strains (perpendicular ⊥ and parallel // to bedding, negative strains for swelling).

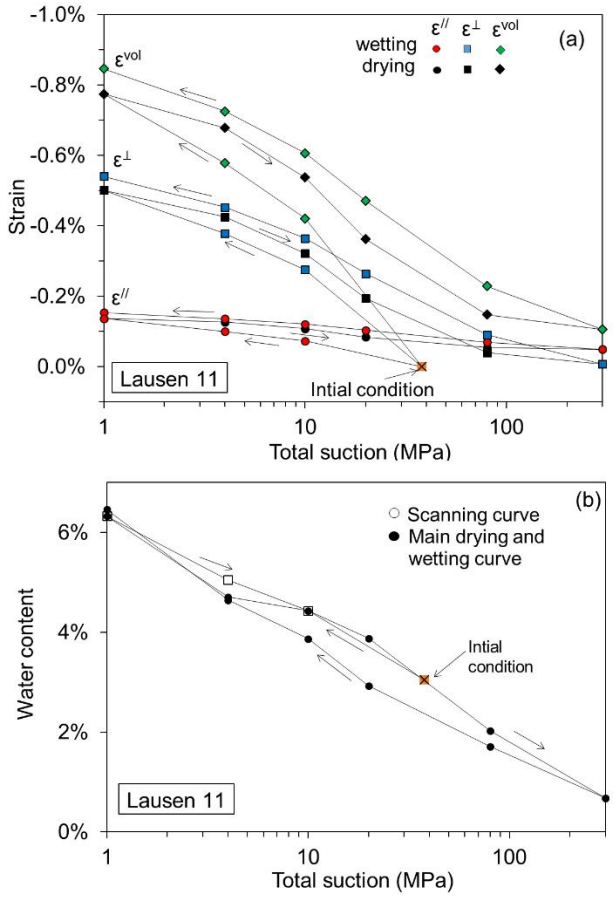

Figure 6-13 Strain evolution versus suction (top) (volumetric εvol, perpendicular ε⊥, and parallel ε// to bedding) and (bottom) water retention curve for the specimen from core 11.

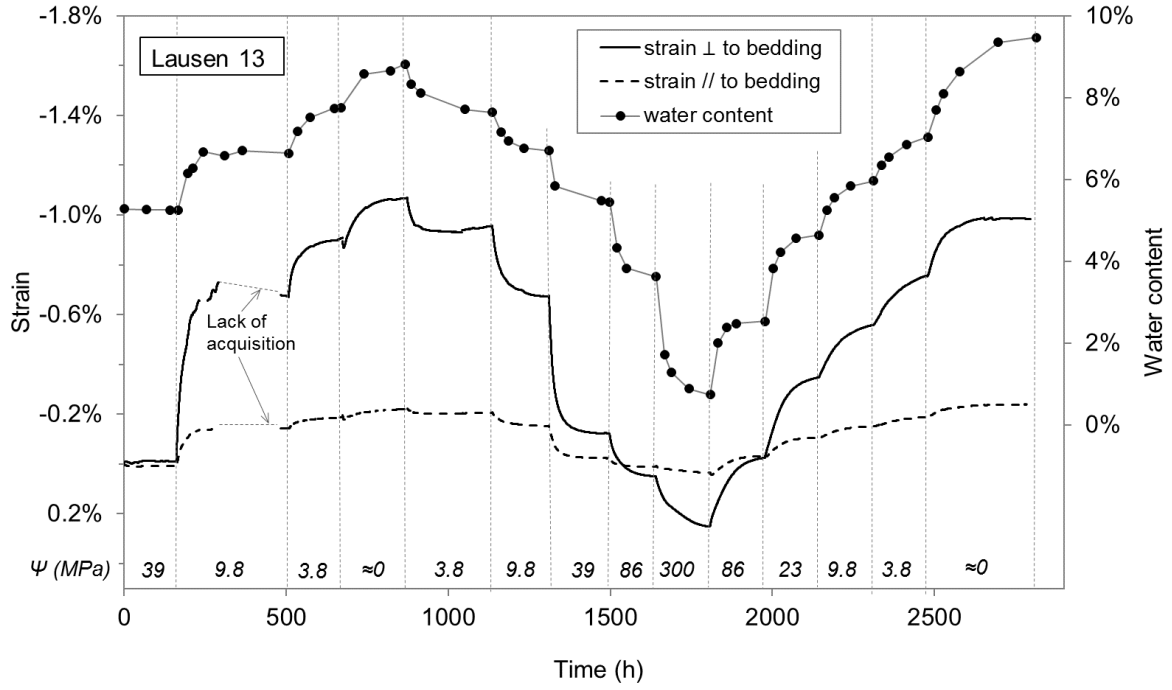

Figure 6-14 Test results of Core 13: evolution in time of the water content and strains (perpendicular ⊥ and parallel // to bedding, negative strains for swelling).

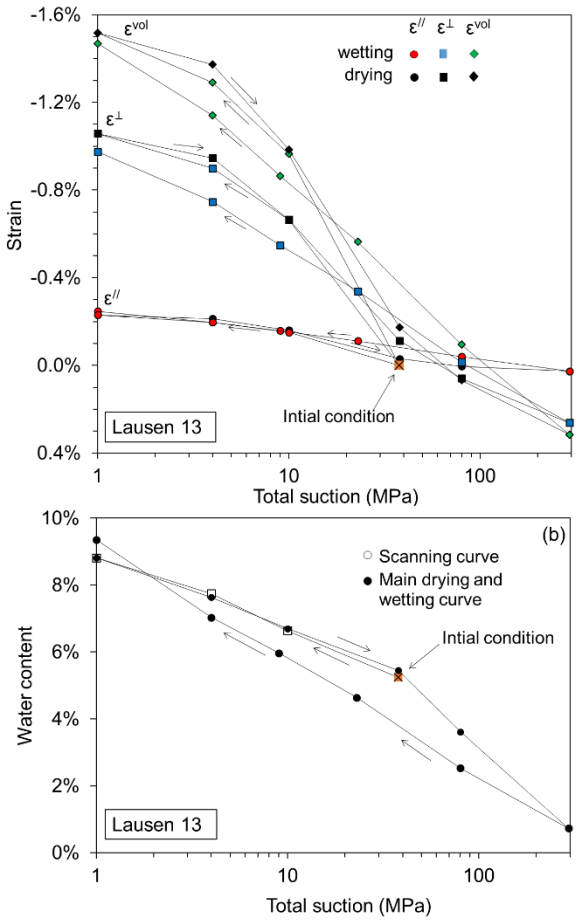

Figure 6-15 Strain evolution versus suction (top) (volumetric εvol, perpendicular ε⊥, and parallel ε// to bedding) and (bottom) water retention curve for the specimen from core 13.

6.5. Discussion

6.5.1. Mineralogy impact on the volumetric response in Lausen specimens

The results from Lausen specimens are compared in Figure 6-16. Figure 6-16 depicts the strain obtained perpendicular to the bedding during (a) wetting, (b) drying and (c) second wetting, and the strain parallel to the bedding during (d) wetting, (e) drying and (f) second wetting. The strains are plotted versus the three main mineralogical components (calcite, quartz and clay minerals).

Despite the differences in the initial conditions, the results show that the higher the clay content is, the higher the volumetric response during the suction loading, both in wetting and in drying. The opposite trend is found for the quartz and calcite content: the higher those components are, the lower the swelling upon wetting and shrinkage upon drying. The consistency among the results suggest that the clay content can be used as an indication of the potential swelling exhibited by the shale, for both the direction perpendicular and parallel to the bedding.

As mentioned before, upon a complete drying-wetting cycle, swelling strains accumulate. Figure 6-17 depicts the percentage increase in the swelling strain from the first saturated condition, at the end of the first wetting, to the end of the second one. For the same specimen, the strains increased similarly in magnitude in both the direction perpendicular and parallel to the bedding. An exception is obtained for specimen L13, for which the second wetting yield to a swelling strain, in the direction perpendicular to bedding, is slightly smaller compared to the initial one (i.e., the increase is slightly below zero) (Figure 6-15). The percentage increase is plotted in Figure 6-17 versus the amount of clay minerals of the specimens. From the obtained results, it is pointed out that the lower the clay content is, the higher the swelling strain increases upon the cycle. In fact, specimens with lower clay content present a higher heterogeneity in the texture and structure. The response to the suction change reflects the heterogeneity. While water absorption would induce significant swelling in clay minerals, this is not the case in the quartz or calcite components. To the non-homogeneous deformations, non-homogenous stresses generate, and at the contact between the various phases, cracks are expected to form. This phenomenon has been observed at the micro and nanoscopic scale in other stiff geomaterials, including swelling and non-swelling components (e.g., Wan et al., 2013; Wang et al., 2014).

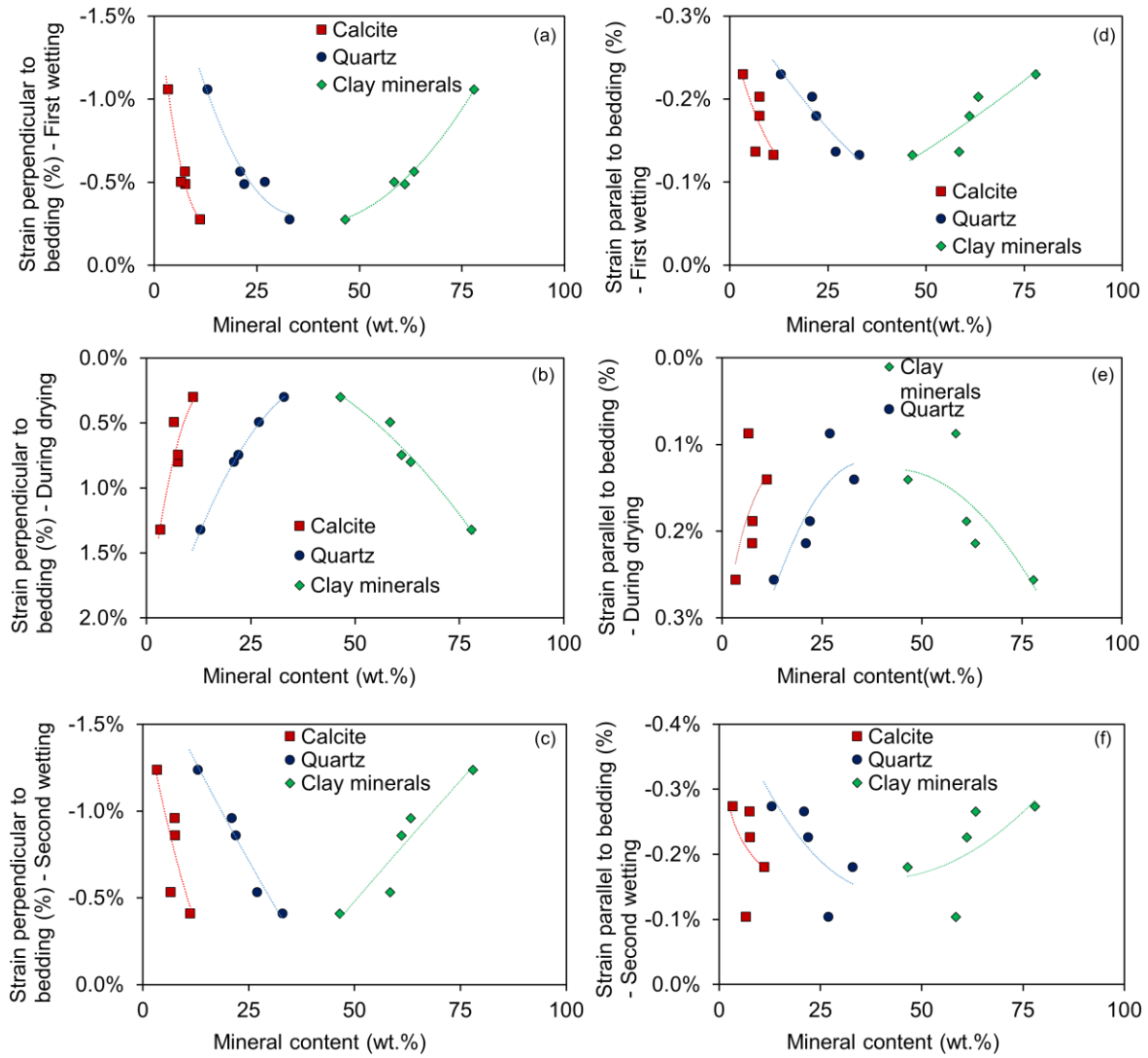

Figure 6-16 Results on Lausen specimens: strain perpendicular to the bedding during (a) wetting, (b) drying and (c) second wetting. Strain parallel to the bedding during (d) wetting, (e) drying and (f) second wetting.

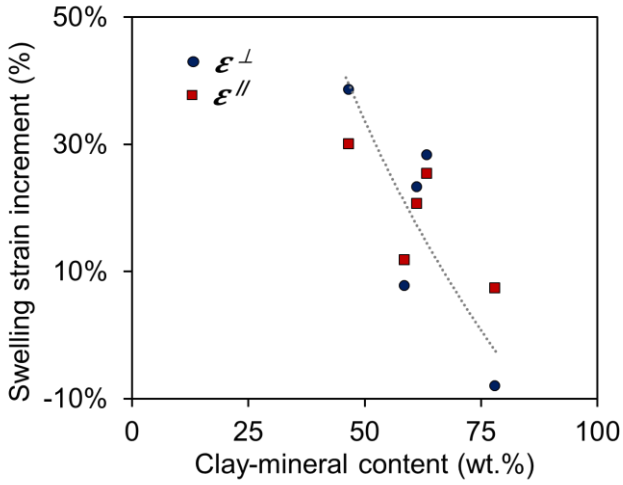

Figure 6-17 Swelling strain increment at saturation from the first to the second wetting phase (Lausen specimens).

6.5.2. Comparison between Lausen and Mont Terri specimens

Very similar behaviours were obtained for specimens from Mont Terri and Lausen. However, the differences in the initial specimen conditions and stress paths make the comparison not straightforward. To compare the responses, the results for the same suction range are considered. During the first wetting path, Lausen specimens were brought to an almost zero-suction condition, that is expected to have generated fissures opening in the specimens. In this case, the drying paths of the various specimens would not be comparable, especially between Lausen and Mont Terri specimens. The first swelling curves obtained within the range of 40-20 MPa to 10 MPa were compared. The selected ranges are reported in Figure 6-18a. The slopes of these swelling paths were determined as $\Delta\varepsilon^{vol}/log(\Delta\Psi)$. The ratio represents a sort of volumetric compressibility parameter, assuming the total suction as an equivalent to the stress variable. The ratios are reported in Figure 6-18b, plotted versus the specimen clay-mineral content. The compressibility parameter results are higher for specimens with high clay-mineral content. A similar dependence of the compressibility on the clay-mineral content was also detected in the saturated mechanical response (Chapter 3).

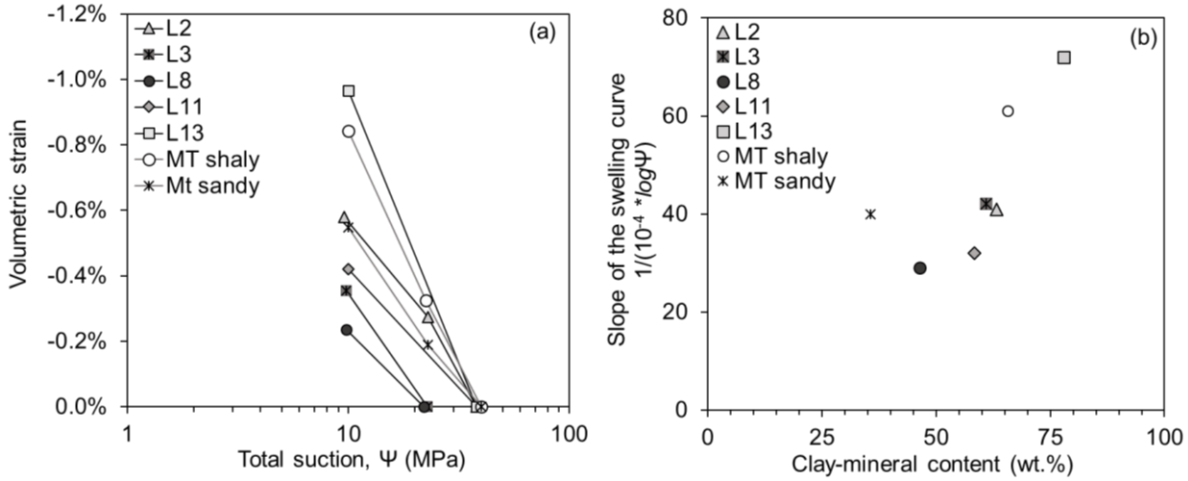

Figure 6-18 Comparison between specimens from the sites of Mont Terri and Lausen: (a) volumetric deformation in the selected suction range, (b) compressibility parameter due to suction change versus the clay-mineral content.

6.6. Swelling and shrinkage crack formations during suction loading: an X-ray micro CT investigation

As mentioned in Section 6.4.2 and 6.5.1, the volumetric behaviour upon wetting-drying was found to be not completely reversible. In particular, an accumulation of swelling strain was detected. The response was attributed to irreversible deformation developed during the wetting-drying process, implying that the geomaterial is damaged during suction cycles. The opening of fissures induced by the desaturation-resaturation process has implications both at the laboratory and the repository scale. For the first, it means that an improper specimen handling

and resaturation may significantly damage the specimens with consequences on their mechanical response and behaviour interpretation. At the repository scale, it implies that the desaturation-resaturation during the repository excavation, installation and closing may contribute to the crack formation and propagation. In the practical application, however, several other aspects (e.g., the stress and temperature conditions, the presence of the excavation damaged zone) need to be taken into account to evaluate the impact of such cracks on the overall formation response.

To further investigate the response of the Opalinus Clay to saturation changes, an ad-hoc test was performed. A specimen of Opalinus Clay from Lausen site was subjected to a wetting-drying-rewetting process in free-swelling conditions, adopting a limited number of suction steps. At selected suction steps, X-ray micro-computed tomography was performed to analyse the evolution of the internal specimen structure due to suction changes.

6.6.1. Experimental setup and procedure

X-ray computed tomography is an established non-destructive technique that allows obtaining a three-dimensional visualisation and characterisation of objects. In brief, the X-rays are directed from a source, through the specimen, to the detectors. The detectors measure how much the X-rays have been attenuated within an object creating an attenuation map which is closely related to the density. The fundamental principle of computed tomography is that several *views* of the specimen are taken over a range of angular orientations. The so obtained 2D radiographs are reconstructed to create slices of the specimen as if it was sliced along several planes (Ketcham and Carlson, 2001).

High-density inclusions can create considerable artefacts in the gathered radiographs, hindering the structure of the specimen. For this reason, in this experiment, strain gauges were not used.

The Opalinus Clay specimen was subjected to several suction steps adopting the vapour transfer technique. At the end of each suction step, the specimen was removed from the desiccator, the weight was measured, and then the specimen was wrapped into paraffin film in order to prevent water loss. An X-ray tomography scan of the wrapped specimen was taken. The paraffin has a very low density compared to the shale and resulted therefore transparent to the X-rays. Scans were performed with the X-ray Ultratom (RX-solutions, PIXE-EPFL) micro-computed tomography (μ-CT) system, which is equipped with a Hamamatsu 230kV X-ray beam source.

The scans were performed at 100 kV, with a current of 150 A, adopting an aluminium filter on the X-ray beam of thickness equal to 0.1 mm.

As for every imaging technique, the resolution (in terms of Pixel or Voxel size), and the field of view (FoV, the dimension of the object observed) are competing. In order to image the entire specimen, a Voxel size of 12-15 μm was obtained. The specimen was installed with an inclination of about 30° on a pedestal to minimise the artefacts at the specimen border. The results were then treated using the RX-solution post-processing software. In particular, it was necessary to use an anti-ring and a beam hardening filters.

The deformations were assessed at the end of each suction step, right after the scan, by adopting a 1D height gauge instrument (Tesa Technology), with a resolution of 1 μm. The instrument uses a tip that measures the vertical distance between two points: e.g., the distance between the specimen surface and a base.

The specimen height was detected on 5 points on the specimen: the centre, and 4 points on the border, from opposite sides (Figure 6-19). The points were drawn on the specimen with a marked. One of the points was marked with a "T" (top) in order to distinguish the specimen sides when rotated. The specimen diameter was measured in 3 positions: at the top, middle and bottom of the specimen. In addition, a small plastic cylinder (diameter 1 mm, length 46 mm) was glued on the specimen side in the "T" position. The plastic is recognisable in the tomography scan and allows to re-orient the specimen scans in order to be matched.

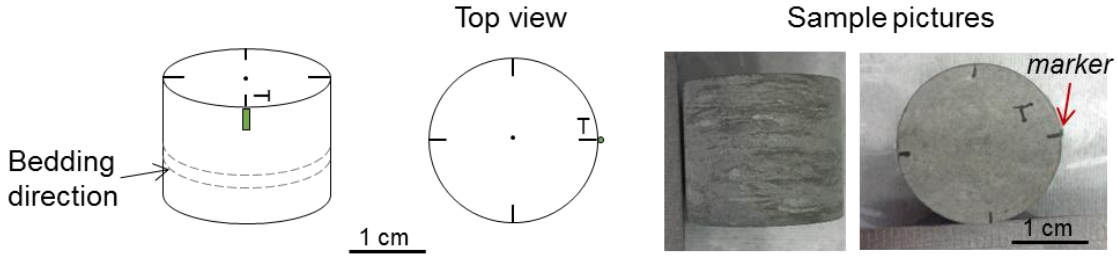

Figure 6-19 Markers on the specimen for the computed tomography.

The cylindrical specimen was prepared using the lathe machine. The initial specimen suction was estimated by a fragment of the same block used to prepare the specimen, in the WP4 dewpoint psychrometer. The suction was found to be around 110 MPa, and therefore, the specimen was left to equilibrate in a desiccator (Figure 6-20) with a saline solution to impose 112 MPa for two weeks.

After the first equilibration phase, the dimensions of the specimen were collected. The average values are reported in Table 6-5, including the specimen height (h), diameter (D) and mass (m).

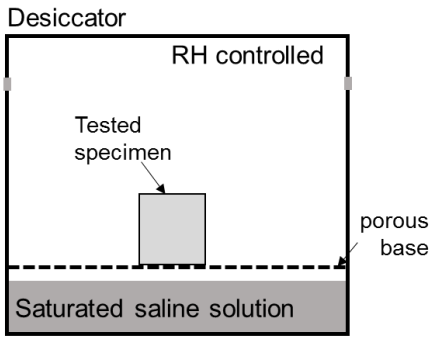

Figure 6-20 Testing configuration for the analysis of the response of the specimen to suction changes.

Table 6-5 Initial specimen dimensions and weight.

Site	h	D	m
	(mm)	(mm)	(g)
Lausen	17.45	20.45	14.0214

The steps of total suction applied to the specimen are reported in Figure 6-21. Each point represents a total suction step, and it is plotted in correspondence of the time at which the step ended. The tomography scans were conducted at the end of the equalisation steps, that last on average two weeks, except for the last re-wetting, that was left equilibrating longer (about eight weeks). The initial condition of about 112 MPa of total suction was imposed for two weeks (point *A*, in the figure). Then, a suction of about 25 MPa was applied (point *B*). Relative humidity equal to 100% (almost 0 MPa suction) was left for two weeks (*C*). After the scan, the specimen was left in the same humidity condition for an additional week, and then a second scan was performed. Points *E* and *F* are located on the drying path, and a scan was performed at the end of step *F*. Long re-wetting (*G*) was performed to assess the reversibility of the behaviour upon the cycle.

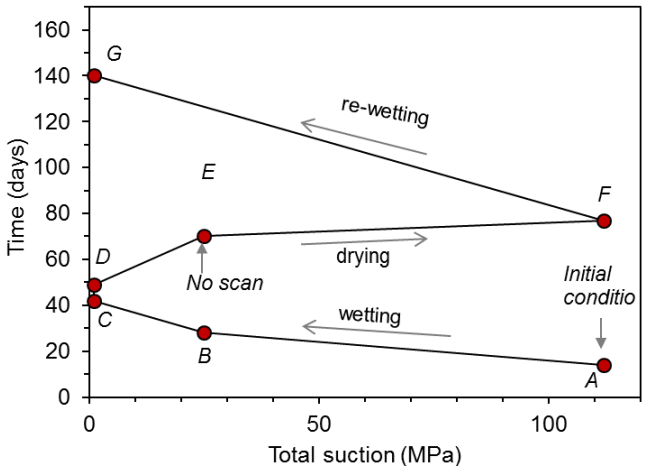

Figure 6-21 Total suction steps applied plotted versus time.

6.6.2. Test results

6.5.2.1. Macroscopical observation

The deformations observed at the various stages of the test are shown in Figure 6-22. In Figure 6-22 the (a) perpendicular, (b) parallel to the bedding and (c) volumetric strains are reported versus the imposed total suction. The evolution in the water content is reported in Figure 6-23.

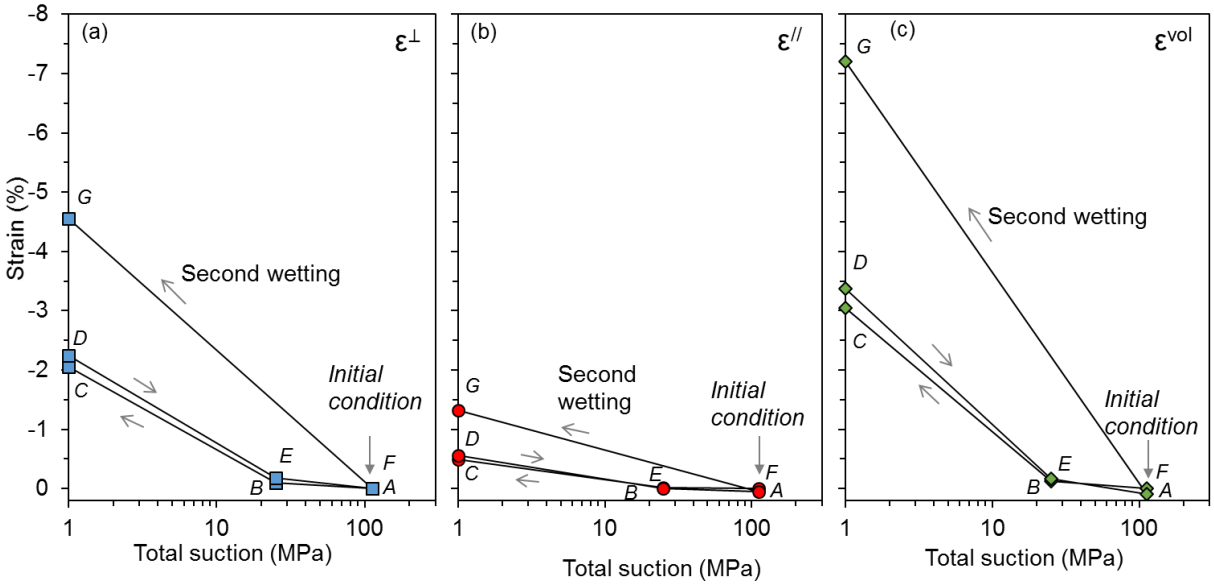

Figure 6-22 Strain (a) perpendicular and (b) parallel to the bedding, (c) volumetric versus total suction.

During the first wetting step (112 MPa to 25 MPa) limited deformation was recorded. The results are in line with the previous test results. During the second step, closer to the saturation, relevant deformations occurred. It is highlighted that in step *D*, the specimen was left equilibrating at the same relative humidity of step *C* (RH=100%, about 0 MPa suction). In this condition, the specimen continued expanding, although sufficient time was allowed to reach equilibrium during step *C*. A minor increase in the water saturation was also detected (Figure 6-23).

During drying, the deformation were recovered almost entirely, and point F and A are almost overlapped. Similarly, also the water content recovered almost completely the initial value. During the prolonged second wetting, the specimen swelled almost double compared to the first wetting, and the water content increased by almost 2% in absolute terms.

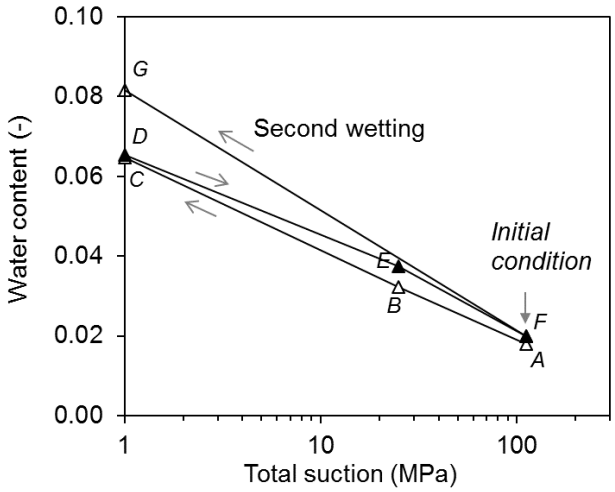

Figure 6-23 Water content evolution during the wetting-drying-wetting process.

The overall trend is similar to what was found in the Lausen testing campaign (Section 6.4.2) and results in other shales (Minardi et al., 2018). However, in this test, the amount of swelling strain recorded in the second wetting phase was higher compared with the previous test results. Among the reasons for the higher swelling, it can be mentioned:

- The specimen was moved from suction of about 112 MPa to about 0 MPa in a single step. Considering the very low permeability of the material, it can be expected that the outer part of the specimen hydrated relatively fast, while the centre stayed in dry condition. The suction gradient between the inner and outer part of the specimen induced a stress concentration that enhanced the fissure opening; in the previous testing campaign, small suction steps were applied, i.e. allowing for a much slower equalisation with the imposed suction.
- The specimen was left at RH=100% for about two months; although in a few weeks the deformation rate usually stabilises, the strains are expected to continue increasing, even at very low strain rate.
- The deformation measured in this configuration is a global measurement, considering the increase in the volume of the specimen in its totality. The previous testing campaign adopted strain gauges that are local measurement; in the occurrence of discrete crack opening, depending on its positioning, the strain gauges may or may not catch the deformation induced by crack opening.

6.5.2.2. Microstructural observation

The micro-computed tomography allows analysing the internal structure of the specimen and its evolution throughout the test. Tomography results were analysed using the software Avizo®,

Thermo Fischer Scientific. The specimen presented compositional heterogeneity, identifiable at the millimetre scale in slices of the tomographic scan, view 1 and view 2, in Figure 6-24. View 1 is a vertical slice of the specimen obtained in the plane of the marker (arrow in Figure 6-24, left). View 2 is a vertical slice of the specimen oriented at 60° from view 1. Figure 6-25 and Figure 6-26 show details of view 1 and 2, respectively, at the various stages of the cycle. The darker grey area is composed of clay matrix. Several large denser grain (possibly quartz or calcite inclusions) are identifiable. Those grains are in the millimetre and submillimetre scale. A high number of inclusions of smaller dimension (tens to hundreds of micron) are also identified. Bright spots are likely pyrite concretions. Given the considerable higher density of the pyrite, it can create artefacts in the tomography. In the close surrounding of the brighter spots, often a more blurred image is obtained.

In the first step (*A*), at 112 MPa, the specimen presented a few cracks. The cracks appeared to be thin, the aperture being in the order of 10-20 micron, i.e. comparable with the resolution of the scan, and yet clearly visible. Those cracks appear to be oriented in the direction of the bedding planes, immersed in the clay matrix, and persistent over several millimetres. These cracks may be attributed to the specimen cutting and handling, during which drying occurred from the in situ saturated conditions, to an initial specimen suction of about 110 MPa. Details (i) and (ii) of Figure 6-24 are analysed in Figure 6-25, Figure 6-26 during the evolution among the steps.

During the first wetting step (*B*, 25 MPa), no structural changes were detected. This observation is in line with the response at the macroscopic scale: the specimen saturation increased, but deformations were limited.

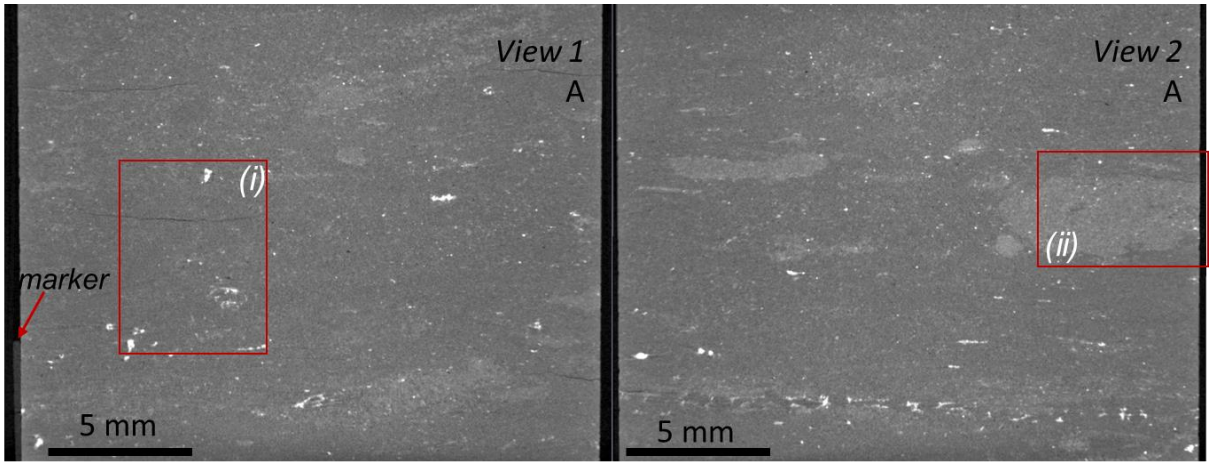

Figure 6-24 Slices (view 1 and view 2) of the tomographic reconstruction of the specimen. Initial condition (A) at total suction 112 MPa.

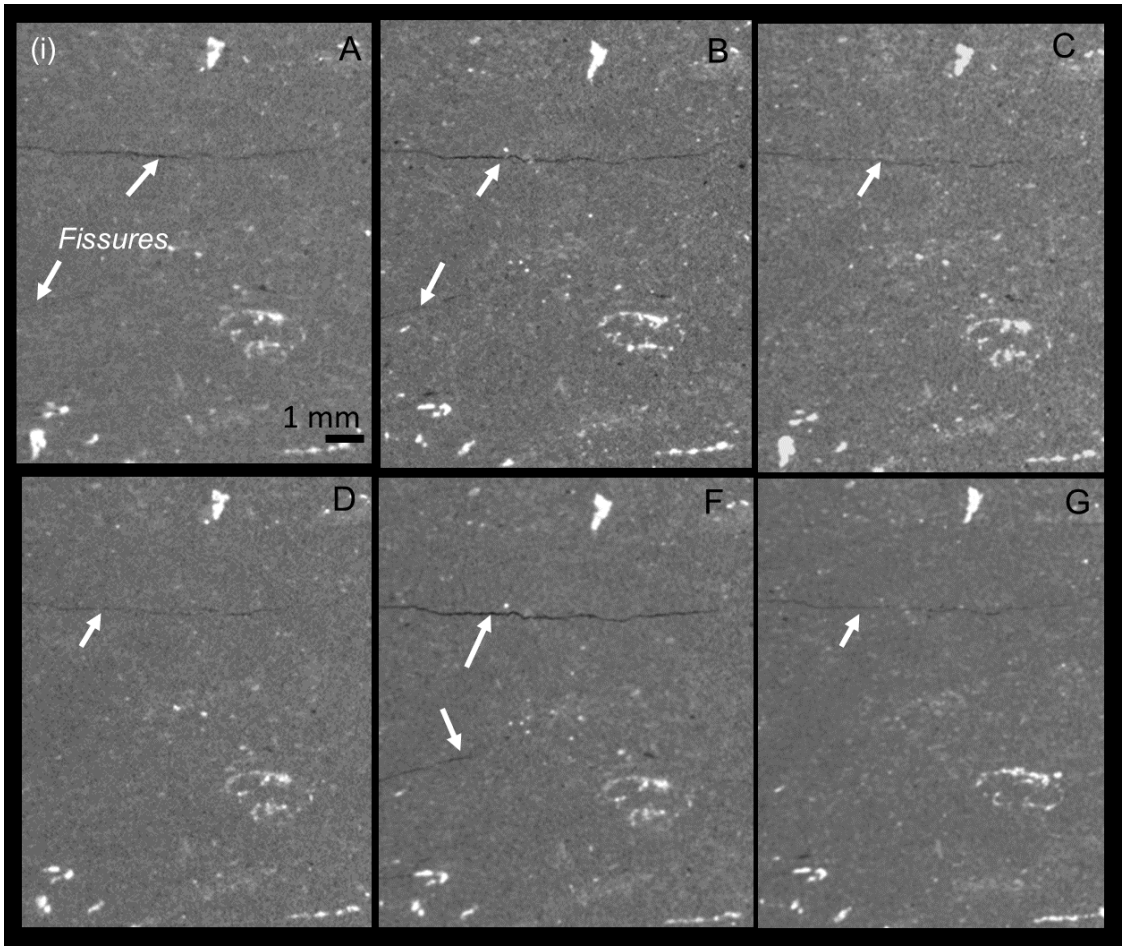

Figure 6-25 Detail of view 1 (i): evolution of a crack in the clay matrix during the suction change.

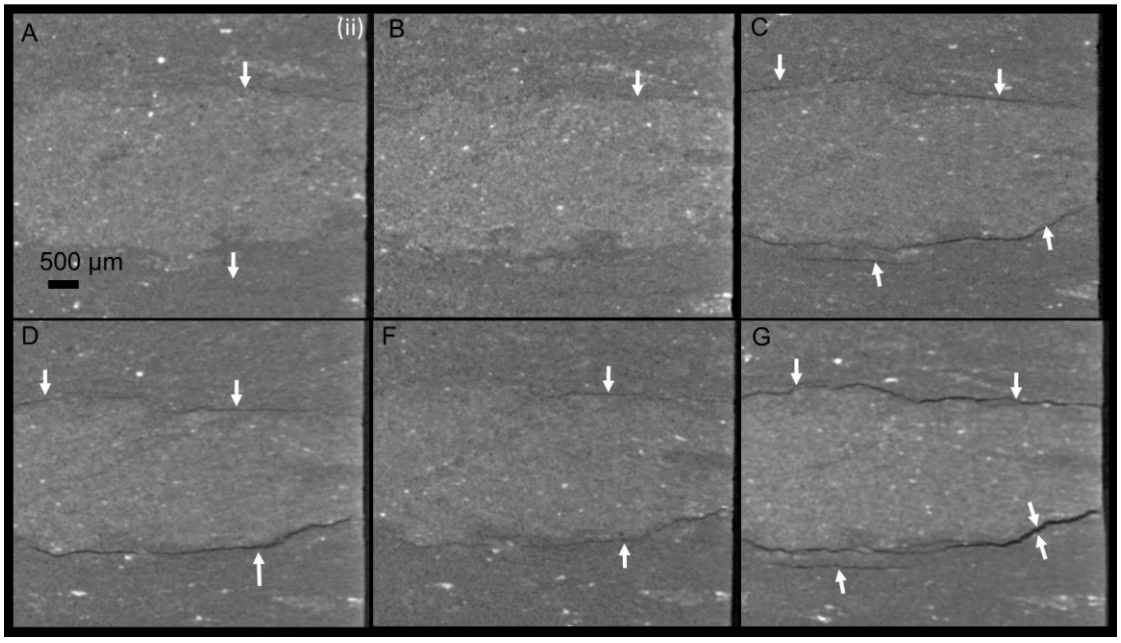

Figure 6-26 Detail of view 2 (ii): evolution of the contact between clay matrix and particles during the suction change.

Differently, in step *C* and *D*, several modifications were detected: during the overall swelling of the specimen, the cracks initially visible in the clay matrix reduced their aperture, becoming

barely visible at the chosen resolution (Figure 6-25). On the other hand, at the contact between the clay matrix and other particles, fissures were formed (Figure 6-26). The fissure opening is particularly evident below the large grain in Figure 6-26 C (white arrows indicate the cracks), where the aperture is about 30 micron.

Step *F* corresponds to the end of the drying. During this step, the opposite response was obtained: several thin fissures in the matrix opened (Figure 6-25), while at the contact between different particles the fissure opening decrease, although they remained still visibly open at the imaging resolution (Figure 6-26). At the macroscopic scale the volumetric response during drying appeared reversible (Figure 6-22).

During Step *G* several cracks opened, with higher aperture compared to step *C* and *D*. Macroscopic swelling is associated with this significant increment of fissure openings. The crack around the particle (Figure 6-26) reaches aperture an over 60 μm, while in the orthogonal plane (not shown) it exceeded 100 μm.

The phenomenon is explained by the application of a significant gradient of suction (and for it, effective stress) was applied around the specimen. The clay matrix absorbs water and tends to swell. This swelling closes cracks in the clay matrix (c.f. Figure 6-25, *B* to *C* and *F* to *G*). For non-swelling minerals, the reduction of suction (i.e. effective stress) induces minor swelling, related to the effective stress decrease. The incompatibility in the deformations generates localised stress that causes the formation of the cracks. This incompatibility is documented in Figure 6-26. While in step *A* the specimen lateral side is regular, in step *G* it is undoubtedly not regular anymore: the clay matrix sections (above and below the grain) swelled more than the coarser particles, hence at the contact fissures formed.

Fissures were segmented, using thresholding on the grey scale histogram of the attenuation response. The segmentation allows identifying the shape and extension of the cracks in the entire specimen in the different phases of the test. Figure 6-27 presents the segmented crack porosity within the specimen at stages *A*, *D*, *F* and *G*. The vertical views (1 and 2), perpendicular to the bedding direction, are also displayed in an orthotopic view. The box in Figure 6-27 A highlights the position of detail *ii* (view 2) in the specimen (Figure 6-25), since around the higher density particle many fissures opened in the following steps.

Very few cracks were found at the initial stage (*A*). During wetting (*D*) cracks with various orientation formed, at the contacts between particles. During drying (*F*), the previously formed cracks reduced, while a new set of cracks, typical of desiccation in clayey geomaterials (e.g.,

Albrecht and Benson, 2001; Peron et al., 2009), well oriented in the direction of the bedding plane, formed. Those cracks formed in particular in the outer part of the specimen, in an annular shape, where the specimen experienced a significant suction gradient. During the last step (*G*), the annular cracks, oriented perpendicular to the bedding, almost disappeared, while at the contact with inhomogeneities, the cracks opened even more than step *D*. In the view 2, detail *ii* the formation of wetting cracks along the particle is particularly evident.

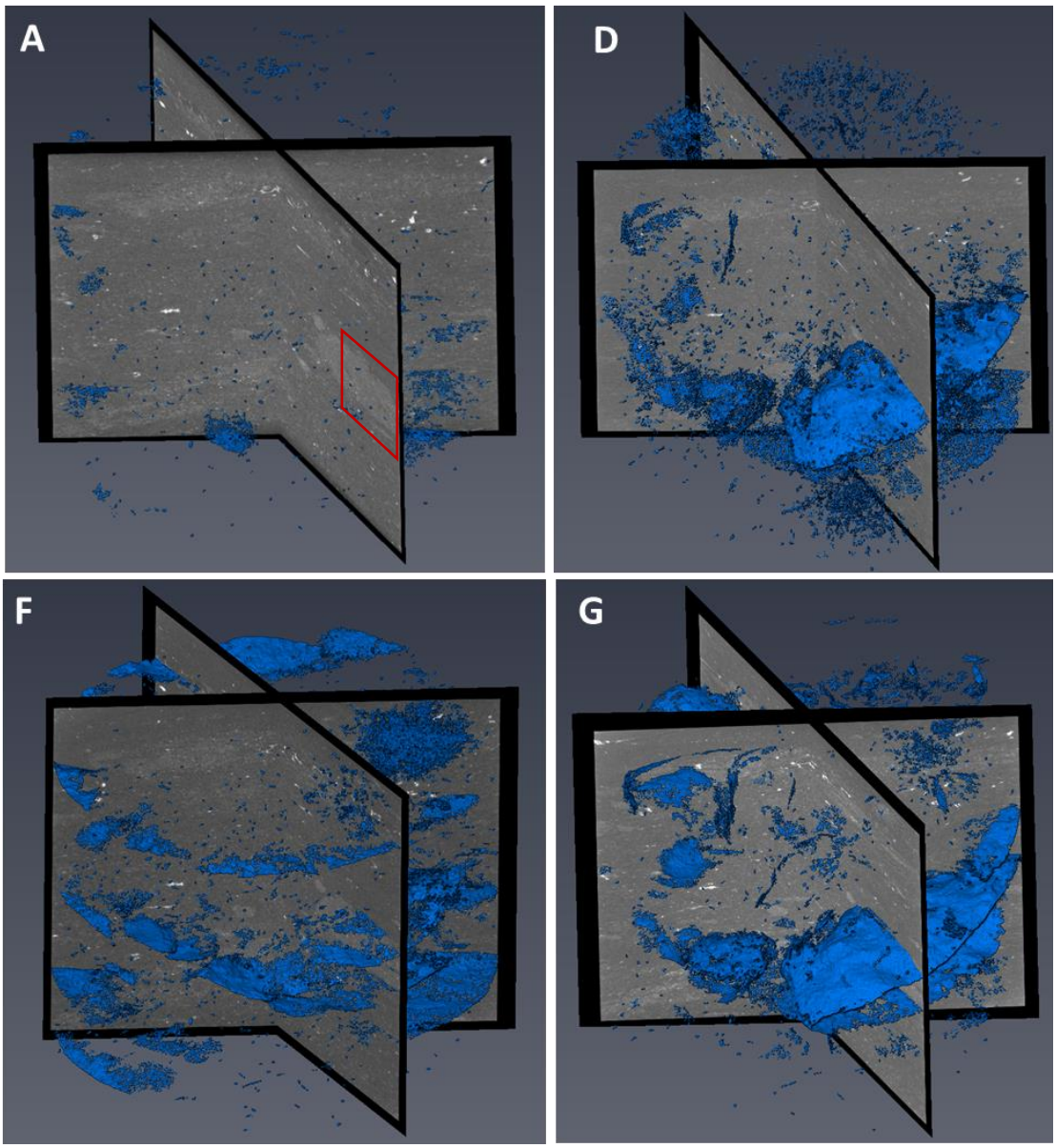

Figure 6-27 3D views of the segmented porous space during the test: step A (Ψ=112 MPa), D (first wetting to Ψ≈0 MPa), F (drying to Ψ=112 MPa), G (second wetting to Ψ≈0 MPa),

6.7. Conclusions

The importance of the coupling between the volumetric and water retention behaviour was demonstrated by the results of the experimental investigation conducted on the two tested facies

of Opalinus clay shale from Mont Terri and on five specimens from the various depths from the Lausen borehole. The volumetric response observed upon wetting and drying processes significantly affects the evolution of the water content, causing a nonlinear anisotropic behaviour of the materials upon total suction change. For all the specimens, a more significant deformation perpendicular to the bedding is observed rather than in the parallel direction.

As a consequence of this behaviour, anisotropic swelling stresses would be expected if the shale was wetted under confined conditions.

The impact of the composition on the shale volumetric response was highlighted. In particular, the higher the clay content, the higher the swelling upon wetting and the shrinkage upon drying were found, consistently for both loading directions, over the cycle. The volumetric response was found to be consistent as a function of the composition also among the specimens from the two sites investigated.

In the framework of nuclear waste disposal, this finding implies that the more clayey part of the formation is more prone to swell during saturation and to potentially close fissures formed inside the geomaterial.

For specimens subjected to the second wetting phases, an accumulation of the swelling strain was detected. In particular, it was pointed out that the increase in swelling strains was more evident for specimens with higher heterogeneity in the composition.

It was shown that the irreversibility of the strains is related to the opening of cracks both during wetting and during drying by performing systematic X-ray tomography of a specimen subjected to a hydraulic load. It was shown that during drying, several small fissures opened, mostly in the clay matrix, in the direction of the bedding planes. On the other hand, during wetting, those fissures closed, and others formed at the contact between clay matrix and inclusions. In this second case, the cracks are not oriented with respect to the bedding but follow the shape of the inclusions. The experiments showed the effect that saturation and desaturation processes have on the shale integrity, that is relevant for the practical applications, but also for the specimen handling in the laboratory. An incorrect specimen handling and resaturation may significantly damage the specimens with expected consequences on their mechanical response and behaviour interpretation. At the repository scale, it implies that the desaturation-resaturation during the repository excavation, installation and closing may contribute to crack formation and propagation. In practical applications, however, several other aspects (e.g., the stress and temperature conditions, the presence of the excavation damaged zone) need to be

taken into account to evaluate the impact of such cracks on the overall formation response. Future investigation should focus on the impact of confinement on the crack developing during suction change, in order to mimic the in situ stress conditions.

6.8. References

Albrecht, B.A., Benson, C.H., 2001. Effect of Desiccation on Compacted Natural Clays. J. Geotech. Geoenvironmental Eng. 127, 67–75. https://doi.org/10.1061/(ASCE)1090-0241(2001)127:1(67)

Cardoso, R., Romero, E., Lima, A., Ferrari, A., 2007. A Comparative Study of Soil Suction Measurement Using Two Different High-Range Psychrometers, in: Schanz, T. (Ed.), Experimental Unsaturated Soil Mechanics, Springer Proceedings in Physics. Springer Berlin Heidelberg, pp. 79–93. https://doi.org/10.1007/3-540-69873-6_8

Delle Piane, C., Dewhurst, D., Siggins, A., Raven, M., 2011. Stress-induced anisotropy in brine saturated shale. Geophys. J. Int. 184, 897–906.

Ferrari, A., Favero, V., Marschall, P., Laloui, L., 2014. Experimental analysis of the water retention behaviour of shales. Int. J. Rock Mech. Min. Sci. 72, 61–70. https://doi.org/10.1016/j.ijrmms.2014.08.011

Ferrari, A., Laloui, L., 2013. Advances in the Testing of the Hydro-mechanical Behaviour of Shales, in: Multiphysical Testing of Soils and Shales. Springer, pp. 57–68.

Fredlund, D.G., Rahardjo, H., 1993. Frontmatter, in: Soil Mechanics for Unsaturated Soils. John Wiley & Sons, Inc., pp. i–xxiv.

Ketcham, R.A., Carlson, W.D., 2001. Acquisition, optimization and interpretation of X-ray computed tomographic imagery: applications to the geosciences. Comput. Geosci., 3D reconstruction, modelling & visualization of geological materials 27, 381–400. https://doi.org/10.1016/S0098-3004(00)00116-3

Leong, E.-C., Tripathy, S., Rahardjo, H., 2003. Total suction measurement of unsaturated soils with a device using the chilled-mirror dew-point technique. Géotechnique 53, 173–182. https://doi.org/10.1680/geot.2003.53.2.173

McLamore, R., Gray, K.E., 1967. The Mechanical Behavior of Anisotropic Sedimentary Rocks. J. Eng. Ind. 89, 62. https://doi.org/10.1115/1.3610013

Minardi, A., Ferrari, A., Ewy, R., Laloui, L., 2018. The impact of the volumetric swelling behavior on the water uptake of gas shale. J. Nat. Gas Sci. Eng. 49, 132–144. https://doi.org/10.1016/j.jngse.2017.11.001

Niandou, H., Shao, J.F., Henry, J.P., Fourmaintraux, D., 1997. Laboratory investigation of the mechanical behaviour of Tournemire shale. Int. J. Rock Mech. Min. Sci. 34, 3–16. https://doi.org/10.1016/S1365-1609(97)80029-9

Peron, H., Laloui, L., Hueckel, T., Hu, L.B., 2009. Desiccation cracking of soils. Eur. J. Environ. Civ. Eng. 13, 869–888. https://doi.org/10.1080/19648189.2009.9693159

Pham, Q.T., Vales, F., Malinsky, L., Nguyen Minh, D., Gharbi, H., 2007. Effects of desaturation–resaturation on mudstone. Phys. Chem. Earth Parts ABC 32, 646–655. https://doi.org/10.1016/j.pce.2006.03.012

Popp, T., Salzer, K., Minkley, W., 2008. Influence of bedding planes to EDZ-evolution and the coupled HM properties of Opalinus Clay. Phys. Chem. Earth Parts ABC 33, S374–S387.

Salager, S., François, B., Nuth, M., Laloui, L., 2013. Constitutive analysis of the mechanical anisotropy of Opalinus Clay. Acta Geotech. 8, 137–154. https://doi.org/10.1007/s11440-012-0187-2

Soe, A.K.K., Osada, M., Takahashi, M., Sasaki, T., 2009. Characterization of drying-induced deformation behaviour of Opalinus Clay and tuff in no-stress regime. Environ. Geol. 58, 1215–1225. https://doi.org/10.1007/s00254-008-1616-2

Stavropoulou, E., Andò, E., Tengattini, A., Briffaut, M., Dufour, F., Atkins, D., Armand, G., 2019. Liquid water uptake in unconfined Callovo Oxfordian clay-rock studied with neutron and X-ray imaging. Acta Geotech. 14, 19–33. https://doi.org/10.1007/s11440-018-0639-4

Valès, F., Nguyen Minh, D., Gharbi, H., Rejeb, A., 2004. Experimental study of the influence of the degree of saturation on physical and mechanical properties in Tournemire shale (France). Appl. Clay Sci. 26, 197–207. https://doi.org/10.1016/j.clay.2003.12.032

Wan, M., Delage, P., Tang, A.M., Talandier, J., 2013. Water retention properties of the Callovo-Oxfordian claystone. Int. J. Rock Mech. Min. Sci. 64, 96–104. https://doi.org/10.1016/j.ijrmms.2013.08.020

Wang, L.L., Bornert, M., Héripré, E., Yang, D.S., Chanchole, S., 2014. Irreversible deformation and damage in argillaceous rocks induced by wetting/drying. J. Appl. Geophys. 107, 108–118. https://doi.org/10.1016/j.jappgeo.2014.05.015

Yang, D.S., Bornert, M., Chanchole, S., Gharbi, H., Valli, P., Gatmiri, B., 2012. Dependence of elastic properties of argillaceous rocks on moisture content investigated with optical full-field strain measurement techniques. Int. J. Rock Mech. Min. Sci. 53, 45–55. https://doi.org/10.1016/j.ijrmms.2012.04.004

Chapter 7

Conclusions

7. Conclusions

7.1. General conclusion

In this thesis work, the impact of the composition and the burial depth on the hydro-mechanical response of Opalinus Clay samples was investigated via an experimental campaign. Results on samples from two burial depths were obtained and analysed together with literature data.

In the shallowest site (Lausen), the formation was exhumated over 1000 m from the original burial, reaching the shallow subsurface. At the field scale, weathering was identified only in the first 20-30 m depth, while on laboratory samples (tested in this work) the effect of the uplifting, below 30 m depth, was negligible. The laboratory results showed that the response of Lausen samples is comparable to that of the samples from Mont Terri (having similar maximum burial depth, about 1100-1300 m) in terms of characterisation, compressibility, permeability and volumetric response to suction change. Except for the first 20-30 m, the formation seems to maintain the same properties that it has in deeper locations, despite the considerable erosion of the overlying strata. This result is encouraging for the evaluation of future scenarios in the evolution of the repository. On the other hand, samples from the greater depth of Schlattingen (literature data), having estimated maximum burial depth of 1700 m, showed a significantly lower porosity and compressibility, clearly distinguished from the shallower sites.

The impact of the sample composition on the hydro-mechanical response of the Opalinus Clay was analysed. The dependence of elastic, elastoplastic and shear strength parameters and unsaturated volumetric response on the composition was discussed. In the comparison of the two main facies (shaly and sandy) identified in the Mont Terri URL, it was highlighted that samples with lower clay content, such as those belonging to the sandy facies tested in this work, showed higher stiffness and shear strength, that may be considered more desirable properties for underground constructions. On the other hand, samples with higher clay content (such as those belonging to the shaly facies) were found to have a higher capacity to swell upon saturation, and therefore to potentially self-seal cracks. Further, they have lower permeability and pore throat diameter, that are desirable properties for a barrier geomaterial.

The results in this thesis expanded the available dataset on Opalinus Clay hydro-mechanical response. The main contributions of this work are the understanding of the variability of the formation response and the study of the dependency of the main elasto-plastic parameters, determined at the laboratory scale, on sample composition and depth. The results can be used

for preliminary estimation of the properties of un tested samples and to limit the number of experimental tests to be performed, that has a significant impact on the characterisation time and costs.

In the following, the main outcomes for each thesis section are summarised.

7.1.1. Opalinus Clay characterisation

The results of the geotechnical and microstructural investigation showed the similarity and differences among samples obtained from different sites and among samples with different composition sourced from the same location. The main mineralogical components are the same among the various samples, although the proportions among them can vary significantly. The following primary outcomes were obtained:

- Higher clay-mineral contents correspond to higher porosity and lower pore throat diameters. Porosity results from Lausen are in line with Mont Terri results, except for the first 20-30 m where the impact of the exhumation on the fissuring is expected. The porosity of samples from Schlattingen appears to be considerably lower, likely because of a higher impact of diagenesis and maximum burial attributed to the different geological history.
- The variation of porosity with respect to the composition has been interpreted with two simplified models: (i) a binary mixture of clay matrix and embedded particles and (ii) an alternation of clay-rich and quartz-calcite-rich layers. The second leads to a better representation of the experimental results, simulating the dependency of the porosity on the composition. For both models, the data corresponding to samples from greater depth needed to be interpreted separately to be able to take into account the reduced porosity of shale from the greater depth.

7.1.2. Hydro-mechanical response in laterally constrained conditions and interpretation

Several tests were performed in laterally confined conditions. In particular, twin samples from Lausen and Mont Terri, with variable composition, were loaded either in the direction perpendicular or parallel to the bedding. The hydraulic conductivity was obtained through the consolidation theory and constant-head tests. Results were compared with literature data on Mont Terri and Schlattingen borehole. The following outcomes are highlighted:

- The key impacts of the mineralogical composition, in particular, the clay component, on the Opalinus Clay mechanical properties have been identified. The higher the clay-mineral

contents, the higher the swelling and compressibility indexes are, disregarding the sourcing depth.

- The elastic behaviour is significantly different in the two loading directions. At high-stress levels, the oedometric moduli in the two loading directions tend to be similar, revealing that the differences diminish at high stresses, towards the normal-consolidation, where the effect of the prior loading history is reduced.
- For the same material composition, lower porosity corresponds lower permeability. For specimens subjected to the same stress level, a higher permeability is found for specimens with lower porosity, corresponding to lower clay contents. This is the result of the larger pore throat sizedetected for samples with lower clay content and higher quartz and calcite content.
- At greater depths than approximately 30 m, the hydraulic conductivity values from in situ and laboratory testing are in broad agreement. In contrast, in the uppermost 30 m of Opalinus Clay, the in situ measurements clearly deviate from the laboratory test results.
- The geomaterial has been interpreted as a layered structure, and the sample compressibility values in the oedometric condition have been evaluated, attributing compressibility and porosity values to each layer type. The combination of layers is analytically solved and compared to the experimental results. The correlation adapts well to theshallower samples, while for the ones sourced from a greater depth, the correlation tends to overestimate the compressibility.

7.1.3. Hydro-mechanical response in triaxial conditions and impact of the composition

A protocol for testing low porosity shale in saturated, drained, triaxial tests was presented. Tests on the sandy facies of the Opalinus Clay were performed and allowed to determine the swelling pressure, the elastic parameters (Young modulus and Poisson's ratio), the shear strength (peak and residual) and the dilatancy for the sandy facies.

The hydro-mechanical response of the Opalinus Clay shale was interpreted as a layered geomaterial, composed of an alternation of two-layer types. The first is composed by a clay matrix in which grains of quartz, calcite or other minerals are embedded. The latter is composed by a compact quartz structure, whose pores are filled with clay. The hydro-mechanical properties of each layer type were estimated via the gathered experimental data. Experimental results were analysed to determine the dependency of the parameters on the shaly volumetric fraction. The primary outcomes are here recalled:

- For the sandy samples, Young modulus increases non-linearly with stress, while the Poisson's ratio stays approximately constant. The higher the shaly fraction, the lower the sample stiffness is, both in drained and undrained conditions.
- Undrained parameters for elastic behaviour can be effectively derived from the drained parameters, by accounting for a layered structure response, and a Skempton B =0.8.
- Peak and ultimate shear strength of a large number of tests from the literature, obtained both in drained and undrained shearing were compared, finding a broad agreement. Friction angle decreases as shaly volumetric fraction increases with a power law, both at peak and ultimate state. The cohesion stays approximately constant among the various compositions, but the value at the ultimate state is halved compared to the peak.

To sum up, it was highlighted that most of the scatter in the experimental results on the hydro-mechanical parameters of Opalinus Clay can be explained when analysing the sample compositions. The layered structure appears to be a good approximation of the shale response at the centimetre scale.

7.1.4. Volumetric response to saturation variation

The importance of the coupling between the volumetric and water retention response to saturation variation was demonstrated by the results of the experimental investigation conducted on specimens from Mont Terri and Lausen. In particular:

- The volumetric response observed upon wetting and drying processes significantly affects the evolution of the water content, causing a nonlinear anisotropic behaviour of the materials upon total suction change. For all the specimens, a more significant deformation perpendicular to the bedding is observed compared to the parallel direction.
- The volumetric response is found to be consistent as a function of the composition among the specimens from the two investigated sites.
- The second wetting phase induces accumulation of the swelling strain. The increase in swelling strains is more evident for specimens with higher heterogeneity in the composition. This is attributed to larger cracks forming at the boundaries between inhomogeneous phases, such as quartz-clay boundaries.
- X-ray tomographies of a specimen subjected to a hydraulic load showed the opening of cracks both during wetting than during drying. During drying, several small fissures open, mostly in the clay matrix, in the direction of the bedding planes. During wetting, those fissures close, and others form at the contact between clay matrix and inclusions. In this

second case, the cracks are not oriented with respect to the bedding but follow the shape of the inclusions.

The volumetric response and the formation and opening of cracks upon saturation changes have a significant impact on the laboratory handling of samples. Strains and in particular, cracks may be induced, and alteration of the hydro-mechanical properties of the shale is envisaged as a consequence. For the practical applications, the response to saturation changes has to be taken into account to understand the capacity of the shale to swell, and in confined conditions, to generate swelling pressure, and for the possible contribution to the crack formations due to desaturation and resaturation processes.

7.2. Future perspectives

In this last section, further perspectives for future work are discussed.

This work focused on the experimental analysis of the Opalinus Clay heterogeneous response at the laboratory scale. A considerable amount of information on the shale response was produced and analysed, together with the literature information.

To cope with the scale of the engineering application, the knowledge so acquired would need to be upscaled. A possible way to do so is to use estimations of the sample compositions derived from calibrated log data. The information of the composition, at the log scale, may be combined with the hydro-mechanical characterisation at the sample scale to extrapolate maps of the hydro-mechanical properties of the formation. The so obtained result may be used to feed in models to simulate the response of the repository in the non-homogeneous formation and to identify critical locations in the repository design.

The response of the sandy facies of the formation has been shown to be very different from the shaly one, and its characterization needs further investigations. In this study, the anisotropic response of Opalinus Clay sandy samples was studied in oedometric conditions, and triaxial conditions by shearing the samples in the direction perpendicular to the bedding. Experimental tests in other loading directions, parallel to bedding and with an angle (e.g., 45°), are suggested to complete the set of parameters needed to describe the response of the sandy Opalinus Clay.

Further, during the lifetime of the radioactive waste disposal, the Opalinus Clay shale will be subjected to multiphysical loads, e.g., thermo-chemo-hydro-mechanical couplings. The impact of temperature or brines on the hydro-mechanical response has been detailed on the shaly facies

of the formation. The response of the sandy part of the formation is only partially explored and would need further studies.

In general, the mechanical response of shales in partially saturated conditions has not been fully understood yet, and further work is required in this direction. In this work, the impact of suction on the volumetric response of Opalinus Clay has been investigated under free swelling conditions. Further studies would require the evaluation of the volumetric response under applied stress, representative of the in situ condition. In addition, the interpretation of the hydro-mechanical response of shales in partially saturated conditions is still challenging, since a definition of effective stress for shales in unsaturated conditions is not developed yet. The measurement of matric suction above few megapascals is still not feasible and using the total suction (in place of the matric suction) in the classical effective stress definitions lead to significant overestimation of the stress acting on the shale. The impact of suction components on the effective stress in shales has not been clarified yet and would require additional research efforts. The advances on this topic would allow the interpretation of the hydro-mechanical response and the development of constitutive and numerical models capable of reproducing the response of shales in unsaturated conditions.

Lastly, many of the applications in which shales are involved, such as radioactive waste disposal and CO_2 sequestration, require the shale to act as a barrier over a long period of time. In the case of waste disposal, the estimated time is up to hundreds of thousands of years. The understanding of the shale behaviour over time is, therefore, crucial to ensure the properties on which the design can rely. The investigations on the long term behaviour of shales are necessary in order to understand their viscous response in various thermo-chemo-hydro-mechanical conditions.

Appendix

Appendix A– Position of the tested samples

In the following, the position of each tested sample is reported on the computed tomography (CT) image of the corresponding core, provided by Nagra. The cores were cut in slices, whose thickness was noted during the cutting operation. Each slice was used for one or more analyses: characterisation (definition of the geotechnical parameters, grain size distribution and MIP), mineralogy, oedometric tests (distinguishing the loading direction) including permeability tests, water retention tests. The corresponding depth of each slice was back-calculated considering the known depth of each core and the thickness of the single slice. The depth values are here reported on the CT scan, referring to the scale reported on each image.

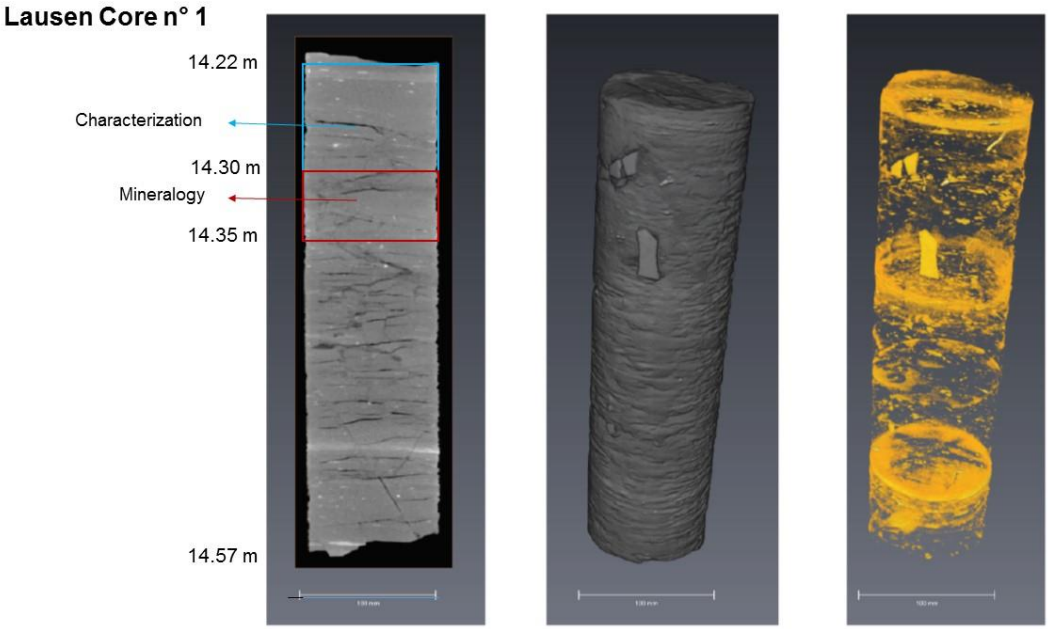

Lausen Core n° 2

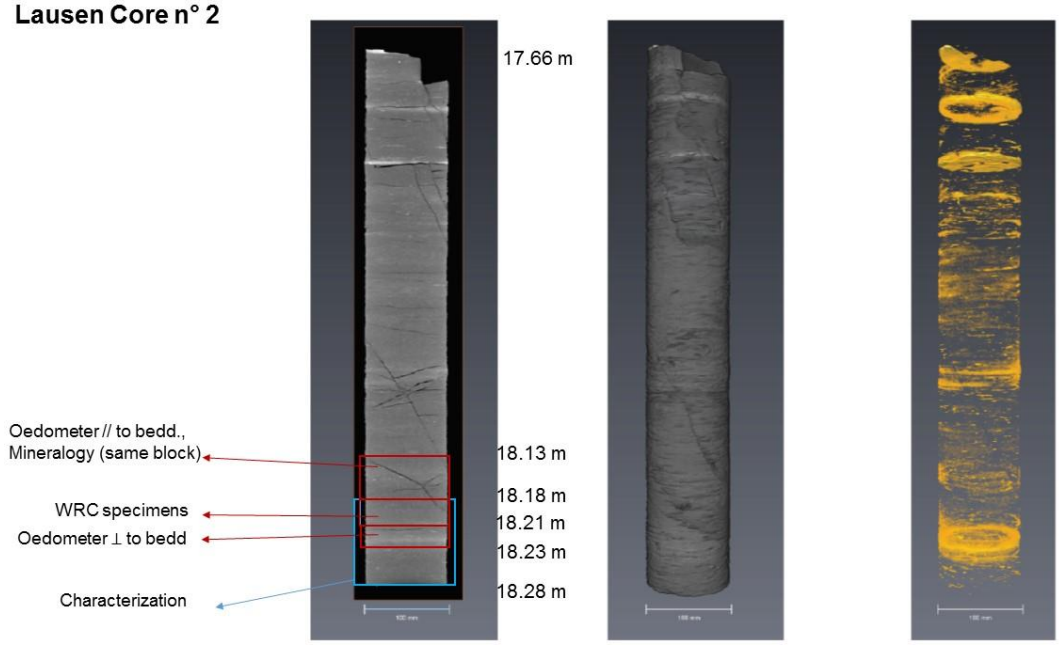

Lausen Core n° 3

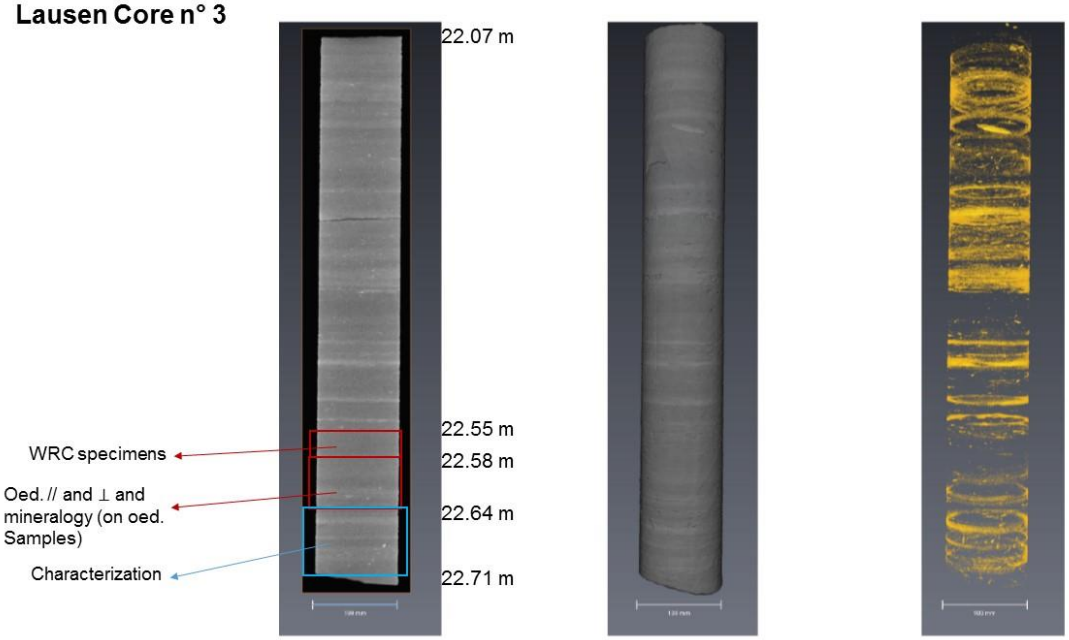

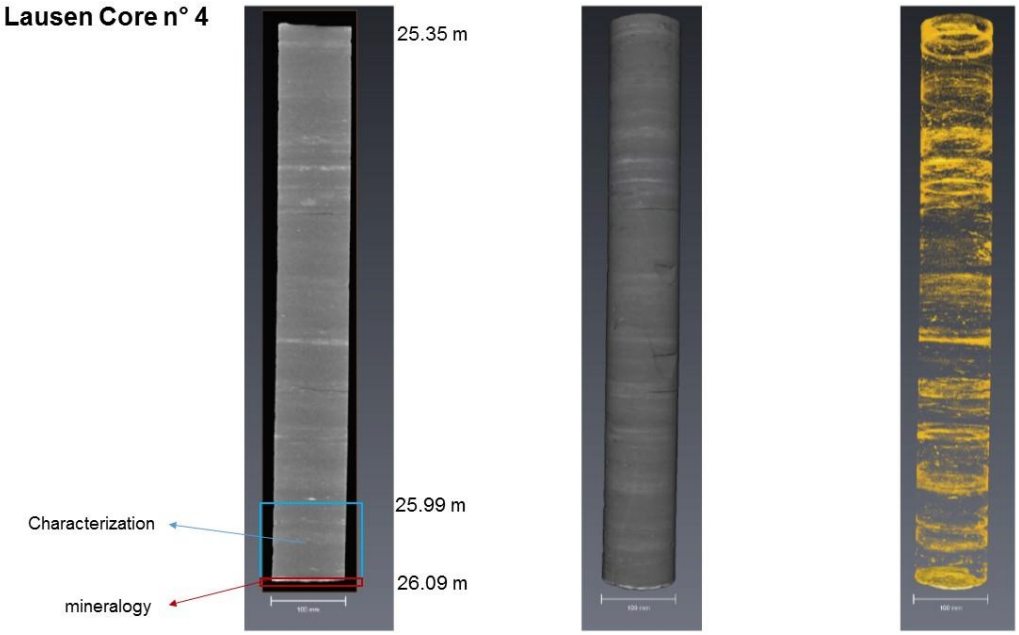
Lausen Core n° 4
25.35 m
25.99 m
26.09 m
Characterization
mineralogy

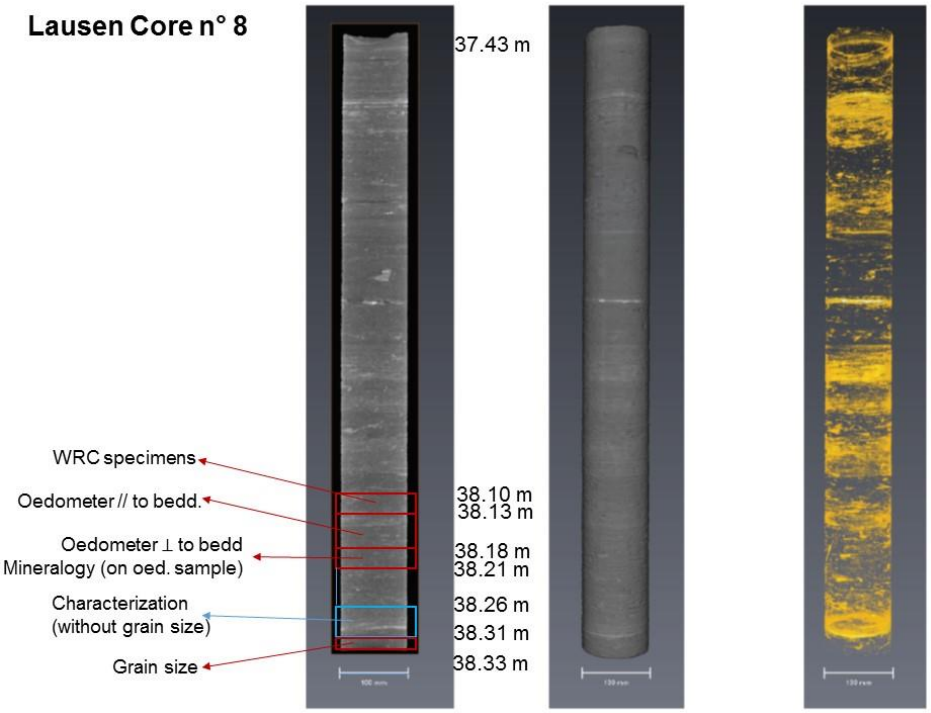
Lausen Core n° 8
37.43 m
WRC specimens
Oedometer // to bedd.
Oedometer ⊥ to bedd
Mineralogy (on oed. sample)
Characterization
(without grain size)
Grain size
38.10 m
38.13 m
38.18 m
38.21 m
38.26 m
38.31 m
38.33 m

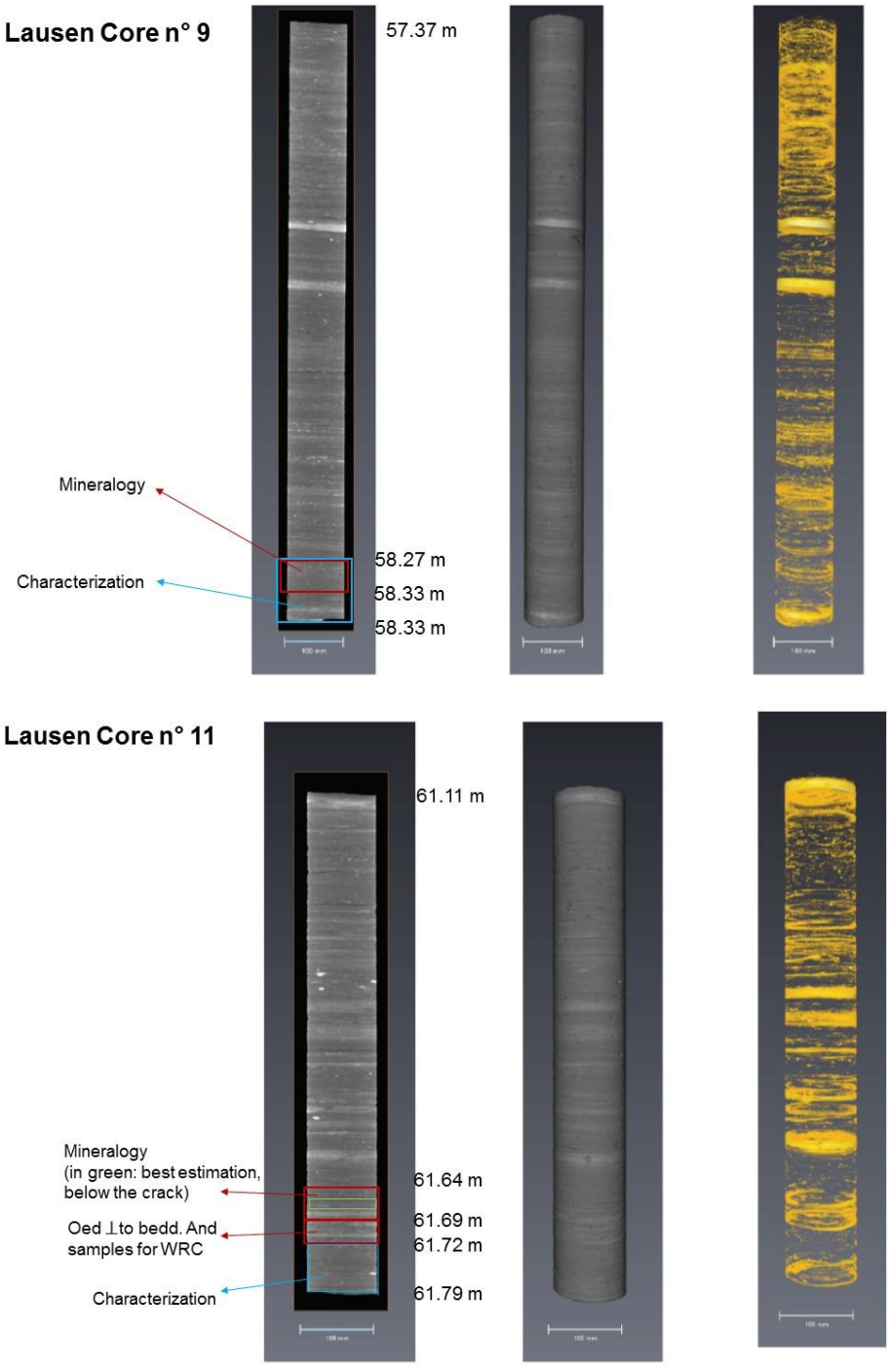
Lausen Core n° 9
57.37 m
Mineralogy
Characterization
58.27 m
58.33 m
58.33 m
Lausen Core n° 11
61.11 m
Mineralogy
(in green: best estimation,
below the crack)
Oed ⊥to bedd. And
samples for WRC
Characterization
61.64 m
61.69 m
61.72 m
61.79 m

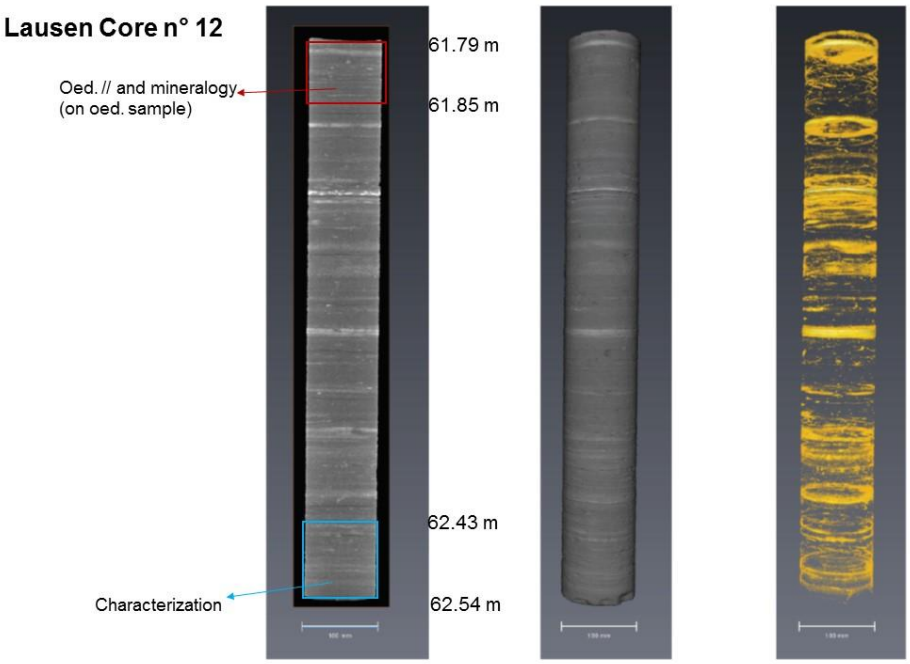
Lausen Core n° 12
Oed. // and mineralogy (on oed. sample)
Characterization
61.79 m
61.85 m
62.43 m
62.54 m

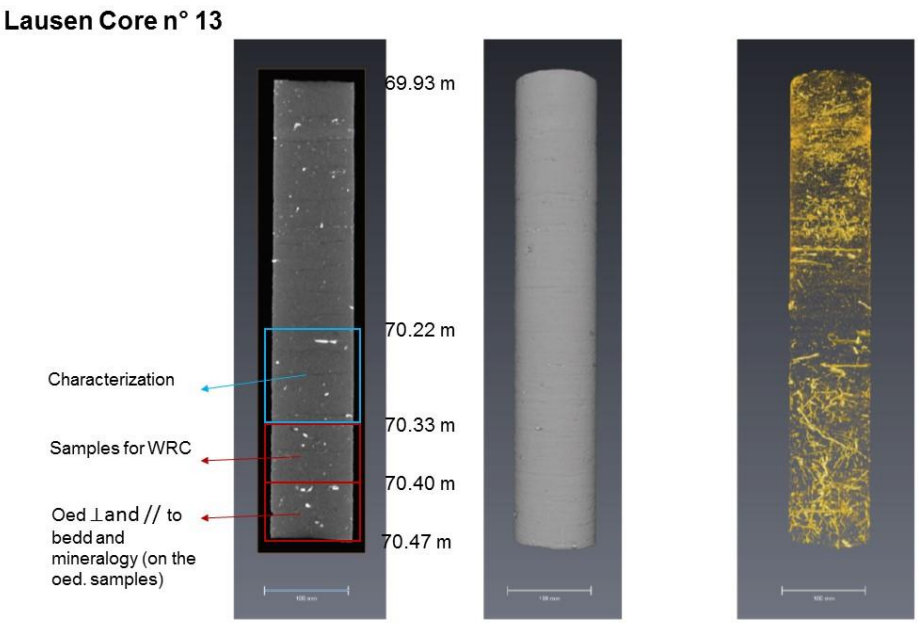
Lausen Core n° 13
Characterization
Samples for WRC
Oed ⊥ and // to bedd and mineralogy (on the oed. samples)
69.93 m
70.22 m
70.33 m
70.40 m
70.47 m

Mont Terri BHA 18

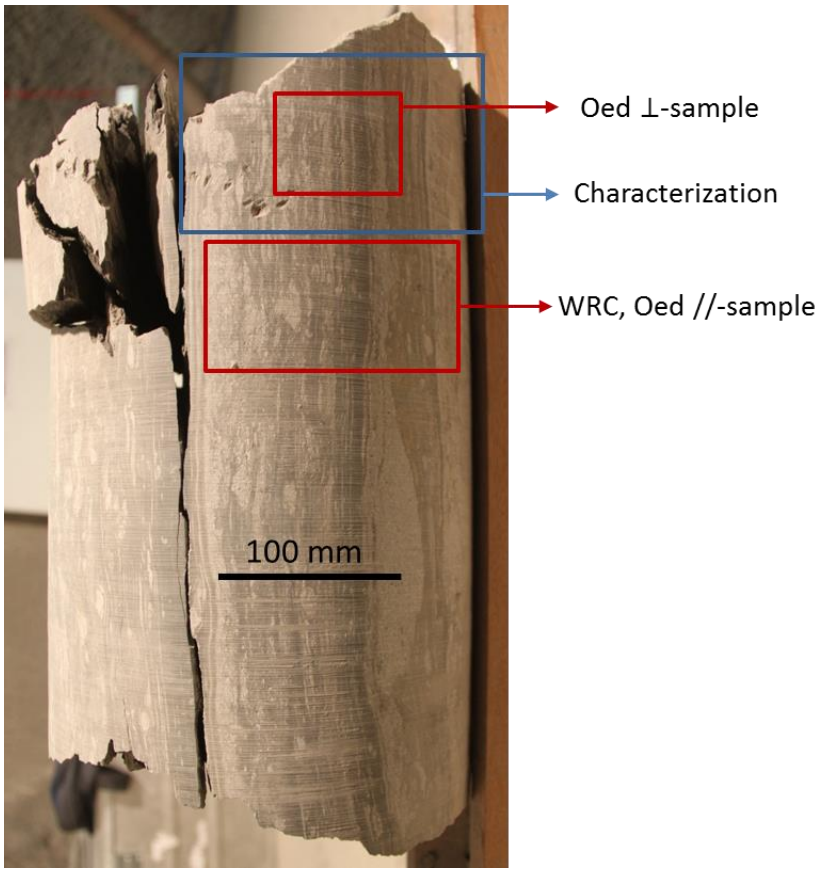

Mont Terri BGC1-14a

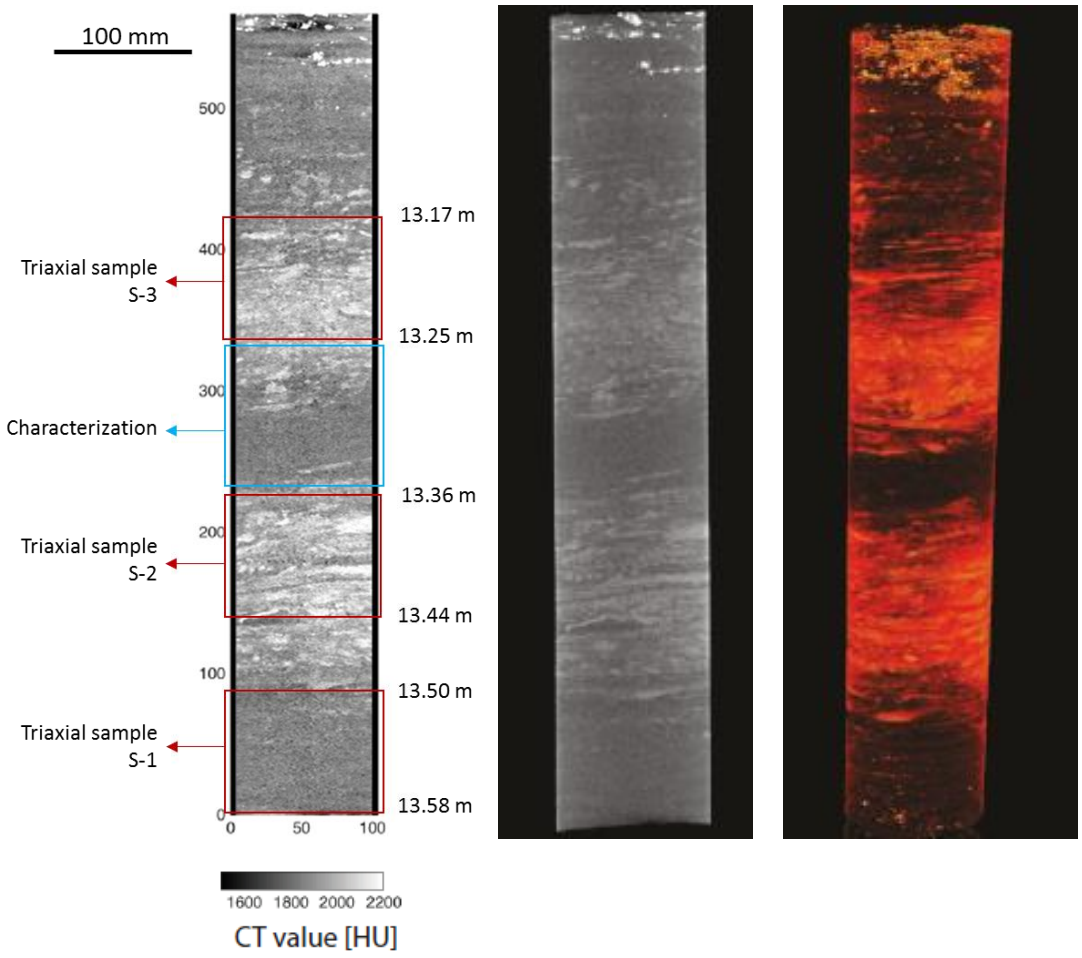

Appendix B– Triaxial samples pictures: pre and post testing

S-1 pre-test

S-1 post-test

S-2 pre-test

S-2 post-test

S-3 pre-test

S-3 post-test

Curriculum Vitae

Eleonora CRISCI

Environmental engineer
eleonora.crisci@epfl.ch
+41 (0) 762732225

Education

09.2015-10.2019 **PhD student in Geomechanics**
Laboratory for Soil Mechanics, LMS. École polytechnique Fédérale de Lausanne, EPFL. Lausanne (Switzerland).

12.2012-04.2015 **Master in Environmental engineering**
Università degli studi di Napoli Federico II. Napoli (Italy)

09.2014-12.2014 **Master project internship**
Laboratory for Soil Mechanics, LMS. École polytechnique Fédérale de Lausanne, EPFL. Lausanne (Switzerland)

09.2009-12.2012 **Bachelor in Environmental engineering**
Università degli studi di Napoli Federico II. Napoli (Italy)

Professional Experience

11.2019-Present **Post-doctoral researcher**
Laboratory for Soil Mechanics, LMS. École polytechnique Fédérale de Lausanne, EPFL. Lausanne (Switzerland)

09.2015-10.2019 **Doctoral assistant, Teaching assistant**
Laboratory for Soil Mechanics, LMS. École polytechnique Fédérale de Lausanne, EPFL. Lausanne (Switzerland).

04.2015-09.2015 **Internship**
Laboratory for Soil Mechanics, LMS. École polytechnique Fédérale de Lausanne, EPFL. Lausanne (Switzerland).

09.2014-12.2019 **Master project internship**
EPFL, LMS. Lausanne (Switzerland).

2010-2011 **Assistant**
Dean secretariat, Engineering Faculty. Università degli studi di Napoli, Federico II. Napoli (Italy)

Journal paper

Crisci, E., Ferrari, A., Laloui, L. (in prep.) Macro and microstructural analysis of shales upon wetting and drying.

Crisci, E., Ferrari, A., Laloui, L. (tech. note in prep.) Drained triaxial tests on low porosity shale: testing protocol and application to Opalinus Clay shale (sandy facies).

Crisci, E., Ferrari, A., Giger, S.B., Laloui, L. (in prep.) Impact of the mineralogical composition on the elastoplastic hydro-mechanical response of Opalinus Clay shale.

Crisci, E., Ferrari, A., Giger, S.B., Laloui, L. (2019). Hydro-mechanical behaviour of shallow Opalinus Clay shale. Engineering Geology 251, 214–227.

Minardi, A., Crisci, E., Ferrari, A. & Laloui, L. (2016) Anisotropic volumetric behaviour of Opalinus Clay shale upon suction variation, in Geotechnique Letters, vol. 6, p. 1-5, 2016

Conference paper

Crisci, E., Ferrari, A., Giger, S.B., Laloui, L., 2019. Anisotropic Behaviour of Shallow Opalinus Clay, in: Ferrari, A., Laloui, L. (Eds.), Energy Geotechnics, Springer Series in Geomechanics and Geoengineering. Springer International Publishing, pp. 442–448.

Crisci, E., Ferrari, A., Giger, S. Laloui, L., 2018. On the swelling behaviour of shallow Opalinus Clay shale. In 7th International conference on unsaturated soils.

Crisci, E., Ferrari, A., Giger, S., Laloui, L., 2017. One Dimensional Consolidation of Opalinus Clay from Shallow Depth, in: Advances in Laboratory Testing and Modelling of Soils and Shales (ATMSS), Springer Series in Geomechanics and Geoengineering. pp. 338–344.

Minardi, A., Crisci, E., Ferrari, A., Laloui, L., 2017. The Role of Anisotropy on the Volumetric Behaviour of Opalinus Clay upon Suction Change, in: Advances in Laboratory Testing and Modelling of Soils and Shales (ATMSS), Springer Series in Geomechanics and Geoengineering, Cham, pp. 315–321.

Crisci, E., Ferrari, A., Urciuoli, G., 2015. Collapse-upon-wetting behaviour of a volcanic soil. Volcanic Rocks and Soils, 133.

Technical report

Ferrari, A., Crisci, E., Laloui, L., 2018. Arbeitsbericht NAB 17-27. Geotechnical Experimental Characterisation of Opalinus Clay Cores from the Borehole Lausen (Prepared for *Nagra*, National Cooperative for the Disposal of Radioactive Waste, Switzerland).

Ferrari, A., P. Dubey, V. Favero, Crisci, E., 2018. Triaxial and simple shear tests on unsaturated MX80 bentonite (Prepared for *SROY*, Saanio-Riekkola Oy, Finland).

Crisci, E., Ferrari, A., 2017. MX-80 bentonite swelling pressure and gas breakthrough tests (Prepared for S*hell Wells R&D*, Netherlands).

Talks (T) and poster presentations (P) at international conferences

2019 6th EAGE Shale Workshop (P). Bordeaux (France)
2019 International Symposium on Energy Geotechnics SEG (T). Lausanne (Switzerland)
2018 7th International conference on unsaturated Soils UNSAT (T). Hong Kong.
2017 International workshop ATMSS - Advances in Laboratory testing and modelling of Soils and Shales (T). Villars sur Ollon (Switzerland)

2017 7th international conference on clays in natural and engineered barriers for radioactive waste confinement (T). Davos (Switzerland

Languages

Italian: native speaker
English: professional knowledge
French: good knowledge

Technical skills

Development of procedures and protocols for laboratory testing
Laboratory testing and analysis for soils and rocks.

Additional training

Mercury intrusion porosimetry (2015). Laboratory of Construction materials, EPFL, (Switzerland)
X-ray micro-computed tomography (2017). Interdisciplinary Platform for X-ray micro-tomography (PIXE), ENAC, EPFL (Switzerland)

Software

Plaxis, MatLab, Avizo, Geoslope, ZSoil, Autocad, ArcGis,

Miscellaneous

2016- Present Member - No profit Association *Sos Eau Giteranyi*
2018 Technical Staff – International Conference Tech4Dev. UNESCO Chair in Technologies for Development: Voices of the Global South. Lausanne (Switzerland)

**Ce document a été imprimé au Centre d'impression EPFL,
imprimerie climatiquement neutre, certifiée myClimate.**